ISSN : 0075-5168
VOLUME : 51
YEAR : 2020

KARNATAK UNIVERSITY

JOURNAL OF SCIENCE

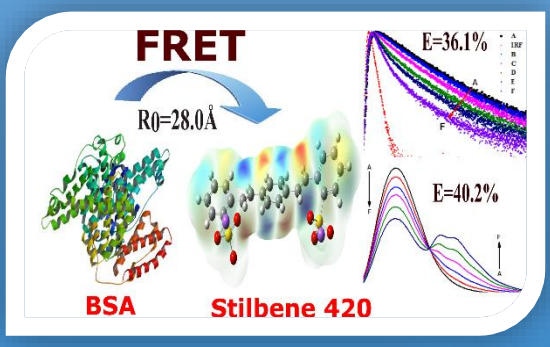

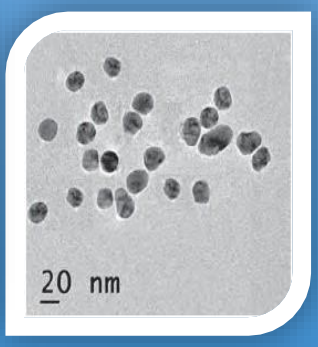

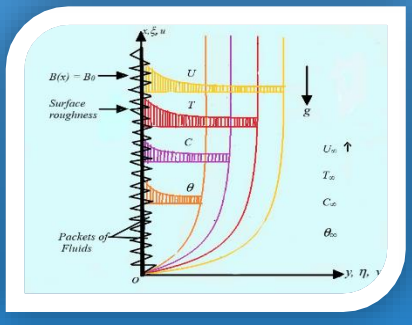

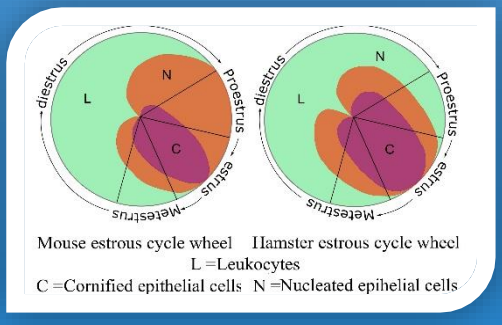

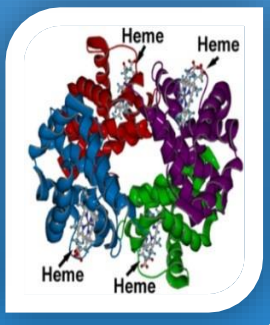

KARNATAK UNIVERSITY, DHARWAD 580003

Karnatak University

Journal of Science

Chief Editor

Dr. Sanjeev R. Inamdar

Professor, Department of Physics

Karnatak University, Dharwad

Vol. 51, September 2020

Editorial Board

FOREWORD

Karnatak University is known for quality research in science since the establishment of the University. The results of research are being published in reputed National and International Journals. The science faculty members have engaged in frontline research and have established collaborative research activities with researchers from Premier Institutions/Universities in India and abroad. This has made possible exchange of ideas, imparting better education and training to our students leading to a surge in the number of students taking up research as a career in National and International laboratories. Many of our science faculty members have been recognized with top awards, fellowships of Premier Science Academies in the country and outside. Some faculty members have successfully generated patents. Many awards from the Central and State Governments have been bestowed to our science departments which have made the University Proud.

The Karnatak University Journal of Science (KUJS) has been showcasing the research output of our science departments since many years and this year its 51st volume is coming out. I am glad to note a remarkable change incorporated in this volume. Firstly, articles have been classified as Mini Reviews, Regular Articles and most importantly two General Articles pertaining to Evolution of Education and Impact of the Prevailing Covid-19 pandemic on Higher Education. I congratulate the Chief Editor, Prof. S.R. Inamdar and the entire Editorial Board comprising of National and International researchers of eminence who have done a wonderful job to elevate the status of the journal. All the publishing ethics on par with international publishers are followed. I hope and I am sure, their efforts will take our journal to greater academic heights. This volume has set the standards for future volumes to come.

5/9/2020

Prof. Vishwanath M.
Acting Vice Chancellor
Karnatak University, Dharwad

From Editor's Desk

Karnatak University Journal of Science has come a long way and we are just bringing out the 51st volume to the scientific community. The previous volumes published research articles from all branches of science viz., Physics, Chemistry, Zoology, Botany, Mathematics, etc. by the faculty of members of the science departments of Karnatak University, Dharwad. It was felt by many that the Journal needed not only needed facelift but also enhancement in its status and further improvement in its quality. Thus with a view to expand its readership and extend its reach outside the university jurisdiction to other universities and premier institutions of the country and abroad we decided to invite articles from outside Karnatak University in addition to those from our own campus. While there was concern as to whether there would be a reasonably good response from researchers outside Karnatak University, we were surprised to receive papers for publication in this journal. Further, there was a need to do away with the monotonous pattern of compilation of regular research articles. Thus, it was decided to publish reviews, regular papers and general articles pertaining to higher education. I am glad that our views were met with success and three general articles were received. Four Mini reviews from our university and other institutions in addition to more than 10 regular articles that reflect on the recent advances in different disciplines have been selected for publication in this issue after peer review by experts. With the proposed New Education Policy we felt a need for an article which can throw light on the Evolution of Education in India. Hence, we are publishing the Teachers' Day Foundation Lecture by Prof. S.K. Saidapur, former Vice Chancellor of our University, delivered on 5th September 2020 at the Karnatak University. The country is suffering from the Covid-19 pandemic and its impact is felt in day-to-day life. More importantly, we need to worry about its impact on education and research. The article on the impact of Covid-19 on higher education in the country by Prof. B.N. Jagatap of IIT Bombay is thought provoking. I am sure, the researchers will welcome the journal with its new features.

Dr. Sanjeev R. Inamdar

CONTENTS

Karnatak University
Journal of Science

ISSN: 0075-5168

Role of Teachers in Changing Education Scenarios

(Educationist's Day and Teacher's Day Address given at Karnatak University on 5th September 2020)

S. K. Saidapur

S. K. Saidapur, "Role of Teachers in Changing Education Scenarios" Karnatak University Journal of Science 51, 1-10 (2020).

Role of Teachers in Changing Education Scenarios

(Educationist's Day and Teacher's Day Address given at Karnatak University on 5th September 2020)

S. K. Saidapur ***FASc., FNA, FTWAS, FNASc.***
Diamond Jubilee Professor (for Life)
Department of Zoology, Karnatak University Dharwad
Former Vice Chancellor, Karnatak University, Dharwad &
Founder Directorof Karnataka State Higher Education Academy, Dharwad-580003
saidapur@gmail.com

Respected acting Vice Chancellor, Prof. M. Vishwanath, Dr. K.T. Hanumantappa the Registrar, Prof. S.R. Inamdar, the Organizing Secretary of Foundation Lectures, Registrar (Evaluation), Members of Faculty, Syndicate and AC, media personnel, invitees, ladies and gentlemen, good morning and Greetings of teacher's day to you all. As an alumnus of this university, I feel greatly honored to be here in the company of my former colleagues and fellow teachers and also meet the new faculty members. As a customary requirement let us remind ourselves of Sir S. Radhakrishnan the illustrious former President of India in whose honor we celebrate, his birthday as 'Teacher's Day'. He was a world teacher and enjoyed great respect. There is so much to talk about Radhakrishnan, his contributions to philosophy, his views on life, his services as diplomat, and relation with the Russian monarch Stalin as well as anecdotes associated with him.

I am equally happy to be part of the 'Foundation Day' celebration observed in recognition of the contributions of the early architect of this university i.e. Dr. D. C. Pavate and deliver Pavate Memorial lecture. He was VC of this university for about 13 years. I took my admission for my Masters Degree in the year 1967 while he was the VC. He was a very strict disciplinarian, and could take hard decisions. He brought eminent faculty members from different parts of the country and that is how good foundation was laid for academic progress of this university. The majestic and very imposing 'Vidya-Soudha' is his contribution to the university. Furthermore, he was the guiding force for me during my term as VC. Therefore, being here today is a double bonanza for me: celebration of University's Foundation Day & Teacher's day together. Thank you for this wonderful opportunity.

In this talk I wish to focus on the fast changing education scenario and consequent compulsions on the teachers to remain relevant. In this context, let us first have a bird's eye view to see how our education system (E 1.0-4.0) evolved, how industrial revolutions (IR 1.0-4.0) took place and the relationship between the two. Finally, we should ask what the way forward is and what factors would guide the future education?

Significance of Education:

First let us ask what education is all about. What is the difference between education and literacy? The latter provides ability to read and write. But, mere literacy and ability to read and write is not education. Education is the manifestation of 'perfection' said Vivekananda. If we accomplish perfection then all conflicts within and between us will at once vanish. A well educated person will not inflict pain on others unduly. Education is for production of human resource; competent people are needed in all facets of human endeavors and to sustain peaceful co-existence of human societies and the nations. It was Jawaharlal Nehru who said in his convocation address of Allahabad University and I quote ***"A University stands for humanism for tolerance, for reason, for the adventure of ideas and for the search of truth. It stands for onward march of the human race towards even higher objectives. If the universities discharge their duties adequately, then it is well with the Nation and the people".*** By implication, all ills of the society can be attributed to declining quality of varsity education. Undoubtedly, University teachers have great obligation to own this single and primarily most important responsibility of building a humane society and congenial ecosystem that is worthy of living in peace and tranquility with all living beings. Quality education is also the key to building human resource of all kinds endowed with skills, competency and commitment – be it in the field of science & technology, engineering, health care, management of environment (ecological resources- utilization and conservation) or social sciences, economics, foreign affairs, trading & business, legal, international and defense related issues and so on. In this globalized world absolute competency is vital for survival of the nations. Statement of Nelson Mandela displayed at the entrance of the University of South Africa reads as: ***"Destroying any nation does not require the use of atomic bombs or the use of long-range missiles. It only requires lowering the quality of education and allowing cheating in the examinations by the students."*** Further it says:

"The patient dies in the hands of the doctor who passed his exams through cheating,

And the buildings collapse in the hands of an engineer who passed his exams through cheating,

And the money is lost in the hands of an accountant, who passed his exams through cheating,

And humanity dies in the hands of a religious scholar, who passed his exams through cheating,

And, justice is lost in the hands of a judge who passed his exams through cheating,

And ignorance is rampant in the minds of children who are under the care of a teacher who passed exams through cheating,

The collapse of education is the collapse of the nation*".*

Prosper Dzitse, a lecturer in the same university added the following (with permission) to the above**:**

"Shoddy laws are made by the politician who passed exams through cheating.

Half or unverified information is given by the journalist who passed exams through cheating.

Unjustifiable/unpatriotic actions are supported by citizens who passed exams through cheating.

Substandard works are done by the public/civil servant who passed exams through cheating.

Half/subjective analysis is given by civil society organizations whose leaders passed exams through cheating.

Uninspiring leadership is given by the leader who passed exams through cheating.

Indeed, the collapse of Education is the collapse of the Nation".

Evolution of Education System:

India is the mother of all civilizations. It represents one of the 45 or so surviving civilizations of the world. She will always be remembered for her several notable contributions in the fields of science and technology, mathematics, medicine, yoga & meditation, metallurgy, architecture and engineering and more importantly universal message of *spirituality* to the whole world (see Gautier 2013, 2019). India may well become the world leader in promoting the pursuit of ultimate truth, knowledge, attainment of wisdom, man's role in the preservation of Mother Nature (biodiversity) and living in harmony with people of all faith, religion, culture and ethos. This is our potential. For this to happen, schooling should help instill *self-esteem* and *national pride* in the minds of the learners and promote embracing lingual, religious and ethnic diversities with equal reverence. Education is the operating system to help realize these goals.

Globalization in the wake of WTO, and GATT have posed many new challenges especially in trade and business, international affairs, international disputes, IT, defense related (e.g. acquisition of deadly weapons of mass destruction) issues and strategies to name a few. Developments in science and technology over the past 3 centuries have led to unexpected developments and industrial revolutions (IR 1.0-4.0) which in turn have great impact on education paradigms. The educational institutions and education systems are also organic entities and as such they are poised to undergo evolution. Let me outline the major landmarks in evolution of education system within India.

Gurukul system of education was the dominant system for centuries and from time immemorial. This apparently represents Education 1.0 (E1.0). Typically for learners education meant passive absorption of knowledge rendered by the scholars initially at their residences, and later in 'Gurukuls' as the number of learners increased. The pupils learnt a bit of literacy, arithmetic, ancient scriptures and many life skills. They rendered services to the Guru and paid Guru Dakshina at the end of their training and returned home. A Guru was held in highest esteem by the entire society.

Under the inescapable influence of the invaders especially the Brits the education system began changing or so to say modernizing. The British rulers greatly felt the need to impart working knowledge of English, teach their mannerisms and customs to native Indians

for smooth communication, record keeping and accounting, and thereby enhance quality of service rendered by the natives to colonial masters. Anglicization of Indian education thus began systematically more so following Sir Wood's dispatch (1854) and a little later Sir Macaulay's well articulated doctrine for transforming native Indians to think and behave like the British, acquire and adopt their customs, manners, and uninhibited appreciation for everything English on one hand and on the other to despise Indian customs, manners and life styles. The strategy meant creating personnel who would be interpreters between natives and the English rulers, a class of people, Indian in blood and color but English in tastes, and more importantly in opinions, in morals and in intellect. Such a population would be happy consumers of British goods and also serve in various lower rank positions. The missionaries then set up colleges in different regions of the country. This marked the genesis of Education 2.0 which persisted with 'chalk and talk' method till mid 20th century or so. In 1860, Indian Universities Act (1860) was passed which enabled setting up of education commissions, and thereafter universities and colleges in cities like the Calcutta, Bombay, Madras and Delhi and etc. These institutions progressively promoted Anglicization of education on one hand and deterioration of knowledge of Indian heritage, ethos, history, Indian medicine and culture. Worst fallout of these is the loss of national pride and self esteem. The hangover of the 'colonial mindset' still looms largely even after 74 years of independence. This is really detrimental and a curse. We must decolonize our mind and mindset at the earliest.

Make no mistake; India had fund of knowledge in the form of Vedas, Upanishads, Puranas, Smritis (Smrutis and Shrutis), epics like Ramayana and Mahabharata, Panini's Ashtadyayi, Kautilya's Arthashastra, Bharata's Natyashastra, Medical treatises of Chakra and Sushruta, Dramas of Shudraka, Bhasa, Kalidasa, teachings of Buddha, Mahaveera, Basaveshawara and innumerable number sages from various parts of India. This wealth of knowledge available then was enough for establishment of Pathashalas, and even universities (e.g., Nalanda and Takshasila) during the early Christian era or more much before it.

Education 1.0 typified by the use of 'chalk and talk' dominated teaching-learning processes till the late 20th century. Education 2.0 is a continuum of E 1.0 that began following the availability of teaching aids, like the over head projectors (OHP) and power point slides (PPTs) as additional tools of teaching during the last quarter of the past century. It did not differ much from the basic framework of education 1.0 except that it was more digitized. With the commencement of the 21st century, learning through newer ways became possible that include use of Smart Boards, Social Media, Emails, Wikis, Blogs, Facebook, Twitters and WhatsApp. The new avenues facilitated production and publication of the contents (even by the learners) and sharing through social networking, as well as open access to educational and research materials, and inter-institutional collaborations. Progresses in digital technology also enabled e-governance of education system (administration, teaching, evaluation and declaration of results etc.). This integration of education with technology represents the onset of Education 3.0 (E 3.0). Digital technology is now playing a key role in educational reforms and their management. Extensive use of complex digital technology is the hallmark of Education 4.0 (E 4.0).

Industrial Revolution:

Education and IRs are closely interlinked, and impact each other. Currently the world is witnessing the IR 4.0. India missed IR 1.0 (in England) and IR 2.0 (in America); both occurred during the time of British colonial regime. Consequently, India remained unmindful of the importance of the linkage between industrial revolution and education. Technological

developments by and large succeed advancements in education and research. Yet, technology may come first without any knowledge of the underlying principles which get revealed later.

Briefly speaking, IR 1.0 took place around the year 1780 in England and was characterized by *mechanization* of productions using water and steam power, and weaving looms. It is noteworthy that England does not grow its own cotton. Where did they obtain cotton and bring about textile revolution? Your guess is as good as mine. From India! The IR 2.0 took place in USA around the year 1870 which enabled *mass production* with assembly lines (division of labor) using *electrical energy*. The third, IR (3.0) took place around the year 1969. It enabled *automation* in the production of goods following advancements in the field of electronics and computer sciences. It was driven by *simple digitization* technology. Unlike the first three IRs there is little gap between 3rd and 4th IRs.

The IR 4.0 which commenced in less than 20 years after the onset of IR 3.0 has a massive impact on people, education, jobs, skill development and so on as it utilizes *complex digitization* technology (cyber physical systems). It is more powerful than the preceding IRs both in speed and impact due to great breakthroughs in internet related developments, robotics, driverless autonomous vehicles, 3-D printing, quantum computation, material science, nanotechnology, biotechnology, energy and data storage facilities, artificial intelligence (AI) and so on. A swift progress in IR 4.0 has made it possible for *mass manufacture* of products, rise in income levels and, improved quality of life. Domino effect of IR 4.0 is *technology driven disruption in jobs*. Several kinds of jobs and industries have succumbed to it. A classic example is the fall down of the leading Kodak Eastman Company which unfortunately did not anticipate the impact of complex digitization technology.

Seemingly simple and affordable devices like smart phones can now do innumerable types of jobs replacing the need for separate and multiple devices (ex: Telephone, TV, Radio, Computer, Calculator, Organizer, GPS, Dictionary & Thesaurus, Camera, Torch, Mobile banking, Online shopping, booking tours & hotels, accessing e-books, journals, content sharing, active participation in social media like the Face book, Twitters, Blogs, Data storage and so on to name a few). As a result, many industries went out of business and were shut down and several types of jobs available hitherto have now disappeared. With specific apps in place, smart phones perform unimaginable number of tasks with ease and swiftness.

Many *transactional* reforms, have also taken place which are simple as well. The major drivers of the 4th IR are: increased use and application of computational technology, AI, rise of smart machines and systems, communication tools, new media literacy and media ecology, super-structured organizations, global connectivity, increase in human longevity etc. All these will greatly impact the labor market, income of workers, and displacement of workers by machine and AI.

Technology driven *disruption in jobs* is indeed a serious issue but one need not become too gloomy because new technologies also create new jobs whose requirements will however change. For instance, maintenance of novel technologies and their up gradation will require new skills. Hence, there will be a growing demand for new skills like critical thinking, creativity, emotional intelligence, cognitive flexibilities, ability for co-working, co-creating with men and machine. In short, IR 4.0 calls for sustained creativity and eternal innovation. Expectedly, usage of 'Internet of Things' (network of physical devices, vehicles, home appliances, and other devices embedded with electronics, software, sensors, actuators, and connectivity which enables these objects to connect and exchange data) will become very

common. In this process, many challenges will surface at the workplaces. So, the present and future generations of youth (Gen Z population) need to be prepared to meet these challenges.

Reimaging Higher Education:

In reimaging education for 21st Century, Universities must address the issues of job disruptions and training the youth such that they shoulder the responsibilities confidently and also emerge successful as creative thinkers, innovators and entrepreneurs. Failing to do so, the prevailing demographic dividend in the form of soaring youth population can turn out to be catastrophic. Therefore, planning future education with great care is warranted to address the issues raised above as there is no escape from the impact of the ongoing industrial revolution. It calls for major changes in our education system, thinking, logistics and management if we have to stay relevant and sail through the global challenges and competitions smoothly. Making innovations will remain the focal point of future education systems.

What are the major challenges posed by IR 4.0 on day to day life? First, it has caused disruptions in jobs. Second, it demands for new skills on a continuous basis. Hence, there is an exigency to redesign and develop a new education system - education 4.0 (E 4.0) with a clear *blueprint* for future teaching-learning processes. The new paradigm broadly includes blended learning, lifetime learning as well as learning to play a constructive role in the society. We need to clearly foresee the future trends and needs and empower education system itself so as to promote innovations. This envisages a shift from *'brain as storage to brain as processor'* model. Obviously, the new education system must focus on interactive learning with discussion, question & answer sessions, quizzes & seminars, problem solving, group learning, and project based learning. Such reforms will provide scope for customization and personalization of educational content and teaching-learning processes in relation to slow or advanced learners as well. Our classrooms will have to be transformed in to virtual and flipped classrooms to make them suitable for adoption of new pedagogies. This will promote conveying lectures (theoretical aspects) online and practical learning (hands-on experience) is done together in the labs not only with the guidance of the teacher but through interaction among the learners themselves. The drivers of future education are mainly the future skills, digital networks and devices, personal data, shared content and resources, collaboration platforms, talent investment, 100 year life expectation, millennial mindset and social progress.

A movement towards education 4.0 envisages a change in the *mind* and the *mindset* of teachers, learners and the education managers. Of these, mind is no serious issue since the Indian mind is as superior as that of say Anglo-Saxon, Caucasian or any other. However, mindset vis-à-vis our *attitude* can be a problem. Fixity in the attitude of the teachers can hamper implementation of future education policies. Anticipative hindrances will arise due to growing digital divide between the teachers and the taught in foreseeable future. Let me explain. Though at present one in thousand persons has a personal computer, the Gen-Z population of youth (those under 20 years of age) have access to smart phones and access to computers. They are also fast learners and more advanced in handling and using these devices compared to their teachers. Therefore, reluctance on the part of teachers to adopt digital mode of teaching though unfortunate is very probable. Many teachers will continue to use 'chalk and talk' method and claim its superiority over the modern methods. True, teaching under the banyan tree or use of chalk and talk method when information was limited had its own merit. In this age of information explosion it is futile to evade modern pedagogies and swim against the current in vain. It is impossible to manage the information boom without the computers with large data storage and swift retrieval facilities. Moreover, teaching is now largely aided by several modern / digital devices that help both teachers and the learners. Therefore, adoption of more

and more learner-centric teaching by meticulously planning to nurture creative thinking, group learning, blended learning, making innovations and so on is rather crucial. In the hanging scenario of education, the teachers themselves have to be creative and continue to be lifetime learners. A teacher is no more a *sage on the stage* but only a *guide on the side*.

The Way Forward:

Education is a dynamic process and it shall remain so always. Currently it is undergoing rapid changes in tune with the technical and academic advances and, industrial revolutions. Teachers have greater responsibility of remaining relevant to the contemporary requirements of the learners and the society at large. Reluctance to change and become accustomed to the novel requirements will harm future generation of students, and stunt national growth. Following paradigms will be the major components of the future education scheme.

(1) Devising learner-centric teaching that is skill based and involves group learning (with due respect to aptitude and ability of learners).

(2) Adoption of new pedagogies to promote Self learning, Group learning, Blended learning (combination of offline and online learning: use of Learning Management Systems-the LMSs), using gadgets like the Smart Phones and Tablets, extensive use of virtual class rooms (Flipped class rooms) and virtual labs, Problem solving and Monitoring progress of each learner, widespread use of Internet based technologies and so on. The time-honored class room teaching may even become outdated.

(3) New methodologies that involve teaching *'creative thinking'* and making scientific *'innovations'* will assume paramount importance in the future teaching processes.

(4) Learning through project mode and group learning will become vital.

(5) Consequently, a future teacher will become more of a facilitator, mentor, guide and confidence builder.

Teachers have to be life-time learners so as to avoid widening the digital divide between them and the learners. Despite the limitation and affordability of digital devices, already half of the world population seems to be linked by the internet. So there is no escape from digital literacy and it's endless up gradations with time. Therefore, teachers have to be creative themselves as well as keep enhancing their own professional competency so as to stay relevant as well as sustain their own importance in the society. Evidently, novel reforms in the curriculum and assessment of learning outcomes are needed as soon as possible. Continuous assessment is more desirable than the semester-end examinations. Therefore, reforms are needed in examination and assessment processes. Further, the recently announced 'National Education Policy-2020' (NEP) will pose many challenges wherein teachers have a pivotal and compelling role in ensuring its smooth implementation as well as success in the national interest.

Before I conclude let me touch upon one more important aspect of education: d*issemination of national pride* and *self esteem.* India's strength lies in areas like: mathematical sciences, astronomy, metallurgy, architecture, Ayurveda, Yoga, Meditation, and, Spirituality to name a few. In addition, India has made significant gains in the field of space science and IT. Ours is the oldest surviving civilization with huge cultural and linguistic diversity. Yet, a matter of great concern for the nation is the loss of self esteem, national pride, respect for

country's culture and ethos, and patriotism in the minds of our learners as these aspects are grossly overlooked in our curriculum. It is time that we now embark rather seriously on teaching true history and culture of India at all levels, from school to University education. For this our history books need to portray the truth (good and bad), but as it happened (Gautier, 2013, 2019) and that should be taught to future generations of students. There is so much to learn from history. Western world periodically recaps mass killing of Jews under German Nazi regime between1941-45 through movies and social media. Likewise, India must remember the sad parts of history like the genocides during the Islamic invasions, destruction of temples, Goa inquisitions, forced religious conversions and Massacre of Sikhs again and again through movies, and TV shows just as we remember Gandhi, Bhagat Singh, Veer Savarkar or other freedom fighters for their sacrifices and their tryst with the nation. Future generation of learners can discover a lot from the historical mistakes on one hand and on the other get inspired by the notable achievements. The new generation of students ought to know the historical truths, ancient wisdom and the very culture and ethos of the country. It is utterly unwise to bury India's history and glory and at the same time hope to learn from it. Let me recall the eminent statement of Prof. D. S. Kothari who said ***"How can we lament lack of national pride in Indians without first acquainting them with the country's phenomenal scientific achievements in the dim distant past"?*** It is time that academicians and the policy makers devise ways, without wasting time, for instilling national pride and self esteem in the minds of learners which is long due.

The recently announced "National Education Policy 2020" addresses major revamping of education system as a whole. Hope it serves as a game changer in both school and collegiate education. While we are yet to fully accomplish education for all and 'right to education' we must plan for 'right education' as well as 'right way of education' (R. A. Mashelkar cited in Saidapur 2019). The key feature of 21st century education is ***education in innovation and innovation in education.*** Failure to recognize this exigency is sure to demolish demographic dividend that we boast of. In a ruthless world that is witnessing rapid progresses in scientific technologies, industrial revolutions and job disruptions, the only way to be successful is by acquiring skills and competitiveness of global standards without further ado. Also, while we need to innovate for our own sake, we must keep track of the global trends while making innovations in order to stay competent and relevant now and in future. If our inventions, discoveries and scientific advancements become trend setters, they can enrich not only India but the whole world. There is no scope for reluctance in transforming our education system or being apologetic about it. Change or perish is the new norm. Universities being the 'organic entities' they cannot afford to remain stagnant and become fossilized.

Lastly, in the fast changing education scenario staying relevant is the biggest challenge of teachers today. We all must note what Alvin Toffler said: *"The illiterates of the 21st century will not be those who cannot read and write but those who cannot learn, unlearn and relearn"*.

Thank you for your patient hearing and best wishes to all.

Additional Reading Material:

[1] Gautier, F., (2013). *A History of India as it Happened: Not as it has been written*. Har-Anand Publications, Pvt. Ltd., New Delhi.
[2] Gautier, F., (2019). *In Defence of a Billion Hindus: One of the most marvelous people on this planet-ever*. Har-Anand Publications, Pvt. Ltd., New Delhi.
[3] Saidapur, S. K., (2017). Revamping Higher Education, Guest Editorial. *Curr, Sci*. **113** (September 10), 831-832

[4] Saidapur, S. K., (2019). *Management of Collegiate Education in the 21st Century: Some Insights* (ed. S. K. Saidapur), Gyan Books, New Delhi. Pages 354.
[5] Saidapur, S. K., (2020). Trends in the 21st Century Education. *University News*, **58** (18) May 04-10, 2020.

Karnatak University
Journal of Science

ISSN: 0075-5168

Rediscovering Higher Education Post Covid-19 Pandemic

B.N. Jagatap

B.N. Jagatap, “Rediscovering Higher Education Post Covid-19 Pandemic” Karnatak University Journal of Science 51, 11-16 (2020).

Rediscovering Higher Education Post Covid-19 Pandemic

B.N. Jagatap*
Department of Physics
Indian Institute of Technology Bombay, Powai, Mumbai 400076
Corresponding author: bnjagatap@gmail.com

1. Introduction

Covid-19 is a crisis unprecedented. The public health concerns have prompted large questions on economy and social life. The pandemic has also severely affected the education sector and in particular the higher education that we are concerned with in this article. The impact can be gauged by closed colleges and universities, disrupted semester, uncertainties over examinations and reopening of institutes, and a bleak job environment. The governments, universities and colleges all over the world are struggling to respond to the rapidly developing situation.

The pandemic has brought into focus the inherent shortcomings of the higher education system in India. Firstly, the closure of colleges and universities has led to a haphazard implementation of online teaching and learning in some pockets. However, the digital divide in the country is challenging the equity in the access of education and posing serious questions over how are we going to deliver education in the near future. Secondly, the economic disruption caused by the pandemic is expected to threaten admissions in the next academic year, since the students from the weaker economic section of the society are more likely to drop out of the higher education. This will prove detrimental to our long cherished dream of education for all. Thirdly, the pandemic has exposed the fragile correlation between education and jobs opportunities in India. The youth of the country is worst affected owing to an evident decline in job opportunities. The higher education system will now need to reposition itself to enhance the employability of the graduating students. The fourth issue is the very weak response of higher education systems to provide solutions to the present crisis. This brings us to the old criticism of higher education in India that it is not connected with the local or national problems.

The issues highlighted above demand a major change in the objectives and delivery of higher education in India. This change has been overdue for a long time; Covid-19 pandemic has only hastened it. At the same time, an intense debate on this need for change is lacking in the academic circles. All over the country, the only sore point of discussion has been the examinations whether they should be conducted or not. This paper discusses these four challenges and makes an attempt to re-imagine higher education in India post Covid-19 pandemic.

2. Material and Methods

Several international organizations such as UNESCO, the World Bank, the World Economic Forum and the Observer Research Foundation have articulated the challenges faced by the education sector due to Covid-19 pandemic [1-5]. Important inferences drawn from these studies are central to the discussion on post pandemic higher education in India. There exist a number of useful surveys carried out during April to July 2020 in India [6-9]. Special mention may be made to the survey of about 40,000 students of universities in Maharashtra carried out by Jagatap and Mapuskar [9]. These studies provide an idea of the ground level situation of the higher education in India.

The economic dimension of the pandemic is expected to play strongly on education sector and it will result in increased dropout rate in poor and low income countries. The widespread economic distress caused by Covid-19 may necessitate students to discontinue education and shift towards income generation to support their families. The economic hardship and closure of educational institutes over a long period of time can have disproportionately large impact on girls' education, as has been observed during the Ebola pandemic in Africa in 2014 [5]. The survey carried out by Jagatap and Mapuskar [9] clearly shows that 82% students anticipate difficulty in funding their education in the next academic year, 27% students fear of break in their education and 73% students feel themselves responsible for supporting their families financially.

Digital divide is a reality even in a country like USA where nearly 25% students do not have access to the digital technology [10]. This divide is seen across countries and between income brackets within countries. The situation in India is rather grave. As per a recent report [6], only 24% Indians own a smart phone, 11% of household have any type of computer, and only 24% household have internet facility. The rural-urban divide in digital technology may be seen from the access of internet, which is 15% in rural and 42% in urban populations. About 37% of household have one room dwelling; it is therefore luxury for majority students of India to attend lectures at home in an undisturbed environment. Survey carried out by Jagatap and Mapuskar [9] among the students enrolled in higher education shows that about 91% students have smart phones, 32% have some type of computer, and 87% have internet facility which is primarily mobile internet. At a gross level, 50% teachers attempted online teaching, 60% students were covered by online education and 33% students felt that online education was useful. Thus the effectiveness of online education is as low as 10%. These observations imply that both the delivery and quality of online education have been questionable. While international educational institutes have taken steps to minimise the digital divide, such efforts are being done in very small pockets in India.

The Covid-19 pandemic has exposed the very basic objective of higher education, that is to develop human capital useful for creating long term economic value. Since unemployment has been on the rise since the outbreak of the pandemic, more and more students have started questioning the ability of their degree in making them job ready. An international survey reports that about 34% students believe that their colleges are not preparing them for success on job market. Survey by Jagatap and Mapuskar [9] shows that only 37% students think that their degree course will help them to find a decent job, 17% responded negative and 45% students have no idea of relevance of their degree in the job market. Overwhelming majority of students (82%) feel that they should do a skill based course in addition to their degree course. These surveys clearly show that the higher education systems must reform to fix the gap between education and employability.

Bender [11] has made some interesting observations about universities – "*Traditionally, universities have been seen as 'in' rather than 'of' a locality; universities have always claimed the world, not its host cities, as their domains*." This old view on the nature of universities now stands challenged by the pandemic. The universities have remained mute spectators in an unabated spread of corona virus, while the local societies have been expecting them to provide solutions in the difficult time. The new paradigm for the universities is how to position themselves to be relevant to the local and national communities and prove their worth.

The data and the major conclusions of the surveys reported earlier forms the basis of discussion on higher education in India.

3. Results and Discussion

The present education system in vogue in USA and Europe is built on the industrial revolution model. Here the primary objective of education is to convert human into human capital. Education imparts knowledge and skills to make us creative, productive and capable of contributing to the economic development. The second objective of education is to teach civility to make students good members of the society. Yet there is a third objective, which is signalling. An educated person can signal his ability to the prospective employer in a far better way compared to an uneducated person. Empowering students with skills required for employment is certainly the top most agenda. These skills may be pertaining to the state of the art skills needed for the present job market as well as those skills which may be required for jobs that are going to be generated in future.

Modern education in India started with a strong focus on the second objective of education mentioned above. It was a biased view of the British masters which laid stress on making Indians cultured or civilized by teaching them English language, history and literature. Development of skills was not considered to be a high priority issue. It is ironical to see that even today, we consider education as an exercise in imparting information to students; the sole purpose is to make a student enlightened by making him/her aware of old and new developments. Development of skills which can use this information for productive purposes is indeed absent in this whole exercise. This is where the disconnect between the education and job market has taken place, and it has a history of more than 150 years. This issue has been highlighted extremely well by H.E. Shri Girija Shankar Bajpai, Hon'ble Governor of Bombay in his address delivered in the third convocation of the Karnataka University in 1952 [12]. He said–"*But though education, especially higher education, is designed to train and sharpen man's intellect and aesthetic faculties, without congenial and remunerative occupation, education becomes an empty accomplishment. Indeed, by reason of the denial of the satisfaction that an educated person needs and seeks, education tends to become a source of torment rather than that of delight to soul*."

Covid-19 pandemic has brought to the front the issue of large scale unemployment of our graduating students. India entered its lockdown with a high unemployment level at 8.7%, and by early May the unemployment rate was at record 27%. The surveys show that the students are not very confident of securing jobs based on their degrees and qualification. Overwhelmingly large percentage of students (82%) think that their job prospects will be enhanced if they take up a skill based course in addition to their degree course. This is an important dimension to the higher education today and the educational institutes must create avenues and mechanisms for the same. The education devoid of skills and social connectivity explains why the higher education systems did not respond to the needs of the society in the Covid-19 pandemic. If one looks at the possible attempts, one finds disinfection device using

UV rays received too much of attention in academic circles. However, a system based on imported mercury lamp is not going to work. Our engineering students could not take up design of ventilators since majority of them had not seen a ventilator in their life. Over the long term, our higher education institutes will have to make themselves relevant to the local and national needs and fashion themselves as centres for innovation and employment creation. The larger context for such a change is provided by 'Atmanirbhar Bharat' campaign.

During the pandemic, Indian education sector responded very enthusiastically to the idea of online education, however, the inadequacy of infrastructure was completely lost in this enthusiasm. In such a digital divide, the biggest question is how are the universities or colleges going to reach every student. In principle, the higher education institutes can raise funds through alumni association and may also look for CSR funding so that at least smart phones and data cards are provided to needy students. This would require consolidation and participation of Alumni Associations in our higher education institutions. Another important issue is how to expand the coverage of students in spite of the digital divide. The developed countries like USA also face digital divide and they have devised alternate ways like television, radio, internet hotspots and even delivery of paper packets to reach the unreached students [10]. Ironically, our response to education during the pandemic has been one-dimensional and it does not include many of these alternate ways. Indian higher education institutes need to think of the future roadmap. When the pandemic comes to an end, the functioning of higher education institutes will require a suitable hybrid model involving correct mix of online and face to face learning, so that the institutes can function using social distancing norms. Such hybrid models of education can provide a very different perspective to the higher education in the country.

The quality of online education is also a matter of concern. It is required for the faculty members to innovate; they need to produce online resources in a manner that the students receive their full advantage. The experience with MOOCs suggest that only 10% of the registered students, complete online courses. It is crucial, therefore, to generate online study material using range of engagement methods and cooperative tools. A strong drive on war footing is needed at this juncture to prepare teachers as well as students for online teaching and learning. It is also required to remove the apprehensions in the minds of students regarding online examinations.

As mentioned earlier, the economic dimension of Covid-19 pandemic is expected to play strongly on the higher education sector. The student community is anxious and is feeling unsettled. It is important for the colleges and universities to keep in touch with the students and parents on continual basis and offer counselling. Educational institutes should activate their counselling centers and also involve students' organization for the purpose of counselling. It is also an opportunity to increase the scope of Earn and Learn schemes to support students. Higher education institutes now need to study the cost effectiveness of higher education. The economic hardship together with closure of educational institutes over a long period of time during the Ebola epidemic in 2014 in Africa had a disproportionate impact on girls' education. It is important to see whether such a gender dimension will play in India post pandemic.

4. Conclusions

The weak links in higher education sector became markedly visible due to Covid-19 pandemic. It is duty of every higher education institute to work on these weak links and evolve higher education that is progressive and socially relevant. In this context, it is worth quoting from an article [13] in Newsday by Michael Hynes, Superintendent of the Port Washington School District–"*Now is the time for our school leaders to generate a new compelling*

philosophy of education and an innovative architecture for a just and humane school system. We must refocus our energy on a foundation built on a sense of purpose, forging relationships and maximizing the potential and talents of all children. Let's take advantage of the possibility that our nation's attention can shift 180 degrees, from obsessing over test scores and accountability to an entirely different paradigm of physical, mental, and emotional well-being for students and staff." He continues, "*It is our collective responsibility to foster engaging and meaningful environments when educating our children in the new era of a post pandemic education. Now is this the time to revolutionize this antiquated system built on old structures and ideologies.*" Can we show this spirit for our higher education in India? Can we imagine a new kind of education, one that allows creativity and able to address current and future challenges?

References

[1] 3 ways the corona virus pandemic could reshape education, Gloria Tam and Diana El-Azar, World Economic Forum, March 13 (2020).

[2] Covid-19: Impact on education, UNESCO, http://en.unesco.org/covid19/educationresponse

[3] How Covid-19 is driving a long overdue revolution in education, S-E Kadri, World Economic Forum, March 12 (2020).

[4] Covid-19 crisis sheds light on the need for a new education model, M.O. Diop and T. Jain, UNESCO, April 14 (2020).

[5] Gender dimension of school closures in India during Covid-19: Lessons from Ebola, Shruti Jain, Observer Research Foundation, May 23 (2020).

[6] Indian education can't go online– only 8% of homes with young members have computer with net link, Protiva Kundu, Scroll.in, May 05 (2020).

[7] 85 percent of students miss interaction with teachers, online classes cannot replace schools, ASSOCHAM, Indian Express, May 26 (2020).

[8] No gadgets, no studies: What online classes mean for 16 lakh poor students in Delhi schools, Annesha Bedi, The Print, April 22 (2020).

[9] Impact of Covid-19 pandemic on higher education in Maharashtra, B.N. Jagatap and Anand Mapuskar, Indian Express, July 12 (2020); Hindustan Times July 13 (2020); Times of India, July 13 (2020).

[10] The scramble to move America's schools online, Benjamin Herold, Education Week, March 27 (2020).

[11] Thomas Bender, The University and the City, Oxford University Press (1991).

[12] The Idea of a Regional University, H.E. Shri Girija Shankar Bajpai, in Diamond Sparkle (Convocation Addresses 1949-2010), Ed. S.K. Saidapur and S.C. Malagi, Published by Karnatak University (2010).

[13] Our children deserve an education revolution, Michael Hynes, Newsday, May 02 (2020).

Karnatak University
Journal of Science

ISSN: 0075-5168

Exploring dimensions, factors and consequences of social exclusion among disadvantaged groups: A qualitative study

Astha Sakshi

Rashmi Kumar

Astha Sakshi and Rashmi Kumar, “Exploring dimensions, factors and consequences of social exclusion among disadvantaged groups: A qualitative study” Karnatak University Journal of Science 51, 17-26 (2020).

Exploring dimensions, factors and consequences of social exclusion among disadvantaged groups: A qualitative study

Astha Sakshi* and Rashmi Kumar
Department of Psychology, University of Allahabad, Prayagraj
Uttar Pradesh, India
***Corresponding author**: astha.sakshi0@gmail.com

Abstract

After the independence, India has revolutionary changes in some areas such as economic growth, exports, and foreign policies etc, but exclusion continued on the basis of caste, disability, religion, ethnicity etc. The notion of social exclusion is prevailing in almost all societies. When a group of people is denied of basic opportunities to grow as an individual as well as a unit of the society or better to say a section of society, a feeling of exclusion emerges among them. The objective of the study was to explore different dimensions of social exclusion, nature of consequences and factors responsible for the social exclusion among disadvantaged groups. In order to get deep understanding of the concept of the social exclusion from the perspective of physical disabled and caste based groups, two disadvantaged groups were chosen for this study, the researcher decided to opt for qualitative approach. The nature of the data collected from qualitative approach is rich and it involves ample amount of unique experiences of an individual which gives an opportunity to advance the understanding of the concept from participant's perspective. Material deprivation, lack of education, poverty, poor housing, discrimination, and feeling of rejection were the common themes emerged from the data.

Key words: - Social exclusion; qualitative study; disadvantaged; caste; physical disabled and material deprivation
Article history: Received: 16 June 2020; Accepted: 9 September 2020

1 Introduction

The concept of social exclusion can be defined as a process which involves denial of fair and equal opportunities to certain groups in multiple spheres in society, resulting in the inability of individuals from excluded groups to participate in the social, political, economic and cultural arena. The term Social exclusion operates in multidimensional way and is found in pluralistic societies which believe in the practice of social equality. Social Exclusion could be in the form of excluding individuals from education, land and property rights, participation in democracy, health and basic services. The concept of Social Exclusion was firstly defined by Rene Lenoir in France in 1974 as a rupture of social bonds. The term was initially coined in France in 1974. Due to this exclusionary process, the quality of life of individuals and the equity and cohesion of society as a whole is affected.

People of disadvantaged groups may have their own unique personal experiences. With the exception of a few subjective evidences, there are only a few studies which have tried to understand exclusion from the perspective of the person who actually suffer from the exclusionary practices prevailing in the society. It is important to understand the process from the person's perspective. It would be beneficial to document and develop a clearer picture of the exclusion process experienced by these people.

There are various dimensions on which people of disadvantaged groups feel excluded. In many studies (Levitas,2007; Ziyauddin & Kasi,2009) dimensions of social exclusion was based on resources, participation and quality of life. Social exclusion is multidisciplinary and multi-dimensional concept. At the same time concept of social exclusion links rights and deprivations of excluded groups together. It is found that people of disadvantaged groups deprived of essential goods and services as well as excluded from security and justice. So with the help of this study researcher tried to explore the dominant dimension of social exclusion from the perspective of caste based and physical disabled groups.

It has been reported in many studies (Shields et.al.2012; McClimens, 2014) that lack social networks, poverty, financial barriers, discrimination, proper housing and safety are the causative factors responsible for social exclusion. Different factors leads to different types of consequences. Disability constitutes a change in a person's life to which s/he must adapt. The specific nature of required adaptations depends on the specific challenges posed by the nature of disability and the same applies to caste based excluded group members. In this study attempt has been made to study the responsible factors of social exclusion from the perspective of disabled and caste based groups.

The present study also made an attempt to understand nature of consequences faced by the people of disadvantaged groups. People from excluded group experiences loneliness, poor self-esteem, anger and jealousy etc as a result of perceived social exclusion. According to Leary (2001) rejection occurs in various social environments which lead to feeling of loneliness. They experience a broader range of consequences and these unique consequences tend to be chronic in nature and intensified by factors responsible for the exclusion. In particular, this study tried to answer following research questions:-
a-What are the dimensions on which individual with physical disability and caste based group feel excluded?
b-What are the psychological consequences of social exclusion among disadvantaged group?
c-What are the possible factors behind their exclusionary state?

2 Method

2.1 Sample

In this study 42 participants were interviewed from the two different disadvantage groups in India. Out of these 42 participants, 20 participants belong to physical disabled group. In the sample of physical disabled group 8 were female and 12 were male, between the age ranges of 18-60 yrs. The mean age of the physical disabled sample was 24 and 29 for female and male respectively. All of them were categorized as loco motor disabled. Educational qualification ranges from Primary to Post Graduate. 12 participants were self-employed, 2 were working in Government sector and 3 were student.

In the caste based sample (SC group) 13 were female and 9 were male participants between the age ranges of 20 to 54 yrs. The mean age of caste based sample was 26 and 28 for female and male respectively. In this sample 3 participants reported that they were illiterate and for rest of the sample educational qualification ranges from Primary to Post graduation. Out of 22 participants 8 were working in private sectors, 5 were working on daily wages, 3 were student.

2.2 Measure

In this study to explore the dimensions, factors and consequences the researcher used semi-structured interview method. The data gathered from interviews allow opportunity to get insiders' perspective. This insider's perspective provides deeper meaning and knowledge of the concept and fulfills the efforts to answer the objectives of the research.

2.3 Procedure

For the process of data collection, the participants were contacted at their workplace or place where they live and after meeting and introducing them, the purpose of the study was explained to them. Researcher explained them that there are few questions related to their social exclusion experiences and they have to answer those questions. To remove their hesitation and anxiety, it was also conveyed to them that their responses will be used only for research purpose and it will be treated in confidential manner and at any time they can withdraw, if they feel uneasy while answering the questions. After obtaining their consent, interviews were scheduled as per as the convenience of the participants. To ensure that the participants feel comfortable during the process of interview, the rapport was established between the participants and researcher prior to the interview. Both the groups were taken as disadvantaged/socially excluded groups, face lots of discrimination from other members of the society, because of their exclusionary state, so researcher tried to maintain the friendly environment while conducting the interview. Interview schedule structure was semi-structured open ended interview schedule. This interviewing style allows researcher to have discussion on important relevant issues rather than focusing on straightforward question and answer format. A list of questions related to the exclusion experiences was prepared. The questions of interview schedule were based on a review of the concerns in relevant literature. Questions were prepared in Hindi and medium of interviewing was in Hindi.

2.4 Analysis

For the purpose of the analysis of the data researcher used qualitative content analysis technique. According to Hsieh & Shanon (2007) qualitative content analysis analyze the data obtained from open-ended interviews, narratives responses and open ended survey questions. In this method of data analysis, data is organized into themes on the basis of similar categories, concept or similar features.

In this research model given by Elo & Kyngas (2008) for qualitative content analysis was adopted. According to Elo & Kyngas there are three main phase of content analysis: Preparation phase; organizing phase and reporting phase.

3 Results

The aim of the study was to explore the dimensions social exclusion, nature of consequences and possible causative of social exclusion. This study aimed at understanding the dimensions on which individual's of caste based and physical disabled group face exclusion and what according to them are the possible factors which lead to their exclusionary state? In addition to this the main aim from the psychological perspective is to gain the knowledge about the consequences they face due to their exclusionary state in the society.

All the interviews were analyzed by the method of qualitative content analysis. The following tables present the major themes along with the definitions and examples from the data.

Table 1. Major themes for dimension of Social Exclusion

Themes	Definition	Example	Frequency
Material deprivation	Material deprivation refers to shortage of resources; deprivation can be in form of land, financial status, income.	Not having own land, lack of proper income	24
Inadequate access to basic rights.	Inadequacy in the access of government and non-government schemes regarding health, education and employment.	Lack of medical help at the time of need	32
Insufficient social integration	This refers to inability to participate in formal and informal social networks and have limited social participation. Experiencing social distance from other groups of the society.	Nobody invites in social functions and restriction to certain place	36
Education and skills	Refers to inability to get any education or; to attain any professional degree; being economically independent; getting a good job to fulfill the basic needs of family.	Not able to get proper education because of our poverty.	23
Personal safety	Refers to the threat of physical violence, being exposed to crime.	People always target due to exclusionary status.	25
Insufficient cultural integration	Lack of compliance with societal norms and values, no involvement with other members of the society at a large level. Regarded as unfit for the public life.	Disregard or ignored in any big events, never consult or value their opinion.	18

Table 2. Major themes of underlying factors of Social Exclusion

o	Themes	Definition	Example	Frequency
1.	Poverty	Lack of money and other important resources necessary for better life.	Sometimes not able to arrange proper meal of the day.	36

2.	Lack of family support	Refers to the interpersonal relationship within the family, not able to maintain cordial relationship with the family members, unable to perform his/her duty efficiently.	In family other members treat as a burden.	12
3.	Lack of Societal Support	Refers to the relationship outside the family, including neighborhood unfriendliness, relatives, friends, colleagues etc. Not able to maintain positive relationship with others in the society, Not able to get any monetary support from others.	Nobody listen ,always people ignore	38
4.	Physical Appearance (deformity)	Being harassed, mocked and bullied by others for the physical appearance.		6
5.	Poor employment prospectus	Refers to lack of employment opportunities for excluded people. It reduces the opportunities to form a social networks and it also lead to limited income.	Not able to get proper employme nt	32
6.	Accommodati on	People of excluded group do not have proper place to live.	Poor houses which do not have proper light, water and electricity.	14
7.	Discriminatio n	People experience exclusion through discrimination on the basis of their caste and abilities to perform any kind of work. Feeling of not being consulted and listened by others.	Authority gives less money and makes them to work more.	26
8.	Restriction	No proper access to work, education, services and socio-cultural activities due to their caste, locomotor restrictions imposed by the state of physical disability.	Sometimes we are not allowed to certain places.	21

Table 3. Major themes for Consequences of Social Exclusion

S.no	Themes	Definition	Example	Frequency

1	Basic psychological need threat	It refers to the threat to individual's desire to maintain stable social relationship. This threat results in lack of self control, poor self esteem, and feeling of worthlessness.	Sometimes I feel that why I am here.	37
2	Learned helplessness	It refers to the belief that things are not in control and lead to the feeling of helplessness which results in frustration, sadness and distress.	Not able to perform daily routines by their own	16
3	Dehumanizing languages	It involves use of derogatory and dehumanizing terms to refer individuals from excluded group.	Use of caste to address the person	15
4	Future apprehension	Uncertainties regarding the future	Not sure about my condition whether it will improve or not in near future.	22
5	Feeling of loneliness	Feeling of being alone, very little number of social contacts.	Nobody wants to listen me and	
6	Lack of freedom of expression	Not able to make any decision regarding anything. Other members of the society disregard them resulting in the deterioration of inter-community relationship.	No one give importance to their thoughts	29
7	Lack of Self-confidence	It refers to the lack inability to perform any kind of task. Imposed feeling of inferiority. Feeling of failure is dominant.	Whatever work I start not able to finish it.	17
8	Negative emotional state	Defined as individual is full of tension, worries and anxiety due to their exclusionary state. This negative emotional state is manifested in the form of anger, humiliation, shame and feeling of guilt.	"Whatever I suffered in my life I pray to god that my kids may see new life".	13

9	Negative orientation towards life	Not able to meet any new challenges in the life, feels that their living condition is not going to be changed.	Most of the times I feel why my life is like this.	27
10	Poor life satisfaction	This refers to the negative condition of life which leads to the instability in one's life, not able to achieve any desired goal.	"It seems that life is full of darkness'	36
11.	Feeling of Rejection	Defined as direct negative attention that a person is not wanted by others, and it decreases the feeling of self acceptance and low self esteem in the individual, feeling ignored or avoided, feeling of aggression	Nobody listen to me in family	22
12.	Feeling of injustice	Refers to the unequal distribution of resources and opportunities, delay in the process of getting justice in any case.	Other people of same age group get more resources.	21

4 Discussion

The main objective of the study was to explore the dimensions of social exclusion; to understand the consequences of social exclusion from disadvantaged group's perspective and to uncover the possible underlying factors responsible for the social exclusion of disadvantaged groups. Issues related to social exclusion in India has been the core of today's paradigm of growth. In India there are certain groups who are denied of equal opportunities in various dimensions of their life. The concept of social exclusion is multi dimensional. The data obtained from the study revealed that the prevalence of social exclusion in India can be illustrated through land deprivation, material deprivation, inadequate access to basic rights, insufficient social integration, lack of education, personal safety and insufficient cultural integration. These are prominent themes emerged from the data. The participants of the study reported that they face exclusion in various dimensions for example social, political and economic spheres of their life. According to Silver 1994; Byrne 2005, concept of social exclusion is describe as a situation in which an individual or group is unable to participate in the basic political, economic and social functioning of the society.

Second objective of this study was to uncover the underlying factors responsible for the exclusion of disadvantaged groups. The factors of exclusion results in the exclusion of individual or group at different level for example they can be excluded at societal, community and individual level. Eight themes related to underlying factors of social exclusion were identified from the data. Factors of social exclusion were categorized at three different levels. At individual level the factors predominantly found in data which play prominent role in the facilitation of social exclusion refers to the lack of access to work, education, services and socio-cultural activities due to their caste and physical disablement. Participants from physical

disabled group often reported that due to the lack of physical mobility, they are highly reliable on their caregivers for small things and they are not able to have a proper access to formal and informal networks, even participants from caste based group also admitted that due to certain restrictions they are not able to get for what they entitled. People of excluded group do not have proper place to live. Poor housing is affected by its cost and individual income and people of these groups do not have proper income. According to social exclusion unit 2004 poverty, low level of income and unemployment experienced by people of excluded groups can result in poor living condition. The outcome of poor housing and homelessness are poor health and wellbeing of an individual.

At societal level, the factors responsible for social exclusion were- lack of societal support, interpersonal support, poverty, physical appearance

An individual always consider himself /herself as a productive part of his/her social environment. Relationship with family members, relatives, neighbors, colleagues are always vitally affected by the nature and extent of harmony or disharmony exists between him and his societal environment. The people with disabilities are less handicapped by their own disability than by the lack of societal and family support. They are not able to maintain positive relationship with other members of the society. According Murphy 2009 disability is considered as a disease of social relations and this relation between disabled and others members of the society are tense, problematic and not positive in nature. They are socially and physically isolated. The interpersonal and societal relationship of disabled person is determined and influenced by the extent and nature of disablement. Participant of physical disabled group reported that sometimes they are "treated as burden" by the family members as well as society because of their severity of disability. Having disabled person in the family increases financial burden of the family. Excessive reliance on the family members has adverse consequences on them for example stress frustration etc. Denial of reality, shame, rejection is the common reactive patterns among the family members of physical disabled person.

Physical appearance theme was dominantly reported by the participants of physical disabled group. People of physical disabled group reported that because of their body image other people make rude remarks and pass harsh comments on their physical appearance. According to Stanford & McCabe 2005, body image plays a very important role in the experience of disability. It affects disabled sense of personal worth confidence and belief in his/her capabilities.

At community level factors responsible for social exclusion is discrimination and poor employment prospectus. According to Social Exclusion Unit 2004, discrimination is identified as a key factor of social exclusion which leads to unpleasant experience among socially excluded group. Practice of discrimination reduces the opportunity to develop various skills. People of socially excluded groups face social hurdles in the form of discrimination and avoidance. They are never consulted and listened by other members of the society. Discrimination creates fear and anxiety and enables people from excluded from participating in the community level activities. In all the emerged themes for factors, the most important factor mentioned by almost all the participants of the study was poor employment prospects. This theme is part of vicious circle along with poverty and lack of education. The employment opportunities are very less for the members of excluded group as they are not highly qualified and not able to form a social network which is essential for opening of new resources.

Third objective of this study was to understand the consequences of social exclusion frequently experienced by the people of excluded groups. Thirteen themes related to

consequences of social exclusion emerged from the content analysis of the interviews. These were , basic need threat, learned helplessness, lack of freedom of expression, negative orientation towards life, aggression, future apprehension, social isolation, feeling of rejection, poor life satisfaction, lack of self-confidence, feeling of injustice.

It is universally evident that human being possesses a fundamental motive to have a stable relationship in family occupation peer and social groups, but due to the exclusionary practices the disadvantaged group (physical disabled and caste based) reported exclusion from these important social relationships. Due to the experience of social exclusion they commonly reported threat to their basic need which refers to the individual's desire to maintain the stable relationship. The outcome of this threat is poor self-esteem, lack of self-control and feeling of worthlessness. According to Baumiester & Leary 1995, Humans are social animals and they possesses a strong need for stable social relationships and much of their daily thoughts, feelings and behavior can be understood within the context of satisfying these needs.

The critical issue is that the laws, policies and schemes related to the betterment of excluded groups have overlooked the overall well-being of the individual's of the socially excluded groups. The results of the study reflect a lot about the conditions, experiences and feelings of members of excluded groups.

References:

[1] Baumeister, R.F. & Leary, M.R. the need to belong: Desire for interpersonal attachment as a fundamental human motivation. Psychological Bulletin, 117(3), 497-529 (1995).

[2] Byrne, D. *Social exclusion*. Maidenhead, England: Open University Press (2005).

[3] Elo, S., & Kyngäs, H. The qualitative content analysis process. *Journal of Advanced Nursing*, *62*(1), 107-115 (2008).

[4] Hsieh, H., & Shannon, S. Three Approaches to Qualitative Content Analysis. *Qualitative Health Research*, *15*(9), 1277-1288 (2005).

[5] Levitas R. The multi-dimensional analysis of social exclusion, Dept. of sociology, university of Bristol (2007).

[6] Murphy, G. Challenging Behavior: A Barrier to Inclusion?. *Journal Of Policy And Practice In Intellectual Disabilities*, *6*(2), 89-90 (2009).

[7] McClimens A, Partridge N, Sexton E. How do people with learning disability experience the city centre? A Sheffield case study. *Health and Place.* 28:14-21 (2007).

[8] Shields N, Synnot AJ, Barr M. Perceived barriers and facilitators to physical activity for children with disability: a systematic review. *British Journal of Sports Medicine.* 46:989-997 (2012).

[9] Stanford, J., & McCabe, M. Sociocultural influences on adolescent boys' body image and body change strategies. *Body Image*, *2*(2), 105-113 (2005).

[10] Silver, H. Social exclusion and social solidarity: Three paradigms. *International Labour Review,*133(5-6), 531-578 (1994).

[11] Ziyauddin, K., & Kasi, E. *Dimensions of Social Exclusion*. Newcastle upon Tyne: Cambridge Scholars Publishing (2009).

Karnatak University

Journal of Science

ISSN: 0075-5168

Mini review

Adjustments in microenvironment of human Hemoglobin upon interactions with members of Gold and Carbon nanofamily

Madhurima Chakraborty

Tapan Ganguly

Madhurima Chakraborty and Tapan Ganguly, “Adjustments in microenvironment of human Hemoglobin upon interactions with members of Gold and Carbon nanofamily” Karnatak University Journal of Science 51, 28-39 (2020).

Mini review

Adjustments in microenvironment of human Hemoglobin upon interactions with members of Gold and Carbon nanofamily

Madhurima Chakraborty[a] and Tapan Ganguly[b*]
[a]Assistant Professor, Department of Biochemistry, West Bengal State University;
madhurima.mbc@gmail.com
[b]Emeritus Professor, School of Laser Science and Engineering, Jadavpur University
***Corresponding author:** tapcla@rediffmail.com

Abstract

The study on the modes of interactions between human hemoglobin (HHb) with different nanoscale molecules has provided useful information for potential biomedical applications. With respect to this spherical gold nanoparticles (GNP) with size of 18-20 nm and carbon quantum dots (CQDs)of size of ~4-5 nm have gained widespread attention as a member of gold and carbon nano-family due to their wide-range of properties that specifically include their cost of preparation and beneficial properties like biocompatibility, non-toxicity and solubility in aqueous medium. This review will focus on the alterations in protein microenvironment upon interaction with GNP and CQD in order to assess the biocompatibility of the nanoparticles in the biological milieu. Also the interactions of biomolecules with nanoparticles and its effects on structure and function are intensely related to the size and shape of the nanoparticles. Thus the behavior of biomolecules like proteins upon interaction with GNP and CQD must also be considered before assessing the biomedical applications of nanoparticles. As such the review will highlight how the multi-subunit HHb interacts with diverse nanomolecules in different manner and manages to retain its secondary structure even after its interaction. Also the alterations in spectroscopic properties of HHb (UV-vis, steady state, time-resolved and synchronous fluorescence) and secondary structural information using CD and FTIR spectroscopy upon interaction with GNP and CQD will be predominantly considered here. The present review will therefore immensely help in understanding the biocompatible nature of GNP and CQ Das well as their prospective application in the biological microenvironments.
Keywords: Gold Nanoparticles; Carbon Quantum Dots; Protein microenvironment; Secondary structure; Time resolved spectroscopy, Circular dichroism.
Article history: Received: 30 June 2020; Revised: 25 August 2020; Accepted: 9 September 2020

1 Introduction

HHb is an extremely multi-talented protein in vertebrate erythrocytes. HHb has not confined itself as an iron-based complex which physiologically performs exceptionally crucial role in binding molecular O_2, but research on hemoglobin has gone beyond the interest in its physiological role as an oxygen carrier. Apparently HHb has been considered from all points of view an ideal model protein for investigating the properties of proteins and enzymes in general. Not only that since HHb has the ability to bind ligands like O_2, HHb will support the binding and delivery of small ligands of clinical and medicinal importance. Here, the foremost perception of the structural alterations of HHb upon interaction with ligand appears to be greatly meaningful. Such information can be accumulated to realize the role of both protein

and ligands of nano-dimension in diverse research fields that include nano-medicine, nano-biochemistry, clinical biochemistry and others.

The function of HHb to bind oxygen is associated with the presence of a bound prosthetic group called heme comprising of a central iron atom and an organic component, protoporphyrin. The protoporphyrin consists of four pyrrole rings linked by methane bridges. Four methyl groups, two vinyl groups, and two propionate side chains are also present in the tetrapyrrole system. HHb, in adults, is a tetrameric protein consisting of two α subunits and two β subunits remaining as a pair of identical αβ dimers ($\alpha_1\beta_1$and $\alpha_2\beta_2$) linked by an extensive interface1-9]. Moreover, HHb possesses a high α-helical content and contains six Trp residues and ten Tyr residues in the tetramer [1-4].

Besides, miniaturization of structures in the form of nanoscale materials has provided a nano platform for upgraded diagnostics and biomedical research involving nano-technology. Due to the small sizes of nanoparticles, they have characteristics compared to the bulk form of the same material. Nanoparticles also present surfaces for interactions with biomolecules and such studies may provide a pathway towards understanding biomolecular functionality as well as the bio-safety and biocompatibility of the nanoparticles with the molecules of nano-dimension. Also the technological advantages of nanoparticles used as drug carriers are its high stability, high carrier capacity and feasibility of variable routes of administration. It must be mentioned here that realizing the role of nanoparticles as drug or drug delivery system, biosensors can be simplified, if interactions between nanoparticles and biomolecules are well analyzed. Knowledge of protein-nanoparticle interactions will thus summarize how nanoparticles will function in biological environment for effective biomedical application.

Also biomolecules like proteins conjugated with gold nanoparticles as efficient drug-delivery system have gained considerable attention since spherical GNP are generally nontoxic, bio safe and biocompatible [5-11].Moreover detection and treatment of cancer cells using GNPs has also been reported [10].Additionally, popular herbal medicine Swarnabhasma has been known to consist of only micrometer and nanometer sized gold particles [11].Furthermore CQDs have also gained importance as a carbon nanoparticle due to their distinct physicochemical characteristics [12-14]. CQDs were first synthesized during purification of single-walled carbon-nanotubes in 2004 with a size of approximately 4-5 nm[15]. Analyzing the structure and functionality of CQDS reveal that they possess cheaper preparation cost, solubility in aqueous medium, biocompatibility and non-toxicity [12-14].The biocompatible properties of CQDs may be utilized for biomedical applications [16-20]that may especially include development of biosensors [17] and also for efficient drug-delivery [18-20] and in various other fields.

Nevertheless the biocompatible properties of CQDs and GNPs will not be utilized unless their effect upon interactions with biomolecules within the biological microenvironment is not gathered. Knowledge of such protein-nanoparticle/ quantum dot interactions may provide insight towards the functionality of nanoparticles in biological milieu for revealing their biomedical application. Also the interactions of biomolecules with nanoparticles and its role on the structure and function are deeply related to the size and shape of the nanoparticles and must be considered.

Largely, the present review focuses on the alterations in HHb's microenvironment and secondary structure alterations upon interaction with members of gold and carbon nanofamily (GNP and CQD) (**Fig. 1**). It must be mentioned here that both GNP and CQD used in our study have been synthesized in our lab following the methods described elsewhere [1, 2].It becomes

apparent that the summary of interactions will be of enormous physiological significance which will further support advancements in the developments of drug-delivery systems, biomedicines and biosensors.

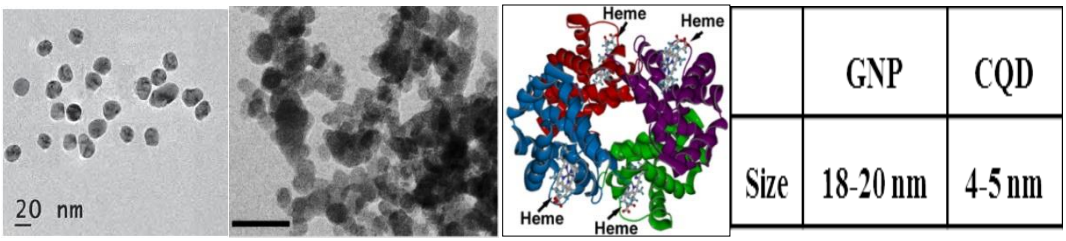

Figure1.HR-TEM image GNP (first panel, Scale bar- 20 nm) and CQD (second panel, Scale bar- 10 nm).Molecular structure of HHb (third panel).Summary of size of GNP and CQD (fourth panel)has been represented here. Modified from Reference [1, 2].

2. Results and Discussion

2.1. Alteration in protein's microenvironment

2.1.1 Comparison of absorption spectral properties of HHb in presence of GNP and CQD

In order to acquire knowledge regarding alterations in HHb's microenvironment upon interaction with GNP and CQD the UV-Vis, steady-state, time-resolved and synchronous fluorescence have been summarized. The UV-Vis absorption spectra of HHb in absence of GNP shows a broad absorption peak at ~270 nm which is observed because of the presence of tryptophan and tyrosine residues within HHb (**Fig. 2, left panel**). Upon addition of increasing concentration of GNP to HHb solution, the entire absorption spectra are observed to undergo a hyperchromic effect without any noticeable spectral shift.

Upon addition of increasing concentration of CQD, enhancement in the absorbance at around 270 nm (hyperchromicity) and peak broadening isnoticed (**Fig. 2, middle panel**).However the hyperchromicity is not accompanied by any spectral shift. Thus the above observations indicate hyperchromicity at around 270 nm in presence of both GNP and CQD that occurs due to absorbance of tryptophan and tyrosine residues,present within heme protein HHb.

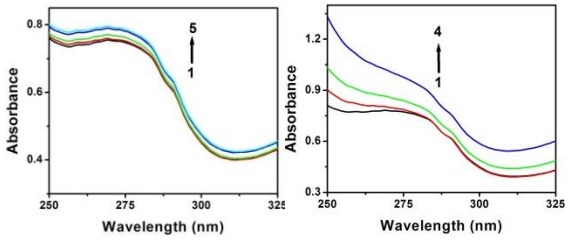

Properties	GNP	CQD
UV-vis absorption (270 nm)	Hyperchromicity ↑	Hyperchromicity ↑

Figure 2. (**a**) UV-vis absorption spectra of HHb in presence GNPat ambient temperature are shown. Concentration of HHb is 5 $\times 10^{-6}$ M. The concentrations of GNP used here are 0 (1), 0.5 x 10^{-6} M (2), 3 x 10^{-6} M (3), 4 x 10^{-6} M (4), 5 x 10^{-6} M(5) (left panel). UV-vis absorption spectra of HHb in presence of CQD under the above mentioned conditions. The concentrations of CQD used here are – 0 (1), 0.84 x 10^{-4} M (2), 1.68 x 10^{-4} M (3), 3.36 x 10^{-4} M (4) (middle panel). Summary of the above observations of UV-vis absorption spectra of HHb upon

interaction with GNP and CQD (right panel) has been represented here.Modified from Reference [1, 2].

2.1.2. Revealing the alterations in protein microenvironment upon interaction with GNP and CQD by steady-state fluorescence analysis

In order to obtain further information regarding HHb's micro environmental alteration the fluorescence spectral properties of HHb are hereby discussed. The effect of noble nanometal GNPs at the ambient temperature on the steady state fluorescence emission of the HHb is shown in **Fig. 3 (left panel)**. The fluorescence emission spectra of HHb when excited at 270 nm show the emission maxima at ~328 nm. Upon addition of increasing concentration of GNP, the fluorescence quenching of HHb is noticed. The fluorescence spectra of HHb in presence of GNP however do not display any detectable spectral shift.

Fluorescence measurements were also executed to monitor the role of CQD in determining the alteration surrounding the microenvironment of tryptophan and tyrosine residues **(Fig. 3, middle panel)**.Interestingly the fluorescence maxima of HHb are enhanced regularly at around 328 nm. The fluorescence environment is accompanied by an increasing red shift of nearly 10 nm (from 328 to 338 nm) upon gradual addition of CQD. Also the emission spectrum of protein is known to be highly sensitive to polarity of the solvent. Thus an increase in red shift probably suggests that the tryptophan and tyrosine moiety within HHb, are possibly getting exposure from a nonpolar hydrophobic environment to a more hydrophilic environment upon interaction with CQD. Thus the steady-state fluorescence properties of HHb get altered in contrasting manner in presence of GNP and CQD.

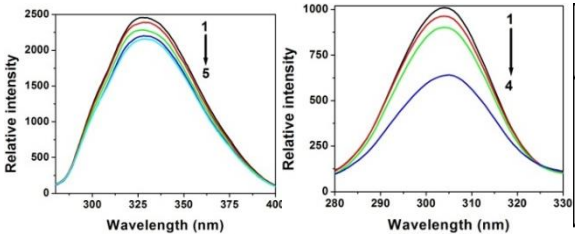

Properties	GNP	CQD
Steady-state	Static quenching ↓	Fluorescence enhancement ↑
fluorescence	No spectral shift	10 nm red shift

Figure 3. (**a**) Steady state fluorescence emission spectra of HHb in presence GNP at ambient temperature are shown. Concentration of HHb is 5 $\times 10^{-6}$ M and λ_{ex} = 270 nm. The concentrations of GNP are 0 (1), 0.5 x 10^{-6} M (2), 1 x 10^{-6} M (3), 3 x 10^{-6} M (4), 5 x 10^{-6} M (5) (left panel). Steady state fluorescence emission spectra of HHb in presence CQD at ambient temperature are shown. The concentrations of CQD used here are 0 (1), 0.84 x 10^{-4} M (2), 1.68 x 10^{-4} M (3), 3.36 x 10^{-4} M (4) (middle panel). Summary of observations of steady-state fluorescence emission spectra of HHbupon interaction with GNP and CQD has been represented here (right panel).Modified from Reference [1, 2].

2.1.3. Alterations in microenvironment tryptophan and tyrosine residues upon interaction with GNP and CQD illustrated by synchronous fluorescence analysis

In order to check whether the interactions of HHb with GNP could produce environmental alternations around fluorescing aromatic residues (tryptophan and tyrosine) as a result of conformational change within HHb, synchronous fluorescence spectroscopy is executed. Synchronous fluorescence spectroscopy is commonly performed by simultaneous scanning of the excitation and emission monochromators during which a constant wavelength interval is maintained between them. Any shift in the synchronous spectra indicate salterations of polarity around the tryptophan and tyrosine residues (fluorophore). When the constant

wavelength interval is kept at Δλ= 15 nm, information regarding microenvironment of tyrosine residues is obtained. When the constant wavelength interval is maintained, Δλ= 60 nm, information regarding microenvironment of tryptophan residues is gathered. Accordingly, the synchronous fluorescence spectra of HHb are measured in presence of increasing concentration of GNP at constant wavelength interval of Δλ= 15 nm and 60 nm and are shown in **Fig. 4 (first and second panel)**. Upon increase in concentration of GNP, the synchronous fluorescence intensity gradually decreases for the tyrosine (Δλ=15 nm) and tryptophan (Δλ=60 nm) peaks. The emission maximum of tyrosine residues had a weak red shift (from 304 to 305 nm) upon addition of GNP. This 1 nm red shift may signify that the polarity around the tyrosine residues gets altered such that the microenvironment of tyrosine residues is exposed to a more hydrophilic environment upon interaction with GNP. The synchronous fluorescence intensity also gradually decreases for the tryptophan (Δλ=60 nm) peaks. However due to absence of any spectral shift the polarity around the microenvironment of the tryptophan residues (emission maxima at 337 nm) remains unaltered eve after interaction with GNP.

The synchronous fluorescence spectra (Δλ= 15 and 60 nm) of HHb in presence of CQD is displayed in **Fig. 4 (third and fourth panel)**. When Δλ= 15 nm (microenvironmental alterations surrounding tyrosine residues), increase in synchronous fluorescence intensity is observed upon addition of CQD. Also a considerable blue shift of the tyrosine peak from 304 to 297 nm (7 nm blue shift) is detected. This blue spectral shift upon addition of CQD probably indicates that the hydrophobicity of the environment surrounding the tyrosine residues is increased, whereas the polarity around the tyrosine residues appears to diminish. Moreover enhancement in synchronous fluorescence intensity is noticed upon addition of CQD also when Δλ was set at 60 nm (micro environmental alterations surrounding tryptophan residues) (fourth panel). Interestingly upon addition of CQD the emission maxima at 337 nm that corresponds to the surrounding microenvironment of the tryptophan residues also reveals a red shift from 337 nm to 339 nm (2 nm red shift). This spectral red shift possibly suggests enhancement in the polarity around the tryptophan residues. Therefore the observations signify that the microenvironment of both tyrosine and tryptophan residues is considerably affected upon addition of GNP and CQD. Furthermore for better understanding, the fluorescence intensity ratio is also evaluated by keeping Δλ at both 15 and 60 nm (**Fig. 4, lower left panel**). From the figure it is evident that the ratio F/F_0 (ratio of synchronous florescence maxima of HHb in presence of indicated concentration of CQD to the synchronous fluorescence maxima in absence of CQD) obtained from the synchronous fluorescence spectra is observed to be higher when Δλ= 60 nm in comparison to when Δλ is set at 15 nm. Perhaps CQD may facilitate closer interaction with tryptophan residues compared to tyrosine residues within HHb. This observation can be understood to some extent since microenvironment of tryptophan residues is observed to exhibit a red shift or getting exposure to a polar environment.

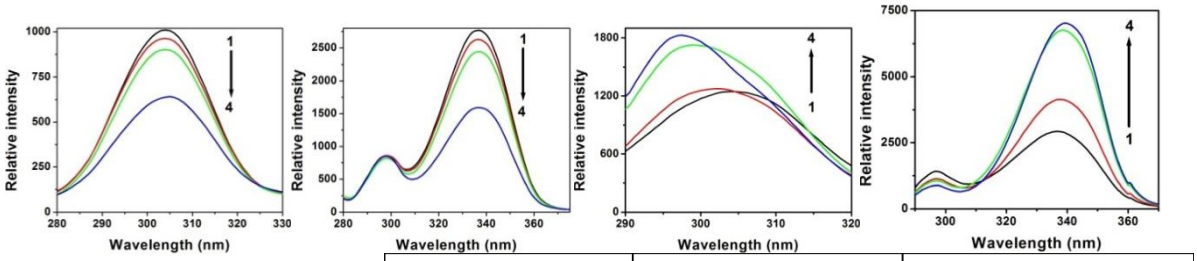

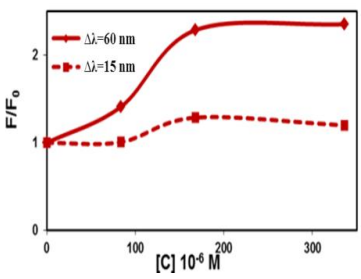

Synchronous fluorescence	GNP	CQD
Δλ=15 nm	Fluorescence quenching ↓	Fluorescence enhancement ↑
	1 nm red shift	7 nm blue shift
Microenvironment of Tyrosine residues	Exposed to more hydrophilic environment	Exposed to more hydrophobic environment
Δλ=60 nm	Fluorescence quenching ↓	Fluorescence enhancement ↑
	No spectral shift	2 nm blue shift
Microenvironment of Tryptophan residues	No change in polarity	Exposed to a more hydrophilic environment

Figure 4. The synchronous fluorescence spectra at Δλ= 15 nm of HHb in presence GNP at ambient temperature are shown. Concentration of HHb is 5 ×10^{-6} M. The concentrations of GNP used here are 0 (1), 1 x 10^{-6} M (2), 4 x 10^{-6} M (3), 25 x 10^{-6} M (4) (first panel). The synchronous fluorescence spectra at Δλ= 60 nm of HHb in presence GNP at the above mentioned conditions are shown. The concentrations of GNP used here are 0 (1), 1 x 10^{-6} M (2), 4 x 10^{-6} M (3), 25 x 10^{-6} M (4) (second panel). The synchronous fluorescence spectra at Δλ= 15 nm of HHb in presence CQD at the above mentioned conditions are shown. The concentrations of CQD used here are 0 (1), 0.84 x 10^{-4} M (2), 1.68 x 10^{-4} M (3), 3.36 x 10^{-4} M (4) (third panel). The synchronous fluorescence spectra at Δλ= 60 nm of HHb in presence CQD at the above mentioned conditions are shown. The concentrations of CQD used here are 0 (1), 0.84 x 10^{-4} M (2), 1.68 x 10^{-4} M (3), 3.36 x 10^{-4} M (4) (fourth panel).Alterations in synchronous fluorescence intensity ratio of HHb in presence of CQD (Δλ=15 and 60 nm) (lower left panel).Summary of observations of synchronous fluorescence spectra of HHb in presence of GNP and CQDhas been represented here (lower right panel).Modified from Reference [1, 2].

2.1.4. Determination of time-resolved fluorescence properties of HHb upon interaction with GNP and CQD

To substantiate the observation of fluorescence properties, time resolved spectroscopic measurements are performed to determine the fluorescence lifetimes using TCSPC (time correlated single photon counting) techniques. For simplicity the average emission lifetime, <τ> obtained from the following equation is only discussed

$$\langle \tau \rangle = \frac{\sum a_i \tau_i^2}{\sum a_i \tau_i} \qquad \ldots.1$$

where a_i signifies the normalized pre-exponential factor and $\tau_i$indicates corresponding lifetime respectively. Using the above equation (1) the average lifetime $\langle \tau \rangle$ for HHbis estimated to be 1.3 ns. The $\langle \tau \rangle$ofHHb-GNP, is calculated to be 1.4 ns (**Fig. 5, lower right panel**). Lifetime of HHb does not change significantly upon addition of GNP thus indicating the quenching to be static in nature.

However the average lifetime of HHb in presence of CQD increases significantly to 2.37 ns upon addition of CQD (**Fig. 5, lower right panel**). Therefore the fluorescence

enhancement in presence of CQD is observed to occur along with an enhancement in average lifetime. It is already known that the time available for the fluorophore to interact with or diffuse in its environment is determined by its lifetime measurements. Thus an increase in $\langle\tau\rangle$,upon addition of CQDmay occur due to exposure of the probably tryptophan residues within HHb to a more hydrophilic environment.

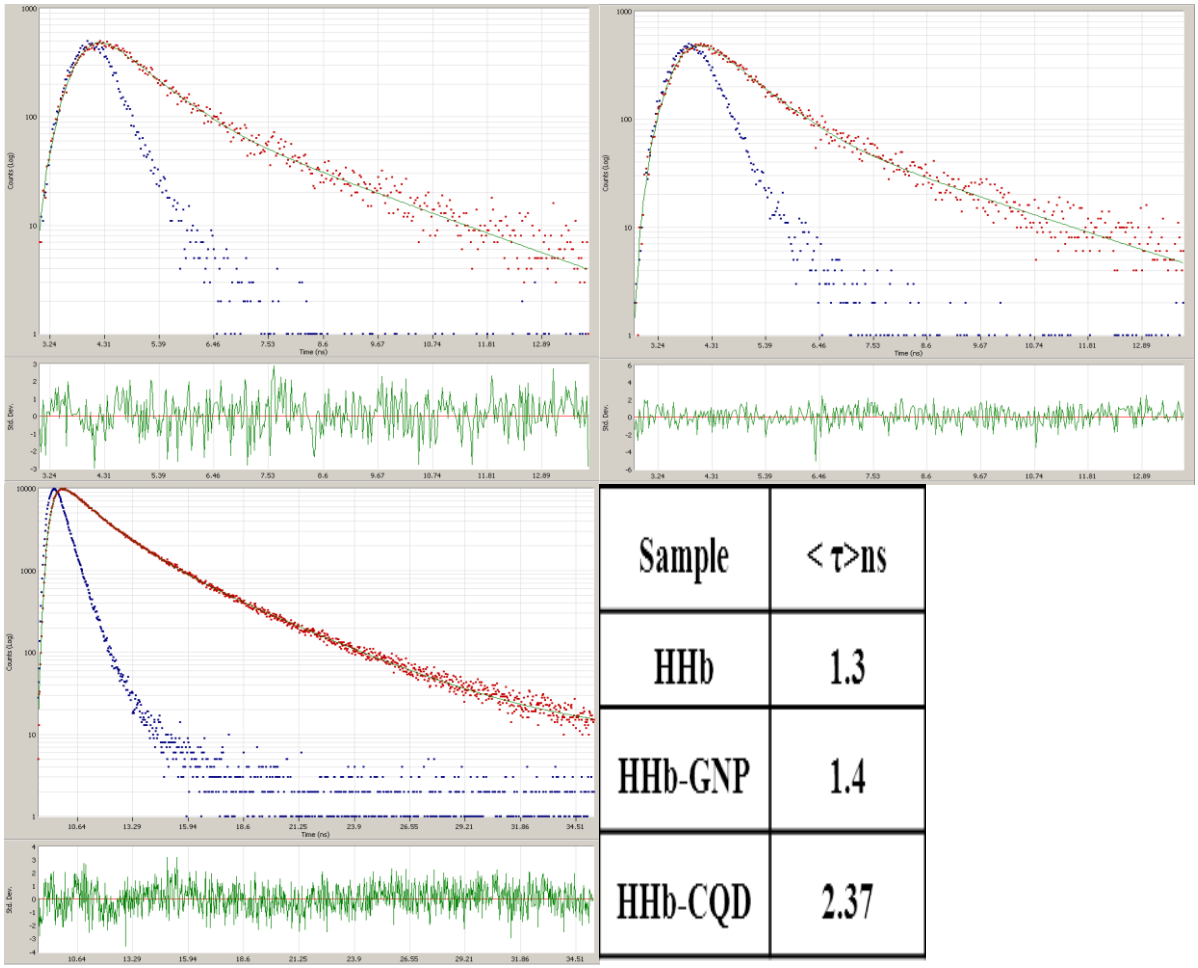

Sample	<τ>ns
HHb	1.3
HHb-GNP	1.4
HHb-CQD	2.37

Figure 5. Fluorescence decay profile of the HHb (red) along with the impulse response. Faster component is shown by blue line and residual is given below. Concentration of HHb is 5 ×10^{-6} M, χ^2 – 1.15 (upper left panel). Fluorescence decay profile of the HHb (red) in presence of GNP, along with the impulse response. Faster component is shown by blue line and residual is given below, χ^2 – 1.06. Concentration of GNP is ~ 5 x 10^{-6} M) (upper right panel). Fluorescence decay profile of the HHb (red) in presence of GNP, along with the impulse response. Faster component is shown by blue line and residual is given below. Concentration of CQD used here is ~ 3.36 x 10^{-4} M, χ^2 – 1.07 (lower left panel).Here, λ_{ex} = 280 nm, λ_{em} = 330 nm. Summary of observations of average lifetime of HHb upon interaction with GNP and CQD has been represented here (lower right panel).Modified from Reference [1, 2].

2.1.5. Revealing the freedom in rotational motions by steady-state and anisotropy measurements

The value of lifetime indicates the time obtainable for tryptophan and tyrosine residues to interact with or diffuse in its environment. An increase in lifetime of HHb in presence of CQD may indicate that the fluorophores are possibly being more exposed to the hydrophilic

environment. Moreover it may happen that CQDs can produce motional freedom within HHb resulting in exposure of tryptophan and tyrosine residues to a more polar environment and thereby facilitating an increase in average lifetime. To monitor the dynamic flexibility of proteins both steady state and time-resolved anisotropy measurements are performed.

As observed in **Fig. 6, right panel** the steady state fluorescence anisotropy (*r*) diminishes in presence of CQD thereby suggesting significant freedom in motion surrounding the microenvironment of tryptophan and/or tyrosine residues within HHb.

Time-resolved anisotropy decay of HHb reveals that the time of anisotropy decay of HHb decreases in presence of CQD **(Fig. 6, left panel)**. The limiting anisotropy (r_0) is also calculated and shown in **Fig. 6, left panel**, for HHb and its interaction with CQD. Here the values of *r(t)* as obtained from the form of time-dependent anisotropy decay may influence the rotational flexibility of the protein.

Also, estimation of complicated vibrational motions by using correlation times is possible. Here the alterations in the vibrational distributions probably will depend on the changes in lifetimes due to changes in protein conformation. One of the ways to interpret the correlation time is by evaluating the overall rotational correlation time (τ_c) of the protein, preferably by means of Perrin's equation,

$$\tau_c = (\langle\tau\rangle r)/(r_0 - r) \quad \ldots. (2)$$

Where r_0 is the limiting anisotropy, r is the steady state anisotropy and $\langle\tau\rangle$ denotes average fluorescence lifetime respectively.

The rotational correlation time that has been calculated is mentioned in **Fig. 6, right panel)**. The rotational correlation time of HHb appears to be reduced significantly in the presence of CQD indicating a freedom in conformational flexibility in HHb during its interaction with CQD. It may happen that the increase in rotational freedom is associated with enhancement in steady-state fluorescence and average lifetime of HHb upon interaction with CQDs.

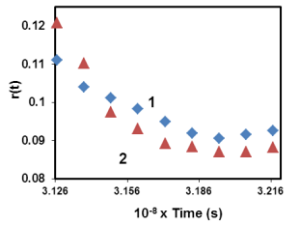

Sample	Anisotropy (r)	Initial /limiting anisotropy (r_0)	Rotational correlation times (τ_c) ns
HHb	0.09	0.11	6.21
HHb-CQD	0.05	0.12	1.69

Figure 6. Time-resolved anisotropy decay of HHb in absence (1) and presence of CQD (2). Concentration of CQD used are (1) 0, (2) ~ 3.36 x 10^{-4} M. (λ_{ex} = 280 nm, λ_{em} = 330 nm) (left panel). Evaluation of parameters of steady-state and time-resolved anisotropy measurements (right panel). Modified from reference [2].

2.2. Secondary structural alterations in HHb in presence of GNP and CQD

2.2.1 Alterations in HHb's backbone conformation upon interaction with GNP and CQD

Evaluation of thermodynamic parameters upon interaction of HHb with GNP and CQD reveals hydrogen bonding interactions to be the predominant mode of interactions in both the cases [1,

2]. FT-IR bands are very sensitive to the conformational changes in the secondary structure of a protein and are related to the backbone conformational alteration preferably involving hydrogen bonding interactions. Thus FT-IR measurements are assessed focusing on the effect on carbonyl(C=O) stretching mode of HHb in absence and in presence of GNP. It is well known that the amide I band located around 1700-1600 cm^{-1}, is associated to C=O and C-N stretching vibrations of peptide backbone. From the **Fig. 7** (**left panel**), it is apparent that the FT-IR spectra of HHb exhibit C=O stretching vibration at 1643 cm^{-1}.This band gets decreased and broadened upon addition of GNP. The alterations in IR bands corresponding to the C=O stretching vibration probably imply that formation of hydrogen bond is preferably occurring by involvement of the C=O group of the polypeptide chain. Here hydrogen bond may occur with the H-atom of the hydroxyl group present within tyrosine moiety since exposure of tyrosine residues to a more hydrophilic environment is already noticed due to 1 nm spectral red shift in synchronous fluorescence measurements. The tryptophan indole N may also participate in hydrogen bond formation but the polarity of the microenvironment surrounding tryptophan residues are remaining unperturbed in spite of any interaction in presence of GNP (as evident in synchronous fluorescence measurements).

In presence of CQD, the IR band of HHb gets diminished but without any spectral shift (**Fig. 7, middle panel**). The changes in the amide I band probably suggests the involvement of the C=O group of the polypeptide backbone in hydrogen bond formation. In this case the indole N atom of tryptophan residues may play dominant role during hydrogen bonding interaction. The observations are going in favor with the earlier results obtained from synchronous fluorescence measurements that reveal exposure of tryptophan residues to more hydrophilic surrounding (red shift of 2 nm). Probably the exposure of tryptophan residues to a hydrophilic environment is facilitating conformational changes in HHb involving the polypeptide backbone.

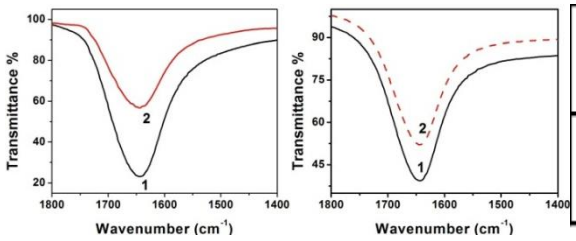

Properties	GNP	CQD
FT-IR signal	Decreased	Decreased

Figure7. FT-IR spectra of HHb (Concentration of HHb~ 5 x 10^{-6} M) and HHb-GNP complex have been represented. Concentrations of GNP are 0 (1), 7.5 x 10^{-6} M (2) (left panel). FT-IR spectra of HHb and HHb-CQD complex have been represented. Concentrations of CQD are0 (1), 3.36 x 10^{-4} M (2) (middle panel). Summary of observations of FT-IR spectra of HHb in presence of GNP and CQD (right panel) has been represented here. Modified from Reference [1, 2].

2.2.2. Alterations in secondary structure of HHb in presence of GNP and CQD: HHb's ability to retain its α-helicity

Too btain further information regarding conformational change of the protein in presence of GNP/CQD, circular dichroism (CD) measurements were performed. CD spectroscopy is a quantitative technique to investigate the conformational changes of proteins at the secondary structural level in aqueous solution. From **Fig. 8,** an intensive positive peak at about 195 nm and negative bands at about 208 and 222 nm were observed which were characteristic of α-helical content of HHb. Thus from far-UV CD data in the wavelength range from 190 to 240

nm a knowledge regarding the secondary structures of HHb can be obtained. The intensities of the negative bands at 208 and 222 nm increases, whereas intensities of the positive peak which is observed at 196 nm decreases with the addition of GNP (**Fig. 8, left panel**). Also minor enhancement in the negative bands at 208 and 222 nm is noticed, whereas a small decrease in the positive peak at 196 nm is observed upon addition of CQD (**Fig. 8, middle panel**).The CD spectra are assessed with the help of mean residue ellipticity (MRE) in degree cm^2 $mol^{-1}$from the following equation

$$[\theta_\lambda] = \frac{\theta}{10nlc} \quad \ldots 3$$

where c is the concentration of protein in g/ml, θ is observed rotation in degree, l is the path length in cm, and n indicates the totalnumber of amino acid residues within HHb (574 amino acid residues).

Evaluation of the percentage of α-helix in HHb in the presence of different concentrations of quencher is estimated from the following equation

$$\%\ of\ \alpha - helix = \frac{-[\theta]_{208} - 4000}{33000 - 4000} \quad \ldots.4$$

$$\%\ of\ \alpha - helix = \frac{[\theta]_{222} + 2340}{-30300} \quad \ldots.5$$

According to Equation 4 and 5, the percentage of α-helix content of HHb has been computed and it shows that HHb has ~ 32.46 % α-helicity at 208 nm and ~ 47.3 % α -helicity at 222 nm (**Fig. 8, right panel**). In presence of GNP, the percentage of α–helicity decreased from~ 32.46 % to ~ 27.02 % at 208 nm and from ~ 47.3 % to ~ 41.23 % at 222 nm (**Fig. 8, right panel**). Thus the CD spectra of HHb at both 208 and 222 nm, in absence and presence of GNP changed slightly and appear to be similar in shape. Thus the observations indicate that the structure of HHb is predominantly α -helical even in the presence of GNP. The CD signal at 222 nm caused by the n-π* amide transition of peptide chain is a more promising probe for the α–helicity because interference caused by other secondary structural elements is relatively weak at this wavelength and any unfolding of a helical protein is detectable.

This observation demonstrates that although small changes had occurred in the secondary structure as expected for the binding of GNP but the overall secondary structure of HHb is mostly retained and its identity is maintained even after complex ation with GNP. All the above observations indicate that GNP could be used as useful drug or should have potential biomedical applications especially as drug delivery system.

Similarly, the percentage of α–helicity slightly increases from 24.5% to ~ 26.5 % upon interaction with CQD. Thus the CD spectra corresponding to 208 nm indicates that the α -helical secondary structure of HHbis remaining nearly unaltered in spite of interaction with CQD (**Fig. 8, right panel**). Also the percentage of α–helicity diminishes from ~ 36.5 % to ~ 31.3 % in presence of CQD at 222 nm (**Fig. 8, right panel**). Thus,minor alterations in the percentage of α–helicity of HHb are observed in presence of CQD. As such the observations indicate that the overall secondary structure of HHb is nearly well retained. Largely, GNP and CQD may emerge as anleading member of gold and carbon nano family respectively that possess biocompatible properties for wide-range of biomedical application specifically including the development of biosensors, drug-delivery system within biological microenvironment.

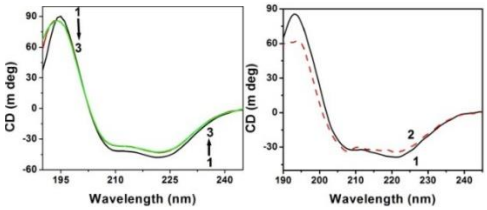

Sample	% of α-helicity at 208 nm	% of α-helicity at 222 nm
HHb-GNP	32.46 % to 27.02 %	47.3 % to 41.23 %
HHb-CQD	24.5 % to 26.5 %	36.5 % to 31.3 %

Figure8.CD spectra of HHb(Concentration of HHb~ 5 x 10^{-6} M) and HHb-GNP complex has been represented. The concentrations of GNP used here are 0(1), 6 x 10^{-6} M (2), 7.5 x 10^{-6} M (3) (left panel). CD spectra of HHb and HHb-CQD complex have been represented. The concentrations of CQD are 0 (1) and 3.36 x 10^{-4} M (2) (middle panel). Summary of observations of CD spectra of HHb in presence of GNP and CQD has been represented here (right panel).Modified from Reference [1, 2].

3 Conclusions

Thus summary of information obtained so far from UV-Vis, steady-state, synchronous, time-resolved, FT-IR, CD spectral analysis highlights that the spectroscopic properties of HHb as obtained respond differently upon interactions with GNP and CQD. In other words alteration in protein microenvironment also occurs in a different manner in presence of GNP and CQD. Remarkably even after the observed alterations in the microenvironment of HHb, due to its interaction with GNP/ CQD, the secondary structure of HHb, is in general nearly remaining unaltered as evident in CD spectral analys is. The observations are truly interesting since both the nanoparticles, GNP (18-20 nm) and CQD (4-5 nm) vary in their size by about ~13 -15 nm and yet alter the spectroscopic properties of HHb in their own in different manner by retaining HHb's secondary structural features. Under such conditions the application of the nanoparticles especially as an efficient drug-delivery system, biosensor and other biological fields will then rely on the characteristics and modes of interactions of the nanoparticles. Thus the utilization of the biocompatible properties of the nanoparticles at the nano bio-interface can be extensively carried out in diverse fields of nano-chemistry, structural biology, medicinal chemistry and others (Scheme 1), only after assessing the nature of interactions between biomolecules and nanoparticles. Furthermore, it appears that different nanomaterials can interact with different biomolecules in their own way and the different nature of interactions can be well revealed by assessing the spectroscopic properties of the same biomolecule like HHb. All in all this review compiles the knowledge regarding the potential applications of GNP and CQD by monitoring the nature of interactions with HHb within its biological environment.

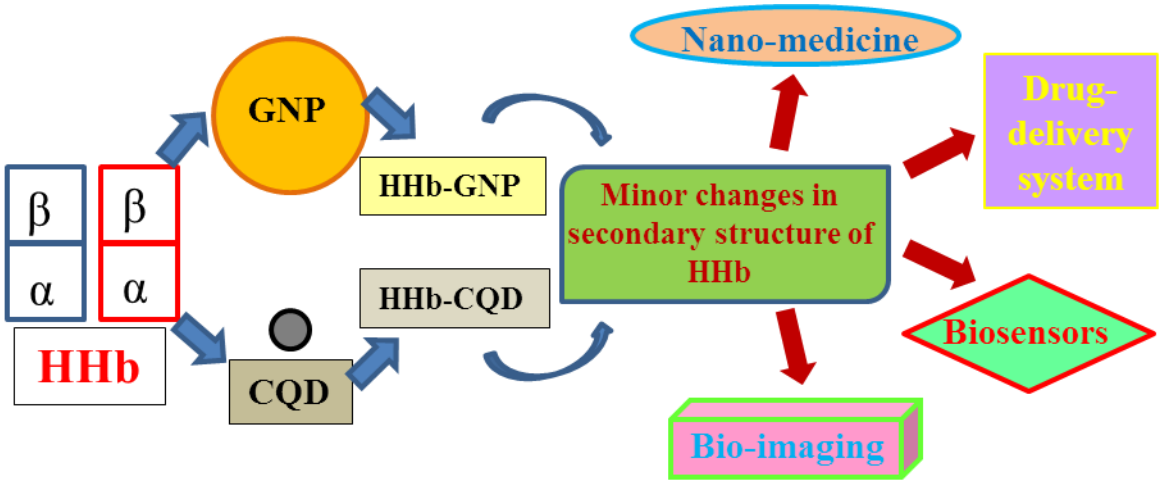

Scheme 1. Bimolecular interaction of HHb and GNP/CQD and the major biomedical application of GNP and CQD have been highlighted

Acknowledgement

TG gratefully acknowledges the University grant commission (UGC), New Delhi, India for awarding Emeritus Fellowship and providing contingency grant (F.6-6/2014-15/EMERITUS-2014-15-GEN-3976) for research purpose.

Reference

[1] M. Chakraborty, S. Paul, I. Mitra, M. Bardhan, M. Bose, A. Saha, T. Ganguly, J. Photochem. Photobiol. B Biol. (Elsevier) 355–366178 (2018).
[2] M. Chakraborty, I. Mitra, K. Sarkar, M. Bardhan, S. Paul, S. Basu, A. Goswami, A. Saha, B. Show, T. Ganguly, Spectrochim.Acta Part A (Elsevier) 215, 313–326 (2019).
[3] S. Sil, M. Kar, A.S. Chakraborti, J. Photochem.Photobiol. B Biol. (Elsevier) 41, 67–72 (1997).
[4] X.-C. Shen, X.-Y.Liou, L.-P.Ye, H. Liang, Z.-Y. Wang, J. ColloidInterf. Sci. (Elsevier) 311, 400–406 (2007).
[5] G. Pal, A. Paul, S.Yadav, M.Bardhan, A. De, J.Chowdhury, A. Jana, T.Ganguly, J Nanosci Nanotechnol. (American Scientific Publishers) 15, 5775-5784 (2015).
[6] S. Eustis and M. A. El-Sayed,Chem. Soc. Rev. (Royal Society of Chemistry) 35, 209-217 (2006).
[7] C. M. Cobley, J. Chen, E. C. Cho, L. V. Wang, and Y. Xia,Chem.Soc. Rev.(Royal Society of Chemistry) 40, 44-56(2011).
[8] T. Ming, X. S. Kou, H. J. Chen, T. Wang, H. L. Tam, K. W. Cheah,J. Y. Chen, and J. F. Wang,Angew Chem. Int Ed. (Wiley)47, 9685-90 (2008).
[9] C. Li, F. Fan, B. Yin, L. Chen, T. Ganguly, and Z. Q. Tian,NanoResearch (Springer) 6, 29-37 (2013)
[10] K. S. Soppimath and G. Betageri, Biomedical Nanostructures, John Wiley &SonsInc, New York (Wiley) (2008).
[11] U. K. Sur, G. Mandal, and T. Ganguly, Nanosci. Nanotechnol. An Indian Jour. (Trade Science Inc) 6 104-107(2012)
[12] Y.Wang, A. Hu, J. Mater. Chem. *C.* (Royal Society of Chemistry)2 6921-6939 (2014).
[13] R. Wang, K. Q. Lu, Z. R. Tang, Y. J. Xu,. J. Mater. Chem. A. (Royal Society of Chemistry) 5 3717-3734 (2017).
[14] Z. L. Wu, Z. X. Liu, Y. H. Yuan, J. Mater. Chem. B(Royal Society of Chemistry)5 3794-3809 (2017).
[15] Xu,R. Ray, Y. Gu, H. J. Ploehn, L.Gearheart, K.Raker, W. A. Scrivens, J. Am. Chem. Soc (American Chemical Society) 126 12736–12737 (2004).
[16] X. He, L. Gao, N. Ma, Sci Rep. (Nature) 3 2825(2013**)**.
[17] [30] T. T. Bui, S. Y. Park, *Green Chem*. (Royal Society of Chemistry)18 4245-4253(2016).
[18] T. Feng, X. Ai, G. An, P. Yang, Y. Zhao,*ACS Nano.*10 (American Chemical Society) 4410-4420(2016).
[19] J. Tang, B. Kong, H. Wu, M. Xu, Y. Wang, D. Zhao, G. Zheng,, Adv Mater. *(Wiley)* 25 6569-6574(2013).
[20] J. Pardo, Z.Peng, R. M. Leblanc, Molecules. (MDPI) 23 378-398(2018).

Karnatak University
Journal of Science

ISSN: 0075-5168

Estrous Cycle in Rodents: Phases, Characteristics and Neuroendocrine regulation

Chaitra R. Sharmaa
Vani, V.
Jayamma, Y.
Laxmi S. Inamdar (Doddamani)

Chaitra R.Sharma, Vani, V., Jayamma, Y., and Laxmi S. Inamdar (Doddamani) "Estrous Cycle in Rodents: Phases, Characteristics and Neuroendocrine regulation" Karnatak University Journal of Science 51, 40-53 (2020).

Estrous Cycle in Rodents: Phases, Characteristics and Neuroendocrine regulation

Chaitra R. Sharma[a], Vani, V.[b], Jayamma, Y.[c], and Laxmi S. Inamdar (Doddamani)[a,*]
[a]Molecular Endocrinology, Reproduction and Development Laboratory, Department of Zoology, Karnatak University, Dharwad 580 003, India
[b]Molecular Reproduction, Development and Genetics Department, Indian Institute of Science, Bangalore 560 012, India
[c]J.S.S.Banashankari Arts, Commerce and S.K. Gubbi Science College, Dharwad

* **Corresponding author**: Prof. Laxmi S. Inamdar
E-mail:ls_doddamani@yahoo.com; Tel: +91-836-2215230 (O);+91-836-2743160 (R)

Abstract:
Estrous cycle is the sequence of events of reproductive cycle in mammals other than primates. The estrous cycle in mice lasts for 4-5 days and is classified as proestrus, estrus, metestrus, and diestrus. Microscopic evaluation of the type of cells present in vaginal smears is the most accepted way of assessment of estrous cycle. The duration and proportion of these cell types vary among species. Cyclic ovarian function is under the control of hypothalamic-pituitary-gonadal (HPG) axis. The gonadotropes responding to gonadotropin-releasing hormone (GnRH), synthesize and release luteinizing hormone (LH) and follicle stimulating hormone (FSH), which induce ovarian folliculogenesis, ovulation and formation of corpus luteum (CL). Greatest GnRH release triggers the preovulatory surge of gonadotropins on the afternoon of proestrus, subsequently plasma estrogen level reaches a peak which stimulates a small surge in FSH followed by a marked surge of progesterone. Ovulation occurs during estrus, when female is highly receptive to male. Mammals were classified based on the ovulation patterns as coitus-induced ovulators and spontaneous ovulators. The rats and mice come under the category of spontaneous ovulators. Species whose estrous period is confined to a certain time of year are referred to as seasonal breeders. The present review is an attempt to provide a comparative account of phases of estrous cyclicity among laboratory mammals, viz. mice, rats and hamsters and the neuroendocrine regulation of estrous cycle. The present review provides the details of various methodologies and formulations utilized in earlier studies to calculate the estrous cyclicity among multiple groups.
Key words: Estrous cycle; mouse; rat; hamster
Article history: Received: 19 August 2020; Received: 3 September 2020**;** Accepted: 5 September 2020

1. Introduction:

Estrous and menstrual cycles are the reproductive cycles occur in mammals and are the phenomenon of cyclic ovarian function. These reproductive cycles are required to produce mature ova through ovulation, which is essential for fertilization in the oviduct. Three interacting components viz., the hypothalamus, anterior pituitary and ovary control cyclic ovarian function. The hypothalamus has neurons that release neuropeptide GnRH into the hypophysial portal vasculature. This neuropeptide acts on the anterior pituitary to stimulate the release of the gonadotropins (LH and FSH). The gonadotropins acting on the ovary supply the signals that control the estrous cycle and stimulate the production of estradiol and progesterone. Estrous cycles are named for the cyclic appearance of behavioural sexual activity (estrus) that

occurs in all mammals except for primates. Estrous cycle is a cascade of hormonal and behavioural events which are progressive, highly synchronized, and repetitive. Menstrual cycles, occurring only in primates, are named for the regular appearance of menses due to the shedding of the endometrial lining of the uterus.

In female reproductive biological research, mice and rats are the most commonly utilized model organisms due to their well-characterized estrous cycle and secure handling. The short span of estrous cycle in rodents lasts for 4-5 days [1, 2] also makes them suitable for research. Female rodents are poly-estric, present spontaneous ovulation, and show regular and successive estrous cycles that may vary with age and species. Study of the estrous cycle in experimental animals is a helpful measure of the integrity of the HPG axis and the functioning reproductive status of the female reproductive system [2]. The present review provides details about estrous cyclicity in rodents and highlights its regulation by the HPG axis.

2. Historical perspective and phases of estrous cycle:

The English Zoologist Walter Heape [3] first used the term "estrus" [4] which is Latin adaptation of the Greek word "oistros" meaning sexual season [5]. Heape defined the progressive stages of the mammalian estrous cycle. The cycle itself divided into four stages, centred around the period of estrus, when mating behaviour was displayed. He called the period preceding estrus "proestrus", which signified the period of follicular growth in the ovary and he termed the period succeeding estrus "metestrus", a recovery period following ovulation, and "diestrus", a period when the ovarian secretions from the corpus luteum prepare the uterus for implantation. If fertilization does not occur, the cycle is repeated. Heape also coined the term "anestrus" to signify the time period when no mating behaviour was displayed [6]. Behavioural, morphological, cytological and histological changes in the reproductive tract, describe the phases of estrous cycle. Therefore, one full reproductive cycle consists of 'anestrous' and 'estrous' period.

Earlier, alterations in the vulva (like vulva swelling), vaginal secretions (like bleeding, and mucous), and uterus (like congestion) as well as microscopic changes in the reproductive tract, were used to characterize different phases of estrous cycle. However, macroscopic analysis was unreliable in small rodents. Histological analysis remains an invasive procedure which is not suitable for estrous cycle staging in live animals. Over time, Stockard and Papanicolaou [7] considered the alterations in vagina during the estrous cycle through histology and cytology which evaded the earlier problems of unreliability andinvasiveness. Later, numerous studies have accepted Stockard and Papanicolaou's methodology.

3. Methodology for assessment of estrous cycle:

Many studies have shown various methods for evaluation of the estrous cycle. These methods include observation of behavioural changes, visual assessment, [2, 8, 9], examining vaginal cytology [1, 2, 8, 10-12] and histological examination of the reproductive organs [13, 14]. The visual assessment and vaginal cytology observation are widely used and considered as a rapid and practical way to determine the phases of the estrous cycle [5].

3.1. Visual assessment: It is simple, non-invasive, fast, inexpensive, less stressful to animals, and can be carried out at anytime and anywhere provided the illumination is adequate. In visual assessment of estrous phase, the mouse should be held in the left hand and laid in the restraint with the forepaws resting on a surface, lifting the tail gently, the vulva be examined and

evaluated as per criteria of Champlin et al. [15]. The morphological appearance of the vagina at different phases of the estrous cycle is presented in Table 1.

3.2. Vaginal smear/cytology: It is the current methodology being used in most of the research laboratories. It is non-invasive, inexpensive, accurate, and reliable [16-18]. However, this method needs skill for microscopic examination of the vaginal smear.

To assess the estrous cyclicity, vaginal smears need to be taken daily at 8.00 AM. First the animal has to be restrained and vagina is exposed. The vaginal secretions are flushed by gently releasing about 100 µl of 0.9% saline using a glass dropper. The smear is then placed on a clean glass slide and observed under microscope or air dried and stained with 0.1% methylene blue or pontamine blue, and observed under a light/compound microscope at 200 X magnification.

The vaginal smear consists of three types of cells, i.e., leukocytes, cornified epithelial cells, and nucleated epithelial cells. Determining the phase of estrous cycle is based on the ratio of these cells in the vaginal smear (Table 1 and Fig. 1).

Table 1. Classification of the phases of oestrous cycle based on the cell typesand appearance of vagina during different phases.

Phases of estrous cycle	Neutrophils	Small nucleated epithelial cells	Large nucleated epithelial cells	Anucleated keratinized epithelial cells	Relative cell density	Appearance of vagina
Proestrus	0 to +	++ to +++	0 to +	0 to +	Low to moderate	Vaginal opening is wide and the tissues are moist and reddish pink.
Estrus	0 to +	0 to +	0 to +	++ to +++	Moderate to high	Vagina appears similar to that seen at proestrus, but the tissues are lighter pink, less moist, and less swollen.
Metestrus	+ to +++	0 to +	0 to +	++ to +++	Moderate to high	The vagina is not open wide, not swollen, looks pale and dry.
Diestrus	++ to +++	+ to ++	+ to ++	0 to +	Low to moderate	Vaginal opening is small, moist, and closed with no tissue swelling. The vaginal tissues are bluish/purple in colour.

3.2.1. Estrous cycle in mice: Based on vaginal smears, the duration of one estrous cycle for mice is four- or five-days (Fig. 1A)

a. Proestrus: The proestrus is a short stage, lasting less than 24 hr in mice. The vaginal smear is dominated by nucleated epithelial cells, which occur singly or in sheet and become progressively acidophilic.
b. Estrus: This is the period of heat, and mating is permitted only at this time. This condition lasts from 12 to 48 hr. Many mitoses occur in vaginal mucosa. As new cells

accumulate, the superficial layer becomes squamous and cornified and their presence in vaginal smears is indicative of estrus. During late estrus, cheesy masses of cornified cells with degenerating nuclei located in the vaginal lumen, but few if any leukocytes are found in the estrus. Also, large basophilic epithelial cells are present.

c. Metestrus: This occurs shortly after ovulation and is intermediate between estrus and diestrus. The period lasts for 10-14 hours and mating is usually not permitted. The smear during this stage contains leukocytes, few cornified cells, and basophilic cells.
d. Diestrus: This lasts 60 to 70 hours. Vaginal smear during diestrus is primarily characterized by polymorphonuclear leukocytes and a few nucleated basophilic cells, and occasional vacuolated cells [9, 19].

In case pregnancy occurs, the cycles are interrupted for the duration of gestation that lasts for 20-22 days. At the end of the pregnancy the animal comes to estrus, but the cycles are again delayed until the termination of lactation [20, 21].

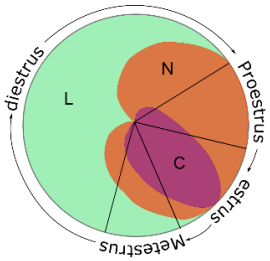

Figure 1A Mouse estrous cycle wheel

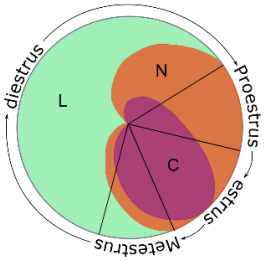

Figure 1B Rat estrous cycle wheel

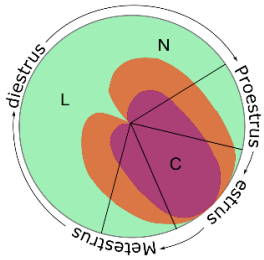

Figure 1C Hamster estrous cycle wheel

L =Leukocytes N =Nucleated epihelial cells C =Cornified epithelial cells

3.2.2. Estrous cycle in rats: Although the major events in rat estrous cycle are similar to those of mice with regard to the timing of events and cell types of vaginal smear, duration of phases and proportion of cell types varies (Fig. 1B). The duration of estrous cycle in rats is also four- or five-days. Duration of proestrus is twelve to fourteen hours. Estrus period lasts for twenty-five to twenty-seven hours. Metestrus lasts for six to eight hours. The duration of the diestrus phase in rats is fifty-five to fifty-seven hours [22-24].

3.2.3 Estrous cycle in hamsters: Hamsters have a short and consistent estrous cycle (4 days), a certain time of ovulation, and short gestation period (16 days). The stages of the cycle are comparable in hamsters and rats, but the durations of the stages differin the two species; proestrus and metestrus are significantly shorter in the hamster than in the rat, whereas diestrus is considerably longer (almost 20 hr longer) in the hamster than in the rat (Fig. 1C). The duration of estrus is similar in both species. In hamsters proestrus lasts for 3 hours, estrus lasts for 12 hours, metestrus lasts for 4 hours and diestrus for 76 hours [25].

4. Histological features of ovary and uterus during different phases of estrous cycle: During proestrus, functional involution of the corpora lutea and preovulatory swelling of the follicles takes place. Fluid collects in the uteri and they become highly contractile. When animal enters estrus, loss of mitotic activity and leukocyte infiltration is noticed. In the ovary, older corpora lutea degenerate and newly formed corpora lutea are small, with cells showing basophilic cytoplasm. In metestrus, the ovaries contain corpora lutea and small follicles, and the uteri have diminished in vascularity and contractility. During diestrus, functional regression of the corpora lutea occurs. The uteri are small anaemic and slightly contractile.

5. Neuroendocrine control of estrous cyclicity: The estrous cycle is under the control of central nervous system (CNS).

Five structurally distinct hypothalamic nuclei are involved in the immediate control of reproduction, including signals inducing the preovulatory gonadotropin surge. The suprachiasmatic nucleus and medial optic nucleus participate in the timing of the LH surge. GnRH released in a pulsatile pattern of rhythmic secretory bursts whose frequency and amplitude vary according to cycle stage. The gonadotropes, responding to GnRH, synthesize and release LH and FSH, which induce ovarian folliculogenesis, steroidogenesis, ovulation, and formation of corpus luteum (Fig 2A and B). The ovarian steroids exert a feedback effect on host of target tissues, including the brain and pituitary gland, which contain estradiol receptors. LH and FSH during the rodent estrous cycle are maintained at low basal levels on estrus, metestrus, diestrus, and on the morning of proestrus. This is primarily due to the effect of negative feedback by estrogen and progesterone. On the afternoon of the proestrus, when the level of estrogen in the blood becomes high, serum level of both FSH and LH start to rise rapidly, generating the preovulatory surge. Ovulation occurs while LH is in ascendancy with a surge of estrogen level. This dramatic surge peaks in the evening of the proestrus, after that serum level of both LH and FSH starts to decline. By the morning of the estrus, LH level has returned to its basal level; serum FSH on the other hand shows secondary surge. In the evening of the estrus serum level of FSH declines to basal level (Fig. 2A and B). The prolonged FSH surge functions to recruit a new cohort of ovarian follicles for the subsequent cycle. The ruptured follicle transferred into a corpus luteum, which becomes functional under the influence of prolactin. The discharge of LH from the anterior lobe seems to be inhibited by rising titers of progesterone (Fig.2A and B) [6, 26].

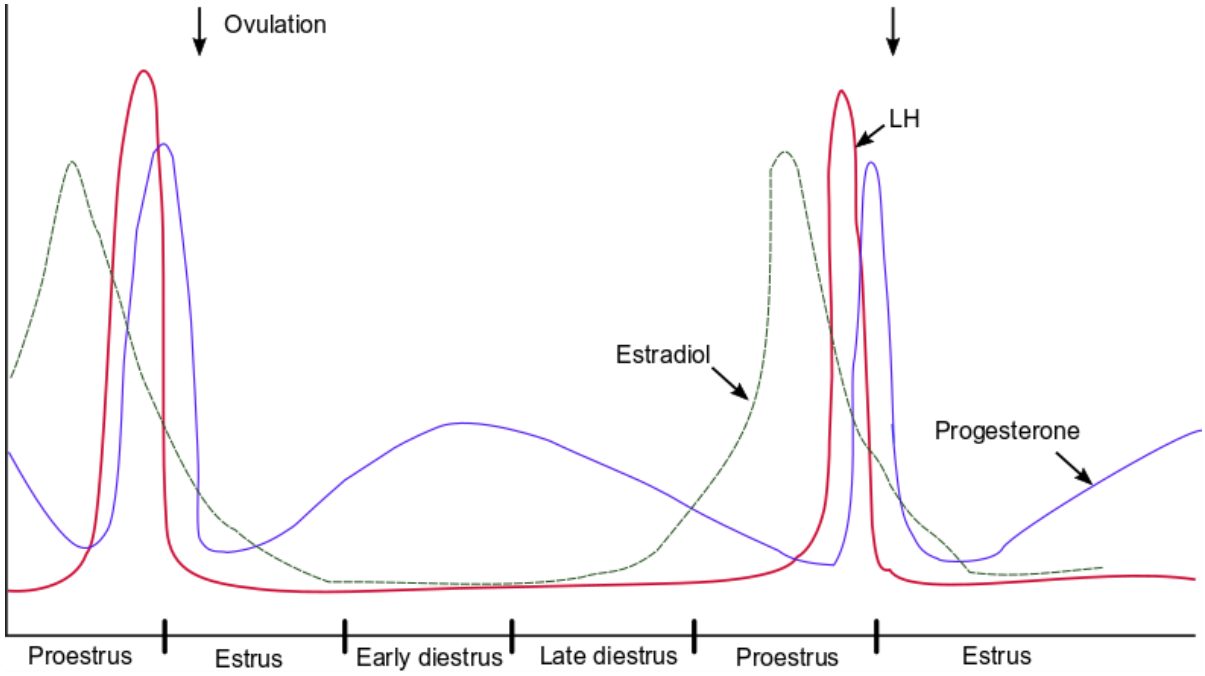

Figure 2A. Schematic diagram showing the hormonal events during the estrous cycle of the 4-day cycling female rat. The progesterone surge following LH surge and prior to ovulation is responsible for increased receptivity in the female for the male. There is a secondary, slow increase and decline in progesterone secretion from the corpus luteum that occurs during diestrus in the unmated female [26]

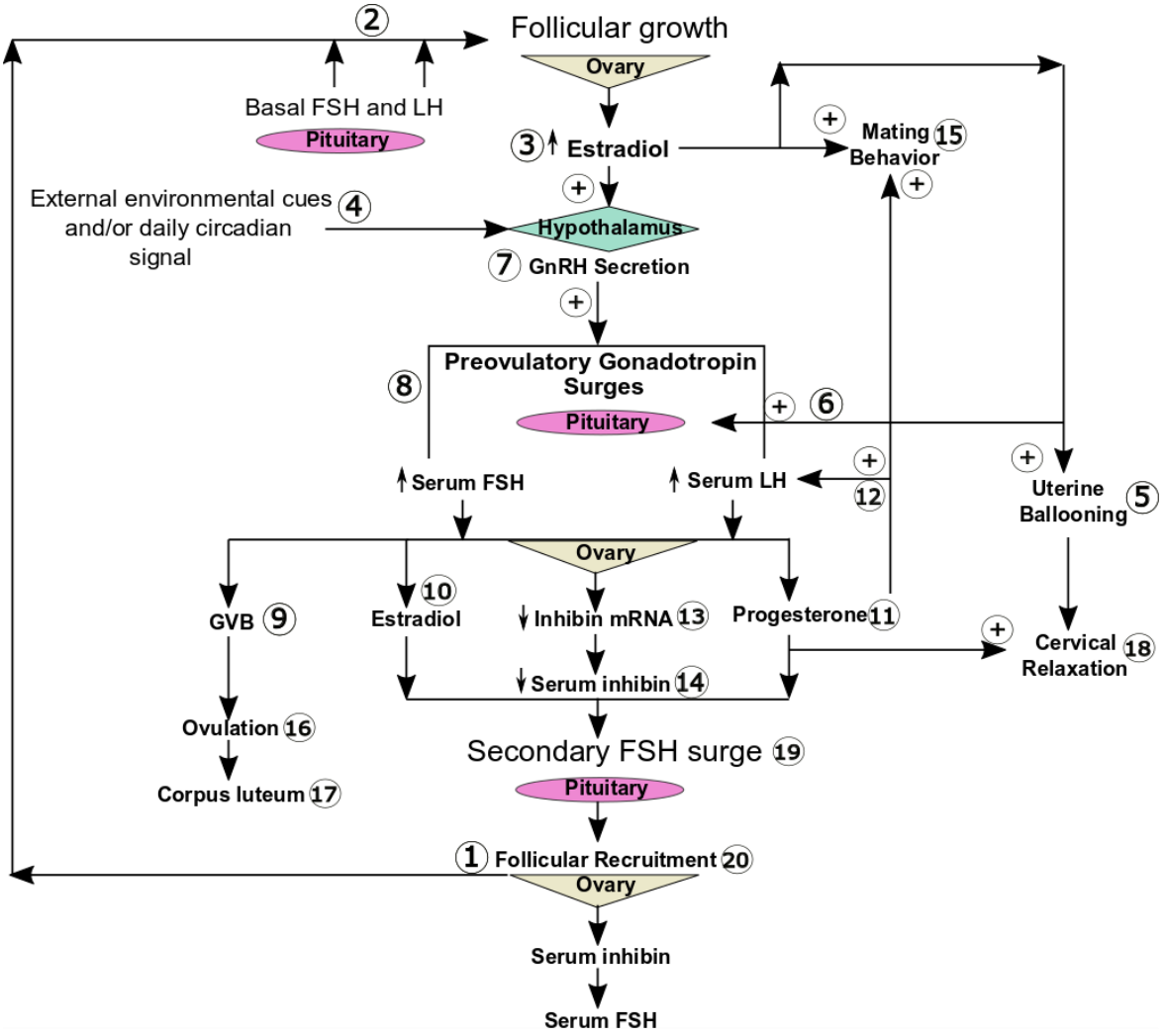

Figure 2B. Schematic chart showing the regulation of estrous cycle in rodents. The secondary FSH surge recruits a cohort of follicles (1) which then matures under the influence of basal levels of FSH and LH (2). These follicles begin to secrete increasing amounts of estradiol (3). Every day, under conditions of a controlled light-dark cycle (14h light: 10 h dark), an excitatory signal arises in the hypothalamus (4). Estradiol sensitizes the hypothalamus (3), causes fluid retention in the uterine lumen (5), primes the anterior pituitary gland by increasing GnRH receptors (6), and triggers the release of GnRH receptors (6), and triggers the release of GnRH at 1400 hr (7), causing LH and FSH preovulatory surges (8). The LH surge causes germinal vesicle breakdown in the oocytes (9), a decrease in estradiol secretion (10), and an increase in serum progesterone (11), which enhances LH release (12). Inhibin synthesis and secretion are suppressed (13, 14). Mating behavior is induced by the progesterone (15), and ovulation occurs (16), leading to formation of corpus luteum (17). The secondary FSH surge (19) causes follicular recruitment of the next cohort of follicles (20), initiating a new cycle.

6. Methodologies for evaluation of estrous cyclicity:

Over the years, attempt to evaluate the estrous cycle in terms of frequency, regularity, length, estrus phase interval, and diestrus index have been done. But these methods do not provide detailed information about relative durations of each phase during the observation period. For example, comparison of the estrous phases of experimental group (drug administration group) with control group is difficult to interpret. In the present review, an attempt is made to summarize all earlier methodologies as well as our methodology.

Following terminologies were frequently being used to calculate estrous cyclicity in most of the published papers:

i. Estrous cycle length: The length or duration of estrous cycle is the time period between proestrus to diestrus. In mice and rats, the regular estrous cycle length is 4-5 days [27, 28]. Some investigators mention estrous cycle length as duration of estrous cycle [29].

ii. Cycle frequency [30]: Cycle frequency is the total number of estrous cycles during observation period. Some authors represent it as number of cycles [31].

iii. Numbers of regular estrous cycles [32]: It is the total number of regular estrous cycles (i.e. 4 -5 days cycles) during observation period. Some investigators report % regular estrous cycles i.e., % of animals exhibiting regular 4-5 day estrous cycles during treatment period [33].

iv. Frequency of occurrence of each phase in estrous cycle [29, 34]: It is the number of times each phase appeared during observation period. It is generally represented in terms of percent using following formula:

$$\text{Stage frequency \%} = \frac{\text{No.of particular phase}}{\text{Duration of experiment}} \text{X } 100$$

Ex: Estrus stage frequency: It is the number of times estrus stage appears during observation period.

$$\text{Estrus stage frequency \%} = \frac{\text{No.of estrusphase}}{\text{Duration of experiment}} \text{ X } 100$$

Some authors refer it as % number of days [35]

v. Diestrus index [36, 37]: It is nothing but diestrus stage frequency. It is calculated using the formula as follows:

$$\text{Diestrus index} = \frac{\text{No.of days with clear diestrus smear X } 100}{\text{Total duration of experiemnt}}$$

vi. Total numbers of each phase during observation period [38-40]: Most of the authors depict the data of estrous cyclicity as total numbers of each phase during observation period. It is nothing but frequency of occurrence of each phase of estrous cycle.

vii. Estrous cycle ratio [41]: It is the proportion of proestrus and estrus to the proportion of metestrus and diestrus.

$$\text{ECR} = (\text{Proestrus} + \text{Estrus}) / (\text{Metestrus} + \text{Diestrus}).$$

In the above mentioned terminologies, no. i, ii and iii are related to frequency and length of the estrous cycle, whereas no. iv, v and vi are related to frequency of each phase during observation period. Further, item number iv and v are one and the same event, using same formula albeit giving different names. However, item no. vi is well recorded in most of the papers.

Further, in this review, we are providing a detailed methodology and sequences for data of estrous cyclicity using control and one treatment group (0.5 mg/kg bwt of stanozolol). For

this, 10 mice were selected and were divided into two groups each group containing 5 animals. Mice in 1st group were treated with vehicle alone (0.5 ml of 1% alcohol) and 2nd group was administered with 0.5 mg/kg bwt of stanozolol (an anabolic-androgenic steroid) for 30 days. Estrous cycle was monitored daily at 8.00 AM. The phases of the estrous cycle from both control and treatment groups were identified and recorded daily for 30 days. They were designated as P-proestrus, E-estrus, M-Metestrus and D-diestrus. Number of estrous cycles during experimental/observation period was calculated (One complete cycle lasts for 4 to 5 days) and duration of estrous cycle was calculated (Table 2) for each animal by using the following formula:

$$\text{Duration of estrous cycle/animal} = \frac{\text{Duration of experiment}}{\text{Total number of estrous cycles}}$$

Where, duration of experiment = period of estrous cycle monitored =30 days

Next, the total number of each phase in each animal was counted and average duration of each phase per cycle was calculated (Table 3)by using below mentioned formulation.

$$\text{Average duration of particular phase/cycle} = \frac{\text{Total no. of particular phase during observation period}}{\text{Total no. of estrous cycles}}$$

$$\text{For example, Average duration of proestrus (P)} = \frac{\text{Total no. of Proestrus}}{\text{Total no. of estrous cycles}}$$

Further, in Table 3 the total duration of each phase was calculated in terms of days. However, mentioning the values of estrous cyclicity in terms of hours is more precise and accurate. Hence to convert the vales from day to hours, the total duration of each phases was multiplied with 24 h (Table 4).

Finally, the duration of each phase per cycle was converted into duration of each phase during experimental period by using following formula

$$\text{Total duration of each phase} = \frac{\text{Duration of each phase X Duration of experiment}}{\text{Average duration of cycle}}$$

The values of total duration of each phase are depicted in Table 5. The data were exported to SPSS statistical software.

Table 2. Showing total number and average duration of estrous cycles per animal during observation period.

Animal no. (Control)	Total observation days	Total number of cycles	Total number of each phase				duration of cycle/animal
			Proestrus	Estrus	Metestrus	Diestrus	
1	30	6	4	6	3	17	5
2	30 30	6	5	7	4	14	5
3	30	7	5	7	4	14	4.285
4	30	7	4	8	5	13	4.285
5	30	7	4	7	4	15	4.285
Animal no. (Treated)	Total observation days	Number of Cycles	Total number of each phase				duration of cycle/animal
			Proestrus	Estrus	Metestrus	Diestrus	
1	30	3	2	4	1	23	10
2	30	3	1	3	2	24	10
3	30	3	1	3	3	23	10
4	30	2	2	2	1	25	15
5	30	3	2	4	3	21	10

Table 3. Showing duration of each phase in an estrous cycle per animal (in days) during observation period

Animal no. (Control)	Duration of each phase / cycle			
	Proestrus (days)	Estrus (days)	Metestrus (days)	Diestrus (days)
1	0.66	1	0.5	2.83
2	0.83	1.16	0.66	2.33
3	0.714	1	0.57	2
4	0.57	1.14	0.714	1.857
5	0.57	1	0.57	2.142
Animal no. (Treated)	Duration of each phase / cycle			
	Proestrus (days)	Estrus (days)	Metestrus (days)	Diestrus (days)
1	0.66	1.33	0.33	7.66
2	0.33	1	0.66	8
3	0.33	1	1	7.66
4	1	1	0.5	12.5
5	0.66	1.33	1	7

Table 4. Showing duration of each phase in an estrous cycle per animal (in hours) during observation period

Animal no. (Control)	Duration of each phase / cycle			
	Proestrus (hours)	Estrus (hours)	Metestrus (hours)	Diestrus (hours)
1	15.84	24	12	67.92
2	19.92	27.84	15.84	55.92
3	17.14	24	13.68	48
4	13.68	27.36	17.13	44.56
5	12	24	13.68	51.4
Animal no. (Treated)	Duration of each phase / cycle			
	Proestrus (hours)	Estrus (hours)	Metestrus (hours)	Diestrus (hours)
1	15.84	31.92	7.92	183.84
2	7.92	24	15.84	192
3	7.92	24	24	183.84
4	24	24	12	300
5	15.84	31.92	24	168

Table 5. Showing total duration of each phase during observation period in hours

Animal no. (Control)	Average duration of each phase during observation period in hours				Total
	Proestrus (hrs)	Estrus (hrs)	Metestrus (hrs)	Diestrus (hrs)	
1	95.04	144	72	407.52	718.56
2	119.52	167.04	95.04	335.52	717.12
3	119.28	168	95.76	336	719.04
4	95.76	191.52	119.28	312.02	718.58
5	95.76	168	95.76	359.76	718.28
Mean duration	**105.07**	**167.71**	**95.56**	**350.16**	718.5
Animal no. (Treated)	Average duration of each phase during observation period in hours				Total
	Proestrus (hrs)	Estrus (hrs)	Metestrus (hrs)	Diestrus (hrs)	
1	47.52	95.76	23.76	551.52	218.56
2	23.76	72	47.52	576	719.28
3	23.76	72	72	551.52	719.26
4	48	48	24	600	720
5	47.52	95.76	72	504	719.28
Mean duration	**38.112**	**76.70**	**47.85**	**556.6**	719.27

In summary, estrous cycle in rodents is typically of 4-5 days in duration and its phases are identified based on the proportion of cell types in the vaginal smear. The present review has given the details of various methodologies and formulations utilized in earlier studies to calculate the estrous cyclicity parameters among multiple groups. It is the first review to provide details and comparisons of various types of calculations used for estrous cyclicity data. Further, we have provided the details of our methodology to calculate the duration of each phase of estrous cycle during experimental/observation period along with examples. These details can be utilized as a reproductive index for spontaneous ovulating mammals.

Acknowledgement:
The work was supported by a research grant from the University Grants Commission, New Delhi under UGC-SAP-DSA-I. One of the authors (LSI) thanks Indian National Science Academy, New Delhi for the INSA Visiting Scientist Award to visit NIRRH, Mumbai. CRS thanks DST, New Delhi for the award of INSPIRE fellowship. All experiments were conducted in accordance with the regulations of CPCSEA guidelines and the Institutional Animal Ethical Committee No.639/GO/02/a/CPCSEA of the Karnatak University, Dharwad, Karnataka, India.

Reference:

[1] W. W. Andrews and S. R. Ojeda, A detailed analysis of the serum LH secretory profiles of conscious free-moving female rats during the time of puberty, Endocrinology (Oxford Academic) 109, 2032–2039 (1981).
[2] T. Auta and A. T. Hassan, Alteration in oestrus cycle and implantation in Mus musculus administered aqueous wood ash extract of Azadirachta indica (neem), Asian Pacific Journal of Reproduction (Hainan Medical University) 5(3), 188–192 (2016).
[3] W. Heape, The "sexual season" of mammals and the relation of the "prooestrum" to menstruation, Quarterly Journal of Microscopical Science (The Company of Biologists) 44, 1–70 (1900).
[4] L. M. Jaramillo, I. B. Balcazar and C. Duran, Using vaginal wall impedance to determine estrous cycle phase in Lewis rats, Lab Animal (Nature) 41, 122–8 (2012).
[5] F. K. Marcondes, F. J. Bianchi and A. P. Tanno, Determination of the estrous cycle phases of rats: some helpful considerations, Brazilian Journal of Biology (Instituto Internacional de Ecologia) 62 (4A), 609–614 (2002).
[6] S. M. Kilen and N. B. Schwartz, Estrous cycle, In: Encyclopedia of Reproduction (Vol 2), E. Knobil, J. D. Neill, eds. Academic Press: California, USA, p127-136 (1999)
[7] C. R. Stockard, G. N. Papanicolaou, The existance of typical oestrous cycle in the guinea-pig-with a study of its histological and physiological changes, American Journal of Anatomy (Wiley) 22, 225-280 (1917).
[8] K. E. Barret, S. M. Barman, S. Boitano, H. L. Brooks, Reproductive development and function of the female reproductive system, In: Ganong's review of medical physiology, 24th edition, McGraw-Hill Education: (2009)
[9] E. Allen, The oestrous cycle in the mouse, American Journal of Anatomy 30, 297–371(1922).
[10] J. J. Lohmiller, S. P. Swing, Reproduction and breeding, In: The laboratory rat, (2nd ed), M. A. Suckow, S. H. Weisbroth, C. L. Franklin, Academic Press: pp. 147-162 (2006)
[11] A. C. McLean, N. Valenzuela, S. Fai and S. A. Bennet, Performing vaginal lavage, crystal violet staining, and vaginal cytological evaluation or mouse estrous cycle staging identification, Journal of Visualized Experiments (My Jove Corporation) 15(67), e4389 (2012).

[12] C. C. Paccola, C. G. Resende, T. Stumpp, S. M. Miraglia and I. Cipriano, The rat estrous cycle revisited: a quantitative and qualitative analysis, Animal Reproduction (Elsevier) 10(4), 677–683 (2013).
[13] S. L. Byers, M. V. Wiles, S. L. Dunn and R. A. Taft, Mouse estrous cycle identification tool and images, PLoS One7(4), e35538 (2012).
[14] S. D. Ramos, J. M. Lee and J. D. Peuler, An inexpensive meter to measure differences in electrical resistance in the rat vagina during the ovarian cycle, Journal of Applied Physiology (The American Physiological Society) 91, 667–670 (2001).
[15] A. K. Champlin, D. L. Dorr and A. H. Gates, Determining the stage of the estrous cycle in the mouse by the appearance of the vagina, Biology of Reproduction (Oxford Academic) 8(4), 491–494 (1973).
[16] H. B. Sahoo, S. Nandy, A. K. Senapati, S. P. Sarangi and S. K. Sahoo, Aphrodisiac activity of polyherbal formulation in experimental models on male rats, Pharmaceutical Research (Springer) 6, 120–126 (2014).
[17] M. C. Cora, L. Kooistra and G. Travlos, Vaginal cytology of the laboratory rat and mouse: review and criteria for the staging of the estrous cycle using stained vaginal smears, Toxicologic Pathology (SAGE) 43, 776–793 (2015).
[18] A. F. Ajayi and R. E. Akhgbe, Staging of the estrous cycle and induction of estrus in experimental rodents: an update, Fertility Research and Practice (BMC) 6(5), 1-15 (2020).
[19] P. Grasso, M. Rozhavskaya and L. E. Reichert, In vivo effects of human follicle-stimulating hormone-related synthetic peptide hFSH-β-(90-95) on the mouse estrous cycle, Biology of Reproduction (Oxford Academic) 58, 821-825 (1998).
[20] J. C. Hoffmann and N. B. Schwartz, Timing of post-partum ovulation in the rat, Endocrinology (Oxford Academic) 76, 620 (1965).
[21] C. D. Turner and J. T. Bagnara, General endocrinology, fifth edition, W.B Saunders Company: Washington, USA, p516 (1971).
[22] E. B. Astwood, Changes in the weight and water content of the uterus of the normal adult rat, American Journal of Physiology (American Physiological Society) 126, 162-170 (1939).
[23] J. A. Long and H. M. Evans, The oestrous cycle in the rat and its associated phenomena, Memorial University of California 6, 1-148 (1922).
[24] A. M. Mandl, The phases of estrous cycle in the adult white rat, Journal of Experimental Biology (The Company of Biologists) 28, 576-584 (1951).
[25] E. Scheibler and F. Wollnik, Oestrus cycle of the Desert hamster (Phodopusroborovskii, Satunin, 1903), Laboratory animals (SAGE) 47, 301-311 (2013).
[26] D. O. Norris, Vertebrate endocrinology, 3rd edition, Academic press: California, USA, p396 (1996).
[27] A. B. Kostellow, D. Ziegler, J. Kunar, G. I. Fujimoto and G. A. Morrill, Effects of cannabinoids on estrous cycle, ovulation and reproductive capacity of female A/J mice, Pharmacology (Karger) 21, 68-75 (1980).
[28] J. F. Nelson, L. S. Felicio, P. K. Randall, C. Sims and C. E. Finch, A longitudinal study of estrous cyclicity in aging c57bl/6j mice: i. cycle frequency, length and vaginal cytology, Biology of Reproduction (Oxford University Press) 27, 327-339 (1982).
[29] C. I. Chika, N. A. Ifeyinwa, U. S. Azubuike and O. David, Oestrous cycle of Wistar rats altered by sterol and triterpenes rich fraction of Adansonia digitata (Linn) root bark - A scientific rationale for contraceptive use, Asian Pacific Journal of Reproduction (Wolters Kluwer Medknow) 8(2), 75-82 (2019).
[30] K. Flurkey, P. K. Randall, Y. N. Sinha, M. Ermini and C. E. Finch, Transient shortening of estrous cycles in aging C57BL/6J Mice: Effects of spontaneous pseudopregnancy,

progesterone, L-dihydroxyphenylalanine, and hydergine, Biology of Reproduction (Oxford University Press) 36:949-959 (1987).

[31] N. M. H. Al-Hamdani and H. N. Yajurvedi, Effect of cypermethrin on the ovarian activity and its impact on fertility and pubertal onset of offspring, Beni-Suef University Journal of Basic and Applied Sciences (Springer) (2017).

[32] S. C. Laws, J. M. Ferrell, T. E. Stoker, J. Schmid and R. L. Cooper, The effects of Atrazine on female wistar rats: An evaluation of the protocol for assessing pubertal development and thyroid function, Toxicological Sciences (Oxford University Press) 58, 366-376 (2000).

[33] A. S. Clark, M. E. Blasberg and E. M. Brandling-Bennett, Stanozolol, oxymetholone, and testosterone cypionate effects on the rat estrous cycle, Physiology and Behaviour (Elsevier), 63, 287-295 (1998).

[34] E. Ngadjui, P. Watcho, T. B. Nguelefack and A. Kamanyi. Effects of Ficus asperifoliaon normal rat estrus cyclicity, Asian Pacific Journal of Tropical Biomedicine (Wolters Kluwer Medknow) 3 (1), 53-57 (2013).

[35] G. A. Essiet, G. C. Akuodor, D. O. J. Aja, M. O. Nwokike, D. O. Eke and A.N. Chukwumobi, Effects of Salacia lehmbachii ethanol root bark extract on estrous cycle and sex hormones of female albino rats, Asian Pacific Journal of Reproduction (Wolters Kluwer Medknow) 7(6), 274-279 (2018).

[36] R. P. Rao and B. B. Kaliwal. Monocrotophos induced dysfunction on estrous cycle and follicular development in mice, Industrial Health (J stage) 40, 237–244 (2002)

[37] T. Auta and A. T. Hassan Alteration in oestrus cycle and implantation in Mus musculus administered aqueous wood ash extract of Azadirachta indica (neem), Asian Pacific Journal of Reproduction (Wolters Kluwer Medknow) 5(3), 188–192 (2016).

[38] A. Islam, S. Naskar, U. K. Mazumder, M. Gupta and S. Ghosal. Estrogenic properties of Phyllanthin and Hypophyllanthin from Phyllanthus amarus against carbofuran induced toxicity in female rats, Pharmacology (Karger) 3, 1006-1016 (2008).

[39] D. N. Kage, V. B. Malashetty, Y. N. Seetharam, P. Suresh and S. B. Patil, Effect of ethanol extract of whole plant of Trichosanthes cucumerinavar. cucumerinaL. on gonadotropins, ovarian follicular kinetics and estrous cycle for screening of antifertility activity in albino rats, International Journal of Morphology (Soc Chilena Anatomia) 27(1),173-182 (2009).

[40] V. C. Obinna and G. O. Agu, Beta cypermethrin exposure and perinatal reproductive development of female f1 generation of albino rats, The Journal of Basic and Applied Zoology (Springer Nature) 80, 44 (2019).

[41] M. J. Adeniyi and F.O. Agoreyo, Estrous cycle ration as a reproductive index in the rats, American Journal of Biomedical Science and Research (Biomedgrid) 100 – 103 (2019).

Karnatak University
Journal of Science

ISSN: 0075-5168

A Mini Review on Vitamins and Available Detection Methods

Megha Vilas Naik
Bhavana Anchan
Saritha Kamath U
Gayathri M. Rao
Ajeetkumar Patil

Megha Vilas Naik, Bhavana Anchan, Saritha Kamath U., Gayathri M. Rao, Ajeetkumar Patil, "A Mini Review on vitamins and Available Detection Methods" Karnatak University Journal of Science 51, 54-69 (2020).

A Mini Review on Vitamins and Available Detection Methods

Megha Vilas Naik[a†], Bhavana Anchan[a†], Saritha Kamath U.[b], Gayathri M. Rao[c], Ajeetkumar Patil[a*]

[a]Department of Atomic and Molecular Physics, Manipal Academy of Higher Education (MAHE), Manipal, -576 104, India
[b]Department of Medical Laboratory Technology, Manipal College of Health Professions, Manipal Academy of Higher Education (MAHE), Manipal-576 104, India
[c]Department of Biochemistry, Kasturba Medical College, Manipal Academy of Higher Education (MAHE), Mangalore-575001, India

†Equal Contributors

* **Corresponding author**: e-mail: ajeetkumar.p@manipal.edu, Phone: (+91) 820-2932206;

Abstract:

Vitamin is organic compounds that are required in our diet in small amounts to perform specific biological functions to maintain health and growth. Vitamins naturally occur in food and are needed in very small amounts for various bodily functions such as energy production and making red blood cells. There are about 15 vitamins based on solubility they are classified as fat-soluble (A, D, E and K) and water-soluble (C and B-groups) needed for cell and blood maturation. Helps to maintain nerve and red blood cells also in DNA replication. This article reviewed various methods used for measuring vitamin, and its principles involved. The detection methods include Immunoassays which utilize the antibody-antigen interaction for the detection and quantification of vitamins.

On the other hand, measurements by radioimmunoassay (RIA), chemiluminescent immunoassay (CLIA), enzyme-linked immunosorbent assay (ELISA) which are highly sensitive immunoassay technique. In addition, there are various techniques for separation and sample preparation. HPLC (High-performance liquid chromatography) is used for non-validate analyst when they are coupled with certain detectors they afford us another principle for measuring vitamin such as mass spectrometry. Choosing the best method for measuring vitamin measurements depends on many factors – including the type of sample, purpose of the test, necessity of pre-processing, time limitations, cost, sensitivity, specificity.

Keywords: Vitamins; HLPC; Mass Spectrometry; immunoassay.
Article history: Received: 25 May 2020; Revised: 9 August 2020; Accepted: 9 August 2020.

1. INTRODUCTION:

Micronutrients are dietary components, often referred to as vitamins and minerals required for the body in small quantities, which plays a vital role in development, growth, and disease prevention. Vitamins are essential micronutrients, complex organic compounds required in milli-grams (mgs) or micro-grams (µgs) for the overall function of the body for ideal health, growth and metabolic processes. Funk in 1913 isolated vitamin from rice polishing and yeast, which could help in curing Beri-Beri in pigeons. Hence termed Vitamine (Greek: vita-life). Co-enzyme or various active forms of the vitamins are essential components of various biochemical functions in human body to maintain optimal health.

Classification of Vitamins:

Vitamins are organic compounds most essential for normal growth and involved in many metabolisms of amino acids and fats. These essential bio compounds come from the dietary components/ other natural sources, which mainly divide into fat-soluble (A, D, E & K) and ii) water-soluble [vitamins -B complex (thiamine, riboflavin, niacin, pantothenic acid, pyridoxine, biotin, folate, and cobalamin) and vitamin C] depending on their solubility comprising of 13 members altogether. Though some vitamins synthesized in the body, either the precursor molecules or pro-vitamin forms to be provided in the diet in adequate amounts to meet the functional needs and to prevent the deficiency. A normal mixed diet/ balanced diet can meet the needs, if required can include the fortified components as supplement. Although adequate intake of all vitamins is important, due to the transient nature of water-soluble vitamins, regular intake is required to avoid deficiency [1-2].

1.1 Fat-Soluble Vitamins:

(i) Vitamin A:

Vitamin A is essential nutrient for good vision, a healthy immune system, production of red blood cells and cell growth. The human body cannot synthesize vitamins, therefore it should be a part of dietary intake. There are two types of vitamin A. This entry is primarily about the active form of vitamin A Vitamin A are available: retinoids – that comes from animal products. Beta-carotene is among the second type of vitamin A, which comes from plants. The important provitamin A carotenoid is beta-carotene; other provitamin A carotenoids are alpha-carotene and beta-cryptoxanthin. These converts plant pigment to vitamin A, also helps in metabolise to active forms and support in biological functions. Most of the body's vitamin A is stored in the liver in the form of retinyl esters [1,3-4].

However, vitamin A deficiency is common in many developing countries, due to limited access to foods containing preformed vitamin A from animal-based food sources and they do not commonly consume available foods containing beta-carotene due to poverty also during infancy, when infants do not receive adequate supplies of breast milk. The most common symptom of vitamin A deficiency in young children and pregnant women is xerophthalmia. Early signs of xerophthalmia is night blindness, or the inability to see in low light or darkness. People with vitamin A deficiency tend to have low iron status, which can lead to anaemia [5-7].

(ii) Vitamin D:

Vitamin D is a fat-soluble secosteroid, requisite for bone health and general cellular functions of the body. There are five different forms of vitamin D, two main forms essential for the human body are vitamin D_2 (ergocalciferol) and vitamin D_3 (cholecalciferol). Both D_2 and D_3 plays an important role in calcium absorption, maintaining strong bones and healthy immune function. In the skin, pre-vitamin D_3 is produced from 7-dehydrocholesterol and ergosterol gets converted into pre-vitamin D_2 under the influence of UV radiation then modified into vitamin D_3 (Cholecalciferol) and vitamin D_2 (Ergocalciferol) respectively [8]. The first hydroxylation at C-25 forms calcidiol which is the major circulating form, used for the assessment of vitamin D status and the second hydroxylation leads to the formation of calcitriol which is the active form[9-10]. Vitamin D is involved in different biological functions

such as bone formation, spermatogenesis, steroidogenesis, implantation and deficiency of this leads to different disorders [11-12].

(iii) Vitamin E:

Vitamin E is a fat-soluble, chain-breaking antioxidant which exists naturally in eight forms, four tocopherols and four tocotrienols having related chromanol structures [13]. RRRa-tocopherol is prolific and exhibits the highest biological activity with regard to fetal resorption assessment[14]. Vitamin E prevents lipid peroxidation which leads to various diseases and clinical conditions such as cardiovascular disease, neurological diseases (Alzheimer's), atherosclerosis and chronic diseases[13][15-16]. Another important biological role is to prevent the oxidation of PUFAs, cell membranes and low-density lipoprotein (LDL) by free radicals. It also inhibits cellular proliferation and increases immune response[17]. Studies have also found the role of vitamin E in improving male and female fertility. It neutralizes free radical activity and protects the sperm from reactive oxygen species [18-19].

(iv) Vitamin K:

Vitamin K is an important nutrient that plays a vital role in blood clotting and bone and heart health. While vitamin K deficiency is rare, less than optimal intake may impair your health over time. Inadequate intake may cause bleeding, weaken your bones and potentially increase your risk of developing heart disease. It is a fat-soluble vitamin essential for the function of various proteins in the body [20] and vitamin K deficiency causes impaired blood coagulation and uncontrolled bleeding. It possesses cofactor activity for y-glutamyl carboxylase. Two naturally existing form of vitamin K are vitamin K_1 (Phylloquinone) and vitamin K_2 (menaquinones) synthesized by green plants and bacteria respectively [21-22]. Vitamin K has surplus potential implications, involving the prevention of arterial calcifications, cardiovascular disease and cancer, improves bone health and insulin sensitivity [23-25]. Additionally, it also plays an important role in warfarin by the stabilization of INR control [26].

1.2 Water-soluble vitamins:

(i) Vitamin B:

Vitamin B is organic compounds most essential for normal health and for the metabolism of amino acids and fats. Vitamin B complex consists of the Thiamine (B_1), Riboflavin (B_2), Niacin (B_3), Pantothenic acid (B_5), Pyridoxine (B_6), Biotin (B_7), Folate (B_9) and the Cobalamins (B_{12}) which are water-soluble vitamins.

Vitamins like thiamine, riboflavin, niacin, pyridoxine and biotin are necessary for energy metabolism at rest and during physical activity; whereas vitamin B_{12} is necessary for red blood cell production, tissue repair, and protein synthesis. Vitamin B_{12} and Folate is essential for fetal growth and development. For the development of the infant brain normally pregnant and breastfeeding women need to keep a track of vitamin B_6 as it is a key player in neuronal signals. Deficiency of these vitamin B complexes may lead to health problems like anemic, neurological injuries, heart diseases and stroke, as well as Alzheimer's disease. Also, inappropriate consumption of supplements of vitamins may also cause unwanted side-effects[27-30].

(ii) Vitamin C:

Vitamin C is a water-soluble essential nutrient for metabolism and also severs as reagent in various industries such as pharmaceutical and food industry. It is needed for the repair of tissues in all parts of the body [1-2]. The important functions of vitamin C include the formation of protein used to make skin, forming scar tissue, ligaments, and blood vessels for healing wounds and tendons, for repairing and maintaining cartilage, bones, and teeth and in ironabsorption [31-33].

Indian dietary components incudes cereals and pulses. Low of nutrition (from vegetables/fruits or dairy products) may be responsible for the identified deficiency status. Some of the components though they are present in adequate amount, inadequate quantity of remaining components or some interfering/limiting factors rich in diet also can hinder their availability due to their inhibiting property at the level of absorption. Other factors to consider along with the dietary availability are the age, environment, health status and the physiological conditions.There are various techniques for detecting vitamins based on different methodologies, sample size, sample types, various assay methods.

2. Detection and sensing:

Among the many analytical methods, spectrophotometric methods are quite simple and low-cost. Several studies use spectrophotometric method for the determination of vitamins. Other optical methods for vitamin estimation include spectrophotometry determination chemiluminescence, HPLC, ELISA and electrochemical, etc.

Table 1: Dietary sources, deficiency and available methods.

Sl. No.	Vitamins	Sources[34]	Deficiency	Sample	Assay/Methods available
1.	Vitamin A	liver, eggs, fortified margarine, butter, cream, cheese, fortified milk, vegetables, fruits, dark green leafy vegetables.	Night blindness Vision disturbances Joint and bone pain Poor appetite Nausea and vomiting Sunlight sensitivity[38-39]	Bovine milk, blood serum.	HPLC*[35] LC-MS** [36-37]
2	Vitamin E	Nuts and seeds, egg yolks, liver, whole grain products, Potato, carrot, broccoli, cereals, olive oil, and orange.	Anemia [38], Neurological problems.	Blood serum or plasma	HPLC* [13][39]
3	Vitamin D	Fatty fish, meat, egg yolk, dairy products.	Rickets, osteomalacia, cardiovascular cancer [40-42]	Blood serum	Immunoassay HPLC* [36-37][42]
4	Vitamin K	Cabbage, broccoli, sprouts, spinach, apple, and banana.	Bleeding diathesis, abnormal blood coagulation diseases[13][15-16]	Blood serum	HPLC* [43-44]
5	Vitamin C	Orange, grapes, potatoes, tomatoes, and peppers.	Scurvy, heart disease and cancer [45][46]	Blood serum	Electro-chemical Spectrophotometric Chemiluminescence HPLC*[47-50] LC-MS**[56]
6	Thiamine (B_1)	Pork, sunflower seeds, and wheat	Irritability in infants Diabetes & Beri-Beri Chronic neurological and Wernicke-Korsakoff syndrome[1-2]	Blood serum or plasma	Spectrofluorimetry[51] HPLC*[52,53,57] Spectrophotometry[57-58] LC-MS**[56]
7	Riboflavin (B_2)	Organ meats, beef, and mushrooms	Burning sensation of the skin Digestive disorders Cheilosis [1-2]	Blood serum	Spectrofluorimetry[52] HPLC*[52,53,57] Spectrophotometry[54] LC-MS**[56]

8	Niacin (B_3)	Chicken, tuna and lentils	Pellagra: affects the skin, nervous system, digestive system[1-2]	Blood serum	HPLC*[53-54][56-57] LC-MS**
9	Pantothenic acid (B_5)	Liver, fish, yogurt, and avocado	Insomnia Depression, irritability Upper respiratory infections [1-2]	Blood serum	HPLC*[52-53][56] LC-MS**[56]
10	Pyridoxine (B_6)	Chickpeas, salmon, and potatoes	Alzheimer's Convulsions Peripheral neuropathy[1-2]	Blood serum or plasma	Spectrofluorimetry[51] Spectrophotometry[55] LC-MS**[56] HPLC*[57]
11	Biotin (B_7)	Salmon, Yeast, cheese, eggs, and liver	Red rash in the face and in the genital area. Hallucination [1-2]	Blood serum	HPLC*[52-53][57] LC-MS**[56]
12	Folate (B_9)	Liver Leafy greens, and beans or in supplements as folic acid	Neurological problems Anemia Rheumatoid arthritis A higher risk of lower bone density[2][30]	Blood serum	LC-MS**[56] HPLC*[57]
13	Cobalamins (B_{12})	Animal sources like meats, eggs, seafood, and dairy	Parkinson's Alzheimer's Pernicious anemia Megaloblastic anemia[2][30]	Blood serum or plasma	LC-MS**[56] HPLC*[57]

* High-performance liquid chromatography (HPLC) **Liquid chromatography-mass spectrometry (LC-MS)

2.1 Immunoassay:

Immunoassays are bioanalytical techniques which utilize the antibody and antigen interaction for the detection and quantification of vitamins. Based on the different labels used for the detection of antibody and antigen there are different types as follows,

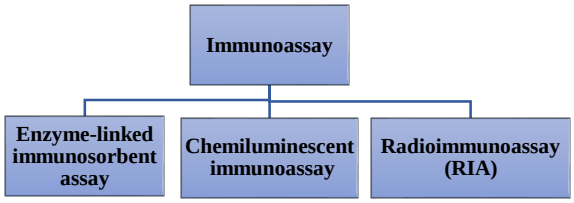

Figure 1. Classification of immunoassay.

(i) Enzyme-linked immunosorbent assay (ELISA):

ELISA is a commonly used laboratory technique for the assessment of different vitamins which uses the reaction of antigen and antibody. It contains 96 well plates and different samples are placed in each well along with negative control and the positive control. The solid surface is coated by the antigen or antibody where the corresponding antibody or antigens present in the sample gets attached and the excess or unbound antigens (antibodies) are washed of using a suitable buffer. Secondary antibodies attached to enzymes are then added to the wells to find the antibody or antigen. After incubation for a particular period, the unbound antibodies are removed by washing and the substrate is added which reacts with the enzyme present to give color. The intensity of the color is measured which indicates the amount of antigen/antibody present [58-59]. There are 3 different types of ELISA,

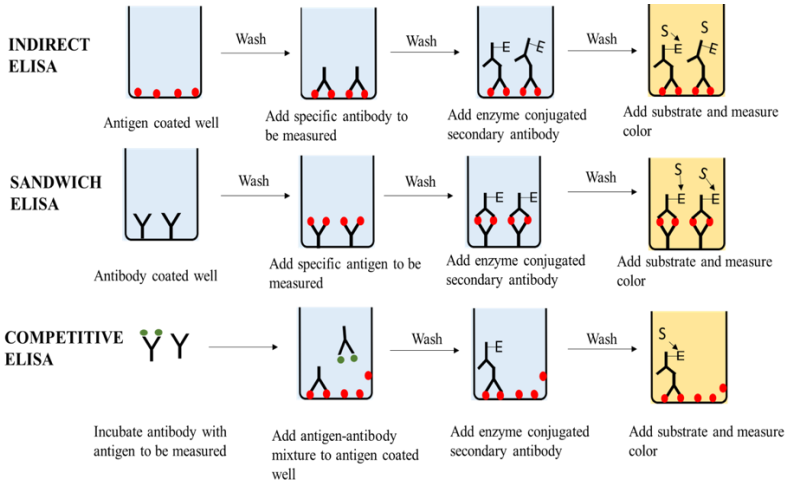

Figure 2. Different types of ELISA technique.

ELISA is the most commonly used diagnostic tool for vitamins. There are various studies where the ELISA method is used for the assessment of vitamins. Analysis of vitamin B_{12} has been carried out in food samples using a competitive ELISA technique, the limit of detection was found to be 10ng/ml and no cross-reactivity ($< 0.01\%$). The method is compared with the HPLC-UV method and the study concluded that the developed ELISA is more sensitive than the HPLC [60]. Another study analysed vitamin D in blood serum through HPLC-UV using the C18 column and the detector was set at 265nm and compared with the ELISA. The study included 46 patients whose blood samples were collected for the assessment of vitamin D_2, vitamin D_3, and their 25-hydroxyl metabolites and the same samples were analysed using ELISA. The limit of detection and limit of quantification for HPLC was found to be 2ng/mL and 5ng/mL respectively and the variation among the subjects was determined by HPLC not by ELISA so it was stated that HPLC is the better tool for determining vitamin D status [61]. The study carried out on the determination of effects of vitamin C supplementation on plasma immunoglobulin carbonyl content was done with ELISA as it is a simple and robust method and facilitates small sample volume and large sample throughput. The primary antibody, mouse IgE anti-DNP and secondary antibody anti-mouse IgE horseradish peroxidase conjugate were used and the absorbance was measured at 490nm. The study demonstrated that certain forms of oxidative protein damage can be reduced by dietary vitamin C supplementation [62].

(ii) Chemiluminescent immunoassay (CLIA):

CLIA is a sensitive technique to find the concentration of samples based on the luminescence intensity emitted by a chemical reaction [63]. Chemiluminescent methods can be direct or indirect using luminophore or enzyme markers. In a direct reaction, two reagents (usually a substrate and an oxidant) react along with the co-factors or in presence of catalyst forming a product or intermediate. The electronically excited product or intermediate, relax to the ground state emitting a photon. The substrate is the chemiluminescent, accountable for light emission or it acts as an energy transfer donor in indirect chemiluminescent. The most widely used chemiluminescent substrate are luminol, isoluminol, and their derivatives, acridinium ester derivatives, peroxidase, and alkaline phosphatase. The indirect chemiluminescent is a process where the excited species transfer its energy to a fluorophore which in turn gets excited, emits a photon while relaxing to the ground state [64-65]. CLIA has an extensive range of applications in clinical diagnosis, food safety, and environmental tracking.

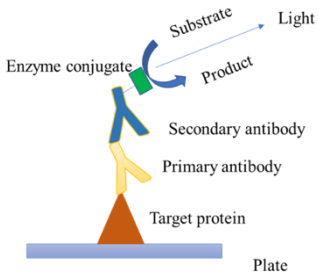

Figure 3. Chemiluminescence immunoassay.

The various study has been investigated the cost-effective and reliable method for the analysis of vitamins as it plays a vital role in the human body. Vitamin D estimation is done using HPLC, CLIA, and ELISA and the techniques are compared. 216 subjects were included in the study and 25-hydroxyvitamin D (25(OH)D) plasma concentration was measured by HPLC using C18 reverse-phase column with gradient elution (acetonitrile/water) and the UV detector was set at 275nm. The concentration of 25(OH)D in serum was also determined with automated chemiluminescent immunoassay technology and ELISA. The results obtained using CLIA were close to HPLC than ELISA. So, CLIA can replace HPLC which is lengthy [66]. The determination of folic acid status in blood serum has been done by using CLIA which displayed a good thermostability and performance and the limitation of detection observed is 0.44 ng/mL. It was concluded that the proposed method is sensitive, rapid, and serves as a better diagnostic tool [67].

(iii) Radioimmunoassay (RIA):

RIA is an in vitro assay which determines the existence of an antigen with great sensitivity. It measures a specific antibody that exists in a biological substance, even in small quantities [68]. The radioactively labelled antigen (125-I labels are usually used and other isotopes such as C14 and H3 are also used) is bound to a particular antibody and a sample is then added to initiate a competitive reaction between the labelled antigens and the unlabelled antigens present in the sample [69]. This emancipates a particular amount of unlabelled antigen and a binding curve is generated which gives the quantity of antigen present in the sample.

Recently, in clinical laboratories, usually immunoassays and HPLC are used for the analysis of fat-soluble vitamins such as A, E, and D. Vitamin D Status in plasma samples were determined by RIA with a ^{125}I labelled tracer. The limit of detection was found to be 2.8µg/L for 25(OH)D, compared well with a liquid-chromatographic method involving specific UV detection [70]. Another study investigated the effect of vitamin E, C combined with β carotene supplementation on cognitive functions in the elderly using RIA as an assessment tool. A total of 276 patients were included, the blood samples were collected and plasma levels of amyloid-β and estradiol were determined by RIA, suggested that vitamin E and C supplementation could decrease plasma Aβ levels and increase E2 levels and observed an improvement in cognitive function [71].

2.2 Liquid Chromatography:

Liquid chromatography or LC is a separation method used to separate the individual components of a mixture. It involves the separation based on the chemical nature of the analyte of interest i.e. polar or non-polar.

It consist of packed column with the porous medium made of a stationary phase, such as polymers and silica, where the sample is injected and the mobile phase (solvent) passes to transport the sample.

When a sample is injected, sample gets adsorbed on the stationary phase, and the solvent passed through the column helps to separate the compounds one by one, based on their nature i.e. hydrophobicity or hydrophilicity. More the affinity to the stationary phase is the last one to separate. This is because high affinity which corresponds to more time to travel to the end of the column.

The Differences between LC and HPLC:

High-performance liquid chromatography (HPLC)is an advanced type of LC. The main difference between LC and HPLC is that the solvent travels by gravitational force in LC. In HPLC, the solvent travels under high pressure obtained by pump to overcome the pressure drop in the packed column, which reduces the time of separation.

2.2 High-performance liquid chromatography (HPLC):

HPLC is a distinct form of column chromatography commonly used in separation, identification, and quantification of biological compounds [72]. It employs a column that contains a stationary phase, a pump that forces the mobile phase through the column which includes a miscible solvent combination such as water or organic solvents, and a detector provides an output to the recorder after detecting the individual molecules coming out [73]. A small amount of sample is introduced to the mobile phase and is retarded based on the interaction with the stationary phase and it depends on the stationary, mobile phase and nature of the analyte. The analyte mixtures are separated on the basis of their affinity towards the mobile phase.

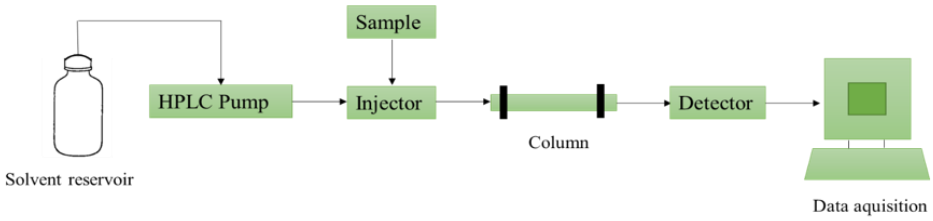

Figure 4. High-performance liquid chromatography

Instrumentation:

a. Solvent reservoir: It contains a mobile phase (polar and non-polar solvents). Based on the composition of the analyte, polar and non-polar solvents will be varied [74].
b. Pump: Pump forces the mobile phase to the column. Its performance is assessed based on the ability to maintain a consistent and reproducible flow rate [72].
c. Columns: Column is generally made of stainless steel with a length of around 50mm-300mm and a diameter of 2-5mm which contains a stationary phase with a molecule size of 3-10µm [73].
d. Detector: The HPLC detector is located at the end of the column differentiates the analytes when they elute. The most commonly used detectors are UV-spectroscopy, fluorescence, mass spectrometric etc. [74-75].

e. Data collection devices: Chromatographic peaks obtained represents a component in the mixture passing through the detector. The software determines the area under the peak which is proportional to the quantity of the substance present.

Several studies have been done on quantification of vitamins using HPLC with a fluorescence detector (HPLC-FL). Simultaneous analysis of vitamin B_1, B_2 and B_6 is done in royal jelly which is used as a food supplement and rich in vitamin B using HPLC. For thiamine analysis, photodiode array UV-Vis detector was arranged to monitor at 245 nm and a fluorescence detector for B_6 to monitor at 295 nm (excitation) and 395 nm (emission) for the first eight minutes and for the last seven minutes B_2 analysis at 450 nm (excitation) and at 525 nm (emission). The detection limits were obtained as 66.90 ng mL^{-1} for vitamin B_1, 6.47 ng mL^{-1} for vitamin B_2 and 7.80 ng mL^{-1} for vitamin B_6. The study concluded that the royal jelly is not a good source of vitamin B after comparing it with the dietary reference intake value [76]. The determination of different antioxidant vitamins was carried out with tomatoes using HPLC-FL. The system delivered an outstanding separation of α, β, γ tocopherols, and tocotrienols. The fluorescence detector also allowed the detection of ubiquinone, which is an antioxidant. Analysis of tocopherol analogy using normal-phase HPLC (mobile phase-hexane-ethanol) with fluorescence detection (excitation 295 nm, emission 320 nm) allowed simultaneous detection which cannot be achieved using UV-Vis detector as it is less sensitive [77].

Among the Other types of detectors used e.g., mass spectrometry, with applications that require higher sensitivity than that provided by UV detectors.

2.3 Mass Spectrometry(MS):

Mass spectrometry (MS)separates out with their molecular masses and charges (mass to charge ratio) as it ionizes atoms or molecules. There are various applications, as an example biochemicals. The processes where sample is converted into a gaseous phase which is ionized to generate cations and ions separate according to their mass/charge ratio by a mass analyser. A detector is used to determines and quantify based on their molecular masses and charges.

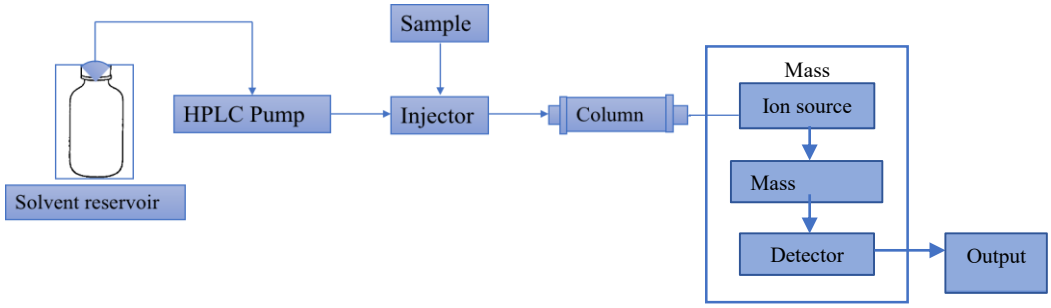

Figure 5. Liquid chromatography-mass spectrometry (LC-

Limitations of MS

MS are accurate and sensitive technique for both in case of separation as well in detection. In case a complex mixture, mass spectrometer cannot perform the separation process alone because few compounds can have molar mass similar. Therefore, combining MS with another separation process, such as HPLC is ideal in case of an highly complex mixture.

2.4 Liquid Chromatography-Mass Spectrometry(LC-MS):

LC-MS is the combination of LC with MS which helps to reduce experimental error and improves accuracy. This technique is very useful in various applications which involves a huge number of compounds, such as environmental effluents. Separation takes place in accordance with their physical and chemical properties, then identifying the components within each peak and detecting based on their mass spectrum. Flow rate is ensured to be less while compared to HPLC,which ensures ionization and maintain the detection sensitivity of the MS. Therefore, the column is smaller which can accommodate solvent with smaller flow rates and sample volumes .

Smaller column makes syringe pumps convenient for LC-MS, they are accurate and deliver low flow rates. In addition, it is possible to use syringe pumps for sample injection into the system as they can deliver very precise sample dosing[79-82].The detection level of vitamin B & D is less than a ng/mL[79][81].Results with excellent accuracy and reproducibility were achieved.

Advantage of current methodology over other methods:

As discussed above, there are several techniques for detecting micronutrients (vitamins).The ELISA method remains the routine method despite the fact that it is time consuming, and has relatively poor precision, and low specificity for the determination of vitamin along with CLIA in some cases. CLIA has a high concordance with ELISA. ELISA and CLIA are based on different test principles. Although CLIA is gradually replacing the ELISA. Moreover, CLIA and radioimmunoassay which are simpler and faster are very expensive and have a higher specificity and sensitivity for detection .On the other hand, HPLC methods include the use of UV-Visible photometry while mass spectrometry becomes laborious. The table 1, shows comparison of various micronutrients detection techniques, detection range and sensitivity for detecting vitamin D as an example in blood-serum.

Table 1. Comparison of various micronutrients detection techniques for detecting vitamin D as an example

Detection Method	Analyte	Detection range ng/ml	Sensitivity ng/ml	Reference
HPLC	Blood serum	1.6–106.3	1.6	[83]
LC-MS/MS	Blood serum	2-100	0.69	[84]
RIA	Blood serum	10.4-62.7	<3	[85]
ELISA	Blood serum	2.4- 144.23	≤ 2	[86]
CLIA	Blood serum	3-150.2	≤4	[87]

3. DISCUSSION AND CONCLUDING REMARKS:

Vitamins play a crucial role, determining the status using most appropriate method is essential. Determination of vitamin requires consideration of the desired sensitivity and specificity, the available time, cost-effective and the process of sample preparation. More importantly, several advantages and disadvantages of each of these methods govern the choosing of the suitable methods. Considering the comparative studies between various techniques for detecting vitamins based on different methodologies, sample size, sample types, various assay methods etc. The ELISA method is an routine method which determines vitamins, despite the fact : time consuming, and haspoor precision, and low specificity. Reasons behind might be because

CLIA and radioimmunoassay are very expensive despite they are simpler and faster. HPLC methods uses UV-Visible photometry, MS etc which are bulky as well.

Determination of vitamin requires consideration of the required/desired sensitivity and specificity, the available time, cost-effective and the process of sample preparation.

The reasons behind measuring vitamin should also play a crucial role in determining the most appropriate method. More importantly, several advantages and disadvantages of each of these methods govern the choosing of the suitable methods.

References

[1] Coates, Paul M., et al., eds. Encyclopedia of dietary supplements. CRC Press, (2010).
[2] Bellows, L., et al. "Water-soluble vitamins: B-complex and vitamin C." Food and nutrition series. Health; no. 9.312 (2012).
[3] Padayatty, S., et al. "Encyclopedia of dietary supplements.": 821-831 (2010).
[4] Dyer, Andrew R., et al. "Vitamin A (December 2016)."
[5] Mayo-Wilson, Evan, et al. "Vitamin A supplements for preventing mortality, illness, and blindness in children aged under 5: systematic review and meta-analysis." Bmj 343 (2011).
[6] Sommer, Alfred. "Vitamin A deficiency and clinical disease: an historical overview." The Journal of nutrition 138.10 (2008): 1835-1839.
[7] Mactier, H., and L. T. Weaver. "Vitamin A and preterm infants: what we know, what we don't know, and what we need to know." Archives of Disease in Childhood-Fetal and Neonatal Edition 90.2 (2005): F103-F108.
[8] Christakos, D. V Ajibade, P. Dhawan, A. J. Fechner, and L. J. Mady, "Vitamin D: Metabolism SYNTHESIS OF 1,25(OH) 2 D 3 FROM VITAMIN D 3 KEYWORDS Vitamin D metabolites Vitamin D hydroxylases Vitamin D binding protein FGF23 Kidney Placenta," Endocrinol. Metab. Clin. NA, (2010).
[9] Lin, Rui. "Crosstalk between Vitamin D metabolism, VDR signalling, and innate immunity." BioMed research international 2016 (2016).
[10] Bikle, Daniel D. "Vitamin D metabolism, mechanism of action, and clinical applications." Chemistry & biology 21.3 (2014): 319-329.
[11] Lavie, Carl J., John H. Lee, and Richard V. Milani. "Vitamin D and cardiovascular disease: will it live up to its hype?." Journal of the American College of Cardiology 58.15 (2011): 1547-1556.
[12] Krishnan, Aruna V., et al. "The role of vitamin D in cancer prevention and treatment." Rheumatic Disease Clinics 38.1 (2012): 161-178.
[13] S. W. Leonard and M. G. Traber, Methods for assessment of Vitamin E. Elsevier Inc., (2019).
[14] Herrera, E., and C. Barbas. "Vitamin E: action, metabolism and perspectives." Journal of physiology and biochemistry 57.1 (2001): 43-56.
[15] Brown, Katrina M., Philip C. Morrice, and Garry G. Duthie. "Vitamin E supplementation suppresses indexes of lipid peroxidation and platelet counts in blood of smokers and nonsmokers but plasma lipoprotein concentrations remain unchanged." The American journal of clinical nutrition 60.3 (1994): 383-387.
[16] Brigelius-Flohe, Regina, and Maret G. Traber. "Vitamin E: function and metabolism." The FASEB Journal 13.10 (1999): 1145-1155.

[17] Yano, Tomohiro, et al. "Vitamin E inhibits cell proliferation and the activation of extracellular signal-regulated kinase during the promotion phase of lung tumorigenesis irrespective of antioxidative effect." Carcinogenesis 21.11 (2000): 2129-2133.
[18] Ahmadi, Sedigheh, et al. "Antioxidant supplements and semen parameters: An evidence based review." International Journal of Reproductive BioMedicine 14.12 (2016): 729.
[19] Tremellen, Kelton. "Oxidative stress and male infertility—a clinical perspective." Human reproduction update 14.3 (2008): 243-258.
[20] DiNicolantonio, James J., JaikritBhutani, and James H. O'Keefe. "The health benefits of vitamin K." Open heart 2.1 (2015): e000300.
[21] Booth, Sarah L., and J. W. Suttie. "Dietary intake and adequacy of vitamin K." The Journal of nutrition 128.5 (1998): 785-788.
[22] Beulens, Joline WJ, et al. "The role of menaquinones (vitamin K 2) in human health." British journal of nutrition 110.8 (2013): 1357-1368.
[23] Geleijnse, Johanna M., et al. "Dietary intake of menaquinone is associated with a reduced risk of coronary heart disease: the Rotterdam Study." The Journal of nutrition 134.11 (2004): 3100-3105.
[24] Habu, Daiki, et al. "Role of vitamin K2 in the development of hepatocellular carcinoma in women with viral cirrhosis of the liver." Jama 292.3 (2004): 358-36
[25] Yoshida, Makiko, et al. "Effect of vitamin K supplementation on insulin resistance in older men and women." Diabetes care 31.11 (2008): 2092-2096.
[26] Schurgers, Leon J., et al. "Regression of warfarin-induced medial elastocalcinosis by high intake of vitamin K in rats." Blood 109.7 (2007): 2823-2831.
[27] Leklem, James E. "Vitamin B6." Handbook of Vitamins, 3rd ed, revised and expanded (2001): 339-396.
[28] Black, Maureen M. "Effects of vitamin B12 and folate deficiency on brain development in children." Food and nutrition bulletin 29.2_suppl1 (2008): S126-S131.
[29] Reynolds, Edward. "Vitamin B12, folic acid, and the nervous system." The lancet neurology 5.11 (2006): 949-960.
[30] Black, Maureen M. "Effects of vitamin B12 and folate deficiency on brain development in children." Food and nutrition bulletin 29.2_suppl1 (2008): S126-S131.
[31] Food, Nutrition Board, and Nutrition Board. "Institute of Medicine. Dietary Reference Intakes for Vitamin C, Vitamin E, Selenium, and Carotenoids." (2000).
[32] Devaki, Sudha J., and ReshmaLaliRaveendran. "Vitamin C: sources, functions, sensing and analysis." Vitamin C. IntechOpen, 2017.
[33] Bates, C. J. "Diagnosis and detection of vitamin deficiencies." British medical bulletin 55.3 (1999): 643-657.
[34] Zhang, Yuan, et al. "A review of the extraction and determination methods of thirteen essential vitamins to the human body: An update from 2010." Molecules 23.6 (2018): 1484.
[35] Dulińska-Litewka, Joanna, et al. "Rapid HPLC method for the determination of vitamin A and E and cotinine concentration in human serum in women with CIN and cervical cancer." Ginekologiapolska 80.4 (2009).
[36] Le, Juan, et al. "New LC-MS/MS method with single-step pretreatmentanalyzes fat-soluble vitamins in plasma and amniotic fluid." Journal of lipid research 59.9 (2018): 1783-1790.
[37] Priego Capote, Feliciano, et al. "Identification and determination of fat-soluble vitamins and metabolites in human serum by liquid chromatography/triple quadrupole mass spectrometry with multiple reaction monitoring." Rapid Communications in Mass Spectrometry: An International Journal Devoted to the Rapid Dissemination of Up-to-the-Minute Research in Mass Spectrometry 21.11 (2007): 1745-1754.

[38] Oski, Frank A., and Lewis A. Barness. "Vitamin E deficiency: a previously unrecognized cause of hemolyticanemia in the premature infant." The Journal of pediatrics 70.2 (1967): 211-220.
[39] Zaman, Zahur, Peter Fielden, and Peter G. Frost. "Simultaneous determination of vitamins A and E and carotenoids in plasma by reversed-phase HPLC in elderly and younger subjects." Clinical chemistry 39.11 (1993): 2229-2234.
[40] Yang, Chen-Yen, et al. "The implication of vitamin D and autoimmunity: a comprehensive review." Clinical reviews in allergy & immunology 45.2 (2013): 217-226
[41] Holick, Michael F. "High prevalence of vitamin D inadequacy and implications for health." Mayo Clinic Proceedings. Vol. 81. No. 3. Elsevier, 2006.
[42] Zerwekh, Joseph E. "Blood biomarkers of vitamin D status." The American journal of clinical nutrition 87.4 (2008): 1087S-1091S.
[43] Booth, Sarah L., Kenneth W. Davidson, and James A. Sadowski. "Evaluation of an HPLC method for the determination of phylloquinone (vitamin K1) in various food matrixes." Journal of Agricultural and Food Chemistry 42.2 (1994): 295-300.
[44] Bates, C. J. "Diagnosis and detection of vitamin deficiencies." British medical bulletin 55.3 (1999): 643-657.
[45] NyyssÖnen, Kristiina, et al. "Vitamin C deficiency and risk of myocardial infarction: prospective population study of men from eastern Finland." Bmj 314.7081 (1997): 634.
[46] Mayland, Catriona R., Michael I. Bennett, and Keith Allan. "Vitamin C deficiency in cancer patients." Palliative medicine 19.1 (2005): 17-20.
[47] Bushway, R. J., et al. "High-performance liquid chromatographic determination of ascorbic acid in fruits, vegetables and juices." Journal of liquid chromatography 11.16 (1988): 3415-3423.
[48] Chiari, Marcella, et al. "Determination of total vitamin C in fruits by capillary zone electrophoresis." Journal of Chromatography A 645.1 (1993): 197-200.
[49] NyyssÖnen, Kristiina, et al. "Vitamin C deficiency and risk of myocardial infarction: prospective population study of men from eastern Finland." Bmj 314.7081 (1997): 634.
[50] Mayland, Catriona R., Michael I. Bennett, and Keith Allan. "Vitamin C deficiency in cancer patients." Palliative medicine 19.1 (2005): 17-20.
[51] Feng, Feng, et al. "Flow injection renewable drops spectrofluorimetry for sequential determinations of Vitamins B1, B2 and B6." Analyticachimicaacta 527.2 (2004): 187-193.
[52] El-Gindy, Alaa, et al. "HPLC and chemometric methods for the simultaneous determination of cyproheptadine hydrochloride, multivitamins, and sorbic acid." Journal of pharmaceutical and biomedical analysis 35.4 (2004): 703-713.
[53] Jegle, Ulrike. "Separation of water-soluble vitamins via highperformance capillary electrophoresis." Journal of Chromatography A 652.2 (1993): 495-501.
[54] López-de-Alba, Pedro L., et al. "Simultaneous determination and classification of riboflavin, thiamine, nicotinamide and pyridoxine in pharmaceutical formulations, by UV-visible spectrophotometry and multivariate analysis." Journal of the Brazilian Chemical Society 17.4 (2006): 715-722.
[55] Özdemir, Durmus, and ErdalDinc. "Determination of thiamine HCl and pyridoxine HCl in pharmaceutical preparations using uv–visible spectrophotometry and genetic algorithm based multivariate calibration methods." Chemical and pharmaceutical bulletin 52.7 (2004): 810-817.
[56] Chen, Zhi, Bo Chen, and Shouzhuo Yao. "High-performance liquid chromatography/electrospray ionization-mass spectrometry for simultaneous determination of taurine and 10 water-soluble vitamins in multivitamin tablets." AnalyticaChimicaActa 569.1-2 (2006): 169-175.

[57] Antakli, Sarkees, and Sarraf. "Determination of water soluble vitamins B1, B2, B3, B6, B9, B12 and C on a C18 column with particle size 3 mM in some manufactured food products by HPLC with UVDAD/FLD detection." Int J Pharm PharmSci 7.6 (2015): 219-224.
[58] Engvall, Eva. "[28] Enzyme immunoassay ELISA and EMIT." Methods in enzymology. Vol. 70. Academic Press, 1980. 419-439.
[59] Voller, A., A. Bartlett, and D. E. Bidwell. "Enzyme immunoassays with special reference to ELISA techniques." Journal of clinical pathology 31.6 (1978): 507-520.
[60] Kumar, L. SagayaSelva, and M. S. Thakur. "Competitive immunoassay for analysis of vitamin B12." Analytical biochemistry 418.2 (2011): 238-246.
[61] Abu el Maaty, Mohamed Abdulla, et al. "Design-of-experiment approach for HPLC analysis of 25-hydroxyvitamin D: a comparative assay with ELISA." Journal of chromatographic science 53.1 (2015): 66-72.
[62] Carty, Julie L., et al. "The effects of vitamin C supplementation on protein oxidation in healthy volunteers." Biochemical and biophysical research communications 273.2 (2000): 729-735.
[63] Chen, W. A. N. G., et al. "Chemiluminescent immunoassay and its applications." Chinese Journal of Analytical Chemistry 40.1 (2012): 3-10.
[64] ul Azim, Mohammad Anwar, et al. "Chemiluminescence immunoassay: basic mechanism and applications." Bangladesh Journal of Nuclear Medicine 18.2 (2015): 171-178.
[65] Cinquanta, Luigi, Desré Ethel Fontana, and Nicola Bizzaro. "Chemiluminescent immunoassay technology: what does it change in autoantibody detection?." Autoimmunity Highlights 8.1 (2017): 9.
[66] Pal, Mrinal, et al. "Comparison between different methods of estimation of vitamin D." Advances in Biological Chemistry 2013 (2013).
[67] Chen, Xiang, et al. "Development of a Sensitive Chemiluminescence Immunoassay for the Quantification of Folic Acid in Human Serum." Journal of analytical methods in chemistry 2019 (2019).
[68] Grange, R. D., J. P. Thompson, and D. G. Lambert. "Radioimmunoassay, enzyme and non-enzyme-based immunoassays." British journal of anaesthesia 112.2 (2014): 213-216.
[69] Perveen Zaidi, Muhammad Hanif, et al. "Efficacy of different medicines used for the treatment of osteoporosis by using dual energy x-ray absorptiometry." African Journal of Pharmacy and Pharmacology 6.28 (2012): 2133-2140.
[70] Hollis, B. W., et al. "Determination of vitamin D status by radioimmunoassay with an 125I-labeled tracer." Clinical chemistry 39.3 (1993): 529-533.
[71] Li, Yonghua, et al. "Effects of vitamins E and C combined with β-carotene on cognitive function in the elderly." Experimental and therapeutic medicine 9.4 (2015): 1489-1493.
[72] Malviya, Rishabha, et al. "High performance liquid chromatography: a short review." Journal of global pharma technology 2.5 (2010): 22-26.
[73] Martin, Michel, and Georges Guiochon. "Effects of high pressure in liquid chromatography." Journal of Chromatography A 1090.1-2 (2005): 16-38.
[74] Y. Kumar, S. M. Mumtaz, and M. Ahmad, “HPLC: Principle and Maintenance with Application,” Int. J. Trend Sci. Res. Dev., (2018).
[75] Chen, Pei, and Wayne R. Wolf. "LC/UV/MS-MRM for the simultaneous determination of water-soluble vitamins in multi-vitamin dietary supplements." Analytical and bioanalytical chemistry 387.7 (2007): 2441-2448.
[76] Seger, Christoph, Sonja Sturm, and Hermann Stuppner. "Mass spectrometry and NMR spectroscopy: modern high-end detectors for high resolution separation techniques–state of the art in natural product HPLC-MS, HPLC-NMR, and CE-MS hyphenations." Natural product reports 30.7 (2013): 970-987.

[77] Presoto, Ana Elisa F., Magda DG Rios, and Ligia B. de Almeida-Muradian. "Simultaneous high performance liquid chromatographic analysis of vitamins B1, B2 and B6 in royal jelly." Journal of the Brazilian Chemical Society 15.1 (2004): 136-139.

[78] Abushita, Abdulnabi A., et al. "Determination of antioxidant vitamins in tomatoes." Food Chemistry 60.2 (1997): 207-212.

[79] Jenkinson, Carl, et al. "High throughput LC–MS/MS method for the simultaneous analysis of multiple vitamin D analytes in serum." Journal of Chromatography B 1014 (2016): 56-63.

[80] Lock, Stephen, Matthew Noestheden, and André Schreiber. "Analysis of the Vitamin B Complex in Infant Formula Samples by LC-MS/MS." Application Note AB SCIEX (2014).

[81] Lee, Jung-Hoon, et al. "Analytical determination of vitamin B12 content in infant and toddler milk formulas by liquid chromatography tandem mass spectrometry (LC-MS/MS)." Korean journal for food science of animal resources 35.6 (2015): 765.

[82] Footitt, Emma J., et al. "Measurement of plasma B 6 vitamer profiles in children with inborn errors of vitamin B 6 metabolism using an LC-MS/MS method." Journal of inherited metabolic disease 36.1 (2013): 139-145.

Karnatak University
Journal of Science

ISSN: 0075-5168

A Mini Review on COVID-19 Assays

Manjunatha D. H.

Manjunatha D. H. “A Mini Review on COVID-19 Assays” Karnatak University Journal of Science 51, 70-78 (2020).

A Mini Review on COVID-19 Assays

Manjunatha D. H.*
Department of Studies in Chemistry, Davangere University, Davangere, India – 577 002
***Corresponding author:** manjunathdh@gmail.com ; manjunathdh@davangereuniversity.ac.in

Abstract

The continued content of infectious COVID-19 is crucial for the common accessibility of SARS-CoV-2 and the accurate and effective diagnosis of antiviral antibodies in diseased people. This mini review discusses different assessment strategies and tests for identification of COVID-19. Almost all tests for premature identification of the COVID-19works on the basis of reverse transcription-polymerase chain reaction. Isothermal nucleic acid enhancement assays such as transcription-mediated enhancement methods are also in the race. The classification of people who have generated antibodies to the COVID-19 virus needs serological tests comprising the enzyme-associated immunosorbent assay and lateral flow immunoassay. Furthermore, this review gives an outline of present advances in COVID-19 identification methods to simplify future development and invention.
Keywords: Pandemic; COVID-19; Diagnostic Techniques; Molecular assay; Immunological assay.
Article history: Received: 05 August 2020**;** Revised: 29 August 2020; Accepted: 4 September 2020.

1. Introduction

The causative agent of COVID-19 (coronavirus disease-2019) is SARS-CoV-2 is a member of the SARS family. This virus is the fresh addition to the list of seven known coronaviruses. Coronaviruses are encircled RNA viruses that cause upper respiratory tract diseases in individuals. Having precise, suitable, and fast analysis can help in eradicating the quiet spread of COVID-19 by viral haulers. Two general methods are used in the diagnosis of COVID-19: (i) the sequence-specific molecular nucleic acid test and (ii) the antigen-specific immunoassay. These methods are the current gold standards for diagnosing acute infection and for monitoring immune response. There are now over 70 COVID-19 diagnostic tests that have been authorized for emergency use by the U.S. FDA [1].The vast majority are molecular assays, while approximately one-fifth are antibody immunoassays. This mini review will describe the general workflow for these methods involved in the process.

One of the many challenges involved in the spread of COVID-19 is the capability to recognize cases without symptoms that lead to the spread of the virus. Therefore, the current number of SARS-CoV-2-infected individuals may be higher than the present, based on positive test results [2].

Since COVID-19 shows a wide variety of clinical manifestations, ranging from mild fever-like symptoms to life-threatening diseases, it is noteworthy to diagnose COVID-19 patients with other diseases in the early stages of infection. It will be helpful for the doctors to give a timely treatment for the COVID-19 patients who are on the high risky side. Until a commercial vaccine comes into market, it is significant to classify the people infested with

COVID-19, symptomatic or asymptomatic, and who already generated antiviral immunity. This authorizes for added analyses of the power and permanence of immunity in people.

Existing COVID-19 tests in the market are fall into two main groups. The first group comprises molecular assays for the identification of viral RNA of COVID-19 by polymerase chain reaction. The other group comprises serological and immunological assays that mainly depend on sensing antibodies generated by infected patients as a result of contact to the virus or on identification of antigenic proteins in them. Testing for viral RNA of SARS-CoV-2 diagnoses COVID-19 patients during pandemic period. Serological testing classifies people who generated antibodies to the COVID-19 and may be natural plasma donors. It improves contact detection capability and monitors the immunity condition of the people over the time [3].

The widespread accessibility of precision and rapid testing methods is extraordinary in dissecting the complex dynamics involved in SARS-CoV-2 infection and its immunity. To end this, various research laboratories, universities, and companies around the globe have been marching to develop and produce critically desired testing kits. Timely diagnosis, effective treatment, and future prevention are keys to manage COVID-19.

2. Molecular Assays

The SARS-CoV-2 molecular assay functions on the basis of identification of specific genetic sequences within the viral genome, by the help of gene-specific primers. Molecular diagnostic tests that have been released normally employ real-time reverse-transcription PCR [Polymerase Chain Reaction]*i.e.,* real-time RT-PCR[Reverse Transcription Polymerase Chain Reaction] or qRT-PCR [Real Time-Quantitative Reverse Transcription Polymerase Chain Reaction].

Sample collection and RNA extraction

Since coronaviruses contain RNA genomes, RNA serves as the starting material for the assay. Samples are collected from upper respiratory fluids that may contain viral units. This may comprise swab samples or aspirates from the nasal cavity, nasopharynx, and throat, as well as saliva. To confirm rapid and reproducible collection of high-quality RNA, some diagnostic tests have validated the use of RNA purification kits. These kits are ready to use and contain all necessary components, such as cell lysis reagents, RNase inhibitors, collection tubes, and binding beads.

2.1. Real-time RT-PCR

Real-time RT-PCR is a multi-step method for quantifying sequences within RNA samples. Using reverse transcriptase, extracted RNA is transformed to cDNA (complementary DNA), serving as the template for the following PCR-based amplification. A DNA polymerase guided by sequence-specific primers will amplify the genetic regions of interest while fluorescent probes rapidly bind to the newly synthesized fragments. Each amplification cycle results in a measurable intensity of fluorescence that, when compared to a standard curve, can be used to quantify the target sequence. For precise identification of SARS-CoV-2 RNA, highly specific genes to the strain would be most ideal. Among the approved diagnostic tests, common targets include genetic regions within the SARS-CoV-2 nucleocapsid (N), envelope (E), spike (S), and ORF1ab.

The instrument essential for this application is the real-time PCR system, which operates as a PCR thermal cycler as well as a fluorescence detector. There are many of these options available in the market with varying features, such as plate format, fluorescence channels, and validated use in diagnostics. Likewise, a number of coronavirus qRT-PCR assays are progressively becoming available for both diagnostic and research use. These complete kits contain the crucial components required for the molecular assay, including primer and probe sets, enzymes, buffers, and nucleotides.

Other molecular assays

With more assay manufacturers providing new options for molecular assays, we also begin to see tests that use methods outside of qRT-PCR. One example is digital PCR (dPCR), whose principle is to carry out PCR reactions within thousands of individually partitioned droplets. Each reaction is digitally detected, enabling absolute quantification of DNA. This method has been reported to accurately quantify samples that suffer from low amounts of nucleic acid or from variable levels of protein contamination. Other molecular diagnostic methods that have been recently granted emergency authorization include endpoint RT-PCR, rapid isothermal amplification, and RT-LAMP (Reverse transcription loop-mediated isothermal amplification)[4].The RT-LAMP method is a single step nucleic acid amplification technique, in which a particular RNA sequences will be amplified. RT-LAMP method is employed to detect infectious disease which caused by RNA viruses.

2.2. Isothermal Nucleic Acid Amplification

RT-PCR requires several temperature changes per cycle, including well equipped thermal cycling equipment [5].Isothermal nucleic acid enhancement is another technique that permits enhancement at a fixed temperature without the requirement of the thermal cycling equipment [6].

2.3. Applicant-Based Metagenomic Sequencing

The term amplicon is used in molecular biology, which is a portion of RNA or DNA that is the source and/or product of magnification or multiplication events. An amplicon can be produced artificially by employing the techniques like PCR or LCR (Ligase Chain Reactions) or naturally by duplication of gene. In this perspective, the term amplification denotes the production of one or more replicas of a genetic fragment or target sequence.

The Amplicon-Based Met agenomic Sequencing method for the SARS-CoV-2 diagnosis, bank on a dual methodology comprising application of metagenomics sequencing and amplicon-based sequencing [7]. The meaning of metagenomics is the study of genome of microorganisms, which are collected from environmental sample. The background microbiome of infected individuals is addressed by the use of metagenomics sequencing. The term microbiome refers to the genetic sequence of all the symbiotic and pathogenic microorganisms which are living in and on all vertebrates. It recognizes the potential of both the SARS-CoV-2 virus as well as other pathogens causative to the secondary infection that influences the severity of symptoms of COVID-19.Amplicon-based sequencing of SARS-CoV-2 enables studies of potential linkage detection, molecular epidemiology and viral evolution[Meaning: Epidemiology-technique used to discover the causes of health outcomes and diseases in populations. Molecular epidemiology emphases on the influence of potential genetic and environmental risk factors, recognized at the molecular level]. Metagenomics methods such as

sequence-independent single primer amplification (SISPA) give further insights into sequence segmentation. This dual strategy is mainly related to SARS-CoV-2 in the evaluation of its rate of mutation and its recombination with other human coronaviruses, both of which have consequences for antiviral effectiveness and invention of vaccine.

2.4. Nucleic Acid Hybridization Using Microarray

For rapid high-throughput identification of nucleic acids of SARS-CoV, microarray assays have been utilized. They depend on cDNA production from viral RNA by cDNA labeling with reverse transcription and specific probes. The cDNAs are labeled and loaded into the wells of microarray trays containing stable-phase oligonucleotides on their surfaces. If they are hybridized, they bind even after washing of the unbound DNA, thus indicating the presence of virus-specific nucleic acid [8]. Microarray evaluation has proven very beneficial in detecting mutations accompanying with SARS-CoV, and the use of 24 single nucleotide polymorphisms (SNPs) related to mutations in the spike (S) gene of SARS-CoVwith very good accuracy [9].

The capacity to identify various emerging strains of SARS-CoV-2 may be essential as the COVID-19 epidemic evolves, and microarray assessments offer a rapid identification of those strains as a result of mutation. Even though the primary disadvantage of microarray testing is that it is generally more expensive, a commercially degrading, non-fluorescent, low-density oligonucleotide array test has been developed that detects multiple coronavirus strains equivalent to that of real-time RT-PCR[10]. Additionally, the microarray chip-based movable diagnostic platform is employed to detect nucleic acids specific to the MERS coronavirus in addition to influenza and respiratory syncytial viruses[11].

3. Immunoassays

Immunoassays work on the basis of exact antibody-to-antigen binding, in which antibodies are used to detect and measure unique signs of pathogen infection. Viruses can be directly diagnosed through targeting of specific viral proteins or antigens. Otherwise, serum immunoglobulins (such as IgG, IgA, and IgM) that an individual has generated as part of an immune response can also be measured. These types of immunoassays are known as antibody tests. Several immunoassays have been authorized for use in diagnostics for COVID-19 using forms such as ELISA and lateral flow.

3.1. Enzyme-Linked Immunosorbent Assay (ELISA)

ELISA method involves enzyme-substrate reactions to generate quantitative signals proportionate to the amount of the target sample. In typical microplate wells, a characteristic feature of ELISA is the immobilization of the target antigen on the solid surface. This can happen by coating the surface with specific antibodies. When the targets are immunoglobulins, the surface is coated with recombinant proteins. The most common method follows a set of progressive steps: sample application and binding of analyte, the addition of enzymes that bind to specific antibodies, incubation with a chemical substrate, and detection in a microplate reader. ELISA kits are highly sensitive that can be used to measure different types of complex analytes.

The COVID-19 IgG ELISA method is planned, established and shaped for the quantifiable measurement of the COVID-19 IgG antibody in serum samples (serology). This serological assay method uses a microplate-based enzyme immunoassay technique [12].

Assay controls and samples are added to the microplate wells of the microplate coated with the COVID-19 peptide antigen nucleocapsid protein. Once the first incubation period is over, the unbound protein matrix is detached during the subsequent washout time. For each well, a horseradish peroxidase (HRP) named COVID-19 IgG tracer antibody was added. After the completion of incubation period, if the tested material contains a coronavirus IgG antibody, an immune-complex (i.e., COVID-19 polypeptide antigen-new coronavirus IgG antibody HRP labeled COVID-19 IgG tracer antibody) will beproduced. The unbound tracer antibody is separated from the subsequent washout step. The HRP labeled tracer antibody bound to the well was then incubated with the substrate solution in a time reaction and then measured on a spectrophotometric microplate reader. The amount of the coronavirus IgG antibody in the tested material is proportional to the enzymatic activity of the tracer antibody bound to the coronavirus IgG on the wall of the microtiter well.

3.2. Lateral flow immunoassays

This is a chromatographic method of assay. In this technique, the antibodies captured are immobilized on the surface of the support membrane (in antibody tests, recombinant proteins are immobilized). When the analyte is applied, its various components move across the membrane. However, target analytics can be trapped in a designated area, producing a color that can be viewed in plain view or by a detection device. In comparison with ELISA, lateral flow assays are usually qualitative instead of quantitative. However, the comparative simplicity of the methodology has led to the extensive development of various point-of-care and direct-to-consumer devices [13].

3.3. Neutralization Assay

Neutralization assay methods estimate the capability of the antibody to supress viral infection of cultured cells and, consequently, the cytopathic effects of viral replication. For this assay method, samples of patients with whole blood, serum or plasma are diluted and diluted to cell cultures. If there are neutralizing antibodies, their concentrations can be measured by estimating the limit they are capable to inhibit viral replication in infected cell cultures. For neutralization assay method, the result time is usually 3-5 days, but recent developments have made the result time from days to hours [14, 15]. This type of testing needs cell culture facilities, and for SARS coronavirus, Biosafety Level 3 (BSL3) laboratoriesare required. In spite of these limitations, the estimation of neutralizing antibodies is essential for the therapeutic application of resilient plasma in the short term and for the development of the vaccine in the long run.

3.4. Luminescent Immunoassay

Luminescent immunoassays include methods for reducing detection limits for antibody-based reagents. In general, they include chemiluminescence and fluorescence. Cai et al. haveestablished [16] a peptide-based magnetic chemiluminescence enzyme immunoassay for COVID-19 diagnostics, and Diazime Laboratories, Inc. (San Diego, California) has announced the availability of two new completely automated serological tests for SARS-CoV-2 [17].

3.5. Biosensor Test

Biosensor tests depend on the specific interaction of biomolecules with optical, electrical, enzymatic and other means of measuring readability. Surface Plasmon Resonance

(SPR) is a method that measures incident light at a solid boundary due to local disturbances like antibody or antigen adsorption. An SPR based biosensor has been developed for SARS diagnostics using coronavirus surface antigen (SCV me) attached on a gold substrate [18]. The SPR chip detects anti-SCV me antibodies in less than 10 min with a limit of detection as low as 200 ng/mL.

Very recently, PathSensors Inc. SARS declared a Canary Biosensor to find novel COVID-19. This technique uses a cell-based immune sensor that captures the virus with signal amplification that gives results within 5 minutes. The biosensor was made available for research purposes since May 2020 [19].

3.6. Rapid Antigen Test

Rapid antigen tests that allow detection of viral antigens are complementary to molecular genetic tests [20, 21]. These tests depend on specific monoclonal antibodies to provide a mechanism for capturing viral antigens from the sample to be analyzed. These rapid antigen tests are not limited to a specific format. For example, the colorimetric enzyme immunoassay for SARS-CoV in 2004 [22], enhanced chemiluminescent method.

Conflicting between molecular tests and immunoassay for COVID-19 diagnostics

There are some basic differences between molecular tests and immunoassays. Molecular assays are specific to viral nucleic acids, but immunoassays sense antigens and proteins. Experimental procedures of the two methods are also varies. Molecular tests usually involve more steps and tools, hence taking more time for the result. PCR amplification comprises repetitive temperature cycling, a rate-limiting step that takes about 1-2 hours to conclude. The full manual process, including sample preparation, RNA extraction and data analysis, completes in few hours.

On the contrary, immunoassay procedures are comparitively simple and require little incubation. ELISAs can take a few hours and some rapid disposable tests can give results in less than an hour. Remarkably, ELISAs and real-time RT-PCR assays in multi-well formats are scalable and can undergo automated procedures, resulting in enhanced throughput. The growth centered on these two contrasting test methods provides a promising pathway to reducing the COVID-19 epidemic, which has now claimed more than 939,000 lives worldwide as on today.

4 Conclusion and Outlooks

There has been a rapid improvement in the diagnostic of COVID-19 over the past few months, as competition continues to develop more sophisticated laboratory techniques and cheaper, point-of-care test kits that can be used on a large scale. This mini review provides a brief summary of molecular analysis and immune modulatory tests for the diagnosis of pandemic COVID-19 disease. Amongst the many assay methods, it is found that the RT-PCR is the leading technique for the identification of viral RNA. Other nucleic acid assays, including isothermal amplification assays, hybridization microarray assays, and amp icon-based meta genomics sequencing, have also been under improvement or permissible tests [23].

The need for time for precise and quick finding of COVID-19 infection is significant, as health systems worldwide are operating during the COVID-19 epidemic. Specifically, molecular and immune testing of infected people and their close contact is estimated to be in

high demand. The results from these assay tests may help in evaluate epidemiologically and use it to manage return to normal conditions. In summary, a substantial advancement has been made in the advancement of diagnostic tests in spite of all the continuing doubts and problems. Constant efforts around the world are developing new analytical evaluation and working on communication and convenience worldwide distribution of test kits. To approve more precise and rapid diagnosis of COVID-19, many organizations support the scientists who involved in developing COVID-19 assay methods by funding them through collaborations. It is likely that the COVID-19 as saymarket will remain to flourish well in future. Ultra-rapid test kits and point-of-care tests are the main focus of progress to accelerate treatment response time and remove the need for sophisticated laboratory and to engage with testing in approved laboratories.

References

[1] Linda J. Carter, Linda V. Garner, Jeffrey W. Smoot, Yingzhu Li, Qiongqiong Zhou, Catherine J. Saveson, Janet M. Sasso, Anne C. Gregg, Divya J. Soares, Tiffany R. Beskid, Susan R. Jervey and Cynthia Liu, Assay Techniques and Test Development for COVID-19 Diagnosis, ACS Cent. Sci. 6, 591−605 (2020).

[2] Bendavid, E.; Mulaney, B.; Sood, N.; Shah, S.; Ling, E.; Bromley-Dulfano, R.; Lai, C.; Weissberg, Z.; Saavedra, R.; Tedrow, J.; Tversky, D.; Bogan, A.; Kupiec, T.; Eichner, D.; Gupta, R.; Ioannidis, J.; Bhattacharya, J. COVID-19 Antibody Seroprevalence in Santa Clara County, Californiamed Rxiv 2020, 2020.04.14.20062463.

[3] Jones, H. The Importance of diagnostic testing for COVID-19. Infectious Diseases Hub; April 2, (2020).

[4] Wei E. Huang, Boon Lim, Chia-Chen Hsu, Dan Xiong, Wei Wu, Yejiong Yu, Huidong Jia, Yun Wang, Yida Zeng, Mengmeng Ji, Hong Chang, Xiuming Zhang, Hui Wang, Zhanfeng Cui, RT-LAMP for rapid diagnosis of coronavirus SARS-CoV-2, Microbial Biotechnology, 13(4), 950-961(2020).

[5] Notomi, T.; Okayama, H.; Masubuchi, H.; Yonekawa, T.; Watanabe, K.; Amino, N.; Hase, T. Loop-mediated isothermal amplification of DNA. Nucleic Acids Res. 28 (12), E63−7 (2000).

[6] Ma, C.P., Wang, F.X., Wang, X.D., Han, L.Z., Jing, H.,Zhang, H., and Shi, C. A novel method to controlcarryover contamination in isothermal nucleic acid amplification. ChemCommun 53: 10696-10699(2017).

[7] Rausch, P., Rühlemann, M., Hermes, B.M. et al. Comparative analysis of amplicon and metagenomic sequencing methods reveals key features in the evolution of animal metaorganisms. Microbiome 7, 133 (2019).

[8] Chen, Q.; Li, J.; Deng, Z.; Xiong, W.; Wang, Q.; Hu, Y. Q. Comprehensive detection and identification of seven animal coronaviruses and human respiratory coronavirus 229E with a microarray hybridization assay. Intervirology 53 (2), 95-104 (2010).

[9] Guo, X.; Geng, P.; Wang, Q.; Cao, B.; Liu, B. Development of a single nucleotide polymorphism DNA microarray for the detection and genotyping of the SARS coronavirus. J. Microbiol. Biotechnol. 24 (10), 1445-1454 (2014).

[10] de Souza Luna, L. K.; Heiser, V.; Regamey, N.; Panning, M.; Drexler, J. F.; Mulangu, S.; Poon, L.; Baumgarte, S.; Haijema, B. J.; Kaiser, L.; Drosten, C. Generic detection of coronaviruses and differentiation at the prototype strain level by reverse-transcription-PCR and nonfluorescent low-density microarray. J. Clin. Microbiol. 45 (3), 1049-1052 (2007).

[11] Hardick, J.; Metzgar, D.; Risen, L.; Myers, C.; Balansay, M.; Malcom, T.; Rothman, R.; Gaydos, C. Initial performance evaluation of a spotted array Mobile Analysis

Platform (MAP) for the detection of influenza A/B, RSV, and MERS coronavirus. Diagn. Microbiol. Infect. Dis. 91 (3), 245-247 (2018).

[12] Christian Bundschuh et al. Evaluation of the EDI enzyme linked immunosorbent assays for the detection of SARS-CoV-2 IgM and IgG antibodies in human plasma. ClinicaChimicaActa. Published 2020 June 8.

[13] Zhenhua Chen, Zhigao Zhang, XiangmingZhai, Yongyin Li, Li Lin, Hui Zhao, LunBian, Peng Li, Lei Yu, Yingsong Wu, and Guanfeng Lin, Rapid and Sensitive Detection of anti-SARS-CoV-2 IgG, Using Lanthanide-Doped Nanoparticles-Based Lateral Flow Immunoassay, Anal. Chem. 92, 10, 7226-723 (2020).

[14] Postnikova, E. N.; Pettitt, J.; Van Ryn, C. J.; Holbrook, M. R.; Bollinger, L.; Yu, S.; Cai, Y.; Liang, J.; Sneller, M. C.; Jahrling, P. B.; Hensley, L. E.; Kuhn, J. H.; Fallah, M. P.; Bennett, R. S.; Reilly, C. Scalable, semi-automated fluorescence reduction neutralization assay for qualitative assessment of Ebola virus-neutralizing antibodies in human clinical samples. PLoSOne 14 (8), e0221407 (2019).

[15] Whiteman, M. C.; Antonello, J. M.; Bogardus, L. A.; Giacone, D. G.; Rubinstein, L. J.; Sun, D.; Tou, A. H. M.; Gurney, K. B. A virus neutralization assay utilizing imaging cytometry. WO 2020/036811. World Intellectual Property Organization, 20 February 2020. Patentscope,

[16] Cai, X.; Chen, J.; Hu, J.; Long, Q.; Deng, H.; Fan, K.; Liao, P.; Liu, B.; Wu, G.; Chen, Y.; Li, Z.; Wang, K.; Zhang, X.; Tian, W.; Xiang, J.; Du, H.; Wang, J.; Hu, Y.; Tang, N.; Lin, Y.; Ren, J.; Huang, L.; Wei, J.; Gan, C.; Chen, Y.; Gao, Q.; Chen, A.; He, C.; Wang, D.; Hu, P.; Zhou, F.; Huang, A.; Liu, P.; Wang, D. A Peptide-based Magnetic Chemiluminescence Enzyme Immunoassay for Serological Diagnosis of Corona Virus Disease 2019 (COVID-19) medRxiv 2020, 2020.02.22.20026617.

[17] Diazyme Laboratories, Inc. Announces Availability of COVID-19 Antibody Tests, News & Media. Diazyme Laboratories, Inc. March 23, (2020).

[18] Park, T. J.; Hyun, M. S.; Lee, H. J.; Lee, S. Y.; Ko, S. A selfassembled fusion protein-based surface plasmon resonance biosensor for rapid diagnosis of severe acute respiratory syndrome. Talanta 79 (2), 295-301 (2009).

[19] Path Sensors, Inc. Announced the Development of a SARSCoV-2 Biosensor. PathSensorsInc, PathSensors News and Press, March 24, (2020).

[20] Analysis of serologic cross-reactivity between common human coronaviruses and SARS-CoV-2 using coronavirus antigen microarray. bioRxiv 2020, 2020.03.24.006544.

[21] Diagnosis of acute respiratory syndrome coronavirus 2 infection by detection of nucleocapsid protein. Med Rxiv 2020, 2020.03.07.20032524.

[22] Che, X. Y.; Qiu, L. W.; Pan, Y. X.; Wen, K.; Hao, W.; Zhang, L. Y.; Wang, Y. D.; Liao, Z. Y.; Hua, X.; Cheng, V. C.; Yuen, K. Y. Sensitive and specific monoclonal antibody-based capture enzyme immunoassay for detection of nucleocapsid antigen in sera from patients with severe acute respiratory syndrome. J. Clin. Microbiol. 42 (6), 2629-2635 (2004).

[23] Service, R. F. Standard coronavirus test, if available, works well-but can new diagnostics help in this pandemic? Science, March 22, (2020).

Karnatak University
Journal of Science

ISSN: 0075-5168

Influence of Magnetohydrodynamics and Mass Transfer on Convective Flow past a Moving rough Plate

P. M. Patil,
Shivanandappa H. Doddagoudar
P. S. Hiremath

P. M. Patil, Shivanandappa H. Doddagoudar, and P. S. Hiremath, "Influence of Magnetohydrodynamics and Mass Transfer on Convective Flow past a Moving rough Plate" Karnatak University Journal of Science 51, 79-95 (2020).

Influence of Magnetohydrodynamics and Mass Transfer on Convective Flow past a Moving rough Plate

P. M. Patil[a,*], Shivanandappa H. Doddagoudar[a,b], and P. S. Hiremath[c]
[a]Department of Mathematics, Karnatak University Dharwad-580003, India
[b]Government First Grade College, Hirekerur-581111, Haveri, India
[c]Department of Computer Science (MCA), KLE Technological University, B. V. Bhoomareddy Campus, Hubballi – 580031, India
*** Corresponding author**
***E-mail addresses*:** pmpmath@gmail.com (P. M. Patil), doddagoudars@yahoo.com (Shivanandappa H. Doddagoudar), and hiremathps53@yahoo.com (P. S. Hiremath).

Abstract: In this work, mixed convective MHD flow past a vertically moving plate with surface roughness and mass transfer is studied. Appropriate non-similarity transformation is employed to transform the partial differential equations with high degree of nonlinearity that model the flow to dimensionless form which are then linearized by applying the method of Quasilinearization. The implicit finite difference method is used to compute numerical solution of the system of linear equations resulting from the quasilinearization process. The influence of governing parameters on non-similar profiles and corresponding gradients defined at the surface is found by analyzing the numerical results presented graphically. The results reveal that the rising value of magnetic parameter enlarges the temperature profile and lowers the Nusselt number. The roughness of the wall surface yields significant changes in the Nusselt number and coefficient of skin-friction. The similar behavior is observed in these gradients due to frequency parameter.
***Keywords*:** Magnetohydrodynamic (MHD) flow; Nanofluid; Moving plate; Finite difference method; Quasilinearization; Mixed convection; Surface roughness.
Article history: Received: 12 June 2020**;** Revised: 20 July 2020; Accepted: 26 July 2020.

1. Introduction

In recent studies, a flow over a vertically moving plate is found to have abundant applications in the aerosol science, civil engineering and aerodynamics, etc. The concept of adding tiny solid particles in the fluid to improve the heat transport was introduced by Maxwell [1]. The idea of nanofluids as a new heat transfer coolant was introduced by Choi [2] in the year 1995 and these fluids possess higher thermal properties than traditional coolants. Suspended nanoparticles (lesser than 10^{-7}m in diameter) can alter the heat transport characteristics and fluid flow of the ordinary base fluids. Nanoliquids have been proven applications in various technologies such as Space, Electronic, Transport, Medical, Industrial cooling, Microchips cooling, Nuclear systems cooling, Defence systems and many more [3]. Srinivasa et al. [4] have studied the profiles and gradients for flow along a moving plate with heat radiation and found that temperature profile increase is more for static plate as compared to that in case of moving plate. Maleki et al. [5] found that Newtonian nanofluids have weaker thermal performance as compared to non-Newtonian nanofluids. In presence of thermal radiation and internal heat generation, Mondal et al. [6] have examined the mixed convection flow of nanoliquid through a porous medium. A nanofluid flow through a porous medium with heat source/sink along a moving plate was studied by Ghosh and Mukhopadhyay [7]. Mahantesh et al. [8] have analyzed the mass and heat transport in the mixed convection of chemically

reacting nanoliquid along a plate and found that by varying volume fraction of nanoparticles, the transport characteristics of heat and mass can be controlled.

The dynamics of liquids such as electrolytes, liquid metals, salt water, that are of the nature of conducting electricity is termed as the magnetohydrodynamic (MHD) flow. MHD describes the interaction between fluid motion and magnetic field. The MHD flows have significant applications in astrophysics and geophysics, metallurgy, fission and fusion, medicine, aerospace industry, nuclear reactors, heat exchangers, MHD pumps, MHD power generators engineering sciences etc. In the year 1930 the systematic studies of magnetohydrodynamic flow began by Hartmann and Lazarus [9] and in the year 1942, the work on Alfven waves [10] finalized the magnetohydrodynamic as an independent stream of science. Ellahi et al. [11] explored the mixed effects of heat transfer and MHD on flow under the impact of slip along a moving plate. Hussain et al. [12] studied the chemical reaction effects, Hall effects and heat absorption on MHD natural convective heat transfer along a moving plate. By considering chemical reaction, heat absorption and thermal radiation, Raju et al.[13] have examined the Soret effect in mixed convective MHD flow over a moving plate. Considering natural convection flow in porous medium under influence of magnetic field, concentration and changing surface temperature, Javaherdeh et al. [14] have investigated mass and heat transport along a moving plate. Singh and Makinde [15] have observed the velocity slip and temperature jump effects in mixed convection over a moving plate and also the effects of buoyancy force, convective heating and velocity slip on the flow along a vertical plate are studied. Investigating a natural convective MHD flow over a moving vertical plate in a porous medium, Tripathy et al. [16] have determined effects of chemical reaction on flow characteristics. Rashidi et al. [17] have analyzed the mixed convective magnetohydrodynamic flow over a moving plate by considering convective boundary conditions.

In various manufacturing processes practically it is not possible to make a perfectly smooth surface. There will always be some micro irregularities on the surface. The nature of such finely spaced micro irregularities on the surface texture is known as surface roughness. The recent works on surface roughness effects in mixed convection regime can be found in [18-21].

The main objective of this research work is to explore the magnetic field effects on the double diffusive mixed convective nanoliquid flow over a moving plate with applied suction/injection. This is the first such work undertaken to assess the impact of nanoparticles on boundary layer characteristics of MHD flow along a moving plate with rough surface. The modelled partial differential equations with high degree of nonlinearity are transformed to dimensionless form which are then linearized for obtaining the solution by applying the method of Quasilinearization and finite differences [22, 23].

2. Problem formulation

A two-dimensional steady mixed convection nanoliquid flow past a moving plate is considered and the flow geometry of the considered problem is as shown in the Fig.1. The process of surface mass transfer is considered along the moving plate. In the Cartesian plane, the flow along the vertical plate being in the upward direction, *x*-axis is chosen along the plate and *y*-axis perpendicular to it. The temperature of the ambient fluid is considered to be less as compared to that of wall. To represent the surface roughness, the deterministic model [24, 25] is used instead of the stochastic model [26, 27]. The wall surface roughness is modelled as a very short-wavelength small-amplitude sine wave. The $U_w(x)$ and $U_\infty(x)$ represent velocity

of the wall and that of the free stream respectively. The constant magnetic field B_0 is being applied perpendicular to the plate. The species concentration and temperature differences in the fluid medium cause the buoyancy force that drives the flow. The governing equations obtained with these assumptions are as follows:

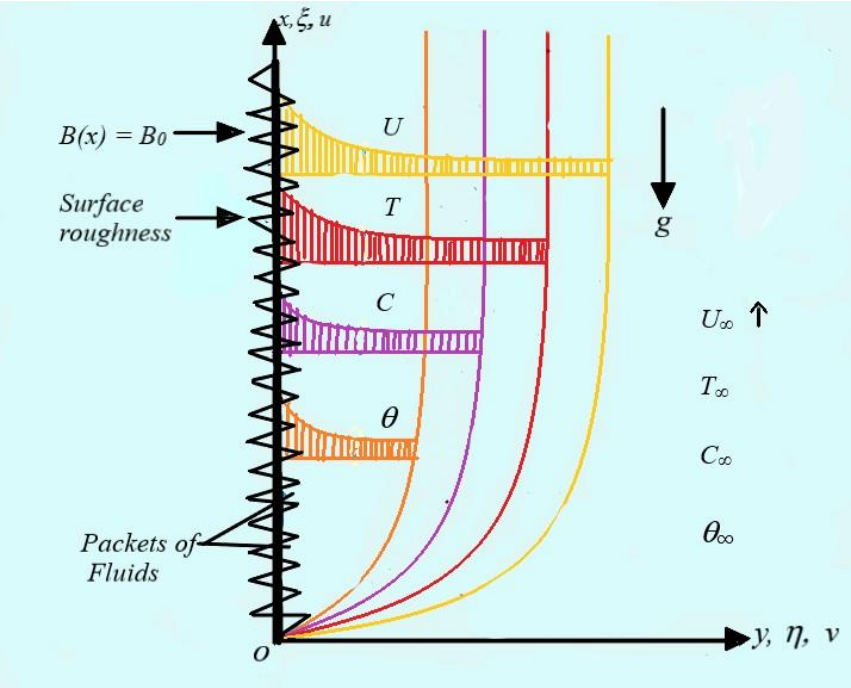

Fig.1 Flow model and geometry

Continuity equation

$$\frac{\partial u}{\partial x}+\frac{\partial v}{\partial y}=0, \tag{1}$$

Momentum balance equation

$$u\frac{\partial u}{\partial x}+v\frac{\partial u}{\partial y}=\frac{\sigma B_0^2}{\rho}\left(U_e-u\right)+\nu\frac{\partial^2 u}{\partial y^2}+(1-\theta_\infty)g[\beta(T-T_\infty)+\beta^*(C-C_\infty)]$$
$$-g\frac{(\rho_p-\rho)}{\rho}(\theta-\theta_\infty)\,, \tag{2}$$

Equation of energy transport

$$u\frac{\partial T}{\partial x}+v\frac{\partial T}{\partial y}=\frac{\nu}{Pr}\frac{\partial^2 T}{\partial y^2}+\frac{\sigma B_0^2}{\rho C_{nf}}\left(U_\infty-u\right)^2+J\left[\frac{D_T}{T_\infty}\left(\frac{\partial T}{\partial y}\right)^2+D_B\frac{\partial \theta}{\partial y}\frac{\partial T}{\partial y}\right], \tag{3}$$

Equation of mass transport

$$u\frac{\partial C}{\partial x}+v\frac{\partial C}{\partial y}=\frac{\nu}{Sc}\frac{\partial^2 C}{\partial y^2}, \tag{4}$$

Equation of nanoparticle mass transport

$$u\frac{\partial \theta}{\partial x}+v\frac{\partial \theta}{\partial y}=D_B\frac{\partial^2 \theta}{\partial y^2}+\frac{D_T}{T_\infty}\frac{\partial^2 T}{\partial y^2}, \tag{5}$$

The physical conditions at the boundary are,

$$u=U_w(x)=U_0\left[\alpha\sin(nx/L)+1\right], \qquad v=v_w, \quad T=T_w, \quad C=C_w, \quad \theta=\theta_w, \text{ at } y=0$$

$$u \to U_\infty, \qquad T\to T_\infty, \quad C\to C_\infty, \quad \theta\to\theta_\infty, \text{ as } y\to\infty. \tag{6}$$

where α and n are the small amplitude and frequency parameter respectively. Applying the following nonsimilar transformations:

$$\xi=\frac{x}{L}, \qquad \eta=\left(\frac{U_0}{\nu x}\right)^{1/2} y, \qquad \psi(x,y)=\left(\nu U_0 x\right)^{1/2} f(\xi,\eta),$$

$$\frac{T-T_\infty}{T_w-T_\infty}=G(\xi,\eta), \qquad \frac{C-C_\infty}{C_w-C_\infty}=H(\xi,\eta), \qquad \frac{\theta-\theta_\infty}{\theta_w-\theta_\infty}=S(\xi,\eta),$$

$$u=\frac{\partial\psi}{\partial y}, \; v=-\frac{\partial\psi}{\partial x}, \; f_\eta(\xi,\eta)=F(\xi,\eta), \; \frac{u}{U_0}=F \text{ and } v=\left(\frac{\nu U_0}{x}\right)^{1/2}\left[\frac{\eta}{2}F-\xi f_\xi-\frac{f}{2}\right], \tag{7}$$

Using the transformations in Eq.(7), the continuity equation (Eq.(1)) is identically satisfied and Eqs. (2) – (5) are reduced to the form as following:

$$F_{\eta\eta}+\left[\frac{f}{2}+\xi f_\xi\right]F_\eta-\xi FF_\xi+\xi M^2 Re\left(\varepsilon-F\right)+\xi Ri\left(G+NcH-NrS\right)=0, \tag{8}$$

$$G_{\eta\eta}+Pr\left[\frac{f}{2}+\xi f_\xi\right]G_\eta+NbPrS_\eta G_\eta+NtPrG_\eta^{\,2}-\xi Pr\; FG_\xi+\xi M^2 RePrEc\left(\varepsilon-F\right)^2=0, \tag{9}$$

$$H_{\eta\eta}+Sc\frac{f}{2}H_\eta+\xi Sc\left[f_\xi H_\eta-FH_\xi\right]=0, \tag{10}$$

$$S_{\eta\eta}+Le\left[\frac{f}{2}+\xi f_\xi\right]S_\eta-\xi LeS_\xi F+\frac{Nt}{Nb}G_{\eta\eta}=0, \tag{11}$$

The corresponding boundary conditions are:

$F = 1+\alpha \sin(n\xi)$, $G = 1$, $H = 1$, $S = 1$, at $\eta = 0$ and
$F = \varepsilon$, $G = 0$, $H = 0$, $S = 0$, as $\eta \to \infty$. (12)

Furthermore, $f = \int_0^\eta F d\eta + f_w$ so that $A\xi^{1/2} = f_w + 2\xi f_\xi$, where $A = -2v_0\left(\frac{L}{\nu U_0}\right)^{1/2}$ =constant, and $A> 0$, $A< 0$ and $A= 0$ signifies the suction, blowing and impermeable surface respectively. The physical quantities defined at the wall are: The relative dominance of free and forced convections is represented by the Richardson number *Ri* and thus, it is referred to as the mixed convection parameter and is defined as, $Ri = \frac{Gr}{Re^2}$, wherein the Grashof number $Gr = \frac{g\beta(T_w - T_\infty)(1-\theta_\infty)\,L}{\nu^2}$, and Reynolds number $Re = \frac{U_0 L}{\nu}$. Further, $Sc = \frac{\nu}{D}$ is Schmidt number, $\varepsilon = \frac{U_\infty}{U_0}$ is the velocity ratio parameter, $Le = \frac{\nu}{D_B}$ is the Lewis number, $Pr = \frac{\nu}{\alpha_m}$ is the Prandtl number, $Nr = \frac{\rho_p - \rho}{\rho}\frac{(\theta_w - \theta_\infty)}{\beta(T_w - T_\infty)}\frac{1}{1-\theta_\infty}$ is the nanoparticle buoyancy ratio parameter, $Nc = \frac{\beta^*(C_w - C_\infty)}{\beta(T_w - T_\infty)}$ is the species buoyancy ratio parameter, $Nb = \frac{JD_B(\theta_w - \theta_\infty)}{\nu}$ is the Brownian diffusion parameter, $Nt = \frac{JD_T(T_w - T_\infty)}{\nu T_\infty}$ is thermophoresis diffusion parameter, $Ec = \frac{U_0^2}{(T_w - T_\infty)C_{nf}}$ is the Eckert number, $M = \frac{B_0^2}{U_0^2}\sqrt{\frac{\sigma\nu}{\rho}}$ is the magnetic field parameter.

Here, $J = \frac{\rho_P C_{nP}}{\rho_f C_{nf}}$ is the ratio of effective heat capacity of nanoparticle material to heat capacity of fluid. The friction coefficient *Cf*, the Nusselt number *Nu*, the Sherwood number *Sh* and Nanoparticle Sherwood number *Nsh* , respectively are defined as follows:

$$Cf = 2\xi^{-1/2}Re^{-1/2}F_\eta(\xi,0)\frac{1}{(1+\alpha\sin n\xi)^2}, \quad \text{i.e.,} \quad Re^{1/2}Cf = 2\xi^{-1/2}F_\eta(\xi,0)\frac{1}{(1+\alpha\sin n\xi)^2}, \tag{13}$$

$$Nu = -\xi^{1/2}Re^{1/2}G_\eta(\xi,0), \quad \text{i.e.,} \quad Re^{-1/2}Nu = -\xi^{1/2}G_\eta(\xi,0), \tag{14}$$

$$Sh = -\xi^{1/2}Re^{1/2}H_\eta(\xi,0), \quad \text{i.e.,} \quad Re^{-1/2}Sh = -\xi^{1/2}H_\eta(\xi,0), \tag{15}$$

$$Nsh = -\xi^{1/2}Re^{1/2}S_\eta(\xi,0), \quad \text{i.e.,} \quad Re^{-1/2}Nsh = -\xi^{1/2}S_\eta(\xi,0), \tag{16}$$

3. Numerical Procedure

The Eqs. (8) - (11), subject to the physical conditions (12) at the boundary are solved using Newton's linearization technique and the iterative equations that arise in this process are as follows:

$$F_{\eta\eta}^{i+1} + A_1^i F_\eta^{i+1} + A_2^i F^{i+1} + A_3^i F_\xi^{i+1} + A_4^i G^{i+1} + A_5^i H^{i+1} + A_6^i S^{i+1} = A_7^i \tag{17}$$

$$G_{\eta\eta}^{i+1} + B_1^i G_\eta^{i+1} + B_2^i G_\xi^{i+1} + B_3^i F^{i+1} + B_4^i S_\eta^{i+1} = B_5^i \tag{18}$$

$$H_{\eta\eta}^{i+1} + C_1^i H_\eta^{i+1} + C_2^i H_\xi^{i+1} + C_3^i F^{i+1} = C_4^i \tag{19}$$

$$S_{\eta\eta}^{i+1} + D_1^i S_\eta^{i+1} + D_2^i S_\xi^{i+1} + D_3^i F^{i+1} + D_4^i G_{\eta\eta}^{i+1} = D_5^i \tag{20}$$

The index i indicates the known functions, while the index $(i + 1)$ indicates the unknown ones. The boundary conditions are given by

$$F^{i+1} = \alpha \sin(n\xi) + 1, \quad G^{i+1} = 1, \qquad H^{i+1} = 1, \qquad S^{i+1} = 1 \quad \text{at } \eta = 0$$

$$F^{i+1} = \varepsilon, \qquad G^{i+1} = 0, \qquad H^{i+1} = 0, \qquad S^{i+1} = 0 \quad \text{at } \eta = \eta_\infty \tag{21}$$

The coefficients occurring in the Eqs. (17) - (20) have the following expressions:

$$A_1^i = \frac{f}{2} + \xi f_\xi, \qquad A_2^i = -\xi\left(M^2 Re + F_\xi\right), \qquad A_3^i = -\xi F, \qquad A_4^i = \xi Ri,$$

$$A_5^i = \xi RiNc, \; A_6^i = -\xi RiNr, \qquad A_7^i = -\xi\left(FF_\xi + M^2 \varepsilon Re\right)$$

$$B_1^i = Pr\left[2NtG_\eta + \frac{f}{2} + \xi f_\xi + NbS_\eta\right], \quad B_2^i = -\xi PrF, \; B_3^i = -\xi Pr\left(G_\xi + 2M^2 ReEc\left(\varepsilon - F\right)\right),$$

$$B_4^i = NbPrG_\eta, \; B_5^i = NtPrG_\eta^2 - \xi PrG_\xi F + NbPrG_\eta S_\eta - \xi M^2 RePrEc\left(\varepsilon^2 - F^2\right),$$

$$C_1^i = Sc\left[\frac{f}{2} + \xi f_\xi\right], \; C_2^i = -\xi ScF, \qquad C_3^i = -\xi ScH_\xi, \qquad C_4^i = -\xi ScH_\xi F,$$

$$D_1^i = Le\left[\frac{f}{2} + \xi f_\xi\right], \; D_2^i = -\xi LeF, \quad D_3^i = -\xi LeS_\xi, \; D_4^i = Nt/Nb, \quad D_5^i = -\xi LeS_\xi F.$$

The backward and central finite differences are applied for derivatives in ξ and $\eta-$ directions in order to solve the Eqs. (17) – (20), which result into system of equations with block tri-diagonal matrix. Varga's algorithm [28] is used to solve this block tri-diagonal matrix equation. The convergence criteria for the numerical solution is that the difference between the current and previous iterations shall be less than 0.0001.

4. Results and discussions

4.1 Velocity profile and skin friction

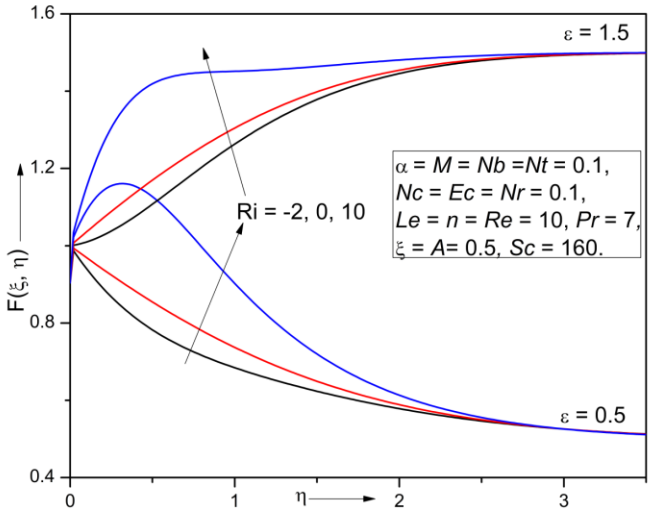

Fig.2 Impact of ε and *Ri* on $F(\xi,\eta)$

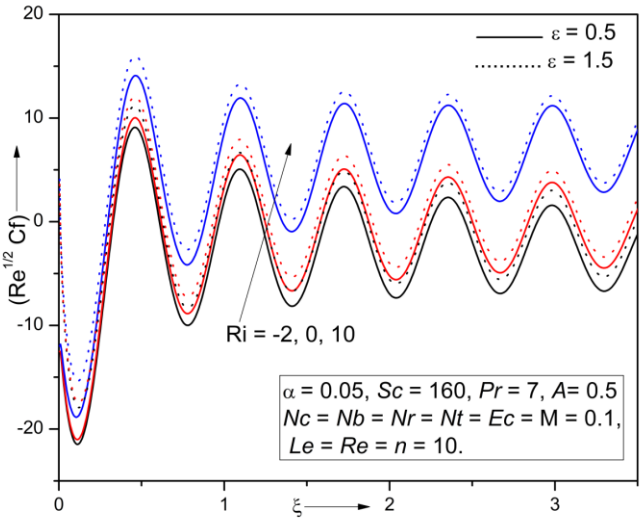

Fig.3 Impact of ε and *Ri* on $(Re^{1/2}Cf)$

The influence of *Ri* and ε on dimensionless velocity distribution *F* and skin-friction coefficient Cf is depicted in the Figs. 2 and 3 respectively. It is revealed that the rise in *Ri* and ε enhances the velocity profile and skin-friction coefficient and also the dimensionless velocity distribution near the wall is significantly higher for higher values of *Ri*. It is noted that the main stream velocity dominates over reference velocity (plate motion) for $\varepsilon = 1.5$, while for $\varepsilon = 0.5$ reference velocity (plate motion) dominates over main stream velocity.

4.2 Temperature profile and Nusselt number

Figs. 4 and 5 exhibit the effect of *Nt* and *M* on dimensionless temperature distribution *G* and wall heat transfer rate $\left(Re^{-1/2}Nu\right)$. As values of *Nt* and *M* increase the temperature profile increases while the wall heat transfer rate reduces. As *Nt* higher values, the nanoparticles gathered at the surface travel into colder fluid region and thus cause rise in the temperature of the fluid. Further, the Lorentz force opposes the fluid motion more strongly for the larger values of magnetic field parameter *M* and, thus, raises the dimensionless temperature distribution. Owing to these facts, the rate of heat transfer from wall into the fluid medium is reduced.

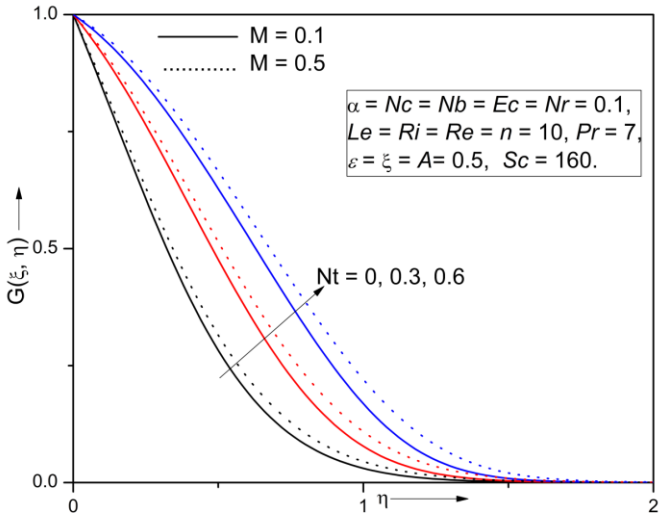

Fig.4 Impact of *M* and *Nt* on $G(\xi,\eta)$

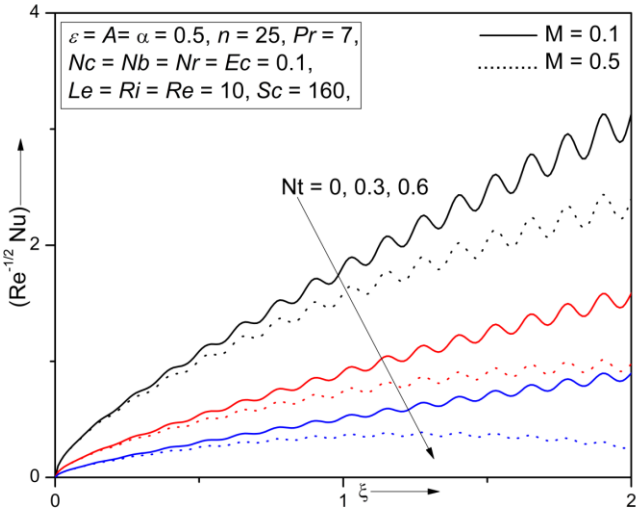

Fig.5 Impact of *M* and *Nt* on $(Re^{-1/2}Nu)$

4.3 Concentration profile and Sherwood number

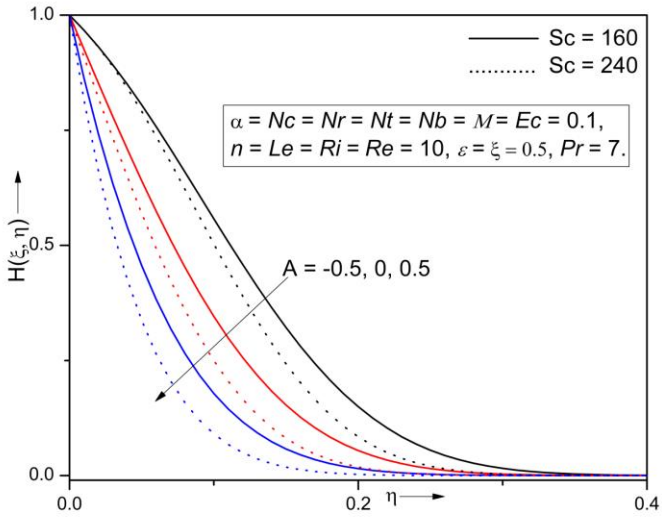

Fig.6 Influence of *Sc* and *A* on $H(\xi,\eta)$

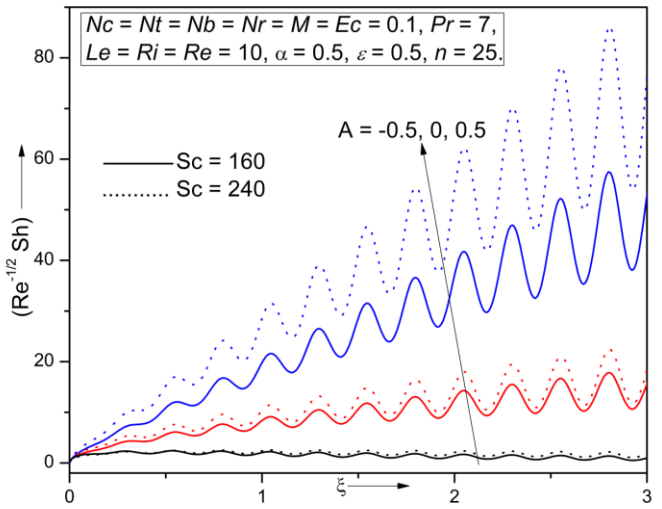

Fig.7 Impact of *Sc* and *A* on ($Re^{-1/2}Sh$)

Figures 6 and 7 depict the impact of Schmidt number *Sc* and suction/blowing parameter *A* on dimensionless concentration distribution $H\left(\xi,\eta\right)$ and Sherwood number $\left(Re^{-1/2}Sh\right)$, respectively. The concentration is found to decrease for larger values of *A* and *Sc* while the Sherwood number rises for the same. Also sinusoidal variations are observed, which are more prominent for larger values of *Sc* and *A*. The higher Schmidt number, i.e. the lesser mass diffusivity, results into reduction in the thickness of concentration boundary layer.

4.4 Nanoparticle volume fraction profile

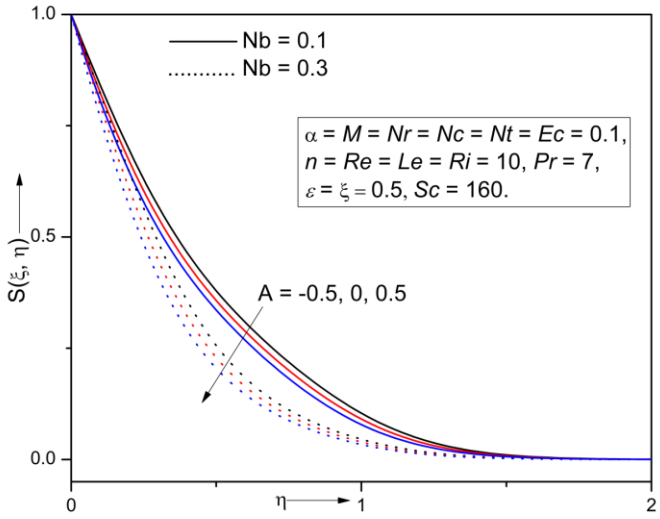

Fig.8 Impact of *Nb* and *A* on $S(\xi,\eta)$

The influence of *Nb* and *A* on volume fraction profile $S\left(\xi,\eta\right)$ and nanoparticle Sherwood number $\left(Re^{-1/2}NSh\right)$ is demonstrated in Figs. 8 and 9, respectively. For enhancing values of surface mass transfer (*A*), both the dimensionless nanoparticle volume fraction *S* and nanoparticle Sherwood number (*NSh*) increase, while for higher *Nb*, the dimensionless nanoparticle volume fraction reduces whereas nanoparticle Sherwood number increases. Physically, for higher *Nb*, nanoparticle motion near the hot plate towards a cold region increases, which enhances the magnitude of nanoparticle Sherwood number and the corresponding gradient. In addition to this, for the case of injection, the fluid particles near the plate gains higher velocity thus the mass transportation increases from hot rough plate to surrounding fluid, which enhances the nanoparticle mass transport rate. Consequently, it declines the dimensionless nanoparticle volume fraction. However, the contrary behavior is observed for the suction case.

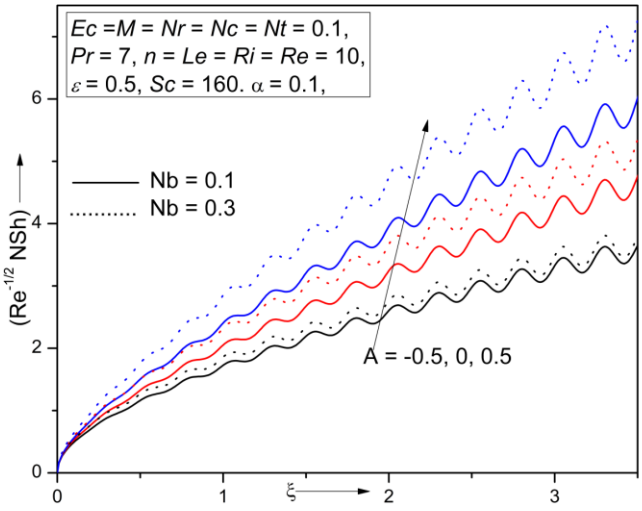

Fig.9 Impact of *Nb* and *A* on ($Re^{-1/2}NSh$)

4.5 Non-similarity effects

The Fig.10 displays the effect of non-similarity variable ξ on non-dimensional velocity (F), temperature (G) and concentration (H) distributions. Here $\xi = 0$ shows the similarity solution and $\xi \neq 0$ shows the non-similarity solution. From the graphs in Fig.10, the velocity profile is found to increase, while concentration and temperature profiles reduce for higher ξ. The enhancing values of ξ signify the adverse pressure gradient, which thickens momentum boundary layer and slims both temperature and concentration boundary layers.

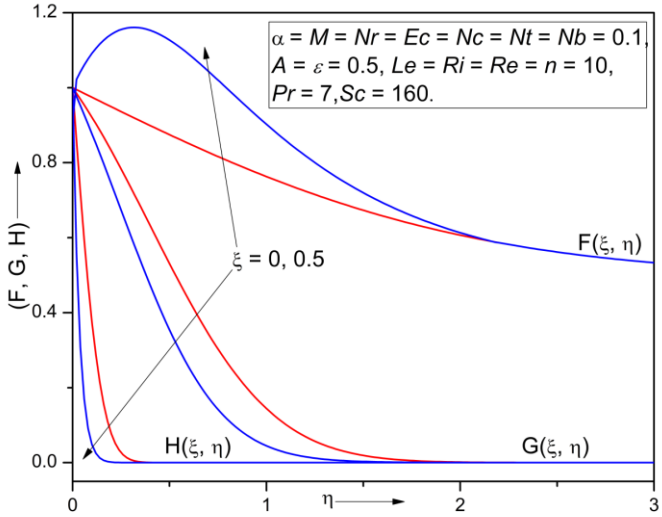

Fig.10 Non-similar profiles *F*, *G*, *H* at ξ =0.5

4.6 Surface Roughness Effects

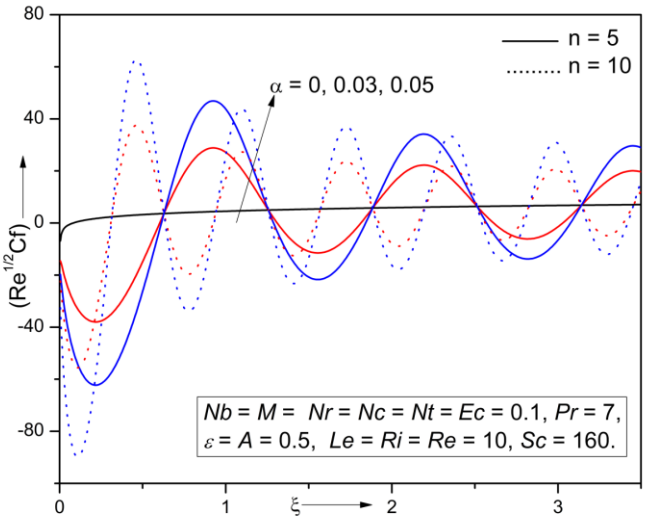

Fig.11 Impact of α and n on ($Re^{1/2}Cf$)

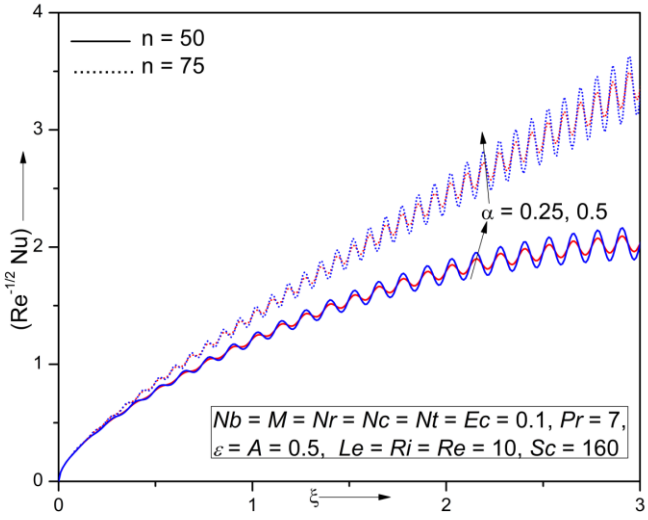

Fig.12 Impact of α and n on ($Re^{-1/2}Nu$)

Figure 11 demonstrates the impact of α and n on surface friction Cf. The influence of roughness $(\alpha \neq 0)$ on surface friction is compared with the corresponding results for smooth surface case $(\alpha = 0)$. The sinusoidal variations in Cf are observed in roughness case, which are more intensified for larger values of α near the origin as compared to that away from the origin. Also, for larger values of n, it shows the stronger fluctuations near the wall. Figure 12 denotes the effect of α and n on Nusselt number Nu. The prominent sinusoidal variations in

Nu are noticed due to roughness, which are more intensified for higher values of α and *n* farther away from the orifice.

4.7 Comparison with other methods

Table 1 presents *Cf* and *Nu* values for the various values of Richardson number *Ri* obtained in the present work, which are matched with the corresponding values obtained by Minkowycz and Sparrow [29] and Mohamad et al. [30] and these outcomes are found to be excellent harmony.

Table 1: Comparison of *Cf* and *Nu* values for the various values of Richardson number *Ri* with $\xi = 0$, $Pr = 0$, $Le = 0$, $Sc = 0$, $Nb = 0$, $Nr = 0$, $Nc = 0$, $\alpha = 0$, $n = 0$, $Nt = 0$, $A = 0$, $\varepsilon = 0$, $M = 0$, $Re = 0$ and $Ec = 0$.

Ri	**Minkowycz and Sparrow [29]**		**Mohamad et al. [30]**		**Present results**	
	Cf	***Nu***	***Cf***	***Nu***	***Cf***	***Nu***
0	0.33206	0.29268	0.3320573	0.2926804	0.33205	0.29270
0.4	0.73916	0.35774	0.7391622	0.3577421	0.73918	0.35773
1.0	1.21795	0.41054	1.2179529	0.4105355	1.21797	0.41056
1.5	1.56566	0.44106	1.5656630	0.4410137	1.56564	0.44107
2.5	2.18819	0.48619	2.1881869	0.4861908	2.18821	0.48621
5.0	3.52696	0.56067	3.5269162	0.5606733	3.52698	0.56065
7.0	4.47647	0.60283	4.4764563	0.6028282	4.47648	0.60281

4.8 Combined impact of magnetic field and surface mass transfer on wall gradients

The tabulated values in Table 2 show that, in both cases of injection and suction, the values of gradients are found to decrease. Further, due to suction, the coefficient of friction (*Cf*) decreases, while heat (*Nu*), mass (*Sh*) and nanoparticle mass (*NSh*) transfer rates increase significantly as compared to that in the injection case. This observation holds in presence as well as absence of magnetic field.

Table 2. Comparison of values of gradients, for absence and presence of magnetic parameter (*M*) values and also for suction and injection cases (*A*), when $\xi = 0.5$, $\alpha = 0.1$, $n = 10$, $\varepsilon = 0$, $Pr = 7$, $Nc = 0.1$, $Re = 10$, $Nr = 0.1$, $Le = 10$, $Nt = 0.1$, $Sc = 160$, $Ec = 0.1$, $Ri = 10$ and $Nb = 0.1$.

Gradients	**A = -0.5**		**A = 0.5**	
	M = 0	**M = 0.5**	**M = 0**	**M = 0.5**
$\left\|Re^{1/2}Cf\right\|$	59.68268	58.50204	58.45825	57.30803
$\left\|Re^{-1/2}Nu\right\|$	0.40546	0.33799	0.85022	0.78099
$\left\|Re^{-1/2}Sh\right\|$	0.39596	0.37917	5.61222	5.55017
$\left\|Re^{-1/2}NSh\right\|$	0.93950	0.90696	1.78765	1.75918

5. Conclusion

In this paper, the effects of magnetic field and surface mass transfer on mixed convective boundary layer flow over a vertically moving plate with rough surface are investigated. Using the appropriate non-similarity transformation, the partial differential equations with high degree of nonlinearity, that model the flow are transformed to dimensionless form, which are then linearized by applying the method of Quasilinearization. The impact of non-dimensional governing parameters namely, magnetic field parameter, surface mass transfer parameter, Richardson number, Thermophoresis parameter, Schmidt number, Brownian parameter, small amplitude roughness parameter and frequency parameter on the dimensionless velocity, temperature, concentration and nanoparticle volume fraction distributions are discussed and presented graphically. Also, the gradients (skin-friction, Nusselt number, and Sherwood numbers for both species and nanoparticles) are discussed. Key results of the present analysis are:

- The rise in *Ri* and ε increases the dimensionless velocity distribution and skin-friction.
- The main stream velocity dominates over reference velocity for $\varepsilon = 1.5$, while for $\varepsilon = 0.5$ reference velocity dominates over main stream velocity.
- For enhancing values of *Nt* and *M*, the dimensionless temperature distribution increases, while the heat transfer rate *Nu* reduces.
- As *A* and *Sc* increase, the concentration decreases, whereas the Sherwood number is found to increase. Also, sinusoidal fluctuations are observed, which are more prominent for higher values of *Sc* and *A*.
- The application of suction rises the nanoparticle Sherwood number, while it reduces the nanoparticle volume fraction distribution.
- For enhancing values of surface mass transfer, the volume fraction and nanoparticle Sherwood number rise, while for higher values of *Nb*, the volume fraction distribution reduces whereas nanoparticle Sherwood number increases.
- The roughness of the wall yields rapid variations in skin-friction and heat transfer rate. The similar behavior is observed in these gradients due to frequency parameter.
- The dimensionless velocity distribution increases, while the temperature and species concentration distributions reduce for larger values of non-similar variable ξ.
- Due to suction, the skin-friction coefficient decreases, while other gradients (pertaining to heat, mass and nanoparticle mass transfer) increase significantly as compared to that in the injection case. This observation holds in absence as well as presence of magnetic field.

References

[1] J. C. A. Maxwell, Treatise on electricity and magnetism, 2nd ed., Claren-don Press, Oxford, UK, (1873).
[2] S. U. S. Choi, Enhancing thermal conductivity of fluids with nanoparticles. Proceedings of the Int. Mech. Eng. Cong. San Francisco USA, ASME, FED231/MD. 66, 99–105 (1995).
[3] J. A. Eastman, S. U. S. Choi, S. Li, W. Yu and L. J. Thompson, Anomalously increased effective thermal conductivities of ethylene glycol-based nanofluids containing copper nanoparticles. Appl. Phys. Lett. 78(6), 718–720 (2001).
[4] C. T. Srinivasa, J. K. Singh, B. J. Gireesha and M. Archana, Heat and mass transfer analysis of casson nanofluid flow past a static/moving vertical plate with heat radiation. J. Nanofluids. 8 (3), 543-549 (2019).
[5] H. Maleki, M. R. Safaei, H. Togun and M. Dahari, Heat transfer and fluid flow of pseudo-plastic nanofluid over a moving permeable plate with viscous dissipation and heat absorption/generation. J. Therm. Anal. Calorim. 135, 1643–1654 (2019).

[6] H. Mondal, P. De, S. P. Goqo and P. Sibanda, Numerical studies on nanofluid flow over a porous vertical plate with internal heat generation and thermal radiation. Int. J. Nonlin. Sci. 27(1), 43-52 (2019).
[7] S. Ghosh and S. Mukhopadhyay, Some aspects of forced convection nanofluid flow over moving plate in a porous medium in the presence of heat source/sink. J. Eng. Thermophy. 28 (2), 291-304 (2019).
[8] B. Mahantesh, B. J. Gireesha and R. S. R Gorla, Heat and mass transfer effects on the mixed convective flow of chemically reacting nanofluid past a moving/stationary vertical plate. Alex. Eng. J. 55(1), 569-581 (2016).
[9] J. Hartmann and F. Lazarus, Theory of laminar flow of an electrically conductive liquid in a homogenous magnetic field. Det kgl Danskc Vidensk.Selsk. Math.fys. Medd. XV, 6 (1937).
[10] H. Alfvén, Existence of electromagnetic-hydrodynamic waves. Nature 150:405 (1942).
[11] R. Ellahi, S. Z. Alamri, A. Basit and A. Majeed, Effects of MHD andslip on heat transfer boundary layer flow over a moving plate based on specific entropy generation. J. Taibah. Univ. Sci. 12(4), 476–482 (2018).
[12] S. M. Hussain, J. Jain, G. S. Seth and M. M. Rashidi, Free convective heat transfer with hall effects, heat absorption and chemical reaction over an accelerated moving plate in a rotating system. J. Magn. Magn. Mater. 422112–123 (2017).
[13] M. C. Raju, A. J. Chamkha, J. Philip and S. V. K. Varma, Soret effect due to mixed convection on unsteady magnetohydrodynamic flow past a semi infinite vertical permeable moving plate in presence of thermal radiation, heat absorption and chemical reaction, Int. J. Appl. Comput. Math. 3, 947-961 (2016).
[14] K. Javaherdeh, M. M. Nejad and M. Moslemi, Natural convection heat and mass transfer in MHD fluid flow past a moving plate with variable surface temperature and concentration in porous medium. Eng. Sci. Technol. Int. J. 18(3), 423-431 (2015).
[15] G. Singh and O. D. Makinde, Mixed convection slip flow temperature jump along a moving plate in presence of free stream. Therm. Sci. 19, 119-128 (2015).
[16] R. S. Tripathy, G. C. Dash, S. R. Mishra and S. Baag, Chemical reaction effect on MHD free convective surface over a moving vertical plate through porous medium. Alex. Eng. J. 54(3), 673-679 (2015).
[17] M. M. Rashidi, N. Kavyani, S. Abelman, M. J. Uddin and N. Freidoonimehr, Double diffusive magnetohydrodynamic (MHD) mixed convective slip flow along a radiating moving plate with convective boundary condition. PLoS ONE 9 10 e109404 (2014).
[18] P. M. Patil, A. Shashikant and P. S. Hiremath, Influence of liquid hydrogen and nitrogen on MHD triple diffusive mixed convection nanoliquid flow in presence of surface roughness. Int. J. Hydro. Energy. 43, 20101-20117 (2018).
[19] P. M. Patil, A. Shashikant, P. S. Hiremath and E. Momoniat, Influence of surface roughness on multidiffusive mixed convective nanofluid flow. Phys. Scr. 945 (2019).
[20] P. M. Patil, A. Shashikant and P. S. Hiremath, Effects of surface roughness on mixed convection nanoliquid flow over slender cylinder with liquid hydrogen diffusion. Int. J. Hydro. Energy. 43, 11121-11133 (2018).
[21] P. M. Patil, S. H. Doddagoudar and P. S. Hiremath, Impacts of surface roughness on mixed convection nanofluid flow with liquid hydrogen/nitrogen diffusion, Int. J. Num. Methods Heat Fluid Flow 29 2146-2174 (2019).
[22] S. V. Subhashini and G. Nath, Unsteady compressible flow in the stagnation region of two-dimensional and axi-symmetric bodies. Acta Mech. 134,135-145 (1999).
[23] A. T. Eswara, S. Roy and G. Nath, Unsteady MHD forced flow due to a pint sink. Acta Mech. 145, 159-172 (2000).
[24] L. Chang, Deterministic modelling and numerical simulation of lubrication between rough surfaces – a review of recent developments. Wear. 184, 155-160 (1995).
[25] H. R. Pasaribu and D. J. Schipper, Deterministic friction model of a rough surface sliding against a flat layered surface. Tribology Lett. 17, 967-976 (2004).

[26] H. Christensen, Stochastic model for hydrodynamic lubrication of rough surfaces. Proceedings of the Ins. Mech. Eng. 184, 1013-1026 (1969).
[27] R. Buczkowski and M. Kleiber, A stochastic model rough surface for finite element contact analysis. Comp. Methods Appl. Mech. Eng. 169, 43-59 (1999).
[28] R. S. Varga, Matrix Iterative Analysis, Englewood Cliffs, NJ, Prentice-Hall (2000).
[29] W. J. Minkowycz and E. M. Sparrow, Numerical solution scheme for local non-similarity boundary-layer analysis, Numerical Heat Transfer, Part B: Fundamentals: An Int. J. Compu. Meth. 1, 69-85 (1978).
[30] R. Mohamad, R. Kandasamy and M. Ismoen, Local non-similarity solution for MHD mixed convection flow of a nanofluid past a permeable vertical plate in the presence of thermal radiation effects. J. Appl. Compu. Math. 4, 261-270 (2015).

Karnatak University
Journal of Science

ISSN: 0075-5168

Wavelet Packet Approximation Theorem: An Overview

Nikhil Khanna

S. K. Kaushik

Nikhil Khanna and S. K. Kaushik, “Wavelet Packet Approximation Theorem: An Overview” Karnatak University Journal of Science 51, 96-107 (2020).

WAVELET PACKET APPROXIMATION THEOREM: AN OVERVIEW

Nikhil Khanna[a] and S. K. Kaushik[b,*]

[a]Department of Mathematics, Motilal Nehru College, University of Delhi, Delhi 110021, India
[b]Department of Mathematics, Kirori Mal College, University of Delhi, Delhi-110007, india
***Corresponding author*:** shikk2003@yahoo.co.in

ABSTRACT. In this paper, we give a systematic update related to the wavelet packet approximation theorem for L^2 and H^r type norms.
Key words and phrases. Wavelet packets; vanishing moments; orthogonal Coifman wavelet packet systems;
Article history: Received: 26 June 2020**;** Revised: 04 August 2020; Accepted: 20 August 2020.

1. Introduction

The theory of Fourier analysis started with the famous treatise of Fourier [11], where he claimed that any periodic function can be represented as a series of harmonically related sinusoids known as Fourier series. In pursue to widen up his novel ideas to functions defined on an infinite interval, Fourier formulated Fourier transform which when applied on a signal decomposes it into a sine wave having different frequencies and phases. Fourier transform has been very beneficial in analyzing harmonic signals or signals, where no local information is required. The major weakness in the Fourier transforms is that the Fourier transform of a function (or signal) enables us to inquisite problems either in the time (space) domain or in the frequency domain, but not synchronously in both domains. In order to consolidate both time and frequency localization information, in 1946, Gabor [12] introduced the short-time Fourier transform (STFT) to represent a signal in both the domains. In this technique, an analysis window of fixed length was introduced that moves through the signal along the time axis so as to carry out a “time-localized" Fourier transform. Basically, on applying STFT, the whole time interval is partitioned into a number of small and equal time intervals so that they can be studied independently using the Fourier transform. The analysis of the signal using STFT contains time and frequency information. But since equal time intervals are not adjustable, there are times when high-frequency bursts, occur for a short duration, are hard to detect. This drawback of short-time Fourier transform persuaded the researchers to pursue for other approaches which helps them to analyze the nonstationary signals. One such approach is known as wavelet transform. In contrast to the STFT technique where the window size is fixed, the wavelet transform enables variable window sizes in analyzing different frequency components within a signal. The construction of wavelet transforms can be traced back to the development of a set of rectangular basis functions (also known as the Haar wavelet) by Haar in 1909. Later, various mathematicians like Littlewood and Paley [21], Stein [17], Ricker [28] and Strömberg [30] have added remarkable contribution from 1930s to the 1980s in the field of wavelet theory, but the major breakthrough in the area was ascribed to Morlet [22] who developed the approach of scaling and shifting of the window functions while studying acoustic echoes in the mid 1970s.

This technique was similar to that of Haar, but the theoretical construction and development of the wavelet transform was attributed to the team of Grossmann and Morlet [13] in 1984.

Thereafter, Grossmann *et al.* [14, 15] studied arbitrary signals using dilations and translations of single wavelet function. Conceivably, the most significant advancement in the success of wavelet theory was the development of multiresolution analysis (MRA) by Mallat [23, 24, 25] and Meyer [26, 27]. Using the theory of MRA, in 1988, Daubechies [8, 10] studied orthonormal bases of compactly supported wavelets and further, generated the Daubechies wavelets.

To run-over this limitation of poor frequency localization of the wavelet bases, Coifman *et al.* [5, 6, 7] in 1990, introduced the notion of wavelet packets, obtained from wavelets related to MRAs. They consist of a rich unit of building block functions that render more flexibility than wavelets in representing different types of signals and build bases that retain many significant characteristics such as smoothness, orthogonality and localization properties of their root wavelets. Wavelet packets emanate a large class of orthonormal bases of $L^2(\mathbb{R})$, each one corresponding to a different splitting of $L^2(\mathbb{R})$ into direct sum of its closed subspaces. Wavelet packets are specific linear combinations of wavelets and are established instinctively into collections and each such collection forms an orthogonal basis for $L^2(\mathbb{R})$. They have numerous applications in image compression, signal processing, fractal theory and coding theory, etc. For various details related to wavelet theory, one may refer [16, 17, 22, 23, 27, 33].

2. PRELIMINARIES

The development begins with a multiresolution analysis (MRA), consisting of a sequence of closed subspaces $(V_j)_{j\in\mathbb{Z}}$, of $L^2(\mathbb{R})$ (see [16]) satisfying

(i) $V_j \subset V_{j+1}$, for all $j \in \mathbb{Z}$;
(ii) $f \in V_j$ if and only if $f\big(2(\cdot)\big) \in V_{j+1}$, for all $j \in \mathbb{Z}$;
(iii) $\bigcap_{j\in\mathbb{Z}} V_j = \{0\}$;
(iv) $\overline{\bigcup_{j\in\mathbb{Z}} V_j} = L^2(\mathbb{R})$;
(v) There exists a function $\phi \in V_0$, such that $\{\phi(\cdot - k): k \in \mathbb{Z}\}$ is an orthonormal basis for V_0.

The function ϕ whose existence is asserted in (v) is called a scaling function of the given MRA. Let ϕ be real valued continuous function that solves the dilation equation (or two-scale difference equation)

$$\phi(x) = \sum_{k\in\mathbb{Z}} r_k\, \phi(2x - k) \tag{2.1}$$

with $\hat{\phi}(0) = 1$ and let ψ be an associated function defined by

$$\psi(x) = \sum_{k\in\mathbb{Z}} s_k\, \phi(2x - k). \tag{2.2}$$

It is well established (see [16]) that a pair of quadrature mirror filter coefficients (QMF), $(r_k)_{k\in\mathbb{Z}}, (s_k)_{k\in\mathbb{Z}} \in \ell^2(\mathbb{Z})$ is associated to the MRA and the following relations

$\hat{\phi}(\xi) = m_0\left(\frac{\xi}{2}\right)\hat{\phi}\left(\frac{\xi}{2}\right)$ and $\hat{\psi}(\xi) = m_1\left(\frac{\xi}{2}\right)\hat{\phi}\left(\frac{\xi}{2}\right)$ are satisfied for $\xi \in \mathbb{R}$, where the symbols m_0 and m_1 are given by

$$m_0(\xi) = \sum_{k\in\mathbb{Z}} r_k\, e^{\iota k\xi} \text{ and } m_1(\xi) = \sum_{k\in\mathbb{Z}} s_k\, e^{\iota k\xi} = e^{\iota\xi}\, \overline{m_0(\xi + \pi)}. \tag{2.3}$$

Also, we have

$$|m_0(\xi)|^2 + |m_0(\xi+\pi)|^2 = 1. \tag{2.4}$$

A family of functions $\omega_n,\ n = 0,1,2,\ldots$ defined as

$\omega_{2n}(x) = \sum_{k\in\mathbb{Z}} r_k\, \omega_n(2x-k)$ and $\omega_{2n+1}(x) = \sum_{k\in\mathbb{Z}} s_k\, \omega_n(2x-k)$, where $\psi = \omega_1$ and $\phi = \omega_0$ are often called mother and father wavelets and considered as basic wavelet packets. Fourier transform of wavelet packets $\{\omega_n\}$ are given by

$$\widehat{\omega}_{2n}(\xi) = m_0\left(\frac{\xi}{2}\right)\ \widehat{\omega}_n\left(\frac{\xi}{2}\right), \tag{2.5}$$

$$\widehat{\omega}_{2n+1}(\xi) = m_1\left(\frac{\xi}{2}\right)\ \widehat{\omega}_n\left(\frac{\xi}{2}\right). \tag{2.6}$$

Also, the set $\{\omega_n(x-k): k\in\mathbb{Z},\ n = 0,1,2,\ldots\}$ is an orthonormal basis of $L^2(\mathbb{R})$. The family of wavelet packets $\{\omega_n\}$ is defined as the family of subspaces of $L^2(\mathbb{R})$ corresponding to some orthonormal scaling function $\phi = \omega_0$ given by

$$U_j^n = \overline{span}\{\omega_n(2^j x - k) : k\in\mathbb{Z}\},\ j\in\mathbb{Z},\ n = 0,1,2,\ldots. \tag{2.7}$$

Note that $U_j^0 = V_j$ and $U_j^1 = W_j$ are such that the orthogonal decomposition $V_{j+1} = V_j \oplus W_j$ can be written as $U_{j+1}^0 = U_j^0 \oplus U_j^1,\ j\in\mathbb{Z}$.

The generalized version of the above expression is $U_{j+1}^n = U_j^{2n} \oplus U_j^{2n+1}$, for $n = 1,2,3,\ldots; j\in\mathbb{Z}$, where U_j^n is defined by (2.7). The decomposition trick (see [16]) for each $j = 1,2,3,\ldots$ yields

$$\begin{cases} W_j &= U_j^1 = U_{j-1}^2 \oplus U_{j-1}^3, \\ W_j &= U_j^1 = U_{j-2}^4 \oplus U_{j-2}^5 \oplus U_{j-2}^6 \oplus U_{j-2}^7, \\ &\vdots \\ W_j &= U_j^1 = U_{j-k}^{2^k} \oplus U_{j-k}^{2^k+1} \oplus\ldots\oplus U_{j-k}^{2^{k+1}-1}, \\ &\vdots \\ W_j &= U_j^1 = U_0^{2^j} \oplus U_0^{2^j+1} \oplus\ldots\oplus U_0^{2^{j+1}-1}, \end{cases}$$

where U_j^n is as defined in (2.7). Moreover, for each $j = 1,2,\ldots,\ k = 1,2,3,\ldots,j$ and $m = 0,1,\ldots,2^k-1$, the set $\{2^{\frac{j-k}{2}}\omega_p(2^{j-k}x-l): l\in\mathbb{Z}\}$ is an orthonormal basis of U_{j-k}^p, where $p = 2^k+m$. However, all the elements of these bases have the general form $\omega_{j,n,k}(x) = 2^{\frac{j}{2}}\omega_n(2^j x-k)$.

An important property of the wavelet transform is the number of vanishing moments that represent the regularity of the wavelet functions and ability of a wavelet transform to capture localized information.

Definition 2.1 *A wavelet $\psi(x)$ is said to have k vanishing moments if*

$$Mom_j(\psi) = \int_{\mathbb{R}} x^j\psi(x)\,dx = 0,\ 0\le j\le k-1,$$

where the given integral is called the j^{th} moment of $\psi(x)$.

The number of vanishing moments is directly related to the regularity of the wavelet. A more regular wavelet has a greater number of vanishing moments.

Recall from [18] that for $f \in L^2(\mathbb{R})$, the wavelet packet expansion of f is

$$f(x) \sim \sum_{n=2^p}^{2^{p+1}-1} \sum_{j,k\in\mathbb{Z}} c_{l,n,k}\ \omega_{l,n,k}(x), \tag{2.8}$$

where $l = j - p,\ p = 0$ if $j < 0$ and $p = 0, 1, 2, \ldots, j$ if $j \geq 0$ and $c_{l,n,k}$ are the wavelet packet coefficients defined as $c_{l,n,k} = \langle f, \omega_{l,n,k}\rangle$.

Suppose $\omega_n, n = 0, 1, 2, \ldots$ be wavelet packets. Then, the orthogonal projections (see [1]) of $L^2(\mathbb{R})$ onto V_j associated with the increasing sequence of subspaces $\{V_j\}_{j\in\mathbb{Z}}$ are given by

$$P_j f(x) = \sum_{m<j} \sum_{n=2^p}^{2^{p+1}-1} \sum_{k\in\mathbb{Z}} \langle f, \omega_{l,n,k}\rangle\ \omega_{l,n,k}(x),\ \text{for}\ f \in L^2(\mathbb{R}), \tag{2.9}$$

where $l = m - p,\ p = 0$ if $m < 0$ and $p = 0, 1, 2, \ldots,\ m$ if $0 \leq m < j$. The projections Q_j^n from $L^2(\mathbb{R})$ onto U_j^n are given by

$$Q_j^n f(x) = \sum_{k\in\mathbb{Z}} \langle f, \omega_{j,n,k}\rangle\ \omega_{j,n,k}(x),\ \text{for}\ f \in L^2(\mathbb{R}). \tag{2.10}$$

To a wavelet packet ω_n, there is associated a natural operator $S_{j,k}^{\sigma} f$ given by

$$(S_{j,k}^{\sigma} f)(x) = \sum_{m<j} \sum_{n=2^p}^{2^{p+1}-1} \sum_{k\in\mathbb{Z}} \langle f, \omega_{l,n,k}\rangle\, \omega_{l,n,k}(x) + (R_{j,k}^{\sigma} f)(x), \tag{2.11}$$

where $l = m - p,\ p = 0$ if $m < 0$ and $p = 0, 1, 2, \ldots, m$ if $0 \leq m < j$, and

$$(R_{j,k}^{\sigma} f)(x) = \sum_{m=1}^{k} \sum_{n=2^p}^{2^{p+1}-1} \langle f, \omega_{l,n,\sigma(m)}\rangle\ \omega_{l,n,\sigma(m)}(x) \tag{2.12}$$

with $l = j - p,\ p = 0$ if $j < 0$ and $p = 0,1,2,\ldots,j$ if $j \geq 0,\ f \in L^2(\mathbb{R})$ and σ is any permutation of $\mathbb{Z}$.

3. Wavelet packet approximation

Daubechies [8] introduced the Daubechies wavelet systems, where vanishing moments were imposed on wavelet function only. In 1991, Coifman proposed orthogonal wavelet systems (with a view to applying them for the algorithms in [2]) (with vanishing moments not only for wavelet functions, but also for scaling functions. Daubechies [10] called these new systems by orthogonal Coifman wavelet systems (or Coiflets) which appeared to be more symmetrical than the Daubechies wavelet systems. She proposed a method to construct these systems with even degrees. Vanishing moments of the wavelet function provides smoothness to the wavelet system, whereas that of the scaling function meliorates the symmetry.

Definition 3.1 *An orthonormal wavelet system with compact support is called an orthogonal Coifman wavelet system of degree N if the vanishing moments of $\phi(x)$ and $\psi(x)$ are both of degree N, i.e.,*

(i) $Mom_0(\phi) = \int_{\mathbb{R}} \phi(x)\, dx = 1,$

(ii) $Mom_p(\phi) = \int_{\mathbb{R}} x^p\, \phi(x)\, dx = 0,\ \text{for}\ p = 1, \ldots, N$ and

(iii) $Mom_p(\psi) = \int_{\mathbb{R}} x^p \, \psi(x) \, dx = 0, \text{ for } p = 0, \ldots, N.$

The choice of equal vanishing moments imparts an optimal wavelet sampling approximation with exponential convergence rate. The Mallat Algorithm tells us how to compute discrete wavelet transform coefficients from one level to the next finer level and without knowing the coefficients at the starting level, there is no meaning to talk about the Mallat Algorithm. This problem was solved by Wells, Jr. and Zhou [34] in 1992 who gave a second order wavelet approximation theorem for square integrable functions by means of a locally finite series of Daubechies wavelets. Sample values of a sufficiently smooth (more precisely, C^2) function can be used as the wavelet transform coefficients and the corresponding wavelet approximation function $S^j(f)$ converges in Sobolev norms of first order to the original function. They proved that

Theorem 3.1 *Let $\phi(x)$ be the scaling function of an orthonormal wavelet system with a finite length scaling vector $\{r_k, \ k \in \mathbb{Z}\}, r_k = 0$ when $|k| > K$ for some positive integer K, $\phi(x) = \sum_{k\in\mathbb{Z}} r_k \, \phi(2x - k)$. We define a constant c by $c := \frac{1}{2}\sum_{k\in\mathbb{Z}} k \, r_k$.*

Assume the function $f \in C^2(\overline{\Omega})$, where Ω is a bounded open set in $\mathbb{R}^2$. Let, for $j \in \mathbb{N}$,

$$S^j f(x,y) := \frac{1}{2^j} \sum_{k,l\in\Lambda} f\left(\frac{k+c}{2^j}, \frac{l+c}{2^j}\right) \phi_{j,k}(x) \, \phi_{j,l}(y), \qquad (x,y) \in \Omega,$$

where the index set $\Lambda = \left\{(k,l) \in \mathbb{Z}^2 : \left(supp\left(\phi_{j,k}(x)\right)\right) \times \left(supp\left(\phi_{j,l}(y)\right)\right) \cap \Omega \neq \emptyset\right\}$, $\phi_{j,i}(x) = 2^{\frac{j}{2}}\phi\left(2^j x - i\right)$. Then

$$\| f(x,y) - S^j f(x,y) \|_{L^2(\Omega)} \leq C \ (1/2^j)^2,$$

and if $\phi(x) \in C^1(\mathbb{R})$,

$$\| f(x,y) - S^j f(x,y) \|_{H^1(\Omega)} \leq C/2^j,$$

where C is a constant depending only on K, the diameter of Ω, and the maximum modulus of the first and second order derivatives of $f(x,y)$ on $\overline{\Omega}$.

The above theorem is also true in $\mathbb{R}^n$ and we now know that the finer the starting level is, the closer the approximation is. Thus we will always take sample values at the finest level whenever possible.

Later, Tian and Wells, Jr. [31, 32] proved wavelet approximation theorem for Coifman wavelet system and found that with the increase in the degree of the vanishing moments, the convergence rate of the approximation increases exponentially. They studied this system with odd degrees. They also found that smoothness of the scaling function plays a significant role in measuring the approximation errors in case of Sobolev spaces. They proved the following:

Theorem 3.2 *For an orthogonal Coifman wavelet system of degree N with the scaling function $\phi(x)$, if $f(x) \in C_0^{N,1}(\mathbb{R})$, define, for $j \in \mathbb{Z}$,*

$$S^j f(x) := 2^{-\frac{j}{2}} \sum_{k\in\mathbb{Z}} f\left(\frac{k}{2^j}\right) \phi_{j,k}(x),$$

where $\phi_{j,k}(x) = 2^{j/2}\phi(2^j x - k)$. *Then*

$$\| f(x) - S^j f(x) \|_{L^2} \leq C\ 2^{-j(N+1)},$$

where C *depends only on* $f(x)$ *and the scaling vector* r_k.

Here we denote by $C_0^{N,1}(\mathbb{R})$ the set of compactly supported functions having derivatives of order $\leq N$ and whose N-th derivative is Lipschitz (thus it contains all compactly supported functions having derivatives of order $\leq N+1$).

Later, they introduced biorthogonal Coifman wavelet systems.

Definition 3.2 *A biorthonormal wavelet system with compact support is called an biorthogonal Coifman wavelet system of degree* N *if the following two conditions are satisfied,*

(i) the vanishing moments of scaling function $\tilde{\phi}(x)$ *and the wavelet function* $\tilde{\psi}(x)$ *are both of degree* N, *i.e.,*

$$Mom_p(\tilde{\phi}) = \int_{\mathbb{R}} x^p\ \tilde{\phi}(x)\ dx = \delta_{0,p},\ \text{for } p = 0,1,\dots,N,$$

$$Mom_p(\tilde{\psi}) = \int_{\mathbb{R}} x^p\ \tilde{\psi}(x)\ dx = 0,\ \text{for } p = 0,1,\dots,N$$

(ii) the vanishing moment of the wavelet function $\psi(x)$ *is of degree* N,

$$Mom_p(\psi) = \int_{\mathbb{R}} x^p\ \psi(x)\ dx = 0,\ \text{for } p = 0,1,\dots,N.$$

Although there is no vanishing moment requirement on analysis scaling function $\phi(x)$, it follows that $\phi(x)$ also has vanishing moments upto degree N, because of the perfect reconstruction condition. Beside the approximation property, biorthogonal Coifman wavelet systems are symmetric, have compact support and growing smoothness with large degrees, and converge to the sinc wavelet system. An attractive feature of biorthgonal Coifman wavelet systems is that all the scaling vectors are dyadic rational, which means we can have a very fast multiplication-free discrete wavelet transform implemented on digital computers. The wavelet approximation theorem for biorthogonal Coifman wavelet systems is given as under:

Theorem 3.3 ([31], [32]) *For a biorthogonal Coifman wavelet system of degree* N *with the analysis scaling function* $\phi(x)$ *and synthesis scaling function* $\tilde{\phi}(x)$, *if* $f(x) \in C_0^{N,1}(\mathbb{R})$, *define, for* $j \in \mathbb{Z}$,

$$f^j(x) := 2^{-\frac{j}{2}} \sum_{k\in\mathbb{Z}} f\left(\frac{k}{2^j}\right) \tilde{\phi}_{j,k}(x),$$

where $\tilde{\phi}_{j,k}(x) = 2^{j/2}\tilde{\phi}(2^j x - k)$. *Then*

$$\| f(x) - f^j(x) \|_{L^2} \leq C\ 2^{-j(N+1)},$$

where C depends only on $f(x)$ and $\tilde{\phi}$. If in addition $\tilde{\phi} \in C^n(\mathbb{R})$, where $n \in \mathbb{Z},\ 0 \leq n \leq N$, then

$$\| f(x) - f^j(x) \|_{H^n} \leq C\ 2^{-j(N+1-n)},$$

where C depends only on $f(x)$ and $\tilde{\phi}$.

Motivated with the above ideas, Khanna et al. [19] introduced the orthogonal Coifman wavelet packet (in short OCWP) systems followed by biorthogonal Coifman wavelet packet (in short BCWP) systems with the vanishing moments distributed equally between the scaling function and the wavelet packet functions $\omega_n, n \neq 0$ and thereby give wavelet packet approximation theorem. These systems have good approximation properties with exponential decay. The wavelet packet approximation theorem illustrates the different roles of the vanishing moments of the wavelet packet functions ω_n.

Definition 3.3 *An orthogonal wavelet packet system with compact support is called an orthogonal Coifman wavelet packet system of degree M if the vanishing moments of the scaling function $\omega_0(x)$ and the wavelet packets $\omega_n(x),\ n \neq 0$ are both of degree M, i.e.,*

(i) $Mom_0(\omega_0) = \int_{\mathbb{R}} \omega_0(x)\, dx = 1,$
(ii) $Mom_p(\omega_0) = \int_{\mathbb{R}} x^p\, \omega_0(x)\, dx = 0,$ for $p = 1, \ldots, M$ and
(iii) $Mom_p(\omega_n) = \int_{\mathbb{R}} x^p\, \omega_n(x)\, dx = 0,$ for $p = 0, \ldots, M,\ n \neq 0.$

Theorem 3.4 ([19]) (*Wavelet Packet Approximation Theorem*)

Let $f \in C^M(\mathbb{R})$ be a function with compact support and the M^{th} derivative of f is Lipschitz, then for an orthogonal Coifman wavelet packet system of degree M with the scaling function $\omega_0(x)$ and $(x-k)\ \omega_n(x) \in L^1(\mathbb{R}),\ f(x)$ can be approximated by

$$f^j(x) = 2^{\frac{-j}{2}} \sum_{k \in \mathbb{Z}} f\left(\frac{k}{2^j}\right)\ \omega_{j,0,k}(x),$$

where $\omega_{j,n,k}(x) = 2^{\frac{j}{2}}\, \omega_n\left(2^j x - k\right),\ j, k \in \mathbb{Z},\ n \in \mathbb{N}$.

Then, this approximation satisfies the following estimate given by

$$\| f(x) - f^j(x) \|_2 \leq C\ 2^{-j(M+1)},$$

where C depends only on $f(x)$ and $\omega_{j,0,k}$.

Biorthogonal Coifman wavelet packet system of degree M is defined in [19] as follows:

Definition 3.4 *A biorthogonal wavelet packet system with compact support is called a biorthogonal Coifman wavelet packet system of degree M if the following two conditions are satisfied,*

(i) the vanishing moments of the scaling function $\widetilde{\omega}_0(x)$ and the wavelet packets $\widetilde{\omega}_n(x), n \neq 0$ are both of degree M, i.e.

$$Mom_0(\widetilde{\omega}_0) = \int_{\mathbb{R}} \widetilde{\omega}_0(x)\, dx = 1,\ Mom_p(\widetilde{\omega}_0) = \int_{\mathbb{R}} x^p\, \widetilde{\omega}_0(x)\, dx = 0,$$

for $p = 1, \ldots, M$ and

$$Mom_p(\widetilde{\omega}_n) = \int_{\mathbb{R}} x^p \, \widetilde{\omega}_n(x)\, dx = 0, \text{ for } p = 0, \ldots, M, \; n \neq 0.$$

(ii) the vanishing moments of scaling function $\omega_0(x)$ and the wavelet packets $\omega_n(x)$, $n \neq 0$ are of degree M, i.e.,

$$Mom_0(\omega_0) = \int_{\mathbb{R}} \omega_0(x)dx = 1, \qquad Mom_p(\omega_0) = \int_{\mathbb{R}} x^p \, \omega_0(x)dx = 0,$$

for $p = 1, \ldots, M$ and

$$Mom_p(\omega_n) = \int_{\mathbb{R}} x^p \;\; \omega_n(x)\, dx = 0,$$

for $p = 0, \ldots, M, \; n \neq 0$.

The following result gives the wavelet packet approximation theorem for biorthogonal Coifman wavelet packet system.

Theorem 3.5 ([19]) *Let $f \in C^M(\mathbb{R})$ be a function with compact support and the M^{th} derivative of f is lipschitz, then for a biorthogonal Coifman wavelet packet system of degree M with the analysis scaling function $\omega_0(x)$ and the synthesis scaling function $\widetilde{\omega}_0(x)$, and*

$(x - k)\, \widetilde{\omega}_n(x) \in L^1(\mathbb{R})$ *can be approximated by*

$$f^j(x) = 2^{\frac{-j}{2}} \sum_{k\in\mathbb{Z}} f\left(\frac{k}{2^j}\right) \widetilde{\omega}_{j,0,k}(x),$$

where $\widetilde{\omega}_{j,n,k}(x) = 2^{\frac{j}{2}} \widetilde{\omega}_n\left(2^j x - k\right)$, $j, k \in \mathbb{Z}$ and $n \in \mathbb{N}$. Then, this approximation satisfies the following estimate given by $\| f(x) - f^j(x) \|_2 \leq C\, 2^{-j(M+1)}$, where C depends only on $f(x)$ and $\widetilde{\omega}_{j,0,k}$.

Note that sometimes the L^2 norm estimate is not sufficient for smooth functions, therefore we need some other estimate like H^r norm which can measure difference of the (weak) derivatives. In context of H^r norm, the wavelet approximation theorem is given as under:

Theorem 3.6 ([31, [32]) *Suppose $\phi(x)$ is an $L^2(\mathbb{R})$ solution of the two-scale difference equation* (2.1)*, where $\{r_k\}$ is a finite length sequence satisfying the vanishing moment conditions upto degree N, i.e.,*

$$\sum_{k\in\mathbb{Z}} (2k)^p \, r_{2k} = \sum_{k\in\mathbb{Z}} (2k+1)^p \, r_{2k+1} = 0, \; for \; p = 1, \ldots, N, \tag{3.1}$$

$$\sum_{k\in\mathbb{Z}} r_{2k} = \sum_{k\in\mathbb{Z}} r_{2k+1} = 1. \tag{3.2}$$

For a function $f(x) \in C_0^{N,1}(\mathbb{R})$, define

$$S^j(f)(x) := 2^{-j/2} \sum_{k\in\mathbb{Z}} f\left(\frac{k}{2^j}\right) \phi_{j,k}(x), \tag{3.3}$$

where $\phi_{j,k}(x) = 2^{j/2}\, \phi\left(2^j x - k\right)$. If in addition $\phi(x) \in C^r(\mathbb{R})$, where $r \in \mathbb{Z}$, $0 \leq r \leq N$, then

$$\| f(x) - S^j(f)(x) \|_{H^r} \leq C\, 2^{-j(N+1-r)},$$

where H^r is the Sobolev space of L^2 functions with weak derivatives of order $\leq r$, and C depends only on f and the sequence $\{r_k\}$.

Khanna and Kaushik in [20] state and prove the analogous version of above theorem with a different approach. Write

$$L^2(\mathbb{R}) = V_0 \oplus \bigoplus_{j=0}^{\infty} W_j.$$

Then, using the decomposition trick [16], we have

$$L^2(\mathbb{R}) = V_0 \oplus \bigoplus_{j=0}^{\infty} \bigoplus_{n=2^j}^{2^{j+1}-1} U_0^n.$$

Therefore, the wavelet packet expansion for $f \in L^2(\mathbb{R})$ is given by

$$f(x) = \sum_{k\in\mathbb{Z}} c_{J_0,k}\, \omega_{J_0,0,k}(x) + \sum_{j=J_0}^{\infty} \sum_{n=2^j}^{2^{j+1}-1} \sum_{k=0}^{2^j-1} d_{0,k}^n\, \omega_{0,n,k}(x)$$

for some $J_0 > 0$ and the wavelet packet orthogonal projection of $f(x)$ at level J is given by

$$(P_J f)(x) = \sum_{k\in\mathbb{Z}} c_{J_0,k}\, \omega_{J_0,0,k}(x) + \sum_{j=J_0}^{J-1} \sum_{n=2^j}^{2^{j+1}-1} \sum_{k\in\mathbb{Z}} d_{0,k}^n\, \omega_{0,n,k}(x)$$

for $J > J_0 \geq 0$. The wavelet packet orthogonal projection is exactly the orthogonal projection of $f(x)$ onto the J^{th} subspace V_J in the multiresolution analysis of the orthonormal wavelet packet system.

In this context, the new version of wavelet packet approximation theorem for H^r type norm is given below.

Theorem 3.7 ([20]) *Let $f \in C^M(\mathbb{R})$ be a function with compact support, the M^{th} derivative of f is Lipschitz, and for an orthogonal Coifman wavelet packet system $\omega_n \in L^2(\mathbb{R})$ of degree M, that satisfy*

(i) $\omega_n(x) \in C^r(\mathbb{R})$, *where* $n \in \mathbb{N}_0$ *and* $r \in \mathbb{Z}$ *for* $r = 0, 1, 2, \ldots, M$,
(ii) $|\omega_n^{(r)}(t)| = O\big((2+t^2)^{-Mj}\big)$ *for* $r = 0, 1, 2, \ldots, M$, *where* $n = 2^j, \ldots, 2^{j+1}-1$ *and* $j \geq 0$,
(iii) $\int_{\mathbb{R}} x^p\, \omega_n^{(r)}(x)\, dx = 0$, *for* $p = 0, 1, \ldots, M-1$, *where* $r = 0, 1, 2, \ldots, M$,
(iv) $\omega_{J,0,k}^{(r)}(x) \in L^2(\mathbb{R})$, *for* $r = 1, 2, \ldots, M$.

Then $f(x)$ can be approximated by sampling approximation

$$S_J(x) = 2^{\frac{-J}{2}} \sum_{k\in\mathbb{Z}} f\left(\frac{k}{2^J}\right)\, \omega_{J,0,k}(x),$$

where $\omega_{j,n,k}(x) = 2^{\frac{j}{2}}\,\omega_n(2^j x - k),\ j,k \in \mathbb{Z}, n \in \mathbb{N}_0$. *Then, this approximation satisfies the following estimate*

$$\| f(x) - S_J(x) \|_{H^r} \leq C\ 2^{-J(M+1)},$$

where H^r *is the Sobolev space of* $L^2(\mathbb{R})$ *functions with weak derivatives of order* $\leq r$, *and* C *depends only on* f *and* ω_0.

References

[1] K. Ahmad, R. Kumar, Pointwise convergence of wavelet packet series, Atti Sem. Mat. Fis. Univ. Modena. **48**(2000), 107-120.

[2] G. Beylkin, R. R. Coifman, V. Rokhlin, Fast wavelet transforms and numerical algorithms I, Comm Pure Appl Math. **44**(1991), no. 2, 141-183.

[3] C. Chui, C. Li, Non-orthogonal wavelet packets, SIAM J. Math. Anal. **24**(1993), no. 3, 712-738.

[4] A. Cohen, I. Daubechies, On the instability of arbitrary biorthogonal wavelet packets, SIAM J. Math. Anal. **24**(1993), no. 5, 1340-1354.

[5] R. R. Coifman, Y. Meyer, S. Quake, M. V. Wickerhauser, Signal processing and compression with wavelet packets, Techn. Report. Yale Univ; 1990.

[6] R. R. Coifman, Y. Meyer, V. Wickerhauser, Size properties of wavelet-packets, Wavelets and their Applications, Jones and Bartlett, Boston, MA, 1992, pp. 453–470.

[7] R. R. Coifman, Y. Meyer, V. Wickerhauser, Wavelet analysis and signal processing, Wavelets and their Applications, Jones and Bartlett, Boston, MA, 1992, pp. 153–178.

[8] I. Daubechies, Orthonormal bases of compactly supported wavelets, Comm. Pure Appl. Math. **41**(1988), no. 7, 909–996.

[9] I. Daubechies, Orthonormal bases of compactly supported wavelets II, Variations on a theme, SIAM J. Math. Anal. **24**(1993), no. 2, 499-519.

[10] I. Daubechies, Ten lectures on wavelets, Society for Industrial and Applied Mathematics (SIAM), Philadelphia, PA, 1992.

[11] J. Fourier, Théorie analytique de la chaleur, Éditions Jacques Gabay, Paris, 1988, Reprint of the 1822 original.

[12] D. Gabor, Theory of communication, J. Inst. Electr. Eng. **93** (1946), 429–457.

[13] A. Grossmann, J. Morlet, Decomposition of Hardy functions into square integrable wavelets of constant shape, SIAM J. Math. Anal. **15** (1984), no. 4, 723–736.

[14] A. Grossmann, J. Morlet, T. Paul, Transforms associated to square integrable group representations. I. General results, J. Math. Phys. **26** (1985), no. 10, 2473–2479.

[15] A. Grossmann, J. Morlet, T. Paul, Transforms associated to square integrable group representations. II. Examples, Ann. Inst. H. Poincaré **45** (1986), no. 3, 293–309.

[16] E. Hernández, G. Weiss, A first course on wavelets, CRC Press, 1996.

[17] S. Jaffard, Y. Meyer, R. D. Ryan, Wavelets, Society for Industrial and Applied Mathematics (SIAM), Philadelphia, PA, 2001.

[18] A. M. Jarrah, R. Kumar, K. Ahmad, Certain characterizations of wavelet packets, Atti Sem. Mat. Fis. Univ. Modena. **53**(2005), 147-164.

[19] N. Khanna, V. Kumar, S. K. Kaushik, Wavelet packet approximation, Integ. Transf. Special Funct. **27**(2016), no. 9, 698-714.

[20] N. Khanna, S. K. Kaushik, Wavelet packet approximation theorem for H^r type norm, Integ. Transf. Special Funct. **30**(2019), no. 3, 231-239.

[21] J. E. Littlewood, R. E. A. C. Paley, Theorems on Fourier series and power series, J. London Math. Soc. **s1-6**(1931), no. 3, 230.

[22] D. Mackenzie, Wavelets: Seeing the Forest and the Trees, National Academy of Sciences,

2001.
[23] S. Mallat, A wavelet tour of signal processing, Third ed., Academic Press, 2009.
[24] S. G. Mallat, Multiresolution approximations and wavelet orthonormal bases of $L^2(\mathbb{R})$, Trans. Amer. Math. Soc. **315** (1989), no. 1, 69–87.
[25] S. G. Mallat, A theory for multiresolution signal decomposition: the wavelet representation, IEEE Trans. Pattern Anal. Mach. Intell. **11** (1989), no. 7, 674–693.
[26] Y. Meyer, Orthonormal wavelets, Wavelets (Marseille, 1987), Inverse Probl. Theoret. Imaging, Springer, Berlin, 1989, pp. 21–37.
[27] Y. Meyer, R. D. Ryan, Wavelets: Algorithms & Applications, Society for Industrial and Applied Mathematics (SIAM), Philadelphia, PA, 1993.
[28] N. Ricker, The form and laws of propagation of seismic wavelets, Geophysics **18** (1953), no. 1, 10–40.
[29] E. M. Stein, G. Weiss, Introduction to Fourier Analysis on Euclidean spaces, Princeton University Press, Princeton, New Jersey, 1971.
[30] J. O. Strömberg, A modified Franklin system and higher-order spline systems on $\mathbb{R}^n$ as unconditional bases for Hardy spaces, Conference on harmonic analysis in honor of Antoni Zygmund, Vol. I, II (Chicago, Ill., 1981), Wadsworth Math. Ser., Wadsworth, Belmont, CA, 1983, pp. 475–494.
[31] J. Tian, R. O. Jr. Wells, Vanishing moments and wavelet approximation, Tech. Rep. CML TR95-01, Computat. Math. Lab., Rice Univ., Houston, TX, Jan. 1995.
[32] J. Tian, R. O. Jr. Wells, A remark of vanishing moments, In Proc. 30th Asilomar Conf. on Signals, Systems, and Computers, Pacific Grove, CA, pp. 983–987, 1996.
[33] D. F. Walnut, An introduction to wavelet analysis, Boston, MA: Birkhäuser, 2002.
[34] R. O. Wells, X. Zhou, Wavelet interpolation and approximate solutions of elliptic partial differential equations. In *Noncompact Lie Groups*, Wilson R, Tanner EA. eds. volume 429, 349-366. Proceedings of NATO Advanced Research Workshop. Kluwer, Boston, 1994.

Karnatak University

Journal of Science

ISSN: 0075-5168

Static and dynamic characteristics of MHD porous parabolic slider bearing lubricated with couple stress fluid

N. B. Naduvinamani

Siddharama Patil

Biradar Kashinath

N. B. Naduvinamani, Siddharama Patil, Biradar Kashinath, “Static and dynamic characteristics of MHD porous parabolic slider bearing lubricated with couple stress fluid” Karnatak University Journal of Science 51, 108-122 (2020).

Static and dynamic characteristics of MHD porous parabolic slider bearing lubricated with couple stress fluid

N. B. Naduvinamani[a*], Siddharama Patil[b], Biradar Kashinath[c]
[a]Department of Mathematics , Gulbarga Univesity,Kalaburagi-585106, Karnataka, India
[b]Department of Science, Government Polytechnic, Shorapur-585224, India
[c]Department of Mathematics, Government First Grade College, Sedam-585222, India
***Corresponding author:** naduvinamaninb@yahoo.co.in

Abstract

This paper deals with the effect of permeability on static and dynamic characteristics of slider bearing with parabolic film shape lubricated with couple stress fluid in the presence of applied transverse magnetic field. Based on the Stokes couple stress theory and Darcy law, the modified Reynolds equation governing fluid film pressure for slider bearings is derived. The closed form expressions for steady film pressure, steady load carrying capacity, dynamic stiffness and damping coefficients are obtained. The bearing characteristics are evaluated for various values of couple stress parameter, Hartmann number and permeability parameter. It is observed that increase in the values of couple stress parameter and Hartmann number enhances the bearing characteristics whereas the increasing values of permeability parameter reduce their values as compared to the solid case. The results obtained in the design example are useful for the design engineers in the bearing design and selection of proper lubricant.
Keywords: Couple stress; MHD; Reynolds Equation; Dynamic stiffness; Dynamic Damping
Article history: Received: 2 July 2020**;** Revised: 08 August 2020; Accepted: 25 August 2020.

1. Introduction

In all classical theories, film region of the bearings are lubricated with Newtonian fluid but researchers realized that the use of such fluids is not practically useful in the designing of bearings. To overcome these problems, investigators diverted towards new lubricants obtained from Newtonian fluid with small amount of additives like long chained organic compounds. Many theories have been proposed to describe these new lubricants and among these Stokes [1] couple stress theory was simplest one. This theory allows for polar effects such as the presence of body couples and couple stresses. Based on the Stokes theory, many researchers studied the effect of couple stresses on bearing characteristics such as slider bearing by Ramanaiah and Priti [2], short bearings by Chandan [3] and parabolic slider bearing by Oladeinde and Akpobi [4]. They concluded that the presence of couple stresses in fluid increases the load carrying capacity and reduces the coefficient of friction.

Magnetohydrodynamics (MHD) is the study of the interaction between conducting fluid and the magnetic field. Agarwal [5] studied the effect of MHD in lubrication of thrust bearing and concluded that applied magnetic field increases load carrying capacity and decreases the frictional force. The MHD effect on characteristics of infinite journal bearing was studied by Kuzma [6] and that of finite journal bearing studied by Malik and Singh [7]. They concluded that the applied magnetic field enhances the load carrying capacity of the bearing. Due to enhanced results obtained in individual effects of MHD and couple stresses researchers interest diverted towards their combined effect on bearing performance. Several authors studied the combined effect of MHD and couple stresses such as load-bearing capacity

of slider bearing by Das [8], parallel rectangular plates by Lin *et al.* [9], different finite plates by Fathima *et al.* [10] and comparative study of slider bearing by Siddharam *et al.*[11]. These studies predicted that the couple stress and presence of magnetic field provide an increase in the load carrying capacity of the bearing.

In the design of bearings, their static and dynamic characteristics play an important role as the static characteristics provide basic reference for bearing design and dynamic characteristic predict stability behaviour of bearing. The dynamic characteristics of long journal bearing with couple stress fluid as lubricant was studied by Liao *et al.*[12] and that of composite slider bearing studied by Lin and Chou [13]. They concluded that the couple stress fluid enhances the dynamic stiffness and damping coefficients as compared to Newtonian fluid. Naduvinamani *et al.*[14] studied the combined effect of MHD and couple stresses on static and dynamic characteristics of slider bearings and concluded that the presence of applied magnetic field and couple stresses provide higher values for bearing characteristics.

Porous bearings are the low cast bearings with simple structure and they are widely used in industry. Supplying of exterior oil is not required and it is one of the advantages of these bearings. The performance of these bearings can be described by a permeability parameter. Murthi [15] studied the porous slider bearing with Newtonian fluid as lubricant and concluded that, the load carrying capacity decreases and friction increases with increase in the permeability parameter. Bujurke *et al.* [16] studied the porous slider bearing with non-Newtonian fluid, Naduvinamani *et al.* [17] studied the porous journal bearing lubricated with couple stress fluid Naduvinamani and Siddangouda [18] studied the porous Rayleigh step bearing lubricated with couple stress fluid. These studies shown that, the load carrying capacity increases with the presence of couple stresses whereas it decreases with the increasing value of permeability parameter.

In the present paper, the combined effects of MHD and couple stress on the static and dynamic characteristics of porous parabolic slider bearings is analysed. For the validity of present work the results obtained are compared with that of the solid case analyzed by Naduvinamani *et al.* [14].

2. Mathematical Formulation

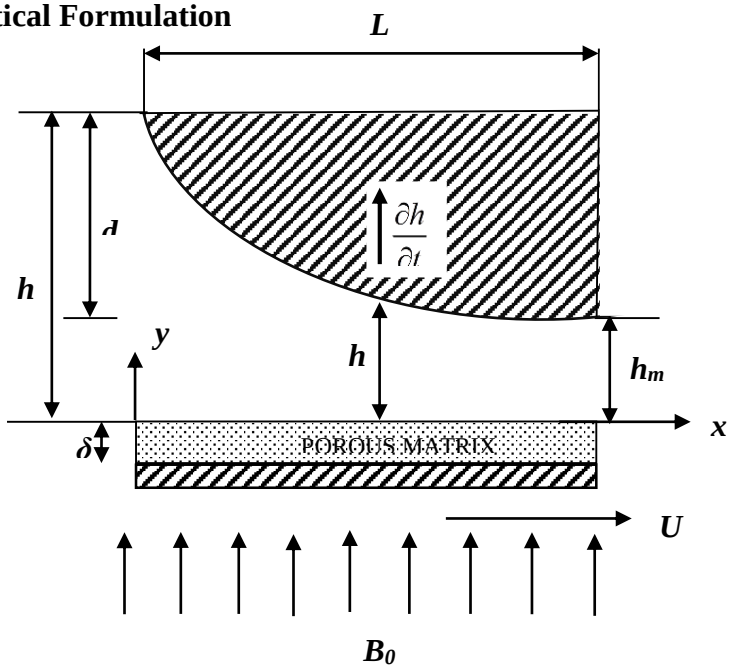

Figure 1. Geometry of porous parabolic slider bearing

The physical geometry of porous parabolic slider bearing of length *L* is shown in Fig. 1. Fluid film is lubricated with conducting couple stress fluid and it is assumed to be thin. The upper surface of the bearing has squeezing effect ($\partial h/\partial t$) whereas its lower surface is moving in the *x* direction with velocity *U*. Uniform transverse magnetic field is applied in perpendicular direction of the bearing and, it is assumed that, induced magnetic field is small as compared to that of applied magnetic field. The body couples and body forces are assumed to be negligible except Lorentz force and the bearing surfaces are assumed as perfect insulators with no external circuit in the fluid. Under these assumptions, the governing equations for MHD couple stress fluid derived by Das [8] reduces to

$$\mu\frac{\partial^2 u}{\partial y^2}-\eta\frac{\partial^4 u}{\partial y^4}-\sigma {B_0}^2 u=\frac{\partial p}{\partial x}+\sigma E_z B_0 \tag{1}$$

$$\frac{\partial p}{\partial y}=0, \tag{2}$$

$$\frac{\partial u}{\partial x}+\frac{\partial v}{\partial y}=0, \tag{3}$$

$$\int_{y=0}^{h}\left(E_z+B_0 u\right)dy=0 \tag{4}$$

Where μ is the lubricant viscosity; η is material constant responsible for couple stresses; σ is the conductivity of the lubricant; *p* is the film pressure; *u*, *v* are the velocity components in the *x* and *y* directions respectively; E_z is the induced electric field in the *z* – direction and B_0 is the applied magnetic field.

The continuity equation for the flow of conducting couple stress fluid in the porous matrix in the presence of applied magnetic field is

$$\frac{\partial u^*}{\partial x}+\frac{\partial v^*}{\partial y}=0 \tag{5}$$

where u^* and v^* are the velocity components in *x* and *y* directions respectively are governed by the modified Darcy's law given by

$$u^*=-\frac{k}{\mu\left(1-\beta+\dfrac{k\delta {B_0}^2}{\mu m}\right)}\left(\frac{\partial p^*}{\partial x}+\sigma E_z B_0\right), \tag{6}$$

$$v^*=-\frac{k}{\mu(1-\beta)}\frac{\partial p^*}{\partial y} \tag{7}$$

In which p^* is pressure in the porous region, *k* the permeability parameter, δ the porous layer thickness and β is the ratio of microstructure size to pore size $(=(\eta/\mu)/k)$

The relevant boundary conditions for velocity components are

$$\text{At } y=h: \qquad u=0, \qquad \frac{\partial^2 u}{\partial y^2}=0, \qquad v=\frac{\partial h}{\partial t}; \tag{8}$$

$$\text{At } y=0: \qquad u=U, \qquad \frac{\partial^2 u}{\partial y^2}=0, \qquad v=v^*. \tag{9}$$

3. Solution of the problem

The solution of equation (1) subject to the relevant boundary conditions given in equations (8) and (9) under the condition (4) is obtained as

$$u = -\frac{U}{2} f_1 - \frac{h_{ms}^{\,2} h}{2l\mu M^2} \frac{\partial p}{\partial x} f_2 \tag{10}$$

Where,

$$f_1 = f_{11} - f_{12}, \qquad f_2 = f_{13} - f_{14} \qquad \text{for } \frac{4M^2 l^2}{h_{ms}^{\,2}} < 1$$

(11a)

$$f_1 = f_{21} - f_{22}, \qquad f_2 = f_{23} - f_{24} \qquad \text{for } \frac{4M^2 l^2}{h_{ms}^{\,2}} = 1$$

(11b)

$$f_1 = f_{31} - f_{32}, \qquad f_2 = f_{33} - f_{34} \qquad \text{for } \frac{4M^2 l^2}{h_{ms}^{\,2}} > 1 \tag{11c}$$

where $l = (\eta/\mu)^{1/2}$ is the couple stress parameter, $M = B_0 h_{ms} (\sigma/\mu)^{1/2}$ is the Hartmann number and h_{ms} is the steady state reference minimum film thickness. The relations in above expressions are provided in **Appendix-A**.

The boundary conditions for the pressure p^* in the porous region are given by

$$\left.\frac{\partial p^*}{\partial y}\right|_{y=-\delta} = 0 \quad \text{(Solid Clocking)} \tag{12}$$

$$p^*(x,0) = p(x,0) \quad \text{(Continuity of pressure)} \tag{13}$$

Using the velocity components u^* and v^* in equation (5) and integrating w.r.t y over the porous layer thickness δ with the use of boundary conditions (12) and (13), we get

$$v^*\big|_{y=0} = \frac{k\delta}{\mu C^2} \frac{\partial}{\partial x}\left(\frac{\partial p^*}{\partial x} + \sigma E_z B_0\right) \tag{14}$$

Where

$$C = \left(1 - \beta + \frac{k\sigma B_0^{\,2}}{\mu m}\right)^{1/2}$$

With the use of relevant boundary conditions given in (8), (9) and the expression for u given in (10), the integration of continuity equation (3) over the film thickness gives the modified Reynolds equation in the form

$$\frac{\partial}{\partial x}\left\{\zeta(h,l,M)\frac{\partial p}{\partial x}\right\} = 6\mu U \frac{\partial h}{\partial x} + 12\mu \frac{\partial h}{\partial t} \tag{15}$$

Where

$$\zeta(h,l,M)=\begin{cases}\dfrac{6h_{ms}{}^2h^2}{lM^2}\left\{\dfrac{a^2-b^2}{\dfrac{a^2}{b}\tanh\left(\dfrac{bh}{2l}\right)-\dfrac{b^2}{a}\tanh\left(\dfrac{ah}{2l}\right)}\left(1+\dfrac{k\delta M^2}{h_{ms}^2hC^2}\right)-\dfrac{2l}{h}\right\} & \text{for } \dfrac{4M^2l^2}{h_{ms}{}^2}<1\\ \dfrac{6h_{ms}{}^2h^2}{\mu lM^2}\left\{\dfrac{2\cosh\left(\dfrac{h}{\sqrt{2}l}\right)+1}{3\sqrt{2}\sinh\left(\dfrac{h}{\sqrt{2}l}\right)-\dfrac{h}{l}}\left(1+\dfrac{k\delta M^2}{h_{ms}^2hC^2}\right)-\dfrac{2l}{h}\right\} & \text{for } \dfrac{4M^2l^2}{h_{ms}{}^2}=1\\ \dfrac{6h_{ms}{}^2h^2}{\mu lM^2}\left\{\dfrac{M\left(\cos b_1h+\cosh a_1h\right)}{h_{ms}\left(a_2\sin b_1h+b_2\sinh a_1h\right)}\left(1+\dfrac{k\delta M^2}{h_{ms}^2hC^2}\right)-\dfrac{2l}{h}\right\} & \text{for } \dfrac{4M^2l^2}{h_{ms}{}^2}>1\end{cases}$$

$$a=\left\{\left(1+\sqrt{1-(4l^2M^2/h_{ms}^2)}\right)\Big/2\right\}^{1/2},\quad b=\left\{\left(1-\sqrt{1-(4l^2M^2/h_{ms}^2)}\right)\Big/2\right\}^{1/2}$$

$$a_1=\sqrt{M/lh_{ms}}\cos(\varphi/2),\quad b_1=\sqrt{M/lh_{ms}}\sin(\varphi/2),\quad \varphi=\tan^{-1}\left(\sqrt{(4l^2M^2/h_{ms}{}^2)-1}\right)$$

$$a_2=\left(b_1-a_1\cot\varphi\right),\quad b_2=\left(a_1+b_1\cot\varphi\right)$$

The modified Reynolds type equation (15) is applicable to porous slider bearings lubricated with couple stress fluid in the presence of transverse magnetic field with the squeezing effect. The mathematical function for the fluid film thickness of parabolic slider bearing is given by

$$h(x,t)=h_m(t)+d\left(1-\frac{2x}{L}+\frac{x^2}{L^2}\right) \tag{16}$$

where $h_m(t)$ is the minimum film thickness, d is the difference between inlet and outlet film thicknesses, L is the length of the bearing.

Defining the non-dimensional quantities,

$$\bar{x}=\frac{x}{L},\ \bar{p}=\frac{ph_{ms}^2}{\mu UL},\ \bar{h}_m=\frac{h_m(t)}{h_{ms}},\ \bar{h}=\frac{h}{h_{ms}},\ \bar{t}=\frac{Ut}{L},\ \ \bar{l}=\frac{2l}{h_{ms}}\ ,\ \bar{\delta}=\frac{\delta}{h_{ms}},\ \bar{d}=\frac{d}{h_{ms}},\ \psi=\frac{k\delta}{h_{ms}^3}$$

and using these in equation (15), the non-dimensional Reynolds type equation is obtained as

$$\frac{\partial}{\partial\bar{x}}\left[\bar{\zeta}\left(\bar{h},\bar{l},M,\psi\right)\frac{\partial\bar{p}}{\partial\bar{x}}\right]=6\frac{\partial\bar{h}}{\partial\bar{x}}+12\frac{\partial\bar{h}}{\partial\bar{t}}, \tag{17}$$

where

$$\bar{\zeta}\left(\bar{h},\bar{l},M,\psi\right)=\begin{cases}\dfrac{12\bar{h}^2}{\bar{l}M^2}\left\{\dfrac{\bar{a}^2-\bar{b}^2}{\dfrac{\bar{a}^2}{\bar{b}}\tanh\left(\dfrac{\bar{b}\bar{h}}{\bar{l}}\right)-\dfrac{\bar{b}^2}{\bar{a}}\tanh\left(\dfrac{\bar{a}\bar{h}}{\bar{l}}\right)}\left(1+\dfrac{\psi M^2}{\bar{h}C^2}\right)-\dfrac{\bar{l}}{\bar{h}}\right\} & \text{for } M^2\bar{l}^2<1\\ \dfrac{12\bar{h}^2}{\bar{l}M^2}\left\{\dfrac{1+\cosh\left(\dfrac{\sqrt{2}\bar{h}}{\bar{l}}\right)}{\dfrac{3}{\sqrt{2}}\sinh\left(\dfrac{\sqrt{2}\bar{h}}{\bar{l}}\right)-\dfrac{\bar{h}}{\bar{l}}}\left(1+\dfrac{\psi M^2}{\bar{h}C^2}\right)-\dfrac{\bar{l}}{\bar{h}}\right\} & \text{for } M^2\bar{l}^2=1\\ \dfrac{12\bar{h}^2}{\bar{l}M^2}\left\{\dfrac{M\left(\cos\bar{b}_1\bar{h}+\cosh\bar{a}_1\bar{h}\right)}{\bar{a}_2\sin\bar{b}_1\bar{h}+\bar{b}_2\sinh\bar{a}_1\bar{h}}\left(1+\dfrac{\psi M^2}{\bar{h}C^2}\right)-\dfrac{\bar{l}}{\bar{h}}\right\} & \text{for } M^2\bar{l}^2>1\end{cases}$$

$$\bar{a} = \left\{\left(1+\left(1-\bar{l}^{\,2}M^{2}\right)^{1/2}\right)\Big/2\right\}^{1/2}, \quad \bar{b} = \left\{\left(1-\left(1-\bar{l}^{\,2}M^{2}\right)^{1/2}\right)\Big/2\right\}^{1/2},$$

$$\bar{a}_1 = \sqrt{2M/\bar{l}}\cos(\bar{\varphi}/2), \quad \bar{b}_1 = \sqrt{2M/\bar{l}}\sin(\bar{\varphi}/2), \quad \bar{\varphi} = \tan^{-1}\left(\sqrt{\bar{l}^{\,2}M^{2}-1}\right)$$

$$\bar{a}_2 = \left(\bar{b}_1 - \bar{a}_1\cot\bar{\varphi}\right), \quad \bar{b}_2 = \left(\bar{a}_1 + \bar{b}_1\cot\bar{\varphi}\right)$$

$$\bar{h}(\bar{x},\bar{t}) = \bar{h}_m(\bar{t}) + \bar{d}\left(1-2\bar{x}+\bar{x}^{2}\right)$$

The pressure boundary conditions are

$$\bar{p} = 0 \quad \text{at} \quad \bar{x} = 0 \text{ and } \bar{x} = 1 \tag{18}$$

Integrating the equation (17) with respect to $\bar{x}$ and using the pressure boundary condition given in (18), the expression for non-dimensional form of fluid film pressure is obtained in the form

$$\bar{p} = 6g_A(\bar{x},\bar{h}_m) + 12\bar{V}g_B(\bar{x},\bar{h}_m) + \xi_1\left(\bar{h}_m,\bar{V}\right)g_C(\bar{x},\bar{h}_m), \tag{19}$$

where $\bar{V}\left(=d\bar{h}_m/d\bar{t}\right)$ represents squeezing velocity in the non-dimensional form,

$$g_A(\bar{x},\bar{h}_m) = \int_{\bar{x}=0}^{\bar{x}} \frac{\bar{d}\left(1-2\bar{x}+\bar{x}^{2}\right)}{\bar{\zeta}(\bar{h},\bar{l},M,\psi)}d\bar{x}, \tag{20}$$

$$g_B(\bar{x},\bar{h}_m) = \int_{\bar{x}=0}^{\bar{x}} \frac{\bar{x}}{\bar{\zeta}(\bar{h},\bar{l},M,\psi)}d\bar{x}, \tag{21}$$

$$g_C(\bar{x},\bar{h}_m) = \int_{\bar{x}=0}^{\bar{x}} \frac{1}{\bar{\zeta}(\bar{h},\bar{l},M,\psi)}d\bar{x}, \tag{22}$$

$$\xi_1\left(\bar{h}_m,\bar{V}\right) = \frac{-1}{g_{C1}(\bar{h}_m)}\left[6g_{A1}(\bar{h}_m) + 12\bar{V}g_{B1}(\bar{h}_m)\right], \tag{23}$$

where $g_{A1}(\bar{h}_m)$, $g_{B1}(\bar{h}_m)$ and $g_{C1}(\bar{h}_m)$ are given as follows

$$g_{A1}(\bar{h}_m) = \int_{\bar{x}=0}^{1} \frac{\bar{d}\left(1-2\bar{x}+\bar{x}^{2}\right)}{\bar{\zeta}(\bar{h},\bar{l},M,\psi)}d\bar{x}, \tag{24}$$

$$g_{B1}(\bar{h}_m) = \int_{\bar{x}=0}^{1} \frac{\bar{x}}{\bar{\zeta}(\bar{h},\bar{l},M,\psi)}d\bar{x}, \tag{25}$$

$$g_{C1}(\bar{h}_m) = \int_{\bar{x}=0}^{1} \frac{1}{\bar{\zeta}(\bar{h},\bar{l},M,\psi)}d\bar{x}. \tag{26}$$

The non-dimensional film force is obtained by integrating the non-dimensional film pressure over the film region as

$$\bar{F} = \frac{Fh_{ms}^{\;2}}{\mu UL^{2}B_0} = \int_{\bar{x}=0}^{1} \bar{p}\,d\bar{x} \tag{27}$$

Use of expression for $\bar{p}$ given in (19) in (27) gives

$$\bar{F} = 6\chi_A(\bar{h}_m) + 12\bar{V}\chi_B(\bar{h}_m) + \xi_1\left(\bar{h}_m,\bar{V}\right)\chi_C(\bar{h}_m). \tag{28}$$

where χ_A, χ_B and χ_C are determined by the following double integrals

$$\chi_A(\bar{h}_m) = \int_{\bar{x}=0}^{1}\int_{\bar{x}=0}^{\bar{x}} \frac{\bar{d}\left(1-2\bar{x}+\bar{x}^2\right)}{\bar{\zeta}(\bar{h},\bar{l},M,\psi)} d\bar{x}d\bar{x}, \tag{29}$$

$$\chi_B(\bar{h}_m) = \int_{\bar{x}=0}^{1}\int_{\bar{x}=0}^{\bar{x}} \frac{\bar{x}}{\bar{\zeta}(\bar{h},\bar{l},M,\psi)} d\bar{x}d\bar{x}, \tag{30}$$

$$\chi_C(\bar{h}_m) = \int_{\bar{x}=0}^{1}\int_{\bar{x}=0}^{\bar{x}} \frac{1}{\bar{\zeta}(\bar{h},\bar{l},M,\psi)} d\bar{x}d\bar{x}. \tag{31}$$

Steady state characteristics

The expressions for the steady film pressure and the steady load carrying capacity in non-dimensional form are obtained from equations (19) and (28) by considering the non-dimensional minimum film height be constant and the non-dimensional squeezing velocity be zero.

$$\bar{p}_s = 6\left[g_A(\bar{x},\bar{h}_m)\right]_s + \left[\xi_1\right]_s\left[g_C(\bar{x},\bar{h}_m)\right]_s \tag{32}$$

$$\bar{W}_s = \left[6\chi_A(\bar{h}_m)\right]_s + \left[\xi_1\right]_s\left[\chi_C(\bar{h}_m)\right]_s \tag{33}$$

Dynamic characteristics

The dynamic stiffness coefficient in non-dimensional form is obtained as the partial derivative of non-dimensional force with respect to non-dimensional minimum film thickness under steady state as

$$\bar{S}_d = -\left(\frac{\partial \bar{F}}{\partial \bar{h}_m}\right)_s = -6\left(\frac{\partial \chi_A}{\partial \bar{h}_m}\right)_s - \left(\frac{\partial \xi_1}{\partial \bar{h}_m}\right)_s (\chi_c)_s - (\xi_1)_s\left(\frac{\partial \chi_C}{\partial \bar{h}_m}\right)_s \tag{34}$$

where subscript s denotes the steady state and

$$\left(\frac{\partial \chi_A}{\partial \bar{h}_m}\right)_s = -\left[\int_{\bar{x}=0}^{1}\int_{\bar{x}=0}^{\bar{x}} \frac{\bar{d}\left(1-2\bar{x}+\bar{x}^2\right)}{\left\{\bar{\zeta}(\bar{h},\bar{l},M,\psi)\right\}^2}\frac{\partial \bar{\zeta}}{\partial \bar{h}_m} d\bar{x}d\bar{x}\right]_s, \tag{35}$$

$$\left(\frac{\partial \chi_c}{\partial \bar{h}_m}\right)_s = -\left[\int_{\bar{x}=0}^{1}\int_{\bar{x}=0}^{\bar{x}} \frac{1}{\left\{\bar{\zeta}(\bar{h},\bar{l},M,\psi)\right\}^2}\frac{\partial \bar{\zeta}}{\partial \bar{h}_m} d\bar{x}d\bar{x}\right]_s, \tag{36}$$

$$\left(\frac{\partial \xi_1}{\partial \bar{h}_m}\right)_s = \frac{-6}{\left[(g_{C1})_s\right]^2}\left[(g_{C1})_s\left(\frac{\partial g_{A1}}{\partial \bar{h}_m}\right)_s - (g_{A1})_s\left(\frac{\partial g_{C1}}{\partial \bar{h}_m}\right)_s\right], \tag{37}$$

$$\left(\frac{\partial g_{A1}}{\partial \bar{h}_m}\right)_s = -\left[\int_{\bar{x}=0}^{1} \frac{\bar{d}\left(1-2\bar{x}+\bar{x}^2\right)}{\left\{\bar{\zeta}(\bar{h},\bar{l},M,\psi)\right\}^2}\frac{\partial \bar{\zeta}}{\partial \bar{h}_m} d\bar{x}\right]_s, \tag{38}$$

$$\left(\frac{\partial g_{C1}}{\partial \bar{h}_m}\right)_s = -\left[\int_{\bar{x}=0}^{1} \frac{1}{\left\{\bar{\zeta}(\bar{h},\bar{l},M,\psi)\right\}^2}\frac{\partial \bar{\zeta}}{\partial \bar{h}_m} d\bar{x}\right]_s. \tag{39}$$

The dynamic damping coefficient in non-dimensional form is obtained as the partial derivative of non-dimensional force with respect to squeezing velocity under steady state as

$$\bar{C}_d = -\left(\frac{\partial \bar{F}}{\partial \bar{V}}\right)_s = -12\left(\chi_B\right)_s - \left(\frac{\partial \bar{\xi}_1}{\partial \bar{V}}\right)_s \left(\chi_C\right)_s \tag{40}$$

where

$$\left(\frac{\partial \bar{\xi}_1}{\partial \bar{V}}\right)_s = -12\frac{\left(g_{B1}\right)_s}{\left(g_{C1}\right)_s} \tag{41}$$

4. Results and discussions

The effect of permeability on MHD bearing lubricated with couple stress fluid is analysed under the steady state condition. The permeability parameter ψ signifies the effect of permeability resulting from the fluid which flows into the porous matrix, signifies the effect of couple stresses resulting from additives added to Newtonian fluid, the Hartmann number H signifies the effect of magnetic field resulting from an externally applied magnetic field. The results of Naduvinamani *et al.* [14] can be recovered as a limiting case with $\psi \to 0$ for solid case.

4.1 Steady film pressure

Figure 2 depicts the variation of non-dimensional steady film pressure $\bar{p}_s$ with non-dimensional coordinate $\bar{x}$ and permeability parameter ψ for different values of couple stress parameter $\bar{l}$ and Hartmann number H with $m = 0.6$, $\bar{d} = 1$, $\alpha = 0.01$, $\beta = 0.1$ and $\bar{h}_{ms} = 1$. It is observed that, the presence of couple stresses increases $\bar{p}_s$ in the film as compared to the corresponding Newtonian case. Further, the application of magnetic field also increases $\bar{p}_s$ as compared to that of non-magnetic case. This increase in the pressure may be attributed to reduced velocity of fluid in the film region on the application of magnetic field. As the

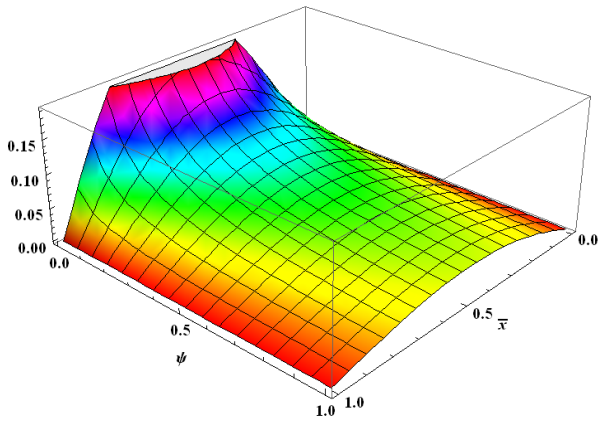

(a) $l = 0,\ M = 0$

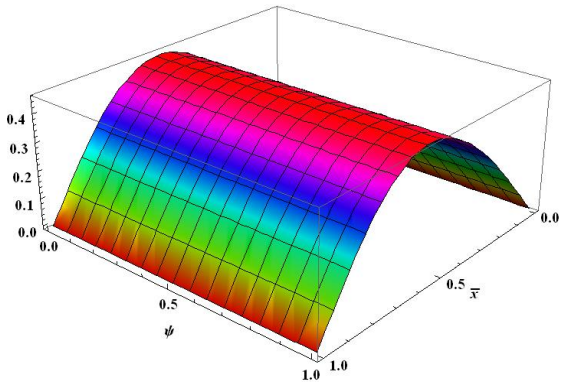

(b) $l = 0,\ M = 5$

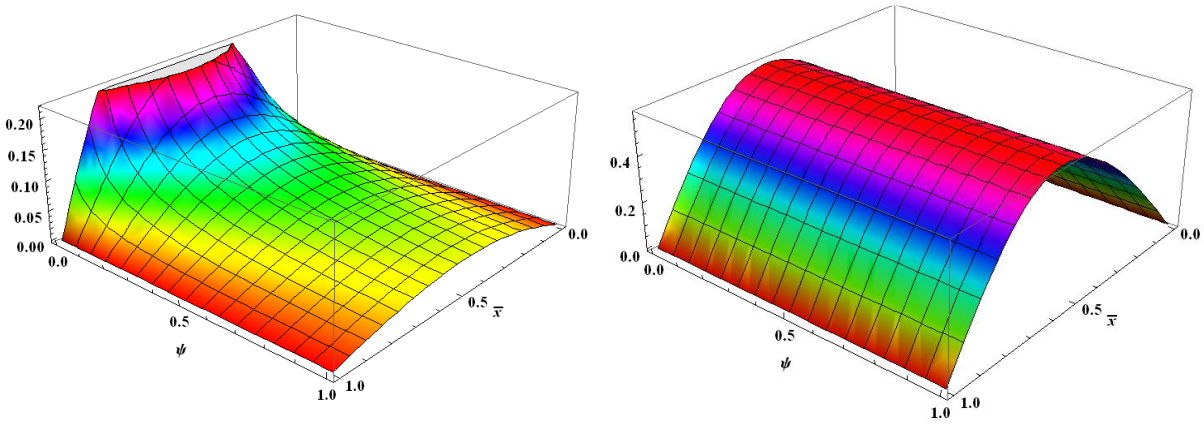

(c) $l = 0.4,\ M = 0$ (d) $l = 0.4,\ M = 5$

Figure 2. Variation of steady film pressure $\bar{p}_s$ with $\bar{x}$ and ψ for different values of M and $\bar{l}$ with $m = 0.6,\ \bar{d} = 0.1, \alpha = 0.01,\ \beta = 0.1\ \bar{h}_{ms} = 1$

permeability parameter takes higher values, the pressure starts decreasing in the absence of magnetic field where as the effect of permeability is marginal in the presence of magnetic field.

4.2 Steady load carrying capacity

The variation of non-dimensional steady load carrying capacity $\bar{W}_s$ with profile parameter $\bar{d}$ and permeability parameter ψ for different values of $\bar{l}$ and M with $m = 0.6,\ \alpha = 0.01,\ \beta = 0.1$ and $\bar{h}_{ms} = 1$ is shown in Fig. 3. It is observed that the applied magnetic field and presence of couple stress both increase the steady load carrying capacity as compared to that of non-magnetic and Newtonian cases respectively. The load carrying capacity increases as a result of increase in the pressure due to reduced velocity of fluid in the film region. In the absence of magnetic field, as the profile parameter value increases the load carrying capacity increases and reaches its maximum then starts decreasing for lower values of permeability parameter whereas load carrying capacity increases with increasing value of profile parameter for larger values of permeability parameter. In the presence of magnetic field, load carrying capacity increases with increase in the value of profile parameter till it reaches maximum and then it becomes constant. It is observed that, the load carrying capacity decreases with increasing values of permeability parameter in the absence of magnetic field, whereas the effect of permeability is negligible in the presence of magnetic field.

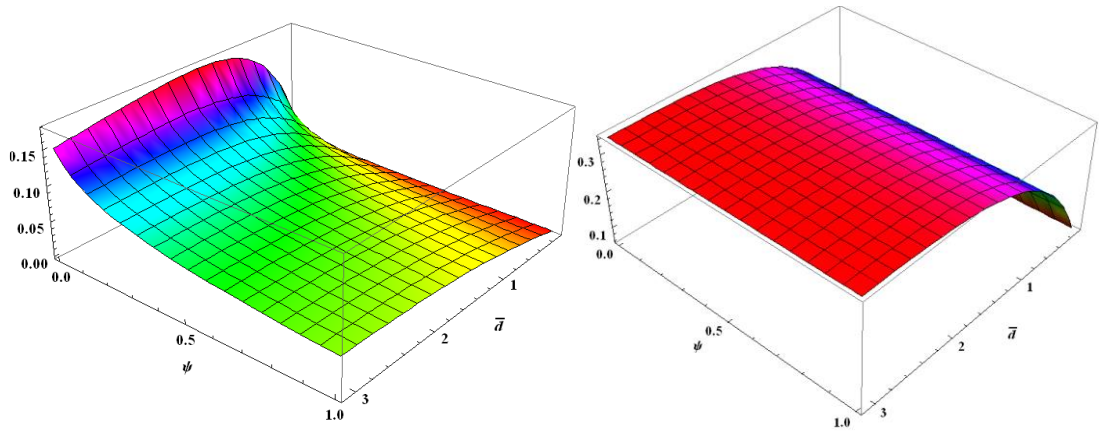

(a) $l=0,\ M=0$ (b) $l=0,\ M=5$

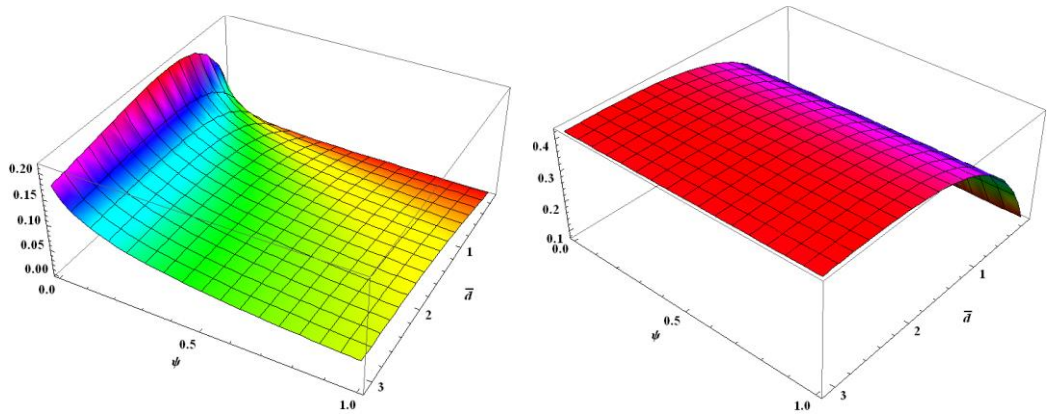

(c) $l=0.4,\ M=0$ (d) $l=0.4,\ M=5$

Figure 3. Variation of steady load carrying capacity $\bar{W}_s$ with $\bar{d}$ and ψ for different values of M and $\bar{l}$ with $m=0.6,\ \alpha=0.01,\ \beta=0.1\ \bar{h}_{ms}=1$

4.3 Dynamic stiffness coefficient

Figure 4 shows the variation of non-dimensional dynamic stiffness coefficient $\bar{S}_d$ with profile parameter $\bar{d}$ and permeability parameter ψ for different values $\bar{l}$ and M under $m=0.6$, $\alpha=0.01$, $\beta=0.1$ and $\bar{h}_{ms}=1$. It is observed that, the dynamic stiffness coefficient increases with increasing values of couple stress parameter and the Hartmann number as compared to the corresponding Newtonian case and non-magnetic case respectively. The dynamic stiffness coefficient increases and reaches its maximum and then decreases. This effect is more accentuated for smaller values permeability parameter. In magnetic case, the dynamic stiffness coefficient increases with increase in the value of profile parameter till it reaches maximum and then it decreases. In non-magnetic case, the dynamic stiffness decreases with increase in the value of permeability parameter whereas the effect of permeability is negligible in magnetic case.

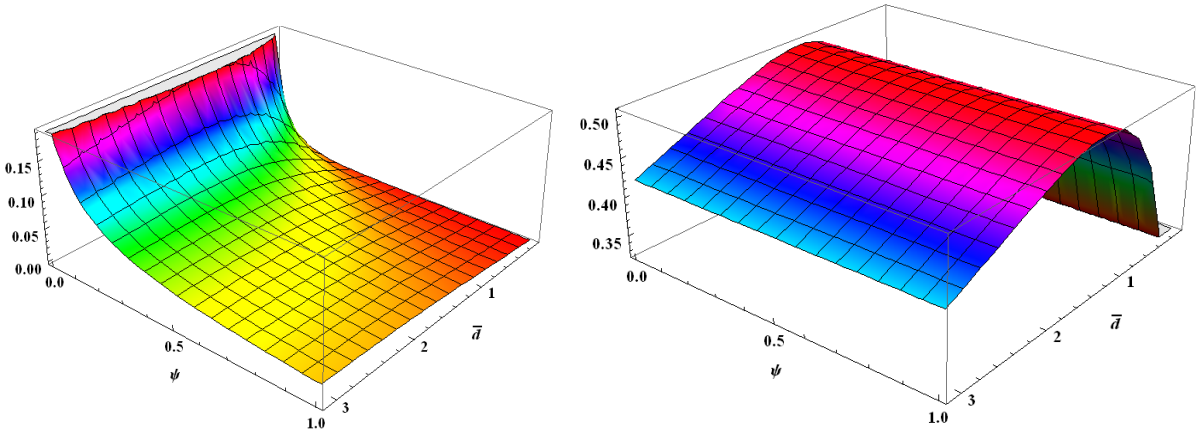

(a) $l=0,\ M=0$ (b) $l=0,\ M=5$

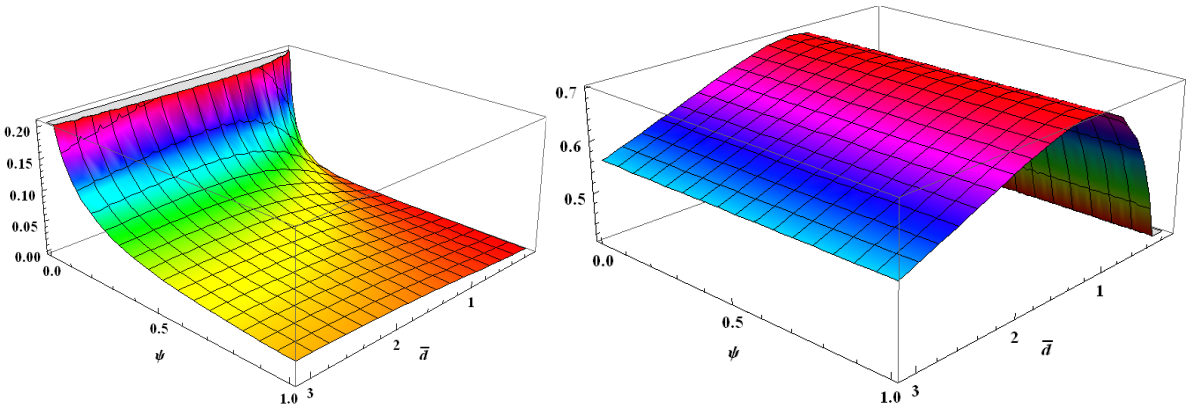

(c) $l=0.4,\ M=0$ (d) $l=0.4,\ M=5$

Figure 4. Variation of dynamic Stiffness coefficient $\bar{S}_d$ with $\bar{d}$ and ψ for different values of M and $\bar{l}$ with $m=0.6,\ \alpha=0.01,\ \beta=0.1\ \bar{h}_{ms}=1$

4.4 Dynamic damping coefficient

The variation of non-dimensional dynamic damping coefficient $\bar{C}_d$ with profile parameter $\bar{d}$ and permeability parameter ψ for different values $\bar{l}$ and M under $m=0.6,\ \alpha=0.01,\ \beta=0.1$ and $\bar{h}_{ms}=1$ is shown in Fig. 5. It is observed that the dynamic damping coefficient increases with increase in the value of the Hartmann number and couple stress parameter. The dynamic damping coefficient decreases with increase in the value of profile parameter and it also decreases with increase in the value of permeability parameter for non-magnetic case whereas permeability parameter effect on the variations of $\bar{C}_d$ is marginal for magnetic case.

Design example

For the use of present work in the design of bearings a design example of porous parabolic slider bearing lubricated with couple stress fluid in the presence of applied transverse magnetic field is presented in Table 1 with values for physical quantities under consideration. With these values of physical quantities, the values of couple stress parameter and Hartmann number are obtained as $\bar{l}=0,,0.2,0.4$ and $M=0,2.5,5$ respectively.

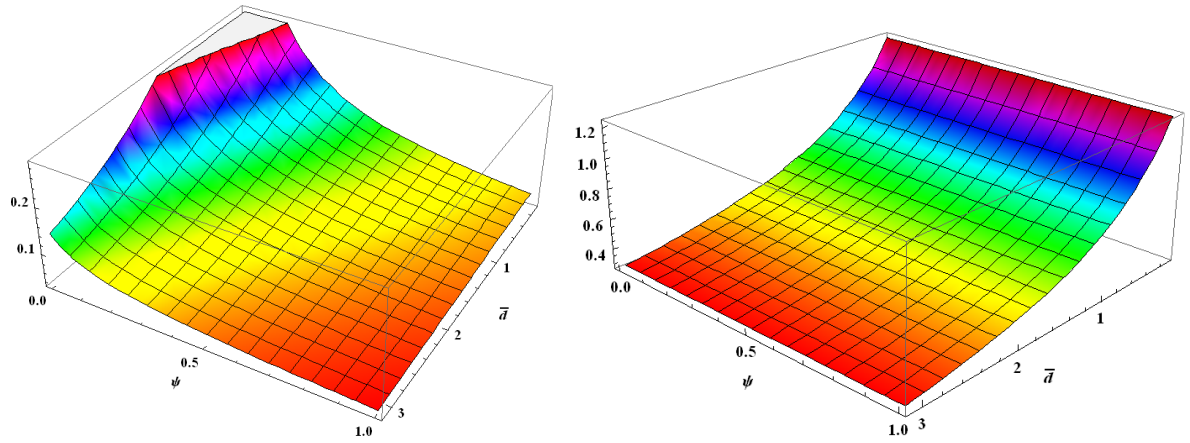

(a) $l=0,\ M=0$ (b) $l=0,\ M=5$

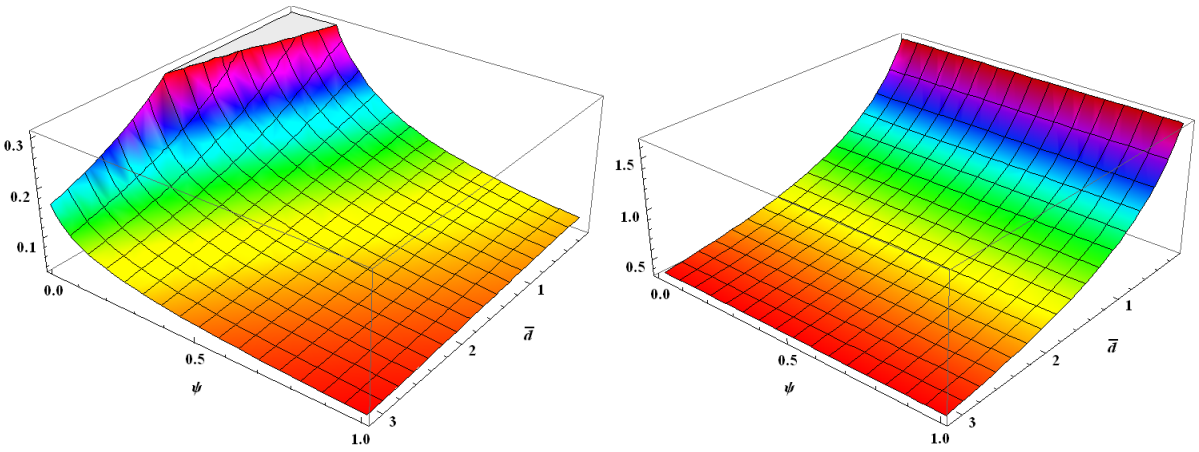

(c) $l=0.4,\ M=0$ (d) $l=0.4,\ M=5$

Figure 5. Variation of dynamic damping coefficient $\bar{C}_d$ with $\bar{d}$ and ψ for different values of M and $\bar{l}$ with $m=0.6,\ \alpha=0.01,\ \beta=0.1\ \bar{h}_{ms}=1$

Physical quantity	Symbol	Value of physical quantity
Length of the bearing	L	$1.0\times10^{-1}m$
Inlet film thickness	h_1	$2.0\times10^{-4}m$
Outlet film thickness	h_{ms}	$1.0\times10^{-4}m$
Profile parameter	$\bar{d}$	1.0
Electrical conductivity	σ	$1.07\times10^{6}mho/m$
Lubricant viscosity	μ	$1.55\times10^{-3}Pa.s$
Applied magnetic field	B_0	0, 0.95, 1.90 Wb/m^2
Couple stress material constant	η	$(0, 1.55, 6.20)\times10^{-13}\ Ns$
Porous layer thickness	δ	$1.0\times10^{-9}m$
Permeability parameter	k	$(0, 0.1, 1, 10)\times10^{-5}m^2$

Table 1. Design example of a parabolic slider bearing lubricated with couple stress fluid in the presence of a magnetic field considering the squeeze effect.

5. Conclusions

The combined effect of couple stress and applied magnetic field on static and dynamic characteristics of parabolic slider bearing with porous surface is analysed. It can be concluded that the steady film pressure, steady load carrying, dynamic stiffness and damping coefficients takes higher values in the presence of couple stress and applied magnetic field as compared to Newtonian and non-magnetic cases. The increase in the permeability parameter value decreases the bearing characteristics values in non-magnetic case whereas its effect is negligible on bearing characteristics in the presence of magnetic field.

References

[1] V. K. Stokes (1966): Couple stresses in fluids, The Physics of Fluids (AIP), 9, 1709-1715 (1966).

[2] G. Ramanaiah and P. Sarakar (1978): Optimum load capacity of a slider bearing lubricated by a fluid with couple stress, Wear(Elsevier), 49, 61-66 (1978).

[3] C. Singh (1981): Lubrication theory for couple stress fluid and its application to short bearings, Wear (Elsevier), 80, 281-290 (1981).

[4] O. M. Humphrey and A. John (2009): Parametric characterization of load capacity of infinitely wide parabolic slider bearing with couple stress fluid, World Academy of Science, Engineering and Technology, 57, 386-390 (2009).
[5] J. P. Agarwal (1963): Magnetohydrodynamic effects in lubrication, Journal of Applied Mathematics and Mechanics (Wiley), 43, 181-189 (2009).
[6] D. C. Kuzma (1963): The magnetohydrodynamic journal bearing, Journal of Basic Engineering (ASME), 85, 424-427 (1963).
[7] M. Malik and D. V. Singh (1980): Analysis of finite magnetohydrodynamic journal bearings, Wear (Elsevier), 64, 273-280 (1980).
[8] N. C. Das (1998): A study of optimum load-bearing capacity for slider bearings lubricated with couple stress fluids in magnetic field, Tribology International (Elsevier), 31, 393-400 (1998).
[9] J. R. Lin, L. M. Chu, C. R. Hung and P. Y. Wang (2012): Derivation of two-dimensional couple-stress hydromagnetic squeeze film Reynolds equation and application to wide parallel rectangular plates, Meccanica(Springer), 48, 253-258 (2012).
[10] S. T. Fathima, N. B. Naduvinamani, B. N. Hanumagowda and J. Santoshkumar (2015): Modified Reynolds equation for different types of finite plates with the combined effect of MHD and couple stresses, Tribology Transactions (Taylor & Francis), 58, 660-667 (2015).
[11] S. Patil, N. B. Naduvinamani and A. Siddangouda (2016): A comparative study of the performance of magneto-hydrodynamic couple stress lubrication of infinitely wide exponential, parabolic and plane inclined slider bearings, Global Journal of Pure and Applied Mathematics (RIP), 12, 222-230 (2016).
[12] W. H. Liao, R. F. Lu, R. D. Chein and J. R. Lin (2005): Linear stability analysis of long journal bearings: couple stress fluid model, Industrial Lubrication and Technology (Emerald), 57, 21-27 (2005).
[13] J. R. Lin and T. L. Chou (2013): Non-Newtonian dynamic characteristics of wide composite slider bearings lubricated with couple stress fluids, Industrial Lubrication and Tribology (Emerald), 65, 44-49 (2013).
[14] N. B. Naduvinamani, A. Siddangouda and P. Siddharam (2017): A comparative study of static and dynamic characteristics of parabolic and plane inclined slider bearings lubricated with MHD couple stress fluids, Tribology Transactions(Taylor & Francis), 60, 1-11 (2017).
[15] P. R. K. Murti(1974): Analysis of porous slider bearings, Wear(Elsevier), 28, 131-134 (1974).
[16] N. M. Bujurke, H. P. Patil and S. G. Bhavi (1990): Porous slider bearing with couple stress fluid, Acta Mechanica(Springer), 85, 99-113 (1990).
[17] N. B. Naduvinamani, P. S. Hiremath and S. T. Fathima (2005): On the squeeze film lubrication of long porous journal bearings with couple stress fluids, Industrial Lubrication and Tribology (Emerald), 57, 12-20 (2005).
[18] N. B. Naduvinamani and A. Siddangouda (2007): A note on porous Rayleigh step bearings lubricated with couple-stress fluids, Proceedings of the Institution of Mechanical Engineers, Part J: Journal of Engineering Tribology (SAGE), 221, 615-621 (2007).

Appendix A

$$f_{11}=\frac{b^2}{\left(a^2-b^2\right)}\left\{\frac{\sinh\left(ah/l\right)-\sinh\left(ay/l\right)+\sinh a\left(h-y\right)/l}{\sinh\left(ah/l\right)}\right\}$$

$$f_{12}=\frac{a^2}{\left(a^2-b^2\right)}\left\{\frac{\sinh\left(bh/l\right)-\sinh\left(by/l\right)+\sinh b\left(h-y\right)/l}{\sinh\left(bh/l\right)}\right\}$$

$$f_{13}=\frac{b^2}{\frac{b^2}{a}\tanh\left(\frac{ah}{2l}\right)-\frac{a^2}{b}\tanh\left(\frac{bh}{2l}\right)}\left\{\frac{\sinh\left(ah/l\right)-\sinh\left(ay/l\right)-\sinh a\left(h-y\right)/l}{\sinh\left(ah/l\right)}\right\}$$

$$f_{14}=\frac{a^2}{\frac{b^2}{a}\tanh\left(\frac{ah}{2l}\right)-\frac{a^2}{b}\tanh\left(\frac{bh}{2l}\right)}\left\{\frac{\sinh\left(\frac{bh}{l}\right)-\sinh\left(\frac{by}{l}\right)-\sinh\frac{b\left(h-y\right)}{l}}{\sinh\left(\frac{bh}{l}\right)}\right\}$$

$$f_{21}=\frac{Sinh\left(\frac{y-h}{\sqrt{2}l}\right)+Sinh\left(\frac{y}{\sqrt{2}l}\right)-Sinh\left(\frac{h}{\sqrt{2}l}\right)}{Sinh\left(\frac{h}{\sqrt{2}l}\right)}$$

$$f_{22}=\frac{yCosh\left(\frac{y-h}{\sqrt{2}l}\right)+yCosh\left(\frac{y}{\sqrt{2}l}\right)-h\,\mathrm{Coth}\left(\frac{h}{2\sqrt{2}l}\right)\mathrm{Sinh}\left(\frac{y}{\sqrt{2}l}\right)}{2\sqrt{2}l\,Sinh\left(\frac{h}{\sqrt{2}l}\right)}$$

$$f_{23}=\frac{ySinh\left(\frac{y-h}{\sqrt{2}l}\right)+y\,\mathrm{Sinh}\left(\frac{y}{\sqrt{2}l}\right)-h\,\mathrm{Sinh}\left(\frac{y}{\sqrt{2}l}\right)}{\left(6l\,Sinh\left(\frac{h}{\sqrt{2}l}\right)-\sqrt{2}h\right)}$$

$$f_{24}=\frac{2Cosh\left(\frac{y-h}{\sqrt{2}l}\right)+2Cosh\left(\frac{y}{\sqrt{2}l}\right)-2Cosh\left(\frac{h}{\sqrt{2}l}\right)-2}{\left(3\sqrt{2}Sinh\left(\frac{h}{\sqrt{2}l}\right)-\frac{h}{l}\right)}$$

$$f_{31}=\frac{\mathrm{Cosh}\,a_1yCosb_1\left(y-h\right)-\mathrm{Cos}\,b_1yCosha_1\left(y-h\right)}{\left(Cosha_1h-Cosb_1h\right)}$$

$$f_{32}=\frac{Cot\varphi\left\{\mathrm{Sinh}\,a_1ySinb_1\left(y-h\right)-\mathrm{Sin}\,b_1ySinha_1\left(y-h\right)\right\}+\left(Cosha_1h-Cosb_1h\right)}{\left(Cosha_1h-Cosb_1h\right)}$$

$$f_{33}=\frac{M}{h_{ms}}\left\{\frac{Cot\varphi\left\{\mathrm{Sinh}\,a_1ySinb_1\left(y-h\right)+Sinb_1ySinha_1\left(y-h\right)\right\}+\left(Cosb_1h+Cosha_1h\right)}{\left(b_1-a_1Cot\varphi\right)Sinb_1h+\left(a_1+b_1Cot\varphi\right)Sinha_1h}\right\}$$

$$f_{34}=\frac{M}{h_{ms}}\left\{\frac{Cosb_1yCosha_1\left(y-h\right)+Cosha_1yCosb_1\left(y-h\right)}{\left(b_1-a_1Cot\varphi\right)Sinb_1h+\left(a_1+b_1Cot\varphi\right)Sinha_1h}\right\}$$

Karnatak University
Journal of Science

ISSN: 0075-5168

Soft Nano Locally Closed Sets in Soft Nano Topological Spaces

P. G. Patil

Spoorti S. Benakanawari

P. G. Patil and Spoorti S. Benakanawari, “Soft Nano Locally Closed Sets in Soft Nano Topological Spaces” Karnatak University Journal of Science 51, 123-130 (2020).

SOFT NANO LOCALLY CLOSED SETS IN SOFT NANO TOPOLOGICAL SPACES

P. G. Patil* and Spoorti S. Benakanawari
Department of Mathematics, Karnatak University Dharwad-580003, Karnataka, INDIA
***Corresponding Author:** pgpatil@kud.ac.in, spoortisb@gmail.com

Abstract: Objective of the present paper is to investigate the purpose of studying sn-Gωlc, sn-Gωlc*and sn-Gωlc** sets, sn-Gωlc continuous, sn-Gωlc*continuous and sn-Gωlc** continuous and the corresponding sn-irresolute functions.
Keywords: sn-Gωlc; sn-Gωlc*and sn-Gωlc** sets, sn-Gωlc continuous, sn-Gωlc*continuous and sn-Gωlc** continuous.
2010 AMS Subject classification: 54A05; 54C05; 54C08.
Article history: Received: 10 July 2020**;** Revised: 21 August 2020; Accepted: 5 September 2020.

1. Introduction:

Kuratowaski and Sierpienski[10] dealt with locally closed sets and their properties. Bourbaki[6], found that locally closed sets are obtained by intersecting open and closed sets. FG represented locally closed set according to Stone[19]. Borges's results explain the role of locally closed sets in simple extensions. The continuation of this study gave rise to LC-continuous and LC-irresolute functions and their decomposition. Among such contributions, the work of Ganster et al.[8] is significant. In 1997, K. Balachandran et.al defined Generalized Locally Closed Sets and GLC-Continuous. P. G. Patil et al.[14] contributed to the concept of decomposition of locally closed set in topological spaces. Many topologists studied related concepts in [1-5, 7, 9, 11-13, 15-18, 20-21].

Throughout this paper $(\tau_{R'}(X_1), U_1, O_1)$ is soft nano topological space, sn-open indicates soft nano open and family of all such sets is given by sn-$O(X_1, O_1)$, sn-closed indicates soft nano open and family of all such sets is given by sn-$C(X_1, O_1)$, sn-$cl(V^*_1, O_1)$ denotes soft nano closure of (V^*_1, O_1) and sn-$int(V^*_1, O_1)$ denotes soft nano interior of (V^*_1, O_1).

In this paper, sn-Gωlc, sn-Gωlc*and sn-Gωlc** sets, sn-Gωlc continuous, sn-Gωlc*continuous and sn-Gωlc** continuous functions and their properties are studied.

2. Preliminaries

Definition 2.1[18]: A function **f**: $(\tau_{R'}(X_1), U_1, O_1) \rightarrow (\tau_{R''}(X_2), U_2, O_2)$ is sn-gω continuous if $f^{-1}(P^*_1, O_1) \in$ sn-$O(X_2, O_2)$ for $(P^*_1, O_1) \in$ sn-$g\omega O(X_1, O_1)$.

Definition 2.2[18]: A function **f**: $(\tau_{R'}(X_1), U_1, O_1) \rightarrow (\tau_{R''}(X_2), U_2, O_2)$ is sn-gω irresolute if $f^{-1}(P^*_1, O_1) \in$ sn-$g\omega O(X_2, O_2)$ for $(P^*_1, O_1) \in$ sn-$g\omega O(X_1, O_1)$.

Definition 2.3[14]: Let $E \subseteq X$. Then E is said to be a $g*\omega\alpha$-locally closed if $E = E_1 \cap E_2$ where $E_1 \in g*\omega\alpha$-$O(X)$ and $E_2 \in g*\omega\alpha$-$C(X)$.

Definition 2.4[5]: Let $P \subseteq (U, \tau_R(X))$, P is known as nano g- locally closed if $P = P_1 \cap P_2$, $P_1 \in$ Ng-O(X) and $P_2 \in$ Ng-C(X).

Definition 2.5[5]: A function **f**: $(U, \tau_R(X)) \rightarrow (V, \tau_{R'}(Y))$ is known as nano locally closed continuous if $f^{-1}(P)$ is NLC-continuous for $P \in NO(X)$.

3. Soft nano gω locally closed sets in soft nano topological spaces

Definition 3.1: A soft nano set $(Z_0^*, O_1)_1$ in $(\tau_{R'}(X_1), U_1, O_1)$, is

i). sn-gω locally closed(sn-gωlc) if it is the intersection of $(R_0^*, O_1)_1 \in$ sn-gωO(X_1, O_1) and $(S_0^*, O_1)_1 \in$ sn-gωC(X_1, O_1).
ii) sn-gω locally closed*(sn-gωlc*) if it is the intersection of $(R_0^*, O_1)_1 \in$ sn-gωO(X_1, O_1) and $(S_0^*, O_1)_1 \in$ sn-C(X_1, O_1).
iii) sn-gω locally closed**(sn-gωlc**) if it is the intersection of $(R_0^*, O_1)_1 \in$ sn-O(X_1, O_1) and $(S_0^*, O_1)_1 \in$ sn-gωC(X_1, O_1).

The family of all sn-gωlc (sn-gωlc*, sn-gωlc**) sets in $(\tau_{R'}(X_1), U_1, O_1)$ is given by sn-Gωlc$(\tau_{R'}(X_1), U_1, O_1)$, sn-Gωlc*$(\tau_{R'}(X_1), U_1, O_1)$, sn-Gωlc**$(\tau_{R'}(X_1), U_1, O_1)$ resp.).

Theorem 3.2: Subsequents are equivalent for $(M_0^*, O_1) \in (\tau_{R'}(X_1), U_1, O_1)$,

i) $(M_0^*, O_1) \in$sn-Gωlc$(\tau_{R'}(X_1), U_1, O_1)$

ii) $(M_0^*, O_1) = (Y^*, O_1) \cap$ sn-cl(M_0^*, O_1) for sn-gωO(X_1, O_1)

iii) sn-cl$_{g\omega}(M_0^*, O_1)$- $(M_0^*, O_1) \in$sn- gωC(X_1, O_1)

iv) $(M_0^*, O_1) \cup [U_1$-sn-cl$_{g\omega}(M_0^*, O_1)] \in$sn-gωO$(X_1, O_1)$

Proof: i)→ ii):For $(M_0^*, O_1) \in$sn-Gωlc$(\tau_{R'}(X_1), U_1, O_1)$, we have (M_0^*, O_1) being intersection of $(Y^*, O_1) \in$sn-gωO (X_1, O_1) and$(S^*_1, O_1) \in$sn-C(X_1, O_1). As (M_0^*, O_1) represents the subset of (Y^*, O_1) and its sn-closures, so $(M_0^*, O_1) \subseteq$sn-cl$_{g\omega}(M_0^*, O_1) \cap (Y^*, O_1)$.

Conversely, here sn-cl$(M_0^*, O_1) \subseteq (S^*_1, O_1)$ and so (M_0^*, O_1) contains $(Y^*, O_1) \cap$sn-cl(M_0^*, O_1).

ii) → i): As $(Y^*, O_1) \in$sn-gωO(X_1, O_1) andsn-cl$(M_0^*, O_1) \cap (Y^*, O_1) \in$sn-Gωlc$(\tau_{R'}(X_1), U_1, O_1)$.

ii) → iii): If $(M_0^*, O_1) = (Y^*, O_1) \cap$ sn-cl(M_0^*, O_1), then sn-cl$_{g\omega}(M_0^*, O_1)$ - (M_0^*, O_1) = sn-cl$_{g\omega}(M_0^*, O_1) \cap (U_1$-$(Y^*, O_1)) \in$sn-gωC$(X_1, O_1)$. Therefore, sn-cl$_{g\omega}(M_0^*, O_1)$ - (M_0^*, O_1) is sn- gω-closed.

iii) → ii): If $(Y^*, O_1) =$ [sn-cl(M_0^*, O_1) - (M_0^*, O_1)], then by the supposition, $(Y^*, O_1) \in$sn-gωO(X_1, O_1). So, $(M_0^*, O_1) = (Y^*, O_1) \cap$ sn-cl(M_0^*, O_1)

iii) → iv): For $(S^*_1, O_1) =$ sn-cl$_{g\omega}(M_0^*, O_1)$ - (M_0^*, O_1), U_1-$(Y^*, O_1) = (M_0^*, O_1) \cup (U_1$-sn-cl$_{g\omega}(M_0^*, O_1))$ is satisfied and $U_1 - (S^*_1, O_1) \in$sn-gωO(X_1, O_1). Therefore $(M_0^*, O_1) \cup (U_1$-sn-cl$_{g\omega}(M_0^*, O_1) \in$sn-gωO$(X_1, O_1)$

(iv) → (iii):Let $(Y^*, O_1) = (M_0^*, O_1) \bigcup (U_1\text{-sn-cl}_{g\omega}(M_0^*, O_1)$.As $U_1\text{-}(Y^*, O_1) \in$ sn-$g\omega C(X_1, O_1)$ and $U_1\text{-}(Y^*, O_1) = \text{sn-cl}_{g\omega}(Y^*, O_1)\text{-}(Y^*, O_1)$ is satisfied. Therefore, $\text{sn-cl}_{g\omega}(M_0^*, O_1) \text{-}(M_0^*, O_1) \in \text{sn-cl}_{g\omega}(X_1, O_1)$

Theorem 3.3: For $(W_0^*, O_1)_1 \in (\tau_{R'}(X_1), U_1, O_1)$, if $(W_0^*, O_1)_1 \in$ sn-$G\omega lc(\tau_{R'}(X_1), U_1, O_1)$ if and only if $(W_0^*, O_1)_1 = (Q^*, O_1) \cap \text{sn-cl}_{g\omega}(W_0^*, O_1)_1$ for $(Q^*, O_1) \in$sn-$g\omega O(X_1, O_1)$.

Proof: For $(W_0^*, O_1)_1 \in$sn-$G\omega lc(\tau_{R'}(X_1), U_1, O_1)$,$(M^*_1, O_1) \in$sn-$O(X_1, O_1)$ and $(Q^*, O_1) \in$sn-$g\omega C(X_1, O_1)$ with$(W_0^*, O_1)_1 = (Q^*, O_1) \cap (S, O_1)$. Then $(W_0^*, O_1)_1 \subseteq (S, O_1)$ implies sn-$\text{cl}_{g\omega}(W_0^*, O_1)_1 \subseteq (S, O_1)$. Here $(W_0^*, O_1)_1 = (W_0^*, O_1)_1 \cap \text{sn-cl}_{g\omega}(W_0^*, O_1)_1 = (Q^*, O_1) \cap (S, O_1) \cap \text{sn-cl}_{g\omega}(W_0^*, O_1)_1 = (M^*_1, O_1) \cap \text{sn-cl}_{g\omega}(M^*_1, O_1)$. Also, $(M^*_1, O_1) \in$sn-$O(X_1, O_1)$, $(W_0^*, O_1)_1 = (Q, O1) \cap \text{sn-cl}_{g\omega}(M_0^*, O_1)$. Since $\text{sn-cl}_{g\omega}(W_0^*, O_1)_1 \in$sn-$g\omega C(X_1, O_1)$. Thus $(W_0^*, O_1)_1 \cap \text{sn-cl}_{g\omega}(W_0^*, O_1)_1 \in$sn- $G\omega lc(\tau_{R'}(X_1), U_1, O_1)$.

Theorem 3.4: For $(Z_0^*, O_1)_1 \in (\tau_{R'}(X_1), U_1, O_1)$ and $(Z_0^*, O_1)_1 \in$ sn-$G\omega lc^{**}(\tau_{R'}(X_1), U_1, O_1)$ then,

i) $\text{sn-cl}_{g\omega}(Z_0^*, O_1)_1 - (Z_0^*, O_1)_1 \in \text{sn-}g\omega C(X_1, O_1)$
ii) $(Z_0^*, O_1)_1 \bigcup (U_1\text{- sn-cl}_{g\omega}(Z_0^*, O_1)_1) \in \text{sn-}g\omega O(X_1, O_1)$

Proof: (i) Let $(Z_0^*, O_1)_1 \in$sn-$G\omega lc^{**}(\tau_{R'}(X_1), U_1, O_1)$. So $(Z_0^*, O_1)_1 = (M^*, O_1) \cap (S^*_1, O_1)$ with $(M^*, O_1) \in$ sn-$O(X_1, O_1)$ and $(S^*_1, O_1) \in$ sn-$g\omega lC(X_1, O_1)$. As we have $(Z_0^*, O_1)_1 \subseteq (M^*, O_1)$ and $(Z_0^*, O_1)_1 \in \text{sn-cl}_{g\omega}(M^*, O_1)$. Hence $(Z_0^*, O_1)_1 \subseteq (M^*, O_1) \cap \text{sn-cl}_{g\omega}(M^*, O_1)$.

Conversely, $\text{sn-cl}_{g\omega}(Z_0^*, O_1)_1 \subseteq (S^*_1, O_1)$ and thus $(M^*, O_1) \cap \text{sn-cl}_{g\omega}(Z_0^*, O_1)_1 \subseteq (M^*, O_1) \cap (S^*_1, O_1) = (M^*, O_1)$ Hence $(Z_0^*, O_1)_1 = (M^*, O_1) \cap \text{sn-clg}\omega(M^*, O_1)$ By the hypothesis, $\text{sn-cl}_{g\omega}(Z_0^*, O_1)_1 - (Z_0^*, O_1)_1 = \text{sn-cl}_{g\omega}(Z_0^*, O_1)_1 \cap (U_1\text{-}(M^*, O_1)) \in$sn-$g\omega C(X_1, O_1)$.

(ii) By (i), $\text{sn-cl}_{g\omega}(Z_0^*, O_1)_1 \text{-}(Z_0^*, O_1)_1 \in$ sn-$g\omega C(X_1, O_1)$. Let $(S^*_1, O_1) = \text{sn-cl}_{g\omega}(Z_0^*, O_1)_1\text{-}(M^*, O_1)$ As $U_1\text{-}(S^*_1, O_1) = (Z_0^*, O_1)_1 \bigcup (U_1\text{-sn-cl}_{g\omega}(Z_0^*, O_1)_1$ is satisfied, we have, $(S^*_1, O_1) \in$sn-$g\omega O(X_1, O_1)$. Thus $(Z_0^*, O_1)_1 \bigcup (U_1\text{-sn-cl}_{g\omega}(Z_0^*, O_1)_1) \in$sn-$g\omega O(X_1, O_1)$.

Theorem 3.5: Let $(P^*_1, O_1), (Q, O_1) \in (\tau_{R'}(X_1), U_1, O_1)$, the family of sn-$g\omega C(X_1, O_1)$ is closed under finite intersection satisfy the following:

i) For $(Q, O_1) \in$sn-$g\omega C(X_1, O_1)$, $(Q, O_1) \in$sn-$g\omega O(X_1, O_1)$ and $(P^*_1, O_1)_1 \in$sn-$G\omega lc(\tau_{R'}(X_1), U_1, O_1)$, then $(P^*_1, O_1) \cap (Q, O_1) \in$sn-$G\omega lc(\tau_{R'}(X_1), U_1, O_1)$.
ii) For $(P^*_1, O_1)_1, (Q, O_1) \in$sn-$G\omega lc^*(\tau_{R'}(X_1), U_1, O_1)$, then $(P^*_1, O_1)_1 \cap (Q, O_1) \in$sn-$G\omega lc^*(\tau_{R'}(X_1), U_1, O_1)$.

Proof:

i). If $(P^*_1, O_1) \in$ sn-$G\omega lc(\tau_{R'}(X_1), U_1, O_1)$, there exist $(Q, O_1) \in$ sn-$g\omega O(X_1, O_1)$ and $(S^*, O_1) \in$ sn-$g\omega C(X_1, O_1)$ with $(P^*_1, O_1) = (M, O_1) \cap (S^*, O_1)$ and hence $(P^*_1, O_1) \cap (Q, O_1) = [(M, O_1) \cap (S^*, O_1)] \cap (Q, O_1)$. For $(Q, O_1) \in$sn-$g\omega O(X_1, O_1)$, $(P^*_1, O_1) \cap (Q, O_1) = [(M, O_1) \cap (Q, O_1)] \cap (S^*, O_1) \in$sn-$G\omega lc(\tau_{R'}(X_1), U_1, O_1)$. For $(Q, O_1) \in$sn-$g\omega C(X_1, O_1)$, $(P^*_1, O_1) \cap (Q, O_1) = (M, O_1) \cap [(Q, O_1)] \cap (S^*, O_1)] \in$sn-$G\omega lc(\tau_{R'}$

(X_1), U_1, O_1). Therefore, $(P^*_1, O_1) \cap (Q, O_1) \in$sn-g$\omega$C$(X_1, O_1)$.Hence $(P^*_1, O_1) \cap (Q, O_1) \in$sn-G$\omega$lc $(\tau_{R'}(X_1), U_1, O_1)$.

ii) . For $(P^*_1, O_1) \cap (Q, O_1) \in$sn-G$\omega$lc*$(\tau_{R'}(X_1), U_1, O_1)$, then there exist (C, O_1), $(D^*_1, O_1) \in$sn-gωO(X_1, O_1) with $(P^*_1, O_1) = (C, O_1) \cap$ sn-cl(P^*_1, O_1) and $(Q, O_1) = (D^*_1, O_1) \cap$ sn-cl(Q, O_1). Then $(P^*_1, O_1) \cap (Q, O_1) = [(C, O_1) \cap$ sn-cl$(P^*_1, O_1)] \cap [(D^*_1, O_1) \cap$sn-cl$(Q, O_1)] = [(C, O_1)] \cap (D^*_1, O_1)] \cap [$sn-cl$(P^*_1, O_1) \cap$ sn-cl$(Q, O_1)] \in$sn-Gωlc*$(\tau_{R'}(X_1), U_1, O_1)$.

Theorem 3.6: The following are true for $(F_0^*, O_1) \in$sn-Gωlc $(\tau_{R'}(X_1), U_1, O_1)$.

i) For $(L, O_1) \in$sn-C(X_1, O_1), $(F_0^*, O_1) \cap (L, O_1) \in$sn-G$\omega$lc $(\tau_{R'}(X_1), U_1, O_1)$.
ii) For $(L, O_1) \in$sn-gωO(X_1, O_1), $(F_0^*, O_1) \cap (L, O_1) \in$sn-G$\omega$lc $(\tau_{R'}(X_1), U_1, O_1)$.
iii) For $(L, O_1) \in$sn-Gωlc $(\tau_{R'}(X_1), U_1, O_1)$, $(F_0^*, O_1) \cap (L, O_1) \in$sn-G$\omega$lc $(\tau_{R'}(X_1), U_1, O_1)$.

Proof:

i) As $(L, O_1) \in$sn-C(X_1, O_1) and $(F_0^*, O_1) \in$sn-Gωlc $(\tau_{R'}(X_1), U_1, O_1)$, then $(F_0^*, O_1) \cap (L, O_1) = [(H^*_1, O_1)_1 \cap (L, O_1)] \cap (S, O_1) = (H^*_1, O_1)_1 \cap [(L, O_1)] \cap (S, O_1)]$ wherein $(S, O_1) \cap (L, O_1) \in$sn-C$(X_1, O_1)$. Hence $(F^*_1, O_1) \cap (L, O_1) \in$sn-G$\omega$lc $(\tau_{R'}(X_1), U_1, O_1)$.
ii) As $(L, O_1) \in$sn-gωO(X_1, O_1) and $(F_0^*, O_1) \in$sn-Gωlc $(\tau_{R'}(X_1), U_1, O_1)$, then $(F_0^*, O_1) \cap (L, O_1) = [(F_0^*, O_1) \cap (L, O_1)] \cap (S, O_1)$, for $(R^*_1, O_1) \cap (L, O_1) \in$sn- g$\omega$O$(X_1, O_1)$. Hence $(F_0^*, O_1) \cap (L, O_1) \in$sn-G$\omega$lc $(\tau_{R'}(X_1), U_1, O_1)$.
iii) For (F_0^*, O_1), $(L, O_1) \in$sn-Gωlc*$(\tau_{R'}(X_1), U_1, O_1)$, then $(F_0^*, O_1) \cap (L, O_1) = [(R^*_1, O_1) \cap (S, O_1)] \cap [(H^*_1, O_1)_1 \cap (N^*, O_1)] = [(R^*_1, O_1) \cap (H^*_1, O_1)_1] \cap [(S, O_1) \cap (N^*, O_1)]$, wherein $(R^*_1, O_1) \cap (H^*_1, O_1)_1 \in$sn-g$\omega$O$(X_1, O_1)$ and $(R^*_1, O_1) \cap (H^*_1, O_1)_1 \in$sn-C$(X_1, O_1)$. Therefore, $(F_0^*, O_1) \cap (L, O_1) \in$sn-G$\omega$lc $(\tau_{R'}(X_1), U_1, O_1)$.

4. Soft nano gω-locally closed continuous functions and Soft nano gω-locally closed irresolute functions.

Definition 4.1: A function f: $(\tau_{R'}(X_1), U_1, O_1) \rightarrow (\tau_{R''}(X_2), U_2, O_2)$ is an sn-locally closed continuous if $f^{-1}(P^*_1, O_1) \in$sn-lc$(\tau_{R'}(X_1), U_1, O_1)$ for $(P^*_1, O_1) \in$sn-O(X_2, O_2).

Definition 4.2: A function f: $(\tau_{R'}(X_1), U_1, O_1) \rightarrow (\tau_{R''}(X_2), U_2, O_2)$ is an sn-g locally closed continuous if $f^{-1}(P^*_1, O_1) \in$sn-Glc$(\tau_{R'}(X_1), U_1, O_1)$ for $(P^*_1, O_1) \in$sn-gO(X_2, O_2).

Example 4.3: Let $U_1 = \{\varepsilon_1, \varepsilon_2, \varepsilon_3, \varepsilon_4\}$ and $O_1 = \{\kappa_1, \kappa_2, \kappa_3\}$.

Now $U_1/R' = \{\{\varepsilon_1\}, \{\varepsilon_3\}, \{\varepsilon_2, \varepsilon_4\}\}$. Let $X_1 = \{\varepsilon_1, \varepsilon_2\} \subseteq U_1$,

Thus, $(\tau_{R'}(X_1), U_1, O_1) = \{U_1, \emptyset, (U_{R'}(X_1), O_1), (L_{R'}(X_1), O_1), (B_{R'}(X_1), O_1)\}$

$(U_{R'}(X_1), O_1) = \{(\kappa_1, \{\varepsilon_1, \varepsilon_2, \varepsilon_4\}), (\kappa_2, \{\varepsilon_1, \varepsilon_2, \varepsilon_4\}), (\kappa_3, \{\varepsilon_1, \varepsilon_2, \varepsilon_4\})\}$

$(L_{R'}(X_1), O_1) = \{(\kappa_1, \{\varepsilon_1\}), (\kappa_2, \{\varepsilon_1\}), (\kappa_3, \{\varepsilon_1\})\}$

$(B_{R'}(X_1), O_1) = \{(\kappa_1, \{\varepsilon_2, \varepsilon_4\}), (\kappa_2, \{\varepsilon_2, \varepsilon_4\}), (\kappa_3, \{\varepsilon_2, \varepsilon_4\})\}$

Let $U_2 = \{\varepsilon'_1, \varepsilon'_2, \varepsilon'_3, \varepsilon'_4\}$ and $O_2 = \{\kappa'_1, \kappa'_2, \kappa'_3\}$.

Now $U_2/R'' = \{\{\varepsilon'_1\}, \{\varepsilon'_3\}, \{\varepsilon'_2, \varepsilon'_4\}\}$. Let $X_1 = \{\varepsilon'_1, \varepsilon'_2\} \subseteq U_1$,

Thus, $(\tau_{R'}(X_2), U_2, O_2) = \{U_2, \emptyset, (U_{R''}(X_2), O_2), (L_{R''}(X_2), O_2), (B_{R''}(X_2), O_2)\}$

$(U_{R''}(X_2), O_2) = \{(\kappa'_1, \{\varepsilon'_1, \varepsilon'_3, \varepsilon'_4\}), (\kappa'_2, \{\varepsilon'_1, \varepsilon'_3, \varepsilon'_4\}), (\kappa'_3, \{\varepsilon'_1, \varepsilon'_3, \varepsilon'_4\})\}$

$(L_{R''}(X_2), O_2) = \{(\kappa'_1, \{\varepsilon'_3\}), (\kappa'_2, \{\varepsilon'_3\}), (\kappa'_3, \{\varepsilon'_3\})\}$

$(B_{R''}(X_2), O_2) = \{(\kappa'_1, \{\varepsilon'_1, \varepsilon'_4\}), (\kappa'_2, \{\varepsilon'_1, \varepsilon'_4\}), (\kappa'_3, \{\varepsilon'_1, \varepsilon'_4\})\}$

Here sn-Glc$(\tau_{R'}(X_1), U_1, O_1) = P(U_1)$ and so the identity function f: $(\tau_{R'}(X_1), U_1, O_1) \rightarrow (\tau_{R''}(X_2), U_2, O_2)$ is sn-glocally closed continuous.

Definition 4.4: A function f: $(\tau_{R'}(X_1), U_1, O_1) \rightarrow (\tau_{R''}(X_2), U_2, O_2)$ is an sn-Gω locally closed(briefly sn-Gωlc) continuous (resp.sn-G*ωlc-continuous, sn-Gωlc**-continuous) if $f^{-1}(K^*_1, O_1) \in$ sn-Gωlc$(\tau_{R'}(X_1), U_1, O_1)$($f^{-1}(K^*_1, O_1) \in$ sn-G*ωlc$(\tau_{R'}(X_1), U_1, O_1)$, $f^{-1}(K^*_1, O_1) \in$ sn-Gωlc**$(\tau_{R'}(X_1), U_1, O_1)$ resp.) for $(K^*_1, O_1) \in (\tau_{R''}(X_2), U_2, O_2)$.

Definition 4.5:A function f: $(\tau_{R'}(X_1), U_1, O_1) \rightarrow (\tau_{R''}(X_2), U_2, O_2)$ is sn-Gω locally closed irresolute (resp.sn-Gωlc*- irresolute, sn-Gωlc**-irresolute) if $f^{-1}(V^*_1, O_1) \in$ sn-Gωlc$(\tau_{R'}(X_1), U_1, O_1)$ (resp.$f^{-1}(V^*_1, O_1) \in$sn-Gωlc*$(\tau_{R'}(X_1), U_1, O_1)$, $f^{-1}(V^*_1, O_1) \in$sn-Gωlc**$(\tau_{R'}(X_1), U_1, O_1)$)for $(V^*_1, O_1) \in$sn-Gωlc$(\tau_{R''}(X_2), U_2, O_2)$ (resp. $(V^*_1, O_1) \in$sn-Gωlc*$(\tau_{R''}(X_2), U_2, O_2)$, $(V^*_1, O_1) \in$sn-Gωlc** $(\tau_{R''}(X_2), U_2, O_2)$).

Theorem 4.6: For a function f: $(\tau_{R'}(X_1), U_1, O_1) \rightarrow (\tau_{R''}(X_2), U_2, O_2)$,

i) If f is sn-lc continuous, then it is sn-Gωlc continuous.
ii) If f is sn-Gωlc (resp.sn-Gωlc*) continuous, then it is sn-Gωlc continuous.
iii) If f is sn-Gωlc-irresolute (resp. sn-Gωlc*irresolute, sn-Gωlc** irresolute) then it is sn-Gωlc (resp. sn-G*ωlc, sn-Gωlc**) continuous.

Proof: For $(I^*_1, O_1) \in$sn-O(X_2, O_2) and for f being sn-lc continuous,

i) $f^{-1}(I^*_1, O_1) \in$sn-lc$(\tau_{R'}(X_1), U_1, O_1)$ and $f^{-1}(I^*_1, O_1) \in$sn-Gωlc$(\tau_{R'}(X_1), U_1, O_1)$ for every $(I^*_1, O_1) \in (\tau_{R''}(X_2), U_2, O_2)$. Thus f is sn-Gωlc continuous.
ii) Each of the sn-Gωlc* and sn-Gωlc** sets is sn-Gωlc set, so the proof is obvious.
iii) As $(I^*_1, O_1) \in$sn-O(X_2, O_2), it is sn-Gωlc, sn-Gωlc* and sn-Gωlc**. The proof follows.

5. Conclusion:

In this paper, we developed the notion of locally closed sets and locally closed continuous functions in soft nano topological spaces. Also, the relationships between these new classes of Nano soft locally closed continuous function with the Nano soft locally closed irresolute are studied. We believe that these results will enhance the study of developments of information systems through Nano soft topological spaces and will help researchers to establish real-life applications through soft nano topology.

6. Acknowledgment:

Authors are thankful to the UGC, New Delhi, India for financial support under UGC SAP DRS-III: F-510/3/DRS-III/2016(SAPI) dated 29th Feb 2016 to the Department of Mathematics, Karnatak University, Dharwad, India.

References

[1] K. Balachandran, P. Sundaram and H. Maki, Generalized locally closed sets and GLC-continuous functions, Indian Journal of Pure and Applied Mathematics, 27(5), 661–669, (1997).

[2] S.S. Benchalli, P.G. Patil, N.S. Kabbur and J.Pradeepkumar, Weaker forms of soft nano open sets, Journal of Computer and Mathematical Sciences, 8(11), 589-599, (2017).

[3] S.S.Benchalli, P.G.Patil, N.S.Kabbur and J.Pradeepkumar, Onδ-operations in soft nano topological spaces, Journal of Computer and Mathematical Sciences, 9(8), 1001-1016, (2018).

[4] S.S. Benchalli, P.G. Patil, N. S. Kabbur and J.Pradeepkumar, On soft nano continuity in soft nano topological spaces and its applications, Annals of Fuzzy Mathematics and Informatics, 15(3), 265-283, (2018).

[5] K. Bhuvaneshwari and K. Mythili Gnanapriya. On nano generalized locally closed sets and NGLC-continuous functions in nano topological spaces, International Journal of Mathematics and its Applications, 4(1-A), 101-106, (2016).

[6] CJR Borges, On extensions of topologies, Canadian Journal of Mathematics, 19, 474-487, (1967).

[7] N. Bourbaki, General Topology, Part I, Addison Wesley, Reading Mass, (1966).

[8] M. Ganster, I. L. Reilly and M. K. Vamanamurthy, Locally Closed Sets and LCContinuous Functions, International Journal of Mathematical Society, 12, 417–424, (1989).

[9] A.Jayalakshmi and C. Janaki, A new form of nano locally closed sets in nano Topological Spaces, Global Journal of Pure and Applied Mathematics,13(9), 5997-6006, (2017).

[10] C. Kuratowski, Sierpinski W. Sar Les Differences de deux ensemble fermes, Tobuku Mathematica Journal,20, 22–25, (1921).

[11] D. Molodtsov, Soft set theory-first results, Computers and Mathematics with Applications, 37, 19-31, (1999).

[12] M. Mohammed Khalaf and Kamal N. Nimer, Nano Ps-open sets and Ps-continuity, International Journal of Contemporary Mathematical Sciences, 10 (1), 1-11, (2015).

[13] A. Nasef, A. I. Aggour and S. M. Darwesh, On some classes of nearly open sets in nano topological spaces, Journal of Egyptian Mathematical Society, 24 (4), 585-589, (2016).

[14] P. G. Patil, S. S. Benchalli and Pallavi S. Mirajakar, Decomposition of Locally Closed Sets in Topological Spaces, Advances in Fuzzy Mathematics, 12(1),101–110, (2017).

[15] P. G. Patil and Spoorti S. Benakanawari, On Soft Nano Resolvable Spaces and Soft Nano Irresolvable Spaces in Soft Nano Topological Spaces, Journal of Computer and Mathematical Sciences, 10 (2), 245-254, (2019).

[16] P. G. Patil and Spoorti S. Benakanawari, Modified forms of Soft Nano Contra Continuous Functions, Journal of Mathematical and Computational Sciences, 10(4), 1176-1191, (2020).

[17] P. G. Patil and Spoorti S. Benakanawari, New Aspects of closed sets in Soft Nano Topological Spaces,(Communicated).

[18] P. G. Patil and Spoorti S. Benakanawari, A Study on Various Soft Nano Continuous Functions and Soft Nano Homeomorphisms, Malaya Journal of Matematik,8(3), 924-929, (2020).
[19] A. Stone, Absolutely FG Spaces, Proc. Amer. Math. Soc. 80, 515–520, (1980).
[20] M. L. Thivagar and Carmel Richard, On Nano continuity, Mathematical Theory and Modeling, 3(7), 32-37, (2013).
[21] M. L. Thivagar and C. Richard, On Nano forms of weakly open sets, International Journal of Mathematical and Statistical Invention, 1(1), 31-37, (2013).

Karnatak University
Journal of Science

ISSN: 0075-5168

Treatment of Anabolic-Androgenic Steroid Stanozolol Hinders Embryo Development and Implantation in Mice

Chaitra R. Sharma
Laxmi S. Inamdar (Doddamani)

Chaitra R. Sharma and Laxmi S. Inamdar (Doddamani), “Treatment of Anabolic-Androgenic Steroid Stanozolol Hinders Embryo Development and Implantation in Mice” Karnatak University Journal of Science 51, 131-139 (2020).

Treatment of Anabolic-Androgenic Steroid Stanozolol Hinders Embryo Development and Implantation in Mice.

Chaitra R. Sharma[1] and Laxmi S. Inamdar (Doddamani)[1,*]
[1]Molecular Endocrinology, Reproduction and Development Laboratory, Department of Zoology, Karnatak University, Dharwad 580 003, India
**** Corresponding author:** Prof .Laxmi S. Inamdar (Doddamani)*
E-mail:ls_doddamani@yahoo.com; Tel: +91-836-2215230 (O); +91-836-2955168 (R)

Abstract:

Anabolic-androgenic steroids (AAS) are synthetic variants of testosterone being abused by athletes and sportsmen to boost muscle strength and to enhance performance in sports. Recently the abuse of these drugs by teenagers is increased dramatically. The present study aimed to evaluate the effect of one of the AAS compounds stanozolol on preimplantation embryos and implantation in mice. Female mice were mated with fertile males in 1:2 ratios. Vaginal plug positive day was considered as gestation day (GD) 0.5. After confirmation of gestation, mice were assigned to two experimental groups. First group served as control received vehicle alone (1% alcohol), second group received stanozolol (0.5 mg/kg bwt in 1% alcohol) from GD0.5 to 9.5. All female mice from the control and treatment group were autopsied on GD9.5. The number of corpora lutea and implantation sites was counted, and preimplantation loss was calculated in both control and treatment group. In general, the number of implantation sites correlates with the number of corpora lutea. However, a decrease in the number of implantation sites was noticed in stanozolol treated mice when compared to control. The observed results reveal an increase in the preimplantation embryo loss in stanozolol treated mice when compared to control. Further, histomorphology of ovary revealed regression of corpora lutea in stanozolol treated mice disclosing induction of luteolysis. It is concluded that the stanozolol may interfere with preimplantation embryo development by negatively regulating LH secretion from pituitary besides it possesses a potent luteolytic activity.
Key words: Corpus luteum; implantation; preimplantation loss; stanozolol; mouse.
Article history: Received: 22 August 2020; Revised: 6 September 2020**;** Accepted: 8 September 2020

1. Introduction:

Anabolic-androgenic steroids (AAS) are the synthetic variants of natural hormone testosterone. The AAS compounds are originally developed for the treatment of (usually in small doses) aplastic anemia, endometriosis, male hypogonadism, inoperable breast cancer, chronic illness, trauma, and osteoporosis [1-3]. However, these are being abused by bodybuilders, both male and female professional and recreational athletes to improve athletic performance, physical appearance, endurance, and vigor [3, 4-6]. The beneficial potential of AAS can come at the cost of a variety of secondary adverse effects like hepatocarcinoma, altered cholesterol and liver enzyme profiles, reproductive and endocrine disturbances [5, 7, 8]. Even though extensive laboratory studies have revealed multiple adverse effects of AAS on the female reproductive system and fertility [9, 10], the efficacy of these compounds on embryo implantation and early pregnancy maintenance is largely unknown. The administration AAS

also leads to histopathological alterations in the ovaries and uterus in rodents [11-14]. In a previous experiment from our laboratory, we have noted that stanozolol (ST) accelerates granulopoiesis and stimulates an immune response (at a physiologic level only), though it alters the lipoprotein profile in mice [15]. In another report, ST interrupted pregnancy in mice and its effect was mediated through a reduction in later stage follicles, principally due to the deficiency of luteal hormones [16]. Unfortunately, there have been no studies that document the effect of AAS on early pregnancy (pre and periimplantation period). Considering these premises, the present investigation was undertaken to evaluate the efficacy of one of the AAS compound stanozolol (17β-hydroxy-17α-methyl-androstano (3, 2-c) pyrazole; ST) on preimplantation embryo development and implantation in mice.

2. Materials and methods:

All protocols used in this experiment adhered to the CPCSEA guidelines for the Care and Use of Laboratory Animals approved by the Institutional Animal Ethical Committee No.639/GO/02/a/CPCSEA at Department of Zoology, Karnatak University, Dharwad.

In total, 20 sexually mature female Swiss albino 'strains' (Two to three months old, weighing 25 to 30 gms) exhibiting regular estrous cyclicity were obtained from mice breeding centre, maintained in the Department of Zoology, Karnatak University, Dharwad. All mice were housed in individual polypropylene cages, maintained 12 h light: dark cycle at 27±1˚C with 40-50% relative humidity. Food (pelleted diet, Goldmohur, Lipton, India) and water supplied *ad libitum*.

2.1. **Mating and Hormone treatment:** In the present experiment, one of the AAS compound stanozolol (ST, Sigma Chemical Co., St. Louis, MO, USA) was used. Female mice were cohabitated with males of proven fertility with 1:2 ratios at proestrus or early estrus phase. Phases of the estrous cycle were determined by cytological evaluation of the vaginal smears performed daily at 8.00 am. Mating was confirmed by the detection of a vaginal copulatory plug and defined as gestation day (GD) 0.5. After confirmation of gestation, 16 female mice were assigned to two experimental groups, and ST was administered via subcutaneous injection [0.5 mg/kg bwt in 0.5 ml of 1% alcohol, n=8; or 0.5 ml of 1% alcohol - vehicle control, n=8] from GD0.5 to GD9.5 of pregnancy.

On GD9.5, the control and ST treated mice were weighed and sacrificed by following CPCSEA guidelines. The ovaries were isolated, and the number of corpora lutea was counted by direct visualization with the aid of a stereomicroscope (Olympus SZ, Tokyo, Japan). The two-horned uteri were removed and visually inspected to identify implantation sites. The rate of preimplantation loss was calculated using the formula as described elsewhere [17, 18].

$$\%\ \text{pre} - \text{implantation loss (PIL)} = \frac{\text{No. of corpora lutea} - \text{No. of implantation sites}}{\text{No. of corpora lutea}} \text{ x } 100$$

2.2. **Histology of the ovary:** Immediately after the autopsy, the ovaries were fixed in Bouin's fluid, dehydrated in a series of increasing concentrations of ethanol (10% - 100%), clarified in benzene, and embedded in paraffin. Paraffin blocks containing tissues were sectioned at 5µm on a rotary microtome (Leica RM 2025, Germany). Tissue sections were mounted on glass slides. Sections were rehydrated in descending concentrations of ethanol, stained with Haematoxylin and Eosin and observed under Nikon Eclipse 80i, and images were acquired using ACT-2U software (Nikon Corporation, Tokyo, Japan).

2.3. Isolation of embryos: The uteri with implanted embryos were rinsed with PBS. Implantation sites were separated and embryos were isolated from the uterus by following the protocol described earlier [19]. The embryos were photographed and fixed in Bouin's fluid.

2.4. Statistical analysis: All data were tested, and normality of the data distribution was established. The weights of the uteri, ovaries, and adrenal, number of implantation sites and corpora lutea, and percent preimplantation loss were calculated in each female and averaged. The comparison of the control group to the treatment group is tested with the help of Independent Samples t-Test. Data were expressed as mean ± SE using the Statistical Package of Social Science (SPSS) version 26.0 (IBM, Chicago, IL, USA). The degree of statistical significance was set at $p<0.05$ and $p<0.01$.

3. Results and Discussion

3.1 Effect on implantation and embryo morphology: In the current study, effect of one of the AAS compounds ST on preimplantation embryo development and implantation has been investigated in mice. The results demonstrate that there was a significant reduction in uterine weight ($P<0.01$) and an insignificant decrease in ovarian weight ($P>0.05$) was noticed in ST treatment group when compared to control. Besides a considerable reduction ($P<0.05$) in the adrenal weight was noticed as compared to the control (Table 1). All female mice in the control group were conceived with a 6.628 ± 2.21 % of preimplantation loss (Fig. 1B). The number of implantation sites (11.50 ± 0.42) correlates with the number of corpora lutea (12.375 ± 0.56, $t_{14}=1.240$, $P > 0.05$, Fig. 1A). The observed results reveal that in ST treated mice, the number of implantation sites were significantly decreased (8.87 ± 0.47, $t_{14} = 5.048$; $P < 0.01$) when compared to the number of corpora lutea (12.50 ± 0.53, Fig. 1A). In addition, an increase in the preimplantation embryo loss in ST treated mice was perceived when compared to control (28.075 ± 4.93 %, $P<0.05$, Fig. 1B). The observed results reveal that exposure to ST may interfere with uterine receptivity, blastocyst survival that may lead to the prevention of implantation. This inhibition could have resulted from the alterations in the levels of steroid hormones and paracrine factors involved during preimplantation embryo development and implantation. It appears that the effect of ST is not directly detrimental to the embryos, but acts either on the ovaries or indirectly via pituitary to inhibit progesterone synthesis, thereby leading to embryo loss and exhibits anti-implantation effect in mice. We further analyzed the morphological features of embryos in both the control and ST treatment group on GD9.5. Embryos recovered from the control group were healthy, and their morphological characteristics were normal (Fig 2A). However, the embryos in the ST treatment group revealed a slight abnormality in the cranial region on GD9.5 (Fig 2B).

Table-1. Organ weight in control and ST treatment group

SI. No.	Observations	Control mice (n=8)	ST treated mice (n=8)	P value
1	Uterus weight (gm)	1.95±0.24	0.80±0.29	<0.01
2	Ovary weight (gm)	0.0098±0.00076	0.0086±0.00096	>0.05
3	Adrenal weight (gm)	0.0078±0.00075	0.0057±0.0013	<0.05

Values are expressed as mean ±SE n=number of mice

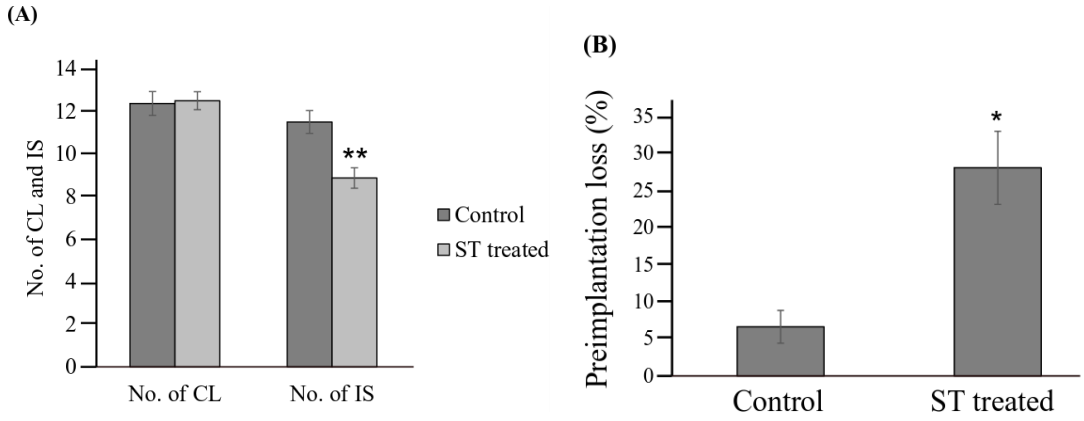

Figure 1. (A) Treatment of ST from GD0.5 to GD9.5 leads to decrease in the number of corpora lutea and number of implantation sites when compared with that of control mice. **(B)** The treatment of ST leads to increased preimplantation loss when compare to control, indicating deleterious impact of ST on preimplantation embryo and implantation. IS- implantation sites; CL- corpora lutea . * = P<0.05; ** = P<0.01.

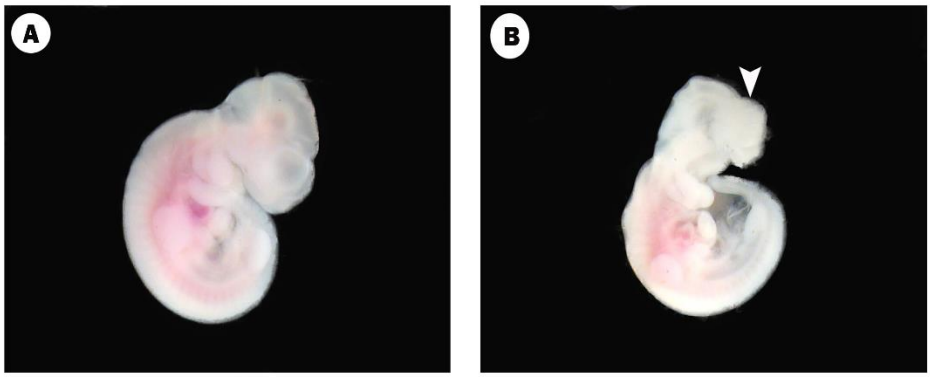

Figure 2. Effect of ST on embryo morphology. **(A)** E9.5 Embryo of control mice. **(B)** E9.5 Embryo of ST treated mice showing slight abnormality in the cranial region (Arrow head). Magnification- 1.6X

Previous studies suggested that androgen levels are higher in women who have recurrent miscarriages than in normal fertile women [20]. High androgen levels had a negative impact on endometrium leading to infertility and miscarriage in women [21]. It is also reported that preimplantation exposure of dehydroepiandrosterone (DHEA) leads to implantation failure in mice [22]. Dihydrotestosterone (DHT), a non-aromatizable androgen, affect the reproductive capacity in female mice by degenerating ova in the oviduct, and there is a significant reduction in the number of females becoming pregnant and bearing normal foetuses [23]. However, in a recent *in vitro* study, neither physiologic nor supraphysiologic doses of DHT affect the preimplantation embryo development in mice [24].

3.1. **Histoarchitecture of Ovary:** The ovarian corpus luteum is known to play a key role in embryo implantation and pregnancy maintenance by continuously secreting progesterone [25]. Exogenous steroid administration at high doses during these critical phases of pregnancy may alter the proper functioning of the uterine microenvironment by affecting ovarian steroidogenesis.The functions of the corpus luteum in rodents are regulated by a luteotropic

hormonal complex. The pituitary plays an indispensable role, particularly in the early part (first half) of the pregnancy, which is mediated through the hypothalamic- hypophyseal-gonadal-adrenal-placental axis [26-28]. Hence, in the current study, the ovaries from control and treatment groups were subjected to histological evaluation of corpus luteum. Transverse section (T.S.) of the ovary of control mice shows large number of well-developed corpora lutea, growing follicles of different stages, and stroma (Fig 3A and C). Ovaries of few but not all animals in the ST treatment group show signs of polycystic ovary syndrome (PCOS) with corpus luteum having pyknotic nucleus signifying luteal regression (Fig 3B and D).

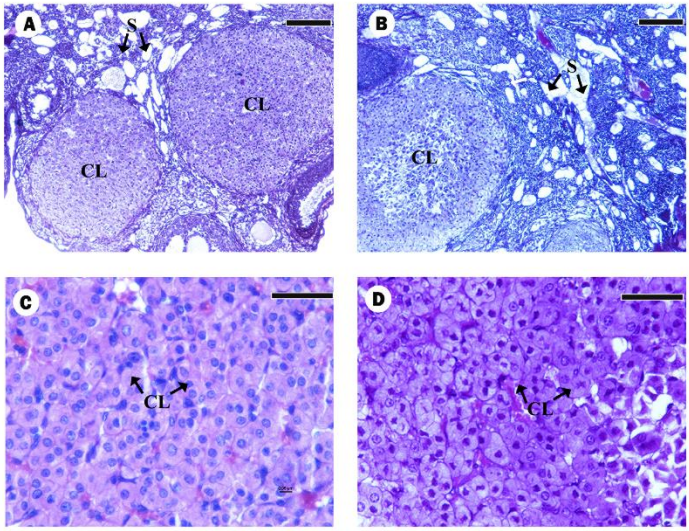

Figure 3. Effect of ST on ovarian histoarchitecture. **(A)** T.S of the ovary of the control pregnant mice showing healthy corpus luteum and ovarian stroma **(B)** T.S of the ovary of the pregnant mouse treated with ST from GD0.5 to 9.5, showing bulky ovarian stroma with vacuoles. 100X magnification. **(C)** Higher magnification of Fig. A. **(D)** Higher magnification of Fig. B, showing pyknotic nucleus indicating luteolytic effect. CL–Corpus luteum; S–Stroma.
Scale bar - A and B – 50µm; C and D - 30µm.

In the present investigation, the progression of luteolysis observed in treatment group indicating that ST may affect implantation by interrupting the functioning of the corpus luteum. As the estrogen and progesterone are obligatory for implantation, the observed results also suggest that inadequate progesterone production is the major cause of infertility and embryo loss since progesterone is essential for both endometrial growth and embryo survival. Regression of corpora lutea in the treatment group indicates that ST may affect the luteal maintenance of early pregnancy by negatively regulating LH secretion from pituitary or may stimulate uterine endometrial luteolytic factor prostaglandin $F_2\alpha$. A previous report from our laboratory on mice reveals that administration of ST from day 8 to 14 and day 8 to 19 of pregnancy interrupts pregnancy, and its effect was mediated through a reduction in later stage follicles, and principally due to deficiency of luteal hormones [16]. The results of the present investigation support the earlier report and suggest that treatment of ST during pre and periimplantation period may affect implantation by disrupting uterine receptivity or preimplantation embryo loss. Besides, it discloses that ST possesses a potent luteolytic activity when administered before day 12.

Conclusion:

Treatment of ST during pre and periimplantation period affects implantation by disrupting uterine receptivity or preimplantation embryo loss by negatively regulating LH secretion from the pituitary. It is inferred that ST possesses a potent luteolytic activity.

Acknowledgement:

All procedures used in this experiment adhere to CPCSEA guidelines for the care and use of laboratory animals approved by the Institutional Animal Ethical Committee No. 639/02 at Department of Zoology, Karnataka University, Dharwad. One of the authors (CRS) thank DST for granting INSPIRE fellowship. The work is financially supported by the UGC, New Delhi under CPEPA and SAP-DSA-I Programme.

References

1. K. Doney, M. Pepe, R. Storb, F. Bryant, C. Anasetti, F. R. Appelbaum, C. D. Buckner, J. Sanders, J. Singer, K. Sullivan, P. Weiden and J. A. Hansen, Immunosuppressive therapy of aplastic anemia: Results of a prospective, randomized trial of anti thymocyte globulin (ATG), methyl prednisolone, and oxymetholone to ATG, very high-dose methylprednisolone, and oxymetholone, Blood (American Society of Hematology) 79, 2566-2571 (1992).
2. C. D. Kochakian, Anabolic-androgenic steroids: A historical perspective and definition, In: Anabolic Steroids in sports and exercise C. E. Yesalis ed., Kinetics Publishers: Inc Champaign, p3-33. (1993)
3. S. E. Lukas, CNS effects and abuse liability of anabolic androgenic steroids. Annual Review of Pharmacology and toxicology (Annual Reviews Inc) 36, 333-357(1996).
4. S. J. Basaria, T. A. Wahlstrom and S. Dobs, Anabolic-androgenic steroid therapy in the treatment of chronic diseases, Journal of Clinical Endocrinology and Metabolism (Endocrine Society) 86, 5108-5117 (2001)
5. C. Maravelias, A. Dona, M. Stefanidou and C. Spiliopoulou, Adverse effects of anabolic steroids in athletes A constant threat, Toxicology letters (Elsevier) 158, 167-175(2005).
6. R. H. Strauss and C. E. Yesalis, Additional effects of anabolic steroids on women. In: Anabolic Steroids in Sport and Exercise, 151–160 (1993).
7. N.A. Evans, Current concepts in anabolic androgenic steroids. American Journal of Sports Medicine (SAGE) 32, 534-542(2004).
8. J. D. Wilson, Androgen abuse by athletes, Endocrine Reviews (Oxford Academic) 9, 181-199 (1988).
9. M. E. Blasberg, C. J. Langan and A. S. Clark, The effects of 17 α - methyltestosterone, methandrostenolone, and nandrolone decanoate on the rat estrous cycle. Physiology and Behavior (Elsevier) 61, 265–272 (1997).
10. A. S. Clark, M. E. Blasberg and E. M. Brandling-Bennett, Stanozolol, oxymetholone, and testosterone cypionate effects on the rat estrous cycle, Physiology and Behavior(Elsevier)63, 287-295(1998).
11. L. G. De Almeida Chuffa, R. B. de Souza, F. Frei, S. F. P. Mesquita and I. C. C. Camargo, Nandrolone decanoate and physical effort: histological and morphometrical assessment in adult rat uterus, Anatomical Records (Wiley) 294, 335-341 (2010).
12. I.C.C. Camargo, A.L.G. Camolezi, F. Frei and S.F.P. Mosque, Effects of anabolic androgenic steroids on the uterus and reproductive parameters of adult rats, Revista

Brasileira de Ginecologia e Obstetricia (Federação Brasileira das Sociedades de Ginecologia e Obstetrícia) 31, 453-460 (2009).
13. J. R. Gerez, F. Frei and I.C.C. Camargo, Histological assessment of ovaries and uterus of rats subjected to nandrolone decanoate treatment, Contraception (Elsevier)72, 77-80 (2005).
14. H. R. Mobini Far, G. Agren, A. Lindqvist, M. Marmendal, C. Fahlke and I. Thiblin, Administration of anabolic androgenic steroid nandrolone decanoate to female rats causes alterations in the morphology of their uterus and a reduction in reproductive capacity, European Journal of Obstetrics and Gynecology and Reproduction Biology (Elsevier) 131, 189-197 (2007).
15. L. S. Inamdar (Doddamani), Y. Jayamma, Acceleration of neutrophil precursors' maturation and immunostimulation of $CD3^+$, $CD4^+$ lymphocytes by stanozolol in mice, Journal of Steroid Biochemistry and Molecular Biology (Elsevier) 129, 172-178 (2012).
16. Y. Jayamma, G. M. Advirao and L.S. Inamdar, Anabolic-androgenic steroids (stanozolol) disrupts ovarian histoarchitecture and gestation in mice, International Journal of Current Research (Radiance Research Academy) 4,32-36(2012).
17. N. Balasinor, P. Parte, M. Gill-Sharma and H. Juneja, Effects of tamoxifen on sperm fertilizing ability and preimplantation embryo development, Molecular and Cellular Endocrinology (Elsevier) 178, 199-206(2001).
18. M. K. Gill-Sharma, K. Gopalkrishnan, N. Balasinor, P. Parte, S. Jayaraman and H. S. Juneja, Effects of tamoxifen on the fertility of male rats, Journal of Reproduction and Fertility (Avicenna Research Institute)99, 395-402 (1993).
19. K. Shea and N. Geijsen, Dissection of 6.5 dpc mouse embryos, Journal of Visual Experiments (MyJove Corp) 2007.
20. M. A. Okon, S. M. Laird, E. M. Tuckerman and T. C. Li, Serum androgen levels in women who have recurrent miscarriages, and their correlation with markers of endometrial function, Fertility and Sterility (Elsevier) 69, 682-690 (1998).
21. E. M. Tuckerman, M. A. Okon, T. Li, & S. M. Laird, Do androgens have a direct effect on endometrial function? An in vitro study, Fertility & Sterility (Elsevier) 74, 771-779 (2000).
22. S.Y. Li, Z. Sog, M.J. Song, J.W, Qin, M.L. Zhao and Z.M. Yang, Impaired receptivity and decidualization in DHEA-induced PCOS mice, Scientific Reports (Nature Research) 6, (2016)
23. T. D. Nandedkar and S. R. Munshi, Effect of dihydrotestosterone on follicular development, ovulation and reproductive capacity of mice, Journal of Reproduction andFertility(Avicenna Research Institute)62, 21-24(1981).
24. N. R. Chappel, H. Sangi-Haghpeykar, W. E. Gibbons and C. S. Blesson, The effects of dihydrotestosterone on mouse early embryonic development, Fertility and Sterility (Elsevier)108 (suppl 3) e155(2017).
25. F. W. Bazer, R. C. Simmen and F.A. Simmen, Comparative aspects of conceptus signals for maternal recognition of pregnancy (1991).
26. D. W. Brann, C. D. Putrum and V. B. Mahesh, Corticosteroid regulation of gonadotrophin and prolactin secretion in the rat, Endocrinology (Oxford Academic) 126, 159-166 (1990).
27. G. Mastorakos, and I. Ilias, Maternal and fetal hypothalamic-pituitary-adrenal axis during pregnancy and postpartum, Annals of the New York Academy of Sciences (Wiley-Blackwell) 997, 136-149 (2003).

28. R. H. Strauss, M. T. Liggett and R. R. Lanese, Anabolic Steroid use and perceived effects in ten weight trained woman athletes, JAMA (American Medical Association) 253, 50-57 (1985).

Karnatak University

Journal of Science

ISSN: 0075-5168

Growth of Ternary Alloy of CdZnS/CdZnSe Nanorod Heterostructures

M. N. Kalasad

M. N. Kalasad, “A Growth of Ternary Alloy of CdZnS/CdZnSe Nanorod Heterostructures” Karnatak University Journal of Science 51, 140-146 (2020).

Growth of Ternary Alloy of CdZnS/CdZnSe Nanorod Heterostructures

M. N. Kalasad*
Department of Studies in Physics, Davangere University, Davangere 577007, India.
***Corresponding author:**mnkalasad@gmail.com

Abstract

The design of ternary alloy of CdZnS/CdZnSe nanorod heterostructures (NRHs) using sequential cation exchange reaction technique. The cationic sublattice can be replaced with different metal ion via fast, simple, partial, fully and reversible exchange. The initial CdS/CdSe NRHs are synthesized using non coordinating solvent route and conversion of CdS/CdSe to CdZnS/CdZnSe nanorod heterostructures by partial cationic exchange reaction without affecting morphological and structural changes of the initial nanorod heterostructures. The tuning of photoluminescence is done by controlling the composition and concentration of cations. These nanoheterostructures exhibit high stability and the PL is purely due to band-edge emission with potential applications as nano-scale optoelectronic devices.
Keywords: NRHs; Alloy; Semiconductor; Nanocrystals; Size; TEM.
Article history: Received: 14 August 2020; Revised: 22 August 2020; Accepted: 24 August 2020;

1. Introduction

Semiconductor nanocrystals (NCs) have received increasing attention during last three decades in basic research and technological applications. Achieving fine-tunability in the optoelectronic properties of colloidal NCs is one of the main focuses of research in nanoscience and engineering, ever since the new field of wet chemical synthesis of these types of materials has emerged [1-3]. The synthesis of colloidal NCs has progressed to a point that fine level of control over structural, shape, size and compositional parameters are possible for lot of materials systems [4-8]. Among these types of (NRHs), the semiconductor - semiconductor heterostructures are those that have been exploited the most. Here, the fine-tuning of the size, shape, spatial orientation, composition, and crystalline structure of the component materials enables a careful adjustment of the relative band alignments of both semiconductors and, thus, allows for a tight control over the physical and optical properties of the hybrid nanostructures.

In recent years semiconductor alloy NCs have gained much attention because of their tunable composition, high quantum yield, better stability and spectral tunability in the blue-yellow region without the need to change the NC size [9, 10]. Colloidal NCs possess anisotropic shapes offers platform for selective chemical modification based on the relative reactivities of the different crystalline facets exposed at the surface. This enables the synthesis of multi component nanostructures through the nucleation and growth of a secondary material on specific facets of the NCs. The methodology of sequential growth has been applied to a broad range of material combinations, its main drawback is that the desired heterogeneous nucleation on the existing nanocrystal surface often fight with homogeneous nucleation of separate NCs of the secondary material. An alternative method for synthesizing nanocrystal

heterostructures, which avoids separate nucleation, is the transformation of a portion of the nanocrystal into a new composition or structural phase [11-13]. A recent technique for the synthesis of NCs by cation exchange reactions by which the sublattice of cations in ionic NCs can be replaced with new sublattice of other cations with preserving the characteristic of the crystallographic sites involved in ion substitution, while the sublattice of anions remain in position, which yields NCs of new material same size and shape of the starting NCs [14, 15]. Therefore, cation exchange reactions provide a new direction to design novel NCs with specific morphology yields have been used to alter the composition of the material by replacing the cations within the nanocrystal lattice with different metal ions.

Herein, the growth of ternary alloy of CdZnS/CdZnSe NRHs by non-coordinating solvent through sequential cation exchange reaction technique to achieve desired size and luminescence.

2. Materials and experimental methods

2.1 Materials

All chemical used in the present work were of analytical grade. CdO (99.9 %), oleic acid (OA, 90 %), 1-octadecene (1-ODE, 90 %), trioctylphosphine (TOP, 90 %), Se powder (99.99%), S powder (99.98%), Zn acetate (99.99%), 1-octadecene (ODE) (90%), oleic acid (OA) (90%), oleylamine (70%), Cu(I) acetate (97%), $ZnCl_2$ (anhydrous 97%), tetrakis (acetonitrile)copper(I) hexafluorophosphate ($Cu(CH_3CN)_4]PF_6$) (97%) were purchased from Sigma-Aldrich and used as purchased.

2.2 Experimental methods

Initially, CdS/CdSe NRHs are synthesized using non coordinating solvent method. The reactions were carried out in a standard Schlenk line under N_2 atmosphere. 11.5mmol of trioctylphosphine oxide (TOPO), (2.5mmol) of ODPA and 0.16 g of CdO in a 50 ml three-neck round bottom flask were degassed at 140^{o}C for 50 min under N_2. Sulphur precursor containing 0.6mmol of S dissolved in 2.0 ml of TOP and was swiftly injected into the three neck flask with a syringe at 365^{o}C.Consequently, the reaction mixture was quenched to 320^{o}C, the growth of CdS nanorods was carried out. 14 min later, the evolution was terminated by cooling to 240^{o}C. Later, 0.20mmol of Se dissolved in 1.3 ml of TOP was slowly injected at 240 ^{o}C at a rate of 1 ml per 12 minutes using syringe pump. The reaction mixture was then allowed to stir for another 10 min at 240^{o}C and cooled quickly by an air jet. Cation exchange reactions were carried out in glove box for the design of CdZnS/CdZnSe NRHs by Cu^+ ions using Cu (I) as source in methanol. Optical absorption measurements were carried out using an Agilent 8453 photodiode array spectrometer. Photoluminescence (PL) spectra were collected using HORIBA JobinYvon FluoroMax-3 spectrofluorometer. Transmission electron measurements (TEM) analysis was carried out using JEOL 2100 TEM at 200 kV. TEM samples were prepared using Cu grid with ultrathin carbon film by drop-casting a solution of NRHs.

3. Results and discussions

The amount of conversion depends on Cu^{+}/Cd^{2+} ratio, where an excess amount of Cu^{+} ions leads to full conversion to Cu_2S [16,17]. Here, cation exchange reaction was partial. The Cu^{+} cation exchange was used to convert Cd^{2+} to Cu^{+} ions leads CdS/CdSe to $Cu_xCd_{1-x}S/Cu_yCd_{1-y}Se$ NRHs. Later, Zn^{2+} cations are incorporated to replace Cu^{+} ions and leads to the formation of ternary alloy of $Cd_xZn_{1-x}S/Cd_yZn_{1-y}Se$ NRHs as shown in Scheme 1.

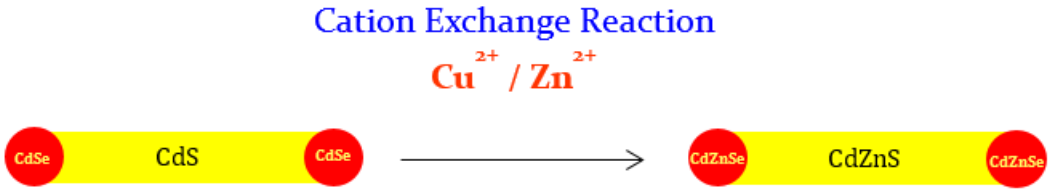

Scheme 1. Schematic illustration of growth of alloy CdZnS/CdZnSe NRHs through cation exchange reaction.

Optical absorption measurements were carried out on initial CdS/CdSe NRHs and CdZnS/CdZnSe NRHs. Figure 1 shows the optical absorption spectrum of initial CdS/CdSe

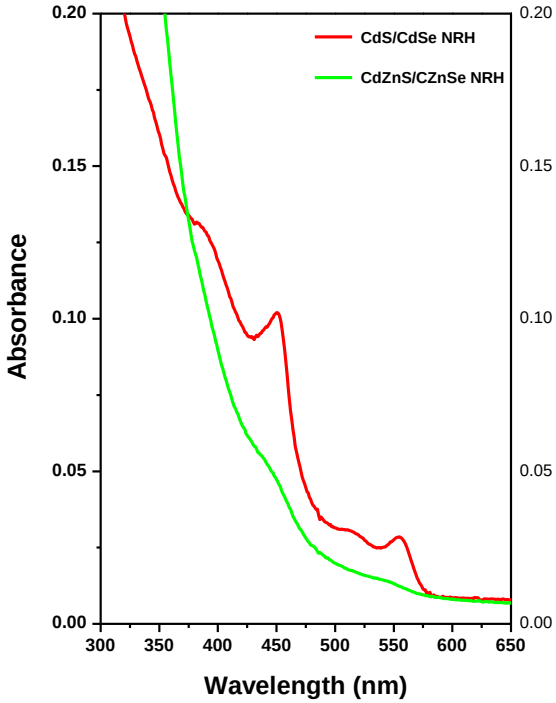

Figure 1. Optical absorption spectra of CdS/CdSe and CdZnS/CdZnSe NRHs.

and CdZnS/CdZnSe NRHs. The well-defined excitonic peak of CdS/CdSe NRHs indicates the narrow size distribution. CdZnS/CdZnSe spectrum indicates absence of excitonic peak at 451 nm and 555 nm due to cation exchange reaction by Zn^{2+} ions.

The fluorescence measurements were recorded for CdS/CdSe and CdZnS/CdZnSe NRHs. The observed single narrow emission peak at 563 nm is due to excitonic band emission and indicates there are no trap states on the surface of CdS/CdSe NRHs. Figure 2 depicts the

PL spectrum of CdZnS/CdZnSe NRHs. The emission peak at 471 nm and 555 nm is due to the presence of Zn and Cd composition. The estimated PL quantum yield (QY) is 32% when excited. By varying the concentration of Cd/Zn ions, the spectral tunability will covered by entire visible spectrum.

TEM measurements were carried out for the morphological study of the CdS/CdSe and alloy CdZnS/CdZnSe NRHs. Figure 3(a) and 3(b) illustrates the TEM and high resolution TEM (HRTEM)micrographs of CdZnS/CdZnSe nanocrystal. The average estimated length of NRHs is 22.30 nm and corresponding width is 2.75 nm. The lattice constant values were calculated using Gatan Digital Micrograph Software. The estimated lattice constant values are 3.95 Å and 4.15 Å at the centreand tip of the rod respectively. The lattice vales indicates the existence of CdZnS at the centre CdZnSe at the tip.

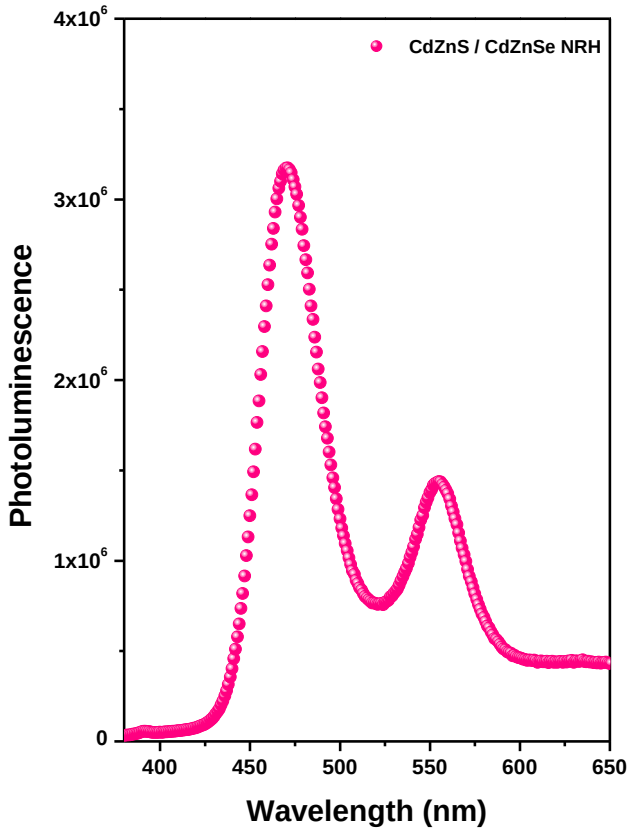

Figure 2. Photoluminescence spectrum of CdZnS/CdZnSe NRHs.

a)

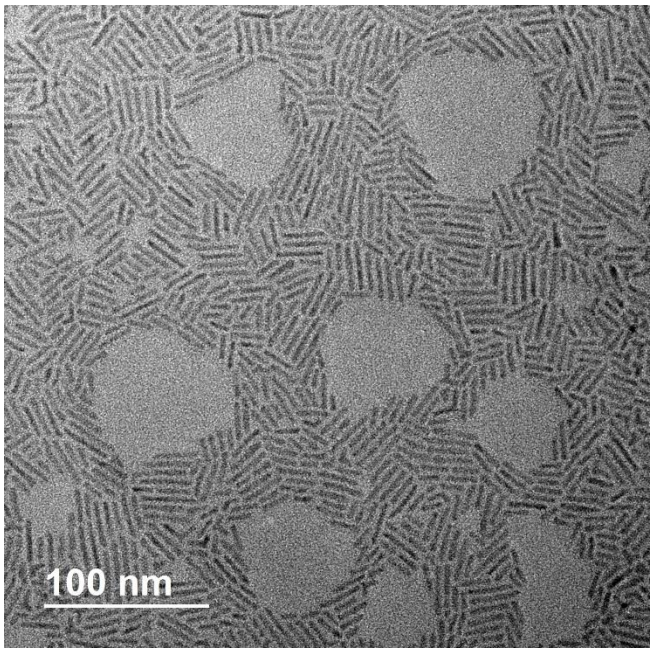

b)

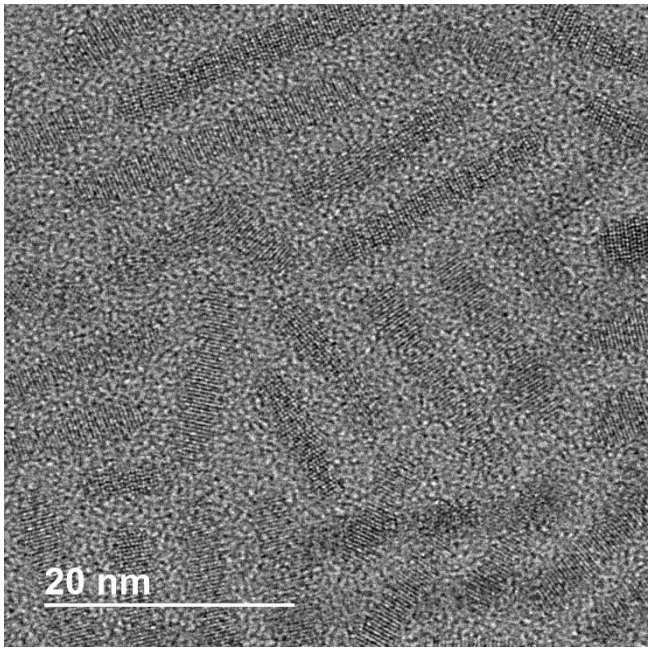

Figure 3. (a)TEM and (**b**) HRTEM images of CdZnS/CdZnSe NRHs.

4. Conclusions

In summary, the prepared alloy CdZnS/CdZnSe NRHs using non coordinating solvent via cation exchange route. These CdZnS/CdZnSe NRHs preserve the morphological and structural features of their parent CdS/CdSe nanoheterostructures. These structures are highly monodisperse in nature. PL emission can be tuned systematically by varying the composition and the concentration of cations. Better spectral tunability can be achieved by entire visible spectrum.

Acknowledgments
Author would like to thank University Grants Commission (UGC), New Delhi for the support of Raman Fellowship for Post-Doctoral Research in USA.

References:

[1] Excitons in nanoscale systemsG. D. Scholes andG. Rumbles,Nat. Mater. (Nature Publ.), 5, 683-696, (2006).
[2] Light-emitting diodes made from cadmium selenide nanocrystals and a semiconducting polymerV. L. Colvin, M. C. Schlamp and A. P. AlivisatosNature (Nature Publ.), 370, 354−357 (1994).
[3] Small Is Different: Shape-, Size- and Composition-dependent properties of some colloidal semiconductor nanocrystalsM. A. El-Sayed Acc. Chem. Res. (ACS), 37, 326-333, (2004).
[4] Synthesis of CdS and CdSe nanocrystallites using a novel single-molecule precursors approachT. Trindade, P. O'Brien andX. ZhangChem. Mater.(ACS), 9, 523-530, (1997).
[5] Prospects of colloidal nanocrystals for electronic and optoelectronic applicationsD. V. Talapin and V. LeeChem. Rev. (ACS), 110, 389-458, (2010).
[6] A general and robust strategy for the synthesis of nearly monodisperse colloidal nanocrystals.Nat. NanotechX. Pang, L. Zhao, Z. Lin(Nature Publ.),8,426-431, (2013).
[7] Colloidal nanocrystal synthesis and the organic-inorganic interfaceY. Yin andA. P. AlivisatosNature (Nature Publ.), 437, 664-670, (2005).
[8] Ambient synthesis and characterization of high-quality CdSe quantum dots by an aqueous routeM. N. Kalasad M. K. Rabinal and B. G. Mulimani Langmuir (ACS), 25, 12729–12735, (2009).
[9] Composition-tunable alloyed semiconductor nanocrystalsM. D. Regulacio and M. HanAcc. Chem. Res. (ACS), 43, 621-630, (2010).
[10] Forging colloidal nanostructures via cation exchange reactionsL D Trizio and L MannaChem. Rev.(ACS), 116, 10852-10887, (2010).
[11] Shape-controlled synthesis of gold and silver nanoparticlesY. Sun and Y. XiaScience(AAAS),298, 2176-2179, (2002).
[12] Reacting the Unreactive: A toolbox of low-temperature solution-mediated reactions for the facile interconversion of nanocrystalline intermetallic compoundsR. E. Cableand R. E. SchaakJ. Am. Chem. Soc.(ACS),128, 9588-9589, (2005).
[13] Cation exchange reactions in ionic nanocrystalsD. H. Son,S. M. Hughes,Y. Yin andA. P. AlivisatosScience (AAAS), 306, 1009-1012, (2004).
[14] Spontaneous superlattice formation in nanorods through partial cation exchangeR. D. Robinson, B. SadtlerandA. P. AlivisatosScience(AAAS), 317, 355-358, (2007).
[15] Nanoheterostructurecation exchange: anionic framework conservationP. K. Jain andA. P. AlivisatosJ. Am. Chem. Soc.(ACS), 132, 9997-9999, (2010).
[16] Extending the spectral range of double-heterojunction nanorods by cation exchange-induced alloyingJ. C. Flanagan, L. Keating, M. Kalasad and Moonsub ShimChem. Mater. (ACS), 31, 9307-9316, (2019).
[17] Selective facet reactivity during cation exchange in cadmium sulfide nanorodsB. Sadtler, A. P. Alivisatos and M. G. Merkle Nature (Nature Publ.),131, 5285-5293, (2009).

Karnatak University
Journal of Science

ISSN: 0075-5168

New 2-Mercaptobenzothiazole carbonyl derivative, benzothiazol-2-yl-malonaldehydeligand, benzo[d]thiazol-2-ylthio)-3-hydroxyallylidene)-N-methylhydrazine-1-carbothioamide,and its Co(II), Ni(II) and Cu(II) complexes: Synthesis, Structural Characterization and Biological Studies (DNA Cleavage, DNA Binding and Anti-Bacterial)

Basappa C Yallur

P MuraliKrishna

Raveendra Melavanki

Basappa C Yallur, P MuraliKrishna, Raveendra Melavanki, "New 2-Mercaptobenzothiazole carbonyl derivative, benzothiazol-2-yl-malonaldehydeligand, benzo[d]thiazol-2-ylthio)-3-hydroxyallylidene)-N-methylhydrazine-1-carbothioamide,and its Co(II), Ni(II) and Cu(II) complexes: Synthesis, Structural Characterization and Biological Studies (DNA Cleavage, DNA Binding and Anti-Bacterial)" Karnatak University Journal of Science 51, 147-164 (2020).

New 2-Mercaptobenzothiazole carbonyl derivative, benzothiazol-2-yl-malonaldehydeligand, benzo[d]thiazol-2-ylthio)-3-hydroxyallylidene)-N-methylhydrazine-1-carbothioamide,and its Co(II), Ni(II) and Cu(II) complexes: Synthesis, Structural Characterization and Biological Studies (DNA Cleavage, DNA Binding and Anti-Bacterial)

Basappa C Yallur[a,*], P MuraliKrishna[a] and Raveendra Melavanki[b,]**

[a]Department of Chemistry, Ramaiah Institute of Technology, Bangalore-560054, Karnataka, India.(Affiliated to Visvesvaraya Technological University, BelagaviIndia)
[b]Department of Physics, Ramaiah Institute of Technology, Bangalore-560054, Karnataka, India.(Affiliated to Visvesvaraya Technological University, Belagavi, India)
Corresponding authors:yallurbc@gmail.com, melavanki73@gmail.com

Abstract

Metal salts of MCl_2. xH_2O [where, M=Co(II), Ni(II) and Cu(II), x=2, 6] reacted with prepared new compound2-Mercaptobenzothiazole Schiff base derivative benzothiazol-2-yl-malonaldehydeligand,benzo[d]thiazol-2-ylthio)-3-hydroxyallylidene)hydrazine-1-carbothioamideyields mono nuclear Ni(II), Co(II), and binuclear Cu(II) complexes. The prepared compounds were characterized using instrumental methods i.e. FT-IR, NMR, Magnetic moments, and ESR. DNA binding constants of the complexes indicates the intercalative binding mode which involves base pairs of DNA and a strong aromatic chromophore. Observed the cleavage of DNA in presence and absence of H_2O_2 for all the metal complexes. Antibacterial studies are not satisfactory but except 2a complex all other compounds shown moderate activity for inhibiting bacterial growth of Staphylococusepidermidis, Bacillissubtilis, Pseudomonas aeruginosa and Escherichia coli.

Keywords: 2-Mercaptobenzothiazole; Schiff base; Transition metal complexes; DNA interactions; Nuclease activity; Antibacterial activity;
Article history: Received: 13 August 2020; Revised: 25 August 2020; Accepted: 25 August 2020

1. Introduction

Benzothiazole organic compounds are well known bicyclic ring systems have various biological activities such as anti-microbial [1], anti-cancer [2,3], anthelmintic [4], antidiabetic [5],activities. These organic derivatives also found in industrial applications as antioxidants, accelerators for vulcanization, radioactive agents in amyloidal imagining [6].antimicrobial [7] anthelmintic, anti-inflammatory, anti-leishmanial, plant protection and anticonvulsant,[8]. Many series of benthiazol-2-yl-dithiocarbamates and their copper complexes evaluated for their in-vitro Schistosomicidal activityagainst Schistosomamansoni.Thiazole/benzothiazolecompound hydrazones and theircomplexes possess various pharmacological activities [9] such as antituberculosis and anticonvulsant Activity [10], antibacterial and antifungal drugs [11], HIV-1-protease [12], anti-leishmanial [13], anti-inflammatory [14], anticonvulsant [15], anti-diabetic [16], diuretic [17]and anti-proliferative agents [18].

2. Experimental

2.1. Materials and equipment's

All analytical grade starting compounds were usedand through the experiments water used was double distilled. The commercially purchased solvents and reagents were used without purifying solvents further unless noted otherwise. 1,1,3,3-tetramethoxy propane 99% (Aldrich), 2-Mercaptobenzothiazole, 99% (Spectrochem), 4-Methyl-3-thiosemicarbazide, 99% (Aldrich), and C, H, N and S estimated on Thermo Scientific Flash 2000 Organic Elemental Analyzer, IISc, Bangalore. Melting points were found out by evacuated capillaries. Electronic spectra of all the compounds were determined on a Elico-150 in DMF solvent. All the infrared spectra were determined in the range of 4000-400cm^{-1} (KBr disc) on a Nicolet protage 460 FT-IR spectrophotometer. ^{13}C-NMR and ^{1}H spectra were taken in DMSO-d^6 at 400 and 100 MHz (Bruker). All the Magnetic susceptibility for the compounds wasre corded using magnetic susceptibility balance (Sherwood Scientific, Cambridge, England), at room temperature and used $CuSO_4.5H_2O$ as standard. Determination of electronic spectra was done in DMF solvent on Elico SL 159 UV-Visible spectrophotometer. EPR spectral data were recorded at liquid nitrogen temperature on various E-112 X-band spectrophotometers in DMSO solvent. Study of compound's DNA cleavage abilities was done using UVITEC, Cambridge, UK. Whatever bacterial strains used are got from Biotechnology Department, MSRIT and Ramaiah Medical college, Bangalore.

2.2. Methods

2.2.1. Preparation of 2-bromomalonaldehyde

Starting material 2-bromomalonaldehyde was prepared using the procedure given in literature [20]. To a 100 ml of aqueous solution of 1, 1, 3, 3-tetramethoxypropane (100g, 0.12M) added concentrated HCl (4.3ml) and stirred until it forms homogeneous solution, then temperature of the reaction mixture maintained to below 35^0C then added slowly bromine (0.15M) solution drop wise, after the complete addition of Bromine stirring continued for another 30 minutes. Then, reaction mixture was concentrated under vacuum maintaining the temperature below 50^0C until

thick slurry obtained, and was washed using with 200 ml cold water and 100 ml of cold dichloromethane and dried in vacuum. Yield: 65%, MP: 148^{0}C (Lit: 148^{0}C [20], 146-147^{0}C [19].

2.2.2. Preparation of benzothiazol-2-yl-malonaldehydeligand (BTM)(1)

To a stirred solution of 2-mercaptobenzothiazole (0.250g, 0.0014 mol) in acetonitrile, 2-bromomalonaldehyde (0.225g, 0.0014 mol) was added drop wise over a period of 15 minutes. Then at room temperature, it is left for vigorous stirring for an hour at room temperature and at 80^{o}C for two hours. Removed the solvent by vacuum. Added acetone and the pale colored solid is filtered, washed by acetone. The compound obtained was dried in vacuum. Yield: 80% (0.283g), MP: 260^{o}C.

2.2.3. Benzo[d]thiazol-2-ylthio)-3-hydroxyallylidene)-N-methylhydrazine-1 carbothioamide (BTMMC)(2)

4-Methyl-3-thiosemicarbazide (0.243g, 0.0023 mol) dissolved in 5% acetic acid and (benzo[d]thiazol-2-yl)malonaldehyde(0.750g, 0.0023 mol) in ethanol were mixed in round bottom flask. The contents were refluxed on water bath and the progression of reaction was monitored on TLC. The compound formed was cooled and filtered, washed with hot water for several times and dried in vacuum. Obtained yellow colour solid compound with 75% (0.562g) yield. MP:250^{o}C.

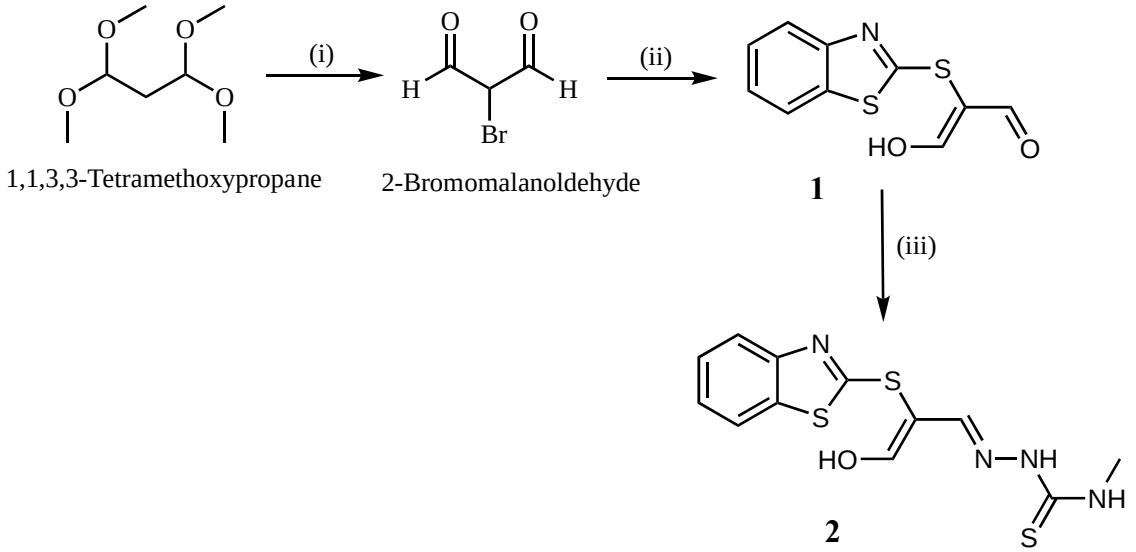

1,1,3,3-Tetramethoxypropane

2-Bromomalanoldehyde

Scheme 1. Synthesis of compound **1**(BTM) and compound **2**(BTMHC**). (i)**. HCl, Br_2;**(ii)**. 2-mercaptobenzothiazole, ethanol; **(iii)**. 4-Methyl-3-thiosemicarbazide, EtOH, Reflux for 2 hrs.

2.2.4. Preparation of the metal complexes

General Procedure: The reaction mixture containing Schiff base (0.0024M) in ethanol and metal salts (0.0012M) dissolved in minimum quantity of hot ethanol heated under reflux for about two hours. By filtration, the separated solid complex was collected and washed with small volume of hot water and ethanol. 2a: Yield: 52% (0.500g), MP: 275^0C**.** 2b**:** Yield: 63% (0.607g), MP: 278^0C**.** 2c: Yield: 77% (1.5g), MP: 255^0C**.**

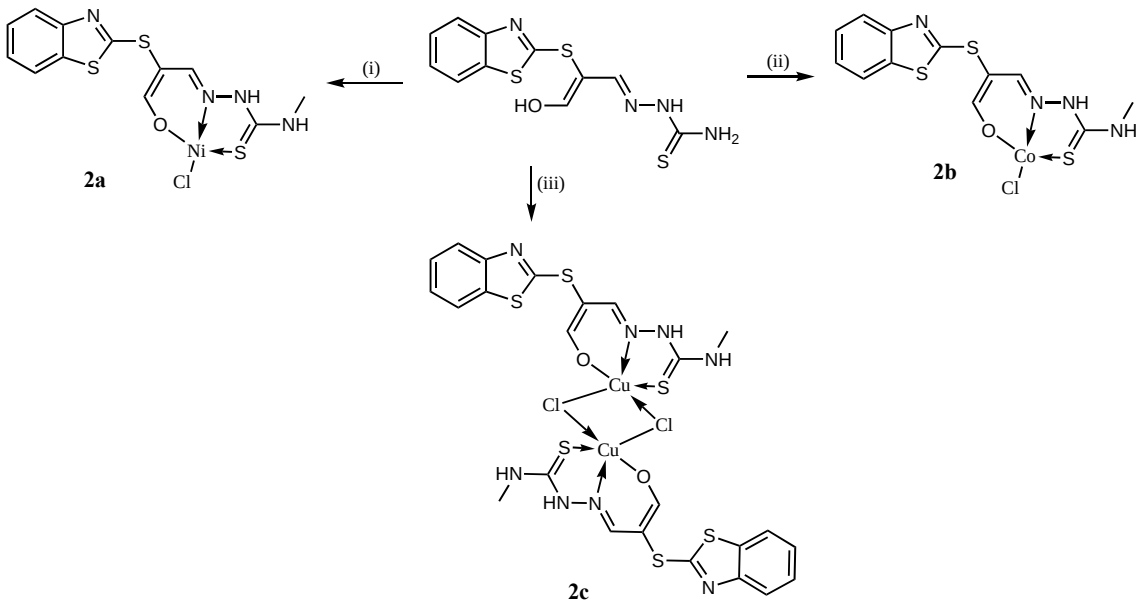

Scheme 2. Synthesis of metal complexes**2a**, **2b**, and **2c**. **(i)**. $NiCl_2.6H_2O$, EtOH, Reflux; **(ii)**. $CoCl_2.6H_2O$, EtOH, Reflux; **(iii)**. $CuCl_2.2H_2O$, EtOH, Reflux.

2.2.5. DNA interaction experiments

Experimental technique to probe interactions of metal ion-DNA used the absorption spectroscopy. A mixture of CT-DNA in 50mM NaCl/50mM Tris–HCl of pH 7.0 showed UV absorbance reading at 260 and 280 nm (A_{260}/A_{280}) to be a ratio of about 1.9, indicating that the DNA is enough free of proteins. Preparation of DNA stock solution was done in 50mM Tris–HCl/50mM NaCl in water (pH 7.0) and CT-DNA concentration was determined per nucleotide by considering absorption coefficient (6600 $dm^3mol^{-1}cm^{-1}$) at 260 nm. By dissolving in buffer solution, preparation of CT-DNA stock solution is done. It was kept at 4°C overnight for complete dissolution as was to be used within 4 days. To prepare the buffer solution double distilled water was used. All the synthesised compounds were dissolved in solvent (DMF) solvent. Experiments for absorption titration were carried out by fixing compounds concentration, while gradually increasing the DNA concentration (20-300 μM). For quantitatively comparing the binding strength of the compounds, determination of their intrinsic binding constants (K_b) with CT-DNA was done by using the following equation [21].

$$[DNA]/(\varepsilon_a-\varepsilon_b) = [DNA]/(\varepsilon_b-\varepsilon_f) + 1/ K_b (\varepsilon_b-\varepsilon_f) \quad (1)$$

ε_a, corresponds to apparent ε_b, is bound and $\varepsilon_f$refers to free metal complexes extinction coefficients respectively. A slope of $1/(\varepsilon_b-\varepsilon_f)$ was noted from [DNA]/$(\varepsilon_a-\varepsilon_f)$ Vs [DNA] plot and also $1/K_b$ $(\varepsilon_b-\varepsilon_f)$ as the Y-intercept where K_b represents the ratio of the slope to the Y-intercept.

2.2.6. DNA cleavage studies

DNA cleavage study of metal complexes and ligands are analysed using method of agarose gel electrophoresis[22]. In order to do the cleavage study of pUC18 DNA, preparation of reaction mixture of 20 µL containing pUC18 DNA of 50mM (1 µL of 200 µg/ml), Tris-HCl (12-19 µL with pH value of 7.1), and all compounds (5µL of 9.5mM) was done in the presence as well as in absence of H_2O_2 (0 or 2 µL of 8.8M). For incubation, all the samples were placed in oven for about 60 minutes at 37 ºC. Buffer was loaded to samples mixture that were incubated (30% glycerol + 0.25% xylene cyanol + 0.25% bromophenol blue) was added and loading of solutions was done on 1% agarose gel which consisted of 5 µL ethidium bromide. Agarose gel electrophoresis was carried out in the buffer of Tris-acetic acid- EDTA (TAE) at 100V for 50 minutes[23]. UV trans-illuminator was used for visualizing the bands. Monitoring the efficiency of DNA cleavage was performed based on the compound capability of converting nicked circular (NC) or linear form DNA from its super coiled (SC) form. Studies mentioned were performed under hydrolytic and/or oxidative conditions.

(2009). The anti-bacterial studies of prepared ligand and its metal complexes were screened according to the Kirby-Bauer method[24].Tested the bacterial activity for gram-positive bacteria Staphylococcus epidermidis, Bacillus subtilis and gram-negative bacterial strains Pseudomonas aeruginosa, Escherichia coli. The sub-culture the bacterial isolation nutrient agar plates were used. And those isolates were sub cultured for 24 hours at temperature of 37^0C. A loop of bacteria cells from nutrient agar plates was incubated at temperature 37 ^{0}C into 50 mL of nutrient broth for 18 hrs. Bacterial cultures (100 µL) were spread on nutrient agar with a sterile glass spreader. The minimum inhibitory concentration (MIC) of the compound was determined by using afar dilution method. Standard antibacterial agent Ciprofloxacin was used. At 37 ˚C the incubation of bacterial strains in oven was done for a duration of 24h. Determination of antibacterial activity after incubation was based on measurement of inhibition zones around the disc in millimetres. For observing the mean of inhibition zones, the measurements were performed in triplicate with ±2 mm of the tested compound.

3. Results and Discussion

3.1. Analytical data

The ligand and its metal complexes are found to be air stable. These metal (II) complexes were easily dissolved in DMF and DMSO which are aprotic solvents. The reason for this solubility can be understood as there is an increase in repulsion because of the substituted groups and so a decrement in molecule aggregation is noted. The alkyl groups and other substituted groups are weakly polar and lipophilic in nature which is why the solubility reduces in ethanol, methanol and water, which are strongly polar solvents. The analytical data of the compounds were shown in Table 1.

3.2. Infrared spectroscopy

Infrared spectra of all the compounds were determined in the range 4000-400 cm^{-1} using KBr disc. Various vibrational bands and their assignments are shown in Table 2. Infrared spectra of all complexes are compared to the ligand spectra. IR spectra of ligand was observed to have two medium bands in 3239-3429 cm^{-1} regions. These are assigned respectively to asymmetric and symmetric stretching vibrational modes of terminal group $-NH_2$. These bands remain unaffected in complexes which signifies the non-participation of terminal $-NH_2$ group in complex coordination. Strong band is observed the spectra of ligand in 1135-1163 cm^{-1} region assigned to υ(C=S) stretching vibration. The absence of stretching vibrational band at 2575 cm^{-1} indicating that in solid state, ligands stay in thione form.

Table 1. Analytical data of ligands and metal complexes

Compounds	Color	Yield (%)	Melting Point (^{0}C)	Elemental analysis found (cal.)%			
				C	H	N	S
BTM **(1)**	Pale	80	263	50.56 (50.62)	3.31 (2.97)	5.45 (5.90)	26.95 (27.02)
BTMMC **(2)**	Pale yellow	70	275	44.78 (44.43)	3.38 (3.73)	17.66 (17.27)	29.91 (29.65)
[Ni(BTMMC)Cl](2a)	Brown	70	278	34.87 (34.52)	2.81 (2.66)	13.81 (13.42)	22.88 (23.03)
[Co(BTMMC)Cl] H_2O(**2b)**	Parrot green	65	255	33.51 (33.07)	3.21 (3.01)	12.81 (12.86)	21.98 (22.07)
$[Cu_2(BTMMC)_2Cl_2]$(**2c)**	Green	75	263	34.04 (34.12)	2.20 (2.62)	12.81 (13.26)	22.58 (22.77)

υ(C=S) band is observed in 1135--1163 cm^{-1} region of metal complexes IR spectra which indicates that there is thione form of sulphur atom. Medium aromatic C-S stretching is assigned between 1054cm^{-1}– 1087 $cm^{-1}$and similarly aliphatic C-S stretching frequencies observed between 587-690cm^{-1}. Strong band is observed in 1597 cm^{-1} region because of azomethine nitrogen (>C=N-) group of ligand.. This band is shifted to lower frequency (1511 cm^{-1}-1559 cm^{-1}) in spectra of complexes that suggests involvement of azomethine nitrogen (>C=N) in chelation.

Table 2. FT-IR spectral data (cm^{-1}) of ligands and metal complexes

Compound	ν(C=O)	V(OH)	ν(CH)	ν(NH)	ν(C=N)	ν(C-N) + ν(N-N)	C=S	ν(C-S)
1	1683 s	3740w	2942w, 3047 w	-	1456m	1078m	-	581w
2	-	3821w	2975w	3431w	1511w	1059m	1150m	689w
2a.	-		2943w	3226w	1520m	1061m	1163 m	690w
2b.	-		2950w	3290w	1577m	1035m	1135 w	631m
2c.	-		2991w	3232w	1559m	1040m	1148 m	587m

3.3. NMR Analysis

^{1}H-NMR and ^{13}C-NMRspectra of ligands were recorded in DMSO-d_6(400MHz) (Figure 1-4). In NMR spectrum of compound 1, the peak obtained at δ 8.99 ppm in ^{1}H and δ183.68 ppm in ^{13}C-NMR confirms the formation of the carbonyl compound.

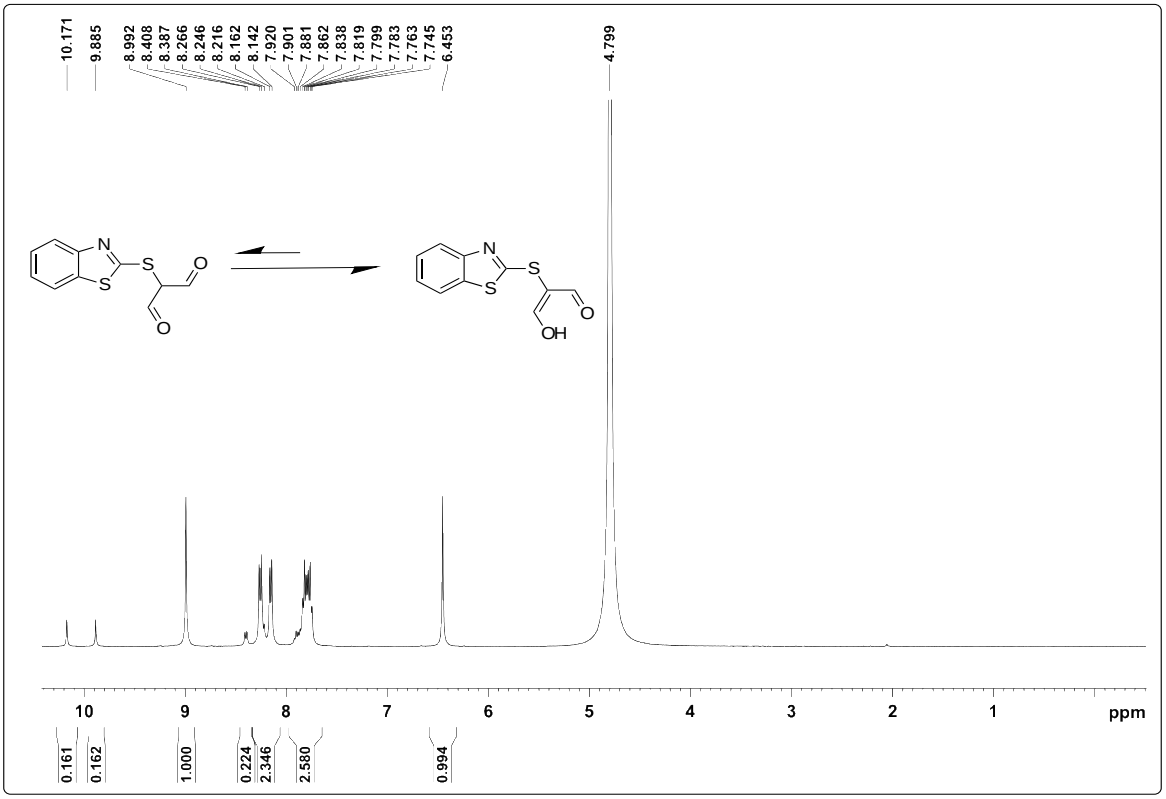

Figure 1. ^{1}H-NMR spetrum of compound 1(BTM)

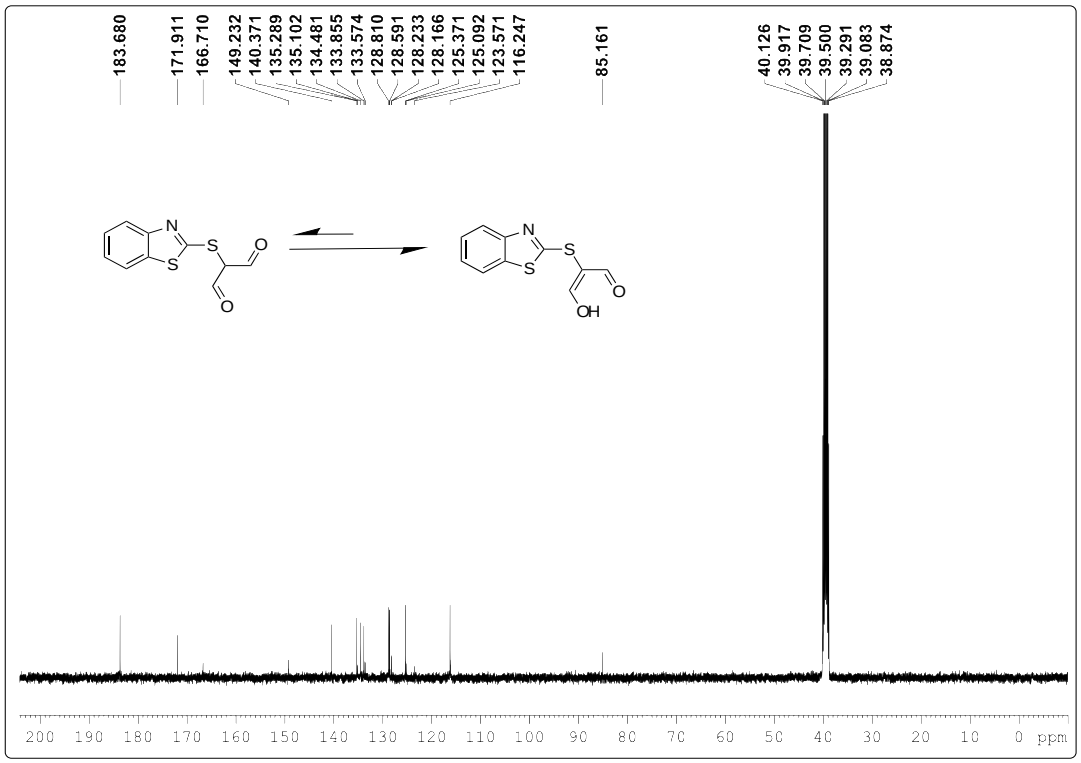

Figure 2. ^{13}C-NMR spetrum of compound 1 (BTM)

^{1}H-NMR and ^{13}C-NMR spectral data of the compounds: Compound 1(IT):^{1}H-NMR (DMSO, 400MHz): δ 6.4 (s; 1H), δ 7.745-7.79 (t; J=8 Hz; 2H), δ 8.14-8.16 (d; J=8 Hz; 2H), δ 8.99 (s; 1H),^{13}C-NMR (DMSO, 100MHz): δ 85.16; 116.24; 123.57; 125.09; 12537; 128.16; 128.23; 128.59; 128.81; 133.57; 133.85; 134.48; 135.10; 135.28; 140.37; 149.23; 166.71; 171.91; 183.68.

3.4 Electronic absorption spectra and magnetic studies of complexes

The electronic spectra were recorded for the ligand and its metal complexes in the spectral range 200–1100 nm (Figure 3) in DMF solvent. Typical electronic spectral data are in Table 4**.** In electronic spectra of the complexes, π→π* electronic transition observed in 32894-33557 cm^{-1} range, charge transfer band in 19723-23310 cm^{-1} and d-d band in12820-16233 cm^{-1} range.

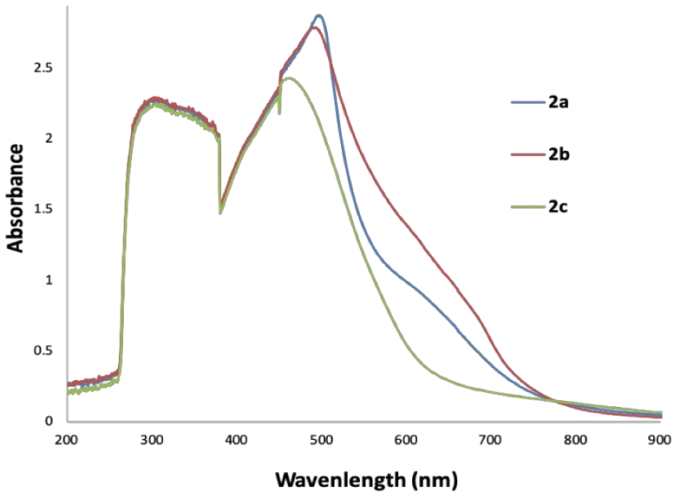

Figure 3. Electronic Spectra of Metal Complexes

Table 3. Electronic spectral data of metal complexes

Complex	$\pi \rightarrow \pi^*$ (cm^{-1})	LMCT– transition (cm^{-1})	d→d transition (cm^{-1})	Magnetic Moment (BM)
2a.	33557 cm^{-1}	19723 cm^{-1}	15384 cm^{-1}	0.00
2b.	32894 cm^{-1}	23310 cm^{-1}	16233 cm^{-1}	3.55
2c.	33557 cm^{-1}	22075 cm^{-1}	12820 cm^{-1}	0.47

The nickel complex, **2a** electronic and magnetic properties. Compound **2a**Diamagnetic Ni (II) complexes are of low spin square planar geometry [25]. Compound **2b** of Co(II) metal complex are suggest that with square planar geometry [26].It's because of anti-ferromagnecity due to the electron spin on neighboring metal ion [27]. Compound **2c** of Cu (II) metal complex is with magnetic moment of 0.47 B.M it is very low than the low spin, spin only value due the electron spin on neighboring metal [28]

3.5 Electron spin resonance spectroscopy

At liquid nitrogen temperature (LNT), the ESR spectra of copper complexes were determined in DMSO solvent. ESR spectra of the compound 2c shown in figure 4 and complexes' spin Hamiltonian parameters are shown in table 4 and table 5.In ESR spectrum, the absence of the half field signal at 1600 T indicates the presence of $m_S = \pm 2$ transitions, and absence of Cu-Cu interaction. The ESR spectrum for complexes show g-tensor parameters to be axially symmetric

with $g_{//} > g_{\perp} > 2.0023$ and were observed to be quite similar which indicates that copper site has a $d_{x^2-y^2}$ ground state, characteristic of square-planar, square base pyramidal or octahedral geometry with D_{4h} symmetry [29]. Rules out the possibility of a trigonal bipyramidal geometry as value are of $g\| > g\perp$ not the $g\| < g\perp$. Kivelson and Nieman[30] studied that for a covalent character of the metal ligand bonding complexes, $g\|$ is less than 2.3 andfor ionic character, it is greater than 2.3.The g_{av} values were calculated using the equations $g_{av} = (g_{\|} + 2g_{\perp})/3$ and are lies in the range 2.12-2.16 for complexes. These values suggest the square planar or distorted octahedral geometry for all the complexes [31]. According to Hathaway [32], if the G-factor value is less than 4, indicates the presence of substantial exchange interaction in the complexes, whereas if it is more than 4 value of G indicates that interaction is insignificant. The calculated G value (>4) for the present complexes implies absence of interaction between copper centres [33]. ESR parameters of complexes i.e. $A\|$, $A\perp$, $g\|$ and $g\perp$ and the d-d transitions energies are used [34] for the evaluation of $K\|$ and $K\perp$ which are orbital reduction parameters. Hathaway [32] showed that $K\perp < K\|$ for in-plane π-bonding, $K\| \approx K \approx 0.77$for the pure σ – bonding and $K\perp > K\|$ for out-of-plane π-bonding. The presence of in plane π-bonding can be noted from table in which $K\perp < K\|$ relationship is observed. Giordano and Bereman [35] suggest identification of bonding groups using the values of dipolar term P. A strong covalent bonding is conferred as there is reduction of P values from the free ion value (0.036 cm^{-1}). The below equations were used for calculating and determining the values of molecular-orbital coefficients$\alpha^2$and β^2. Here α^2 refers to the measure of the covalency of the in-plane σ-bonding between the 3d orbital and the ligand orbitals whereas β^2refers to the covalent in-plane π –bonding [36].

$$\alpha^2 = (A\|/0.036) + (g\|-2.0023) + 3(g\perp - 2.0023)/7 + 0.004$$

$$\beta^2 = (g\|-2.0023)\, E/-8\lambda\, \alpha^2$$

where $\lambda = -828\ cm^{-1}$ for the free copper ion and E denotes electronic transition energy.

The empirical factor ($f = g\|/A\|$ cm) index of deviation from idealized geometry. The values of f factor for the compound2c is 172 higher and the geometry must be with considerable distortion [37].

Table4. ESR spectral assignments for the Cu(II) complex.

Complex	$g_{//}$	$g\perp$	g_{av}	G	$A_{//}$ (10^{-4})	$A\perp$ (10^{-4})	A_{avg} (10^{-4})
2c	2.3637	2.0492	2.1540	7.7	137.95	32.745	0.0067

Table5: ESR bonding parameters for the Cu(II) complex.

Complex	$K_{//}$	$K\perp$	K	α^2	β^2	γ^2	f
2c	0.9343	0.3365	0.6511	0.7660	1.1395	0.1478	172

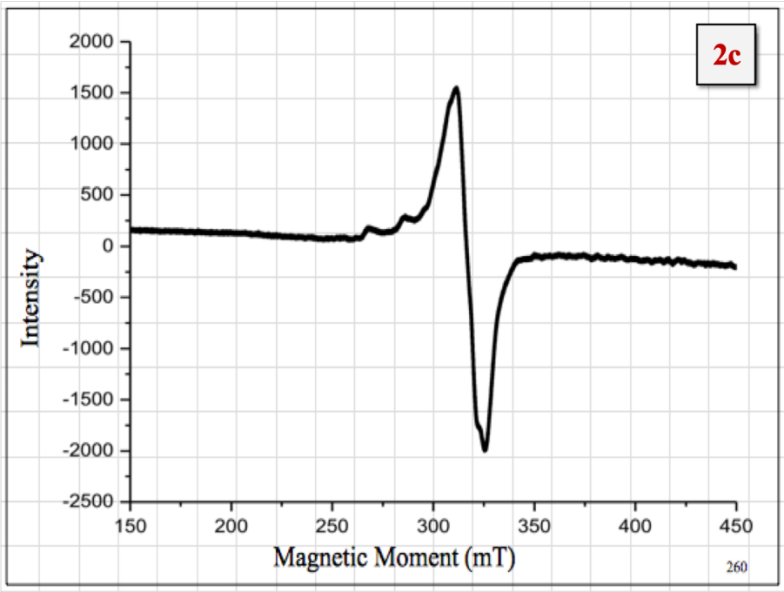

Figure 4. ESR spectra of **2c**for X-band in liquid nitrogen temperature (LNT) in DMSO

3.6 Antibacterial studies

Newly prepared ligand and its metal complexes were assessed for their in-vitro anti-bacterial activity by using well diffusion method. Bacterial studies were performed with gram-positive strains Bacillus subtilis, Staphylococcus epidermidisand gram-negative strains Escherichia coli, Pseudomonas aeruginosa. The efficiency of the tested compounds was compared with the standard drug Ciprofloxacin (Figure 5) (Table 6).

Table 6. Antibacterial activities of the compounds as MIC values (µg/mL)

Compound	Bacterial Strain Zone of Inhibition (in mm)			
	Bacillis subtilis	**S. epidermidis**	**P.aeruginosa**	**E. coli**
1	3	4	8	6
2	3	4	5	4
2a	0	0	0	0
2b	7	8	9	8
2c	3	2	6	6
Ciprofloxacin	25	25	25	25

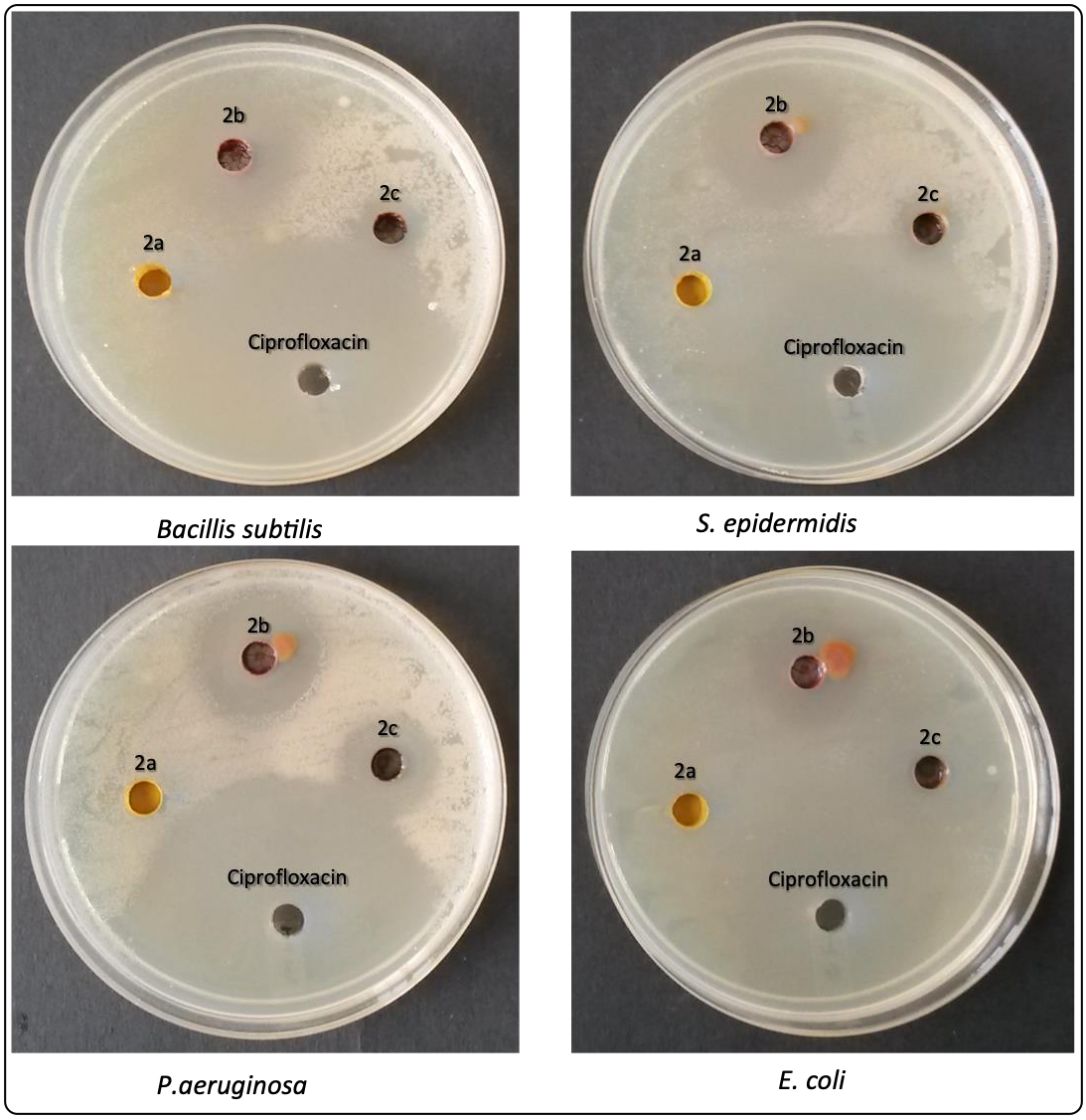

Figure 5. Anti-bacterial activity of metal complexes

From the antibacterial screening data, it is observed that, except the nickel metal complex ligands, cobalt, and copper metal complexes shown better activity for all the stains used for the study. Increment in antibacterial activity of the metal chelates may be caused because of the effect of metal ion on normal cell process and can be explained depending on the Chelation theory and Overtone's concept [38].Overtone's theory of cell permeability states that the lipid membrane which environs the cell favors the only channel of lipid soluble materials which makes liposolubility a significant factor to regulate the antimicrobial activity. And according to chelation, the metal ion polarity is reduced to a greater level as a result of ligand overlapping, orbital and partial contribution of metal ion positive charge with donor groups [39].

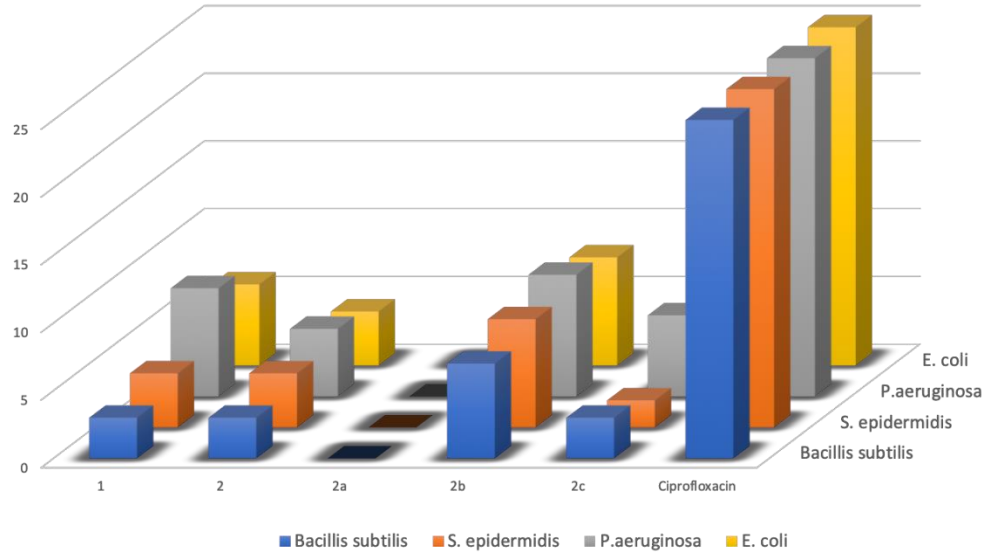

Figure 6. Column 3-D cylindrical chart of the anti-bacterial activity of all the compounds.

Overall, both carbonyl, carbamide ligands, cobalt, and copper metal complexes shown the better activity against the tested organisms and compared to all the compounds cobalt metal complex shown better than all other compounds. The comparison of anti-bacterial activity of all the tested compounds was shown in column 3-D cylindrical chart (Figure 6).

3.7 DNA binding studies

The DNA interactions with newly synthesized complexes were investigated using absorption spectrophotometric titrations and results given in Table 7. Figure 7 illustrates the absorption spectra. The spectrum is then analyzed in the presence and absence of CT-DNA is analysed and is then used for evaluating the binding constant, K_b. The DNA intrinsic binding constants are in the order of 10^6 M^{-1}. An intense band observed around 237-350 nm was attributed to $\pi \rightarrow \pi^*$ intra-ligand transition. Further on addition of DNA to metal complexes showed Further, on addition of CT-DNA to the complexes shows hypochromism. Literature survey suggests that hypochromism is observed when a complex through intercalation binds with DNA in consequence of a strong staking interaction between a base pair of DNA and an aromatic chromophore. Thehypochromism extent along with or without small red or blue shift commonly reflects the intercalative binding strength [40-43]. And it may be because of strong stacking interaction between a base pairs of DNA and an aromatic chromophore. Based on the results, the cobalt complex (2b) showed higher binding efficiency of DNA than the other metal complexes of corresponding ligand.

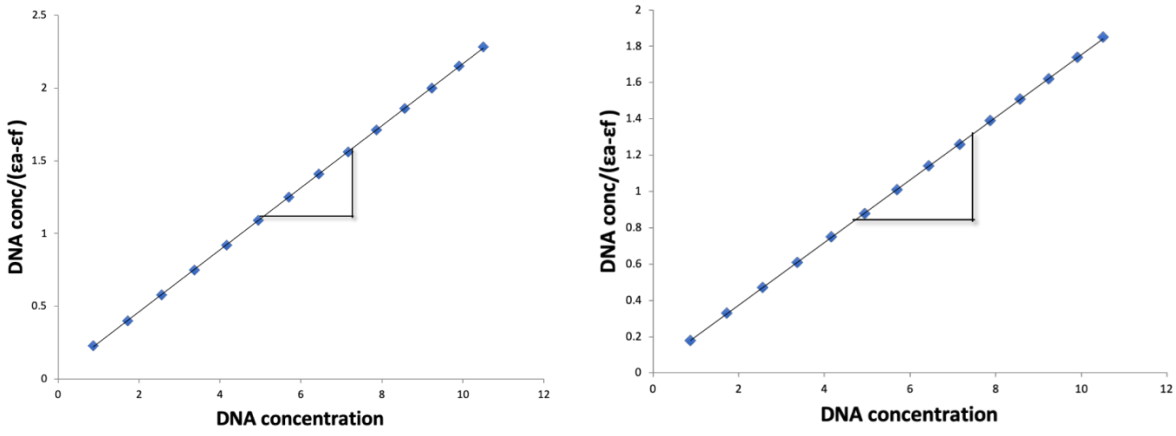

2b **2c**

Figure 7. The plot of [DNA]/(εa-εf) vs [DNA] for the titration of DNA with complexes.

Table 7. Electronic absorption data upon addition of CT-DNA to the complexes

Complex	λ_{max} (nm)		$\triangle\lambda$ (nm)	%H	K_b (M^{-1})
	Free	Bound			
2a	-	-	-	-	-
2b	284	287	3	40.83	$49.68X10^6$
2c	287	289	2	29.88	$47.43X10^6$

3.8 DNA Cleavage studies

The electrophoresis of agarose gel is a DNA migration-based technique. This technique is also dependent on migration of DNA fragments subjected to the influence of an electric potential. Cleavage reactions for ligands and its complexes were carried out in both absence as well as presence of H_2O_2 for comparison purposes. Agarose gel electrophoresis of ligand and metal complexes are shown in Figure 8. From the Figure it observed that the ligand did not show any cleavage activity in the absence and presence of H_2O_2 but on complexation the activity enhanced moderately. All the complexes, except the 2a- nickel metal complex in absence of H_2O_2all other metal complexes showed cleavage activity. A role of metal ion in isolated DNA cleavage reaction can be inferred from results. Supercoiled DNA was converted into open circular DNA by the metal complexes [44]. It can be concluded from these results that there is a close relation between DNA cleavage process and the oxidation of metal ions of complexes.

Figure 8. Gel electrophoresis diagram: Lane 1: DNA control; lane 2: DNA + H_2O_2; lane 3: compound **2** + DNA; lane 4: compound **2** + DNA + H_2O_2; lane 5: compound **2a** +DNA; lane 6: compound **2a** + DNA + H_2O_2; lane 7: compound **2b** + DNA; lane 8: compound **2b** + DNA + H_2O_2; lane 9: compound **2c** + DNA; lane 10: compound **2c** + DNA + H_2O_2.

4. Conclusion

Here we reported the characterization and synthesis of new imidazolidinethione carbazone derivative and its metal complexes of Ni, Co and Cu with their biological activities. All compounds shown DNA binding with intercalation in hyperchromism and bathochromism of the absorption band due to the intercalative mode involving a strong aromatic chromophore and base pairs of DNA. Studied the biological activities like anti-bacterial, DNA-binding and DNA cleavages. Cobalt metal complex shown better activity than other ligands and metal complexes. And cleavage activity all the complexes, except the 2a- nickel metal complex in absence of H_2O_2all other metal complexes showed cleavage activity. Study of DNA binding indicates that all complexes show intercalation mode of binding.

Acknowledgements:

The authors thank Dr. Kandikere Ramaiah Prabhu, Department of Organic Chemistry, Indian Institute of Science, Bangalore, for kind technical support.

References:

[1]. a). S. Gupta, N. Ajmera, N. Gautam R. Sharma, D. Gauatam,I. J. Chem. 48B, 853-858 (2009). b). R. M. Kumbhare, V. N. Ingle,I. J. Chem. 48B, 996-1000 (2009). c). Y. Murthi, D. Pathak,J. Pharm. Res.7(3), 153-155(2008). d). B. Rajeeva, N.Srinivasulu, S. Shantakumar, E-Journal of Chemistry 6(3), 775-779(2009). e). M. Maharan, S. William, F. Ramzy, A. Sembel, Molecules12, 622-633(2007).

[2]. a). S. Kini, S. Swain, A. Gandhi, I. J. Pharm. Sci. 46-50(2007), b). H. L. K. Stanton, R. Gambari, H. C. Chung, C. O. T. Johny, C. Filly, S. C. C. Albert, Bioorg. Med. Chem. 16, 3626-3631(2008). c). M. Wang, M. Gao, B. Mock, K. Miller, G. Sledge, G. Hutchins, Q. Zheng, Bioorg. Med. Chem. 14, 8599-8607(2006). d). I. Hutchinson, M. S. Chua, H. L. Browne, V. Trapani, T. D. Bradshaw, A. D. Westwell, J. Med. Chem. 44, 1446-1449(2001).

[3]. Y. Heo, Y. Song, B. Kim, J. Heo, Tetrahedron Lett.47, 3091-3094(2006).

[4]. P. Reddy, Y. Lin, H. Chang, Arkivoc xvi, 113-122(2007).

[5]. M. Sreenivasa, E. Jaychand, B. Shivakumar, K.Jayrajkumar, J. Vijaykumar, Arch. Pharm. Sci and Res.1(2), 150-157(2009).

[6]. S. Pattan, C. Suresh, V. Pujar, V. Reddy, V. Rasal, B. Koti, Indian J. Chem. 44B, 2404-2408(2005).

[7]. a). Z. Fan, Z. Yang, H. Zhang, N. Mi, H. Wang, F. Cai, X. Zuo, Q. Zheng, H. Song, J. Agric. Food. Chem.58, 2630(2010). b). Z. H. Wang, Y. Z. Guo, J. Zhang,L. Ma, H. Song,

Z. J. Fan, J. Agric. Food. Chem.58, 2715(2010). c). B. Rizwana, S. L. Santha, Int. J. ChemTech. Res. 4(1), 464-473(2012).
[8]. O. Du, W. Zhu, Z. Zhao, X. Qian, Y. Xu, J. Agric. Food Chem. 60, 346-353(2012).
[9]. a). L. Sumalan, D. Macarovici, M. Neamtu,M. Coman,Rev. Roum. Chim.42, 277-280(1997). b). I. Yilmaz, A. Çukurovali, Polish J. Chem.78, 663-772(2004).
[10]. L. Katz,J. Amer. Chem. Soc. 73, 4007-4010(1951).
[11]. G. D. Tiwari, A. R. Tripathi, A. N. Tripathi, O.Kumari, M. V. B. Reddy, J. Indian Chem. Soc. 71, 755-756(1994).
[12]. S. Nagarjan, G. Crescenzo, D. Getman, H. Lu, J. Sikorski, J. Walker, J. McDonald,K. Houseman, G. Kocan, N. Kishore, P. Mehta, C. Shippy, L. Blystone, Bioorg. Med. Chem.11, 4769-4777(2003).
[13]. F. Delmas, A. Avellaneda, C. Giorgio, M. Robin, E. Clercq, P. David, J. P.Galy, Eur. J. Med. Chem.39, 685-690(2004).
[14]. E. M. H. Abbas, K. M. Amin, W. S. El-Hamouly, D. H. Dawood, M. M. Abdulla, Res. Chem. Intermed.41, 2537-2555(2015).
[15]. P. Lemoine, B. Viossat, Huy, N. Dung, A. Tomas, G. Morgant, F. T. Greenaway, J. R. J. Sorenson, J. Inorg. Biochem.98, 1734-1749(2004).
[16]. S. R. Pattan, C. Suresh, V. D. Dujar, V. V. K. Reddy, V. P. Rasal, B. C. Koti, Indian. J. Chem.44B, 2404-2408(2005).
[17]. D. A. Ibrahim, D. S. Lasheen, M. Y. Zaky, A. W. Ibrahim, D. Vullo, M. Ceruso, C> T. Supuran, Abou, D. A. El-Ella, Bioorg. Med. Chem.23, 4989-4999(2015).
[18]. L. Racane, V. Tralic-Kulenovic, R. P. Kitson, G.Karminski-Zamola, Monatsh Chem.137, 1571-1577(2006).
[19]. S. Trofimenko, J. Org. Chem. 28, 3243–3245(1963). b). J. W. Tomsho, J. J. McGuire, J. K. Coward, Org. Biomol. Chem. 3,3388-3398(2005).
[20]. M. J. Grard, Compt. Rend.190, 187-189(1930).
[21]. A. Wolf, G. H. Shimer, T. Meehan, Biochemistry 26, 6392-6396(1987).
[22]. T.A. Brown, Mol. Biol. A Pract. Approach 1, 51–52(1990).
[23]. K. Sampath, S. Sathiyaraj, C. Jayabalakrishnan, Spectrochim. acta. A 105, 582–592(2013).
[24]. A. W. Bauer, W. M. M. Kirby, Am. J. Clin. Pathol. 45, 493-496(1966).
[25]. A. Bottcher, H. Elias, E. G. Jager, H. Langelderova, M. Mazur, L. Muller, H. Paulus, P. Pelikan, M. Rudolph, M. Valko, Inorga. Chem. 32(19), 4131-4138(1993).
[26]. R. L. Duta, A. Syamal, "Elements of magnetochemistry" 2nd edition (New Delhi: Elsevier).1992.
[27]. W. Assefa, V. J. T. Raju, Y. Chebude, N. Retta, Bull. Chem. Soc. Ethiop. 23, 187–196(2009).
[28]. G. Giordano, R. D. Bereman, J. Am. Chem. Soc. 96(4), 1019-1023(1974).
[29]. R. K. Ray, G. M.Kaufiman, Inorg. Chim. Acta,173(2), 207-214(1990).
[30]. D. Kivelson, R. Neiman, J. Chem. Phys.35, 149- 155(1961).
[31]. A. Emara, B. El-Sayed, E. S. Ahmed, Spectrochim. acta A. 69, 757–769(2008).
[32]. B. J. Hathaway, Struct. Bond. (Berlin) 57, 55-118(1984).
[33]. R. R.Pulimamidi, R.Nomula, R.Pallepogu, H. Shaik,Eur. J. Med. Chem. 79, 117-127(2014).
[34]. K. L. Reddy, S. Srihari, P. Lingaiah, J. Indian Chem. Soc.61, 801(1984).
[35]. G. Giordano, R. D. Bereman, J. Am. Chem. Soc.96(4), 1019-1023(1974).

[36]. K. Jeyasubramanian, S. A. Samath, S. Thambidurai, R. Murugesan, S. K. Ramalingam, Transition Met. Chem.20, 76-80(1996).
[37]. R. C.Chikate, B. R. Avadhoot, P. B. Subhash, X. W. Doulas,Polyhedron 24, 889-899(2005)
[38]. A. Manimaran, C. Jayabalakrishnan, J. Adv. Res. 3, 233–243(2012)
[39]. R. Prabhakaran, S. Anantharaman, M. Thilagavathi, M. V. Kaveri, P. Kalaivani, R. Karvembu,N. Dharmaraj, Spectrochim. acta. A,78, 844–853(2011)
[40]. G. Pratviel, J. Bernadou, B. Meunier, Adv. Inorg. Chem. 45, 251-312(1998)
[41]. Li, You-Shan, B. Peng, Li. Ma,C. Sheng-Li, B. Lu-Lu, Y. Chao-Rui,W. Chong-Qing,Hao-Jie, Yan, D. Pan-Pan, L. Zhong-Feng, J. Liao,M. Ying-Ying, W. Hai-Long, L. Jing, X. Xingzhi, Eur. J. Med. Chem.127, 137-146(2017)
[42]. N. Perin, R. Nhili, M. Cindric, B. Bertosa, D. Vusak, I. Martin-Kleiner, M. Hranjec,Eur. J. Med. Chem.122, 530-545(2016)
[43]. A. Kung, T. Pieper, R. Wissiack, E. Rosenberg, B. K. Keppler, J. Biol. Inorg. Chem. 6, 292-299(2001).
[44]. T. A. Yousef, G. M. A. El-reash, O. A. El-gammal, R. A. Bedier, J. Mol. Struct. 1035, 307–317(2013).

Karnatak University
Journal of Science

ISSN: 0075-5168

Förster resonance energy transfer studies between Bovine Serum Albumin and Stilbene 420 dye

Kotresh M. G
Mallikarjun K. Patil
Sanjeev R. Inamdar

Kotresh M. G, Mallikarjun K. Patil, Sanjeev R. Inamdar "Förster resonance energy transfer studies between Bovine Serum Albumin and Stilbene 420 dye" Karnatak University Journal of Science 51, 165-174 (2020).

Förster resonance energy transfer studies between Bovine Serum Albumin and Stilbene 420 dye

Kotresh M. G[a*], Mallikarjun K. Patil[b] and Sanjeev R. Inamdar[b]

[a]Department of Physics, VSK University, Ballari-583 105, India.

[b]Laser Spectroscopy Programme, Department of Physics, Karnatak University, Dharwad-580 003, India.

***Corresponding author:** kotreshm26@gmail.com*

Abstract

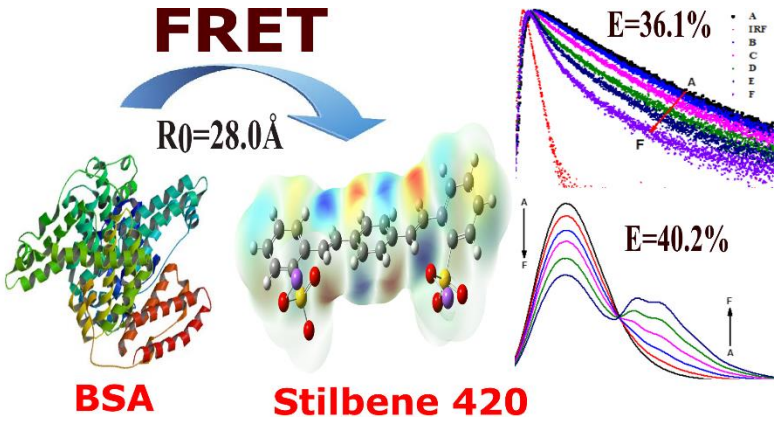

In the present work, we report evidence for efficient Förster resonance energy transfer (FRET) between Bovine Serum Albumin (BSA) and Stilbene 420 (S420) dye based on both steady-state and time-resolved (TR) fluorescence spectroscopic measurements. This study predominantly shows that decrease in the Photoluminescence (PL) intensity of BSA and enhancement PL intensity of S420 dye provides the information about efficient energy transfer (ET) between the two fluorophore. This is a signature that, BSA acts as a proficient donor and S420 dye as an excellent acceptor in FRET mechanism. The Spectral overlap integral (J(λ)), Forster distance (R_0), intermolecular distances (r), and energy transfer efficiency (E) are obtained experimentally from FRET theory. The ET efficiency of up to 36% has observed in this FRET system from TR measurements. The Stern-Volmer plot suggests that the quenching mechanism is dynamic and bimolecular quenching rate constants (k_q) shows this interaction is not diffusion-controlled process.

Keywords: BSA; Stilbene 420; FRET; Spectral overlap; Forster distance; Stern-Volmer.

Article history: Received: 6 July 2020**;** Revised: 8 August 2020**;** Accepted: 9 August 2020

1. Introduction

Förster/fluorescence resonance energy transfer (FRET) is a process in which an excited state donor chromophore can transfer energy to a proximal acceptor chromophore (typically less than 10 nm) through a long-range nonradiative dipole-dipole coupling [1-4]. It has been extensively and intensively studied as a powerful analytical technique to interrogate changes in molecular conformation, association and the assembly or disassembly of biomolecular machinery [2]. The interest has been growing quickly amongst researchers in the field of FRET sensors, which are used to quantify molecular dynamics in protein-protein interactions, protein-DNA interactions, and protein conformational changes [2, 5]. The advantage of the FRET

technique is such that, it is a ratiometric method that allows measurement of the internal distance in the molecular frame rather than in the laboratory frame, which makes it largely immune to instrumental noise and drifts [6].

FRET is considered as a novel tool in biophysics and biochemistry and is commonly used for detection of various chemical and biological analytes [7]. Various research works have been conveying on the sensing of ions and biomolecules based on the FRET machinery. Sun et al. [8] reported an efficient FRET-based biosensor for the quick detection of unfolded collagen fragments at the nM level. Bhatnagar et al. [9] designed a FRET-based cardiac immune sensor for early detection of heart attack by amine-functionalized graphene quantum dots. Shi et al. [10] established a FRET-based sensor for the recognition of epithelial cell adhesion molecule at the nM level and reported that the proposed sensor has been successfully utilizing for breast cancer detection. Murray et al. [11] have shown a FRET-based assay for the sensing of various metal ions.

Bovine serum albumin (BSA) is a type of serum protein, which is abundant in the circulatory system and constitutes the majority of plasma fluid in a variety of organisms [7, 12]. Its structure and composition are similar to Human serum albumin (HSA) [13]. Thus, the central objective of the present study is to examine the ability of BSA to act as a donor in FRET assembly in the presence of efficient laser dye Stilbene 420 as an acceptor using steady-state and time-resolved fluorescence techniques.

2. Materials and experimental methods

2.1 Materials

Bovine serum albumin (BSA) and Stilbene 420 dye were purchased from *Sigma-Aldrich* Chemicals Co., USA. Further, solutions of both the samples are prepared in double-distilled water.

2.2 Experimental methods

UV-Vis absorption measurements were carried out with Hitachi U-2800, UV-Vis spectrophotometer in the wavelength range of 250-600 nm. Fluorescence measurements were performed by using the HORIBA Jobin Yvon Fluoromax-4 spectrofluorometer. The quartz cuvette of path length of 10 mm was used with excitation and emission slits width of 3 nm with an interval of 1nm. PL lifetimes of BSA-S420 conjugates were performed using TCSPC technique (ISS ChronosBH, TCSPC spectrofluorometer) with a pulsed diode laser as an excitation source at 290 nm for exciting BSA molecules. Decay data were analyzed using the Vinci multidimensional software.

3. Results and discussions

3.1 Steady-state measurements

According to Förster's theory, the requirement for effective ET in the FRET system is that the PL spectrum of the donor molecule must overlap sufficiently with the absorption spectrum of the acceptor molecule [14-16]. Fig. 1 shows the overlapping between normalized absorption spectra of S420 dye and PL spectra of BSA recorded at room temperature 300 K. The emission peak of BSA is finding at 345 nm and the absorption peak of S420 dye is noticed at 347 nm. Fig. 1 indicates that the emission spectrum of the BSA molecule has a good spectral overlap

with the normalized absorption spectrum of S420 dye and this can be intended by using the equation (1)

$$J(\lambda) = \int_0^{\infty} F_D(\lambda)\varepsilon_A(\lambda)\lambda^4 d\lambda \quad (1)$$

where $F_D(\lambda)$ is the corrected fluorescence intensity of the donor molecule in the wavelength range λ to $\lambda + \Delta\lambda$ with the normalized total intensity and $\varepsilon_A(\lambda)$ is the absorption coefficient of the acceptor fluorophore at λ, which is normally in the units of $M^{-1}cm^{-1}$ [15]. The intended value of the spectral overlap is gathered in Table 1.

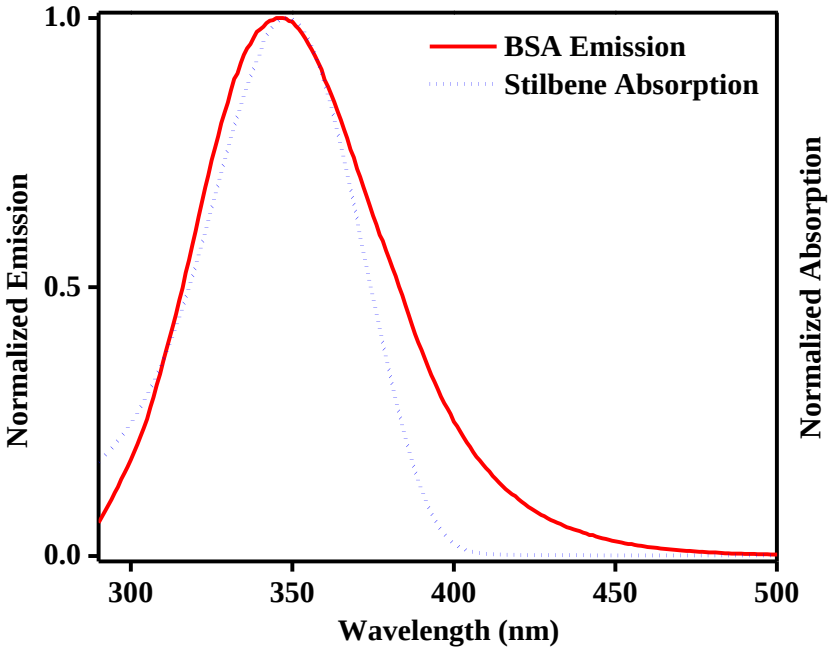

Figure 1. Normalized PL spectrum of BSA laterally with the absorption spectrum of S420 dye

The FRET efficiency (E) is defined as the fraction of excitons that are transferred from the donor fluorophore to the acceptor nonradiatively [15], and is determined by using equation (2)

$$E = \frac{R_0^6}{R_0^6 + r^6} \quad (2)$$

The FRET efficiency is depends on Förster distance (R_0) and is sensitive to proximity distance (r). Förster distance (R_0) is the distance at which 50% of the energy of donor fluorophore is transferred to the acceptor fluorophore [14, 15], and it is given by

$$R_0^6 = \frac{9000\ln(10)k^2\varphi_D J(\lambda)}{128\pi^5 N_A n^4} \quad (3)$$

where φ_D is the quantum yield of the donor (BSA), n is the refractive index of the medium of both BSA and S420 molecule's, N_A is Avogadro's number, and k^2 is the relative orientation constant of donor-acceptor dipoles. $J(\lambda)$ is the spectral overlap between normalized PL spectra of donor (BSA) and absorption spectra of acceptor fluorophore (S420). Considering the values for $\varphi_D = 0.15$, $k^2 = ⅔$, and $n = 1.36$ [15] the obtained Förster distance (R_0) for BSA-Stilbene 420 FRET pair is 2.80nm.

The PL quenching of BSA at sequential changing in concentration of S420 (0.2×10^{-4}M to 1×10^{-4}M) is deliberated in Fig. 2 and signifies the PL spectra of the BSA alone and in the presence of successive variation in concentration of S420. It is observed that BSA shows strong PL peak at 345 nm and decrease in its intensity is seen with steady increase in the concentration of S420. This variation in the characteristic PL peak of BSA designates the interaction occurring between BSA and S420. The steady-state efficiency of ET was considered by using following Equation (4)

$$E = 1 - \frac{F_{DA}}{F_D} \tag{4}$$

where F_D and F_{DA} is PL intensity of the donor BSA molecule in the absence and in the presence of the acceptor fluorophore (S420). The observed efficiency value is 40% for BSA-Stilbene FRET pair.

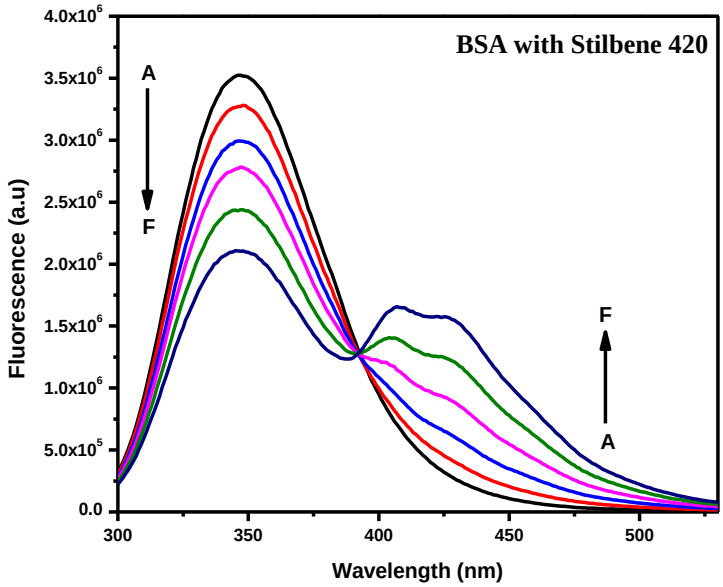

Figure 2. Quenching of PL intensity of BSA with an increase of S420 dye concentrations increasing from A to G. BSA concentration was fixed at $1x10^{-4}$ M. Concentrations S420 dye were (A) 0, (B) 2×10^{-5} M, (C) 4×10^{-5} M, (D) 6×10^{-5} M, (E) 8×10^{-5} M, (F) 1×10^{-4} M.

Table 1. FRET parameters obtained using steady state and time resolved measurements

Parameters	Steady-state measurements	Time resolved measurements
ET efficiency (E)	40.2%	36.1%
Spectral overlap (J(λ))	1.72×10^{-14} $M^{-1}cm^{-1}nm^4$	
Förster distance (R_0)	2.80 nm	
Intermolecular distance (r)	3.33 nm	
Stern-Volmer constant (K_{sv})	6.31×10^3 M^{-1}	6.51×10^3 M^{-1}
Bimolecular constant (k_q)	1.06×10^{12} $M^{-1}s^{-1}$	1.10×10^{12} $M^{-1}s^{-1}$

3.2 Time-resolved (TR) measurements

Time-resolved measurements are the most sensitive than steady-state PL quenching efficiencies because fluorescence lifetime is not been influenced by variations in excitation source intensity and it is independent of concentration [14-17]. In order to validate the type of quenching mechanism involved in the BSA with S420 dye we have implemented excited state lifetime measurements using time-correlated single photon counting (TCSPC). We used pulsed Laser diode of excitation 290 nm to measure the decay time of BSA alone and BSA with S420 at the maximum PL peak of BSA. Fig. 3 shows the TR fluorescence decay curve of BSA in absence and presence S420 dye and all the decay profiles are best fitted to bi-exponential function.

$$I(t) = (A_1\tau_1 + A_2\tau_2) \tag{5}$$

where A_1 and A_2 are normalized amplitude components with τ_1 and τ_2 represents the shorter and longer lifetime components respectively. The average lifetime value of BSA alone is 5.90 ns and this has been reduced up to 3.79 ns in the presence of highest concentration of S420 dye (Table 2). The reduction in the lifetime of BSA in the presence of S420 dye which is one of the trademarks of efficient FRET between donor-acceptor molecules. This quenching of donor fluorescence lifetime is due to the ET from BSA to Stilbene 420 dye. The ET efficiency from BSA to Stilbene 420 dye using time resolved measurements are calculated by using following equation

$$E = 1 - \frac{\tau_{DA}}{\tau_D} \tag{6}$$

where τ_D and τ_{DA} is the life time of BSA without and with S420 dye. The intended ET efficiencies from BSA to Stilbene 420 dye is 36.1%. Further, by using the TR-FRET efficiency values, one can easily estimate the intermolecular distance between donor and acceptor fluorophore using the equation (2) and gathered in Table 1. The ET efficiency values obtained in TR measurements are less than the values found by steady state measurements due to TR measurements are independent of concentration and variation in light intensity [18]. Excited states of both BSA and S420 dye interact via FRET mechanism; this can be considered as a communication link between the biological (BSA) and laser dye components of the conjugate and which opens interesting possibilities for optical applications of bio specific assemblies of NPs [15].

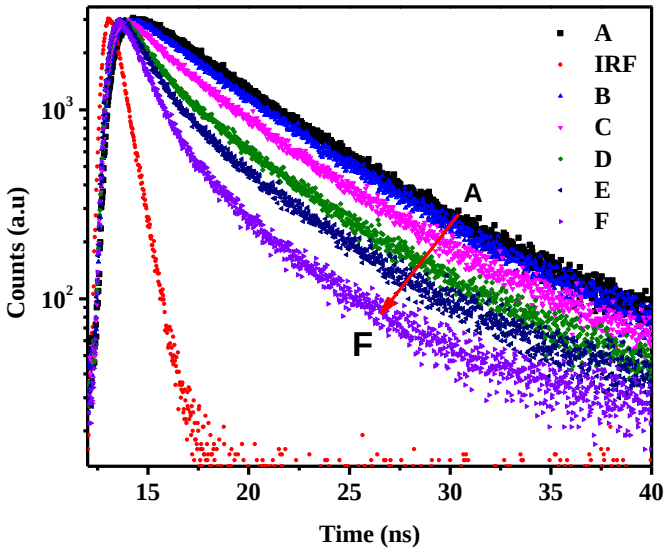

Figure 3. PL decay curves of BSA in the presence of various concentrations of S420 dye [(A) 0, (B) 2 × 10^{-5} M, (C) 4 × 10^{-5} M, (D) 6 × 10^{-5} M, (E) 8 × 10^{-5} M, (F) 1 × 10^{-4} M.]

Table 2. *Time resolved decay measurements*

FRET system	T_1 (ns)	T_2 (ns)	A_1	A_2	<T> (ns)
BSA alone (A)	3.04	6.44	0.15	0.85	5.93
B	2.18	6.27	0.11	0.89	5.83
C	0.84	5.84	0.14	0.86	5.13
D	0.83	5.80	0.19	0.81	4.87
E	0.72	5.60	0.25	0.75	4.36
F	0.71	5.33	0.33	0.67	3.79

Note: Samples are BSA in the presence of various concentrations of S420 dye [(A) 0, (B) 2×10^{-5} M, (C) BSA+4×10^{-5} M, (D) BSA+6×10^{-5} M, (E) BSA+8 × 10^{-5} M, (F) BSA+1×10^{-4} M.]

Relationship between quenching of excited states of BSA studied as function of varying concentration of S420 dye, and that has been described by using Stern-Volmer (SV) equation and that is given by

$$\frac{F_D}{F_{DA}} = 1 + K_q \tau_D [Q] = 1 + K_{sv}[Q] = \frac{\tau_D}{\tau_{DA}} \qquad (7)$$

where F_D and F_{DA} are the relative PL intensity in the absence and presence of S420 respectively, K_{sv} is the SV quenching constant which measures the efficiency of quenching, Q is the concentration of Stilbene 420, K_q is the bimolecular quenching rate constant , τ_D is the average lifetime of BSA and τ_{DA} is lifetime of BSA and S420 conjugates, respectively. A linear SV

plot of F_D/F_{DA} or τ_D/τ_{DA} vs. quencher concentration [Q] is shown in Fig. 4, that indicates, the quenching mechanism is dynamic, due to collision between fluorophore and the quencher, then

$$K_{sv} = K_q \tau_D \quad (8)$$

where K_q is bimolecular quenching constant and τ_D luminescence lifetime of BSA in the absence of Stilbene 420. By linear fitting of the data, the slope of plot SV constant (K_{sv}) was found to be 6.31 x 10^3 M^{-1} and 6.51x10^3 M^{-1} by steady-state and time resolved SV plots, respectively. The estimated rate constant (K_q) values are 1.06x10^{12} $M^{-1}s^{-1}$and 1.10x10^{12} $M^{-1}s^{-1}$ by steady-state and time resolved SV plots, respectively. The diffusion-controlled quenching process naturally results in values of k_q near to 1×$10^{10}M^{-1}s^{-1}$. The smaller values of k_q can result from steric shielding of the BSA. In this study, the higher value of diffusion-controlled quenching rate constant indicates some type of binding interaction between BSA and Stilbene 420 dye [18].

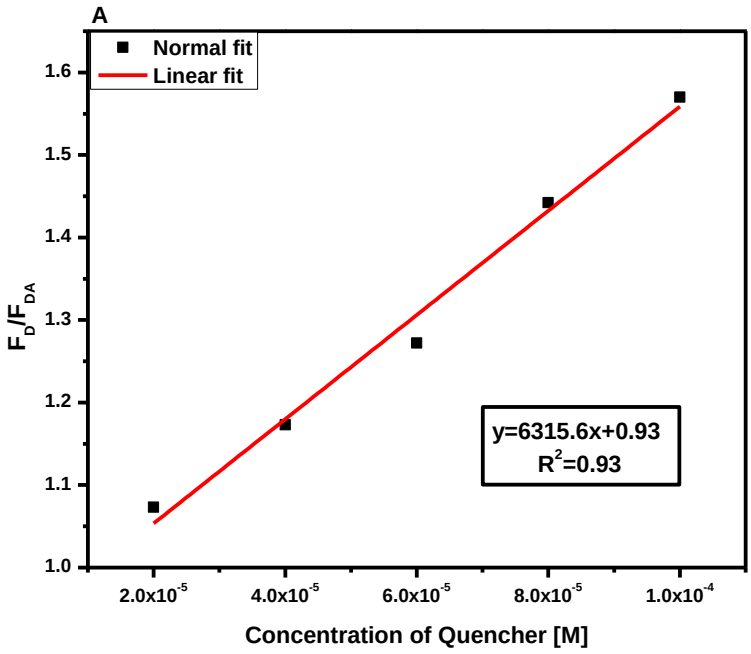

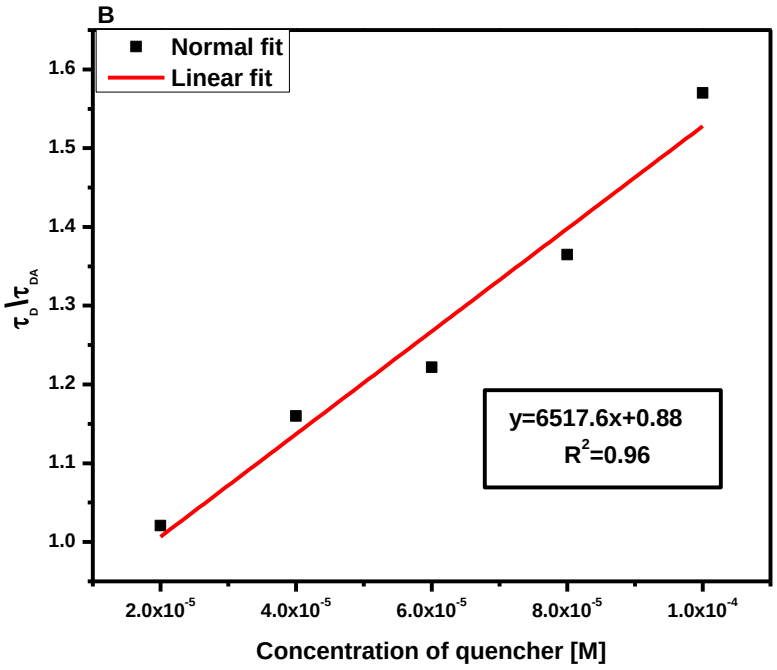

Figure 4 (A-B). Steady-state and time-resolved Stern-Volmer graph

4. Conclusion

The ET between BSA and Stilbene 420 was studied by using steady-state and TR spectroscopy and obtained ET efficiency of up to 36%. The Occurrence of dynamic quenching is further confirmed by steady-state and time-resolved SV plots. The obtained values of bimolecular quenching constant indicate that the interaction between BSA and Stilbene 420 dye is not diffusion-controlled process. Various FRET parameters are determined experimentally and calculated energy transfer efficiency from BSA to S420 dye is 36% for highest concentration of S420. This ET mechanism from BSA to Stilbene 420 dye will lead to potential biomedical applications such as biomolecules sensing, drug delivery, disease diagnosis, and treatment.

5. Acknowledgments

The author KMG greatly acknowledges the Laser Spectroscopy Laboratory, Department of Physics, for supporting to carry out fluorescence and absorption experiments. The authors also thank USIC, Karnatak University, Dharwad for TCSPC measurements.

References:

[1] Helms V, Fluorescence Resonance Energy Transfer-Principles of Computational Cell Biology. Weinheim: Wiley-VCH. p. 202. (2008). ISBN 978-3-527-31555-0.

[2] Fluorescence resonance energy transfer sensor between quantum dot donors and neutral red acceptors and its detection of BSA in micelles. S. Ge, J. Lu, M. Yan, F. Yu, J. Yu, X. Sun. Dyes Pigm. (Elsevier), 91, 304-308 (2011).

[3] Fluorescence resonance energy transfer between quantum dot donors and dye-labeled protein acceptors. Aaron R.C, Igor L.M, Matthew M, Brent R.F, Moungi G.B, Hedi M, J. Am. Chem. Soc. (ACS), 126, 301-10, (2004)

[4] Fluorescence resonance energy transfer in CdSe/ZnS-DNA conjugates: probing hybridization and DNA cleavage. Ron G, Itamar W, Itzhak S, Uri B, J. Phys. Chem. B (ACS), 109, 23715-9, (2005).

[5] The use of FRET imaging microscopy to detect protein-protein interactions and protein conformational changes in vivo. K. Truong, M. Ikura, Curr. Opin. Struc. Biol. (Elsevier), 11 (5) 573-8, (2001).

[6] A Practical Guide to Single Molecule FRET. R. Roy, S. Hohng, T. Ha, Nat. Methods (Nature), 5(6), 507-516, (2008).

[7] Förster resonance energy transfer between MoS2quantum dots and polyaniline for turn-on bovine serum albumin sensing. H. Swaminathan, K. Balasubramanian, Sensor Actuat. b-chem. (Elsevier), 264, 337-343, (2018).

[8] A graphene oxide-based FRET sensor for rapid and specific detection of unfolded collagen fragments. X. Sun, J. Fan, Y. Zhang, H. Chen, Y. Zhao, J. Xiao, Biosens. Bioelectron. (Elsevier), 79, 15-21, (2016).

[9] Graphene quantum dots FRET based sensor for early detection of heart attack in human. D. Bhatnagar, V. Kumar, A. Kumar, I. Kaur, Biosens. Bioelectron. (Elsevier), 79, 495-499, (2016).

[10] A fluorescence turn-on biosensor based on graphene quantum dots (GQDs) and molybdenum disulfide (MoS2) nanosheets for epithelial cell adhesion molecule (EpCAM) detection. J. Shi, J. Lyu, F. Tian, M. Yang, Biosens. Bioelectron. (Elsevier), 93, 182-188, (2017).

[11] Quenching of $[Ru(bpy)_3]^{2+}$ fluorescence by binding to Au nanoparticles. T. Huang, R.W. Murray, Langmuir (ACS), 18, 7077–7081, (2002).

[12] Conjugation of gold nanorods with bovine serum albumin protein. S. Alam, A. Mukhopadhyay J. Phys. Chem. B (ACS), 118, 27459-27464, (2014).

[13] In situ measurement of bovine serum albumin interaction with gold nanospheres. S. D. Medina, S. McDonough, P. Swanglap, C.F. Landes, S. Link, Langmuir (ACS), 28, 9131-9139, (2012).

[14] J. R. Lakowicz, Principles of Fluorescence Spectroscopy, 3 ed., New York: Springer, (2006).

[15] Interaction and energy transfer studies between bovine serum albumin and CdTe quantum dots conjugates: CdTe QDs as energy acceptor probes. M. G. Kotresh, L. S. Inamdar, M. A. Shivkumar, K. S. Adarsh, B. N. Jagatap, B. G. Mulimani, G. M. Advirao, S. R. Inamdar, Luminescence (Wiley), 32(4), 631-639, (2017).

[16] Zwischenmolekulare energiewanderung und fluoreszenz. Förster T, Ann. Phys. (Elsevier) 2, 55-75, (1948).

[17] Interaction between proteinase K and stilbene 420: Occurrence of efficient FRET. Mallikarjun K. P, M. G. Kotresh, S. R. Inamdar, AIP Conference Proceedings, 2104, 030028 (2019).

[18] Spectroscopic Investigation of Alloyed Quantum Dot-Based FRET to Cresyl Violet Dye. M. G. Kotresh, K. S. Adarsh, M. A. Shivkumar, B. G. Mulimani, M. I. Savadatti, S. R. Inamdar, Luminescence (Wiley), 31(3) 760-768, (2016).

Karnatak University
Journal of Science

ISSN: 0075-5168

Comparative study on Size and Composition dependent energy transfer from core-shell and alloyed Quantum dots to Rhodamine 640 dye

K.S. Adarsh

K.S. Adarsh, “Comparative study on Size and Composition dependent energy transfer from core-shell and alloyed Quantum dots to Rhodamine 640 dye” Karnatak University Journal of Science 51, 175-187 (2020).

Comparative study on Size and Composition dependent energy transfer from core-shell and alloyed Quantum dots to Rhodamine 640 dye

K.S. Adarsh*

***Department of Physics, Jain College of Engineering and Technology, Sainagar, Unkal, Hubballi-58003, India.*

****Correspondence author**:* shettiadarsh@gmail.com, Tel: +91-8150019430

Abstract

Semiconductor Quantum dots (QDs) have emerged as a new class of fluorophore, with unique special characteristics photoluminescence properties, has found extensive applications spanning from optoelectronics to bioimaging. In the present work, we report a comparative investigation on efficient Förster Resonance Energy transfer (FRET) between core-shell CdSe/ZnS, alloyed CdSeS/ZnS QDs (donor) and Rhodamine 640 dye (acceptor) by using steady-state and time-resolved fluorescence spectroscopy. The FRET parameters such as spectral overlap integral, Förster distance; Intermolecular distance and Energy Transfer (ET) efficiency were determined and studied the variation of these parameters concerning the size and composition of QDs. It is found that the ET efficiency significantly increases with varying sizes of QDs and tuning the composition of QD by keeping size is fixed. And also we observed higher ET efficiency in composition dependent energy transfer. Further, engages in understanding optical and carrier Core-shell relaxation dynamics and alloyed QDs are developed by using steady-state and time-resolved fluorescence spectroscopy techniques.

Keywords: Quantum Dots; fluorescence resonance energy transfer;Förster distance; Spectral overlap.

Article history: Received: 24 June 2020; Revised: 7 July 2020; Accepted: 9 August 2020

1. Introduction

Semiconductor Quantum dots (QDs) have recently attracted considerable interest in a broad range of potential applications ranging from optoelectronic devices to biomedical tags [1-3]. The typical diameter of QDs is about a few nanometers and the size and the shape can be controlled by an appropriate growing environment. This will give us the size and composition-dependent optical property for the both absorption and emission process. When excited by the photon, the electron in the semiconductor energy band gap of the core region will jump over the band and leave a positive hole in the lower energy band (electron-hole pair) are created and on their recombination fluorescence light is emitted due to the small size quantum effect playing an important role [4,5]. In recent years binary types II to VI of the various semiconductor materials nanocrystals with visible light has undergone intensive research [6, 8]. Work has focused on the last two decades preparing various color-emitting Nanocrystals of different particle sizes of binary or core-shell [1, 9]. Tunable optical properties have also been obtained by changing the constituent stoichiometries in mixed ternary nanocrystals [10-12]. A color-tunable emission of the alloyed ZnxCd1-xSe nanocrystals can be synthesized by changing the particle composition besides the particle size [12]. Further, photoluminescence quantum yield of these alloyed nanocrystals can be greatly enhanced by growing a layer of the wider bandgap material ZnS on alloyed nanocrystal core [13]. With the progress of fluorescence-based techniques, great attention has been paid to fluorescence

resonance energy transfer (FRET) among molecular groups or complexes. FRET is the overriding non-radiative energy transfer (ET) mechanism between a donor and an acceptor fluorophore in nanometer proximity [14]. The FRET process usually proceeds through a dipole-dipole coupling between the transition moments of the two fluorophores, the donor and the acceptor (both fluorescent and QDs). Factors influencing the ET include a spectral overlap of the emission spectrum of the donor with the absorption spectrum of the acceptor and the distance between the donor and acceptor. The distance at which the FRET efficiency is 50%, called the Förster radius (R_0), typically lies in the range of 20 - 100 Å [14, 15]. Now, colloidal semiconductor quantum dots (QDs) are of significant interest as energy donors and acceptors for FRET nanoassemblies, due to their unique optical properties, such as narrow, tunable emission features, broad absorption bands, and high quantum yields. Medintz et al.[16] reported the potential of luminescent semiconductor quantum dots for the development of hybrid inorganic-bio receptor sensing materials. The shape-dependent resonance energy transfer between nanoparticles and dye has been reported [17]. Schrier et al.,[18] theoretically demonstrated the shape dependence of resonance energy transfer between semiconductor nanocrystals. Size heterogeneity effect on FRET has been shown by Pons et al.[19] between the QD donor and the proximal dye acceptor. Again, it is reported that the composition of quantum dots plays a significant role in the energy transfer between QD donor and proximal dye acceptors because the spectral overlap varies with changing composition without changing the particle size [20]. Here we present a comparative study on the size and composition-dependent QD based donor-acceptor pairs with a systematic change in spectral overlap integral and its influence on the efficiency of the photoinduced energy transfer process.

2. Materials and Methods

The alloyed core-shell CdSeS/ZnS QDs (6 nm dia), -COOH functionalized, dispersed in water (Sigma-Aldrich Chemicals Co., USA) and Toluene solutions of CdSe/ZnS core-shell (Lumidot) QDs were purchased from Sigma-Aldrich Chemicals Co. USA were used as donors and Rhodamine 640 (RH- 640) dye (Exciton Inc. USA) as acceptor. Absorption and fluorescence spectra of QDs (donor) and RH -640 dye (acceptor) in solution were obtained at room temperature with the UV-vis absorption spectrophotometer (HITACHI, model U-2800) and a fluorescence spectrofluorometer (Horiba, model Floromax-4), respectively. Coumarin 540A and Rhodamine 110 (Exciton Inc., USA) were employed as standard dyes for quantum yield measurements.

Time-resolved measurements were performed with a time-correlated single-photon counting (TCSPC) system (ChronosBH with picoseconds time resolution) with a laser diode (Horiba) as the source of excitation at 375 nm having a pulse width of ~80 ps, a peak power of ~50 mW, and repetition rate of 20 MHz. The fluorescence decays were collected by a fast photomultiplier tube (Hamamatsu, model H5773) detector. The instrument response function was measured using starch in water as a scatterer and multi-exponential curve fitting has been done with Vinci Analysis software (ISS, USA).

2.1 Quantum Yield Measurement

The photoluminescence quantum yields of alloyed QDs (φ_S) were determined by comparing with a standard dye [20]. The method implicates for measuring two absorbance values and two emission spectra. The element of absorption must be precisely determined for solutions with a low absorbance, typically A<0.1. Under these circumstances, there is a linear relationship between absorption and integrated emissions, and therefore no corrections for inner filter effects were conducted [20, 21]. Fluorescence quantum yield is expressed as

$$\varphi_S = \varphi_R \frac{I_S}{I_R} \frac{OD_R}{OD_S} \frac{n_S^2}{n_R^2} \quad (1)$$

where I_S and I_R are the integrated fluorescence emission intensities of the sample (QDs) and the standard dye (Coumarin 307, φ_R = 56% Coumarin 540A, φ_R = 53%; Rhodamine 110 φ_R = 92%;in ethanol)[22 23] respectively, φ_S represents the quantum yield, OD, the optical density and the refractive index with subscripts S and R denoting sample and reference, respectively. The values of and are determined from the spectrum of photoluminescence by integrating the emission intensity over the desired spectral range and correction of instrumental response.

3. Results and discussion

3.1 Steady-state measurements

The normalized emission spectra of core-shell CdSe/ZnS, alloyed CdSeS/ZnS quantum dots and absorption spectra of RH- 640 dye are as shown in the Fig.1. The emission spectra of core-shell CdSe/ZnS quantum dots (size 2.5, 3.3 nm) retain sharp emission peak at 480 and 530 nm and alloyed CdSeS/ZnS quantum dots (Size 6.0 nm) emission 490 and 525 nm respectively when excited at 375 nm.

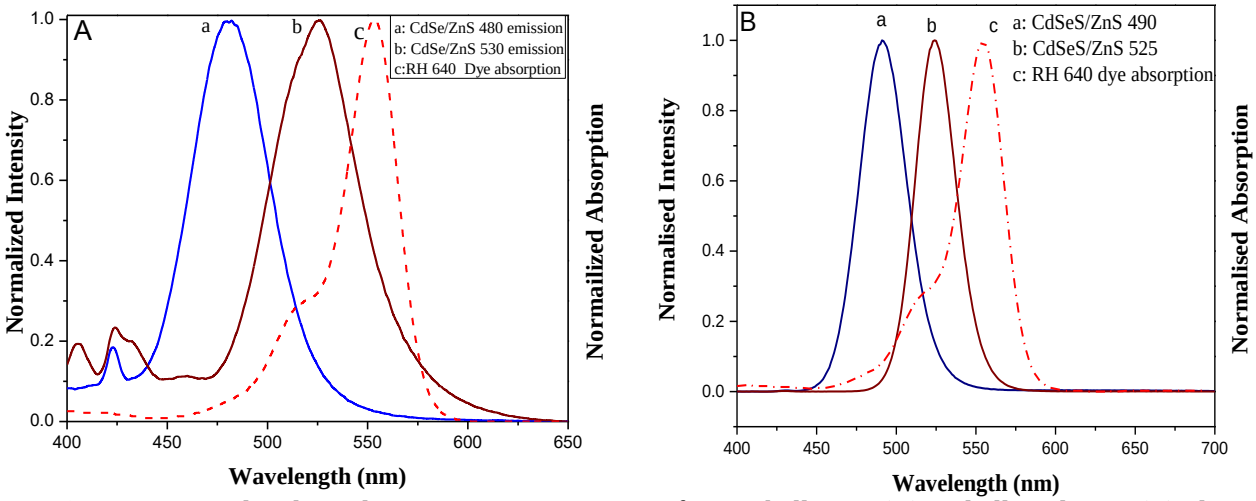

Figure1. Normalized steady-state emission spectra of core-shell QDs (A) and alloyed QDs (B) along with absorption spectrum of RH 640 dye.

It can be seen from Fig. 1(A and B) that there is significant overlap within the donor emission spectrum and a spectrum of acceptor absorption. Remember that the acceptor dye RH- 640 does not show any absorption at 375 nm and therefore exclusive excitation of donor and a pure photo-induced energy transfer from donor to acceptor is highly probable. This in turn, clearly allows for excitation of QDs (Donor) during the FRET process. The acceptor RH-640 dye has broad absorption spectra and exhibiting peak absorption at 555 nm which helps to satisfy the primary conditions of FRET that is spectral overlap. The spectral overlap between these FRET pairs is calculated using the following formula:

$$J(\lambda) = \int_0^\infty F_D(\lambda)\varepsilon_A(\lambda)\lambda^4 d\lambda \quad (2)$$

where $F_D(\lambda)$ is the corrected fluorescence intensity of the donor in the wavelength range λ to $\lambda+\Delta\lambda$ with the total intensity (area under the curve) normalized to unity, and ε_A is the absorption coefficient of the acceptor at wavelength λ (in nm).

The calculated values of the spectral overlap and FRET parameters are presented in Table 1. The spectral overlap between these FRET pairs is seen to increase with increasing sizes of QDs (Fig. 1A) this suggests that the size of QDs plays an important role in tuning the spectral overlap between the FRET pairs. Also in Fig. 1B that there is a significant overlap between the donor emission spectra and the acceptor absorption spectrum. Here, the band gap of alloyed CdSeS/ZnS QDs can be tuned between the energy levels of same sized CdSe and CdS QDs by modifying the composition of chalcogen [selenium (Se) and sulfur (S)] in QD rather than the size.

Table 1. Photophysical properties of CdSe/ZnS and CdSeS/ZnS QDs

QDs	Size (nm)	Emission (nm)	Reference dye	φ_R [a]	φ_S [b]
CdSe/ZnS480	2.5	480	Coumarin 307	0.56	0.38
CdSe/ZnS 530	3.3	527	Rhodamine 110	0.92	0.42
CdSeS/ZnS 490	6.0	490	Coumarin 540A	0.53	0.34
CdSeS/ZnS 525	6.0	527	Coumarin 540A	0.53	0.51

a: Quantum yield of reference dye
b: Quantum yield of sample (QDs)

The fluorescence emission bands of QDs are switching from blue to red upon increasing the ratio of Se to S while keeping their size as constant [24-26].Spectra with absorption and fluorescence QDs CdSeS/ZnS indicate that QDs have broad excitation bands, greater photostability, and narrow emission (FWHM ~27 nm) for the compositions of 490 to 525 nm. The fluorescence quantum yield of QD increases with the rise in Se:S ratio with the emission of the QD shifting to the higher wavelength region. Consequently, the overlap integral is observed to vary with changing composition of these QDs and gives additional benefit without changing the size.

The steady-state emission spectra of core-shell CdSe/ZnS and alloyed QDs CdSeS/ZnS in the presence of RH 640 dye excited at 375 nm are shown in Fig. 2(A-D).

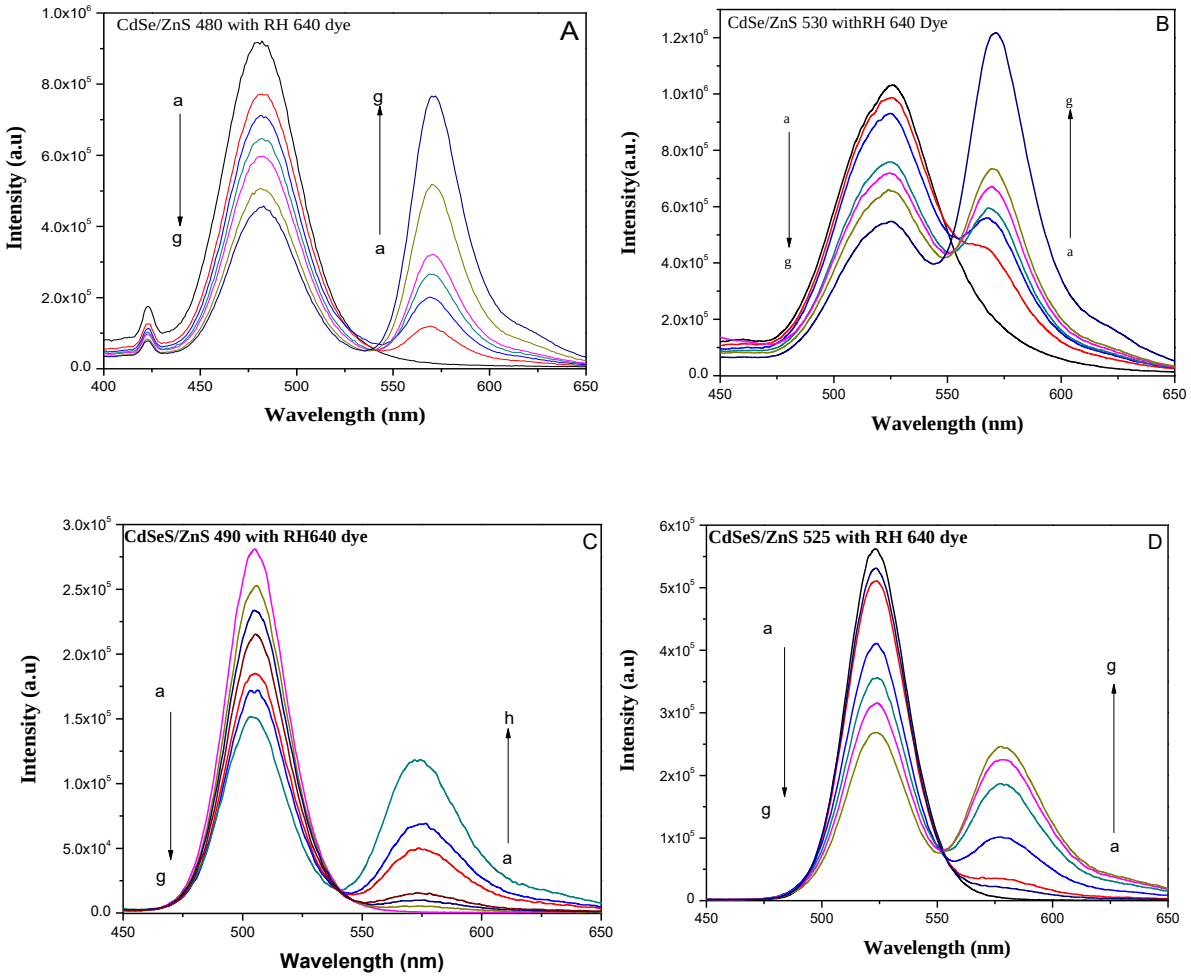

Figure 2(A-D). Steady-state emission spectra of donor core-shell QDs CdSe/ZnS 480 (A),CdSe/ZnS 530 alloyed CdSeS/ZnS 490(C) and CdSeS/ZnS 525 (D) with acceptor RH 640 dye excited at 375 nm. The enhanced emission at 575 nm corresponds to the RH 640 dye resulting from energy transfer from the QDs. QD alone (a), QD with RH 640 0.1x10^{-6}M (b), QD with RH 640 0.2 x10^{-6}M (c), QD with RH 640 0.3x10^{-6}M (d), QD with RH 640 0.4x10^{-6}M (e), QD with RH 640 0.5x10^{-6}M (f), QD with RH 640 0.6x10^{-6}M (g).

As it's clear from this figure, a systematic quenching of fluorescence intensity of QDs with increasing dye concentration is observed. The fluorescence intensity of the acceptor fluorophore is increased with increasing QD:dye ratio and, at the same time, the fluorescence intensity of the donor fluorophore decreased gradually. It's because of an increase in the efficiency of FRET from the donor to the acceptor fluorophore. Hence, from this, one can say that nonradiative resonance energy transfer from core-shell and alloyed QDs to RH-640 dye is occurring and the formation of an emission peak at 570 nm corresponds to the RH-640 dye resulting through FRET process.

The average energy-transfer efficiency (E) can be estimated from steady-state fluorescence data for FRET pairs using the expression:

$$E = 1 - \frac{F_{DA}}{F_D} \qquad (3)$$

where F_D and F_{DA} are the fluorescence intensities of the donor in the absence and in the presence of acceptor. The Energy Transfer efficiency (E) obtained for core-shell CdSe/ZnS (480, 530)-RH 640 dye FRET pairs are 20.10 % and 39.51 % respectively. Similarly for alloyed CdSeS/ZnS (490, 525)-RH 640 dye FRET pairs are 21.32 % and 42.14 % in Table2, respectively.

It reveals that the PL quenching process depends on size as well as the composition present in the QDs. It can be explained that the overlap integral between the emission spectrum of QD and the absorption spectrum of dye varies with change in the size and composition of QD but observed more FRET efficiency in composition dependent QDs.

Another quantitative parameter characterizing the efficiency of ET is Förster distance R_0, defined as the distance of separation between donor and acceptor at which ET is 50% efficient.

Table 2 FRET parameters

[a]Steady-state measurements

FRET System	$J(\lambda)$ $(\mathrm{M^{-1}cm^{-3}})\,\mathrm{x}10^{-13}$	R_0(nm)	r(nm)	E^a(%)
CdSe/ZnS 480-RH640	1.40	4.29	4.69	20.10
CdSe/ZnS 530-RH640	5.55	5.52	5.38	39.51
CdSeS/ZnS 490-RH640	1.44	4.33	4.73	21.32
CdSeS/ZnS 525-RH640	5.84	5.75	5.73	42.14

$$R_0^6 = 8.79X10^{23}(k^2 n^{-4}\varphi_D J(\lambda)) \qquad (4)$$

with φ_D being the fluorescence quantum yield of the donor in the absence of acceptor, n is the refractive index of the medium, $J(\lambda)$ is spectral overlap between donor emission and acceptor absorption spectrum, and k^2 is a constant reflecting the relative orientation of donor and acceptor dipoles. For FRET studies using QDs, an approximation is made to treat the QD-excited state as an oscillating point dipole and assuming isotropic orientation of the dipoles, k^2 equals to 2/3.The Förster distance calculated using Eq. (4) is presented in Table 2, and it depends strongly on the donor's quantum yield and spectral overlap between donor emission and acceptor absorption. The obtained values of R_0 for present FRET pairs are typically in the range 40–60 Å which are comparable with the diameter of many proteins and thickness of membranes [27]. It should be noticed that for each FRET pairs the Förster distance is linearly increased with the increase in spectral overlap as the emission of QD shifts to longer wavelength. From the values of R_0, it is observed that increasing spectral overlap between the donor emission and acceptor absorption spectra lead to an enhancement in the value of R_0 and, simultaneously, the efficiency of ET also increases with an increase in the R_0, suggesting that these FRET pairs are more efficient even with larger distances between them.

3.2 Time-Resolved Measurements

Time-resolved measurements are the most sensitive measurements to understand the nature of QD-dye pairs with a view to further confirmation of energy transfer from QDs to dye molecules. The advantage of using the fluorescence lifetime is to provide significant and reliable information about the molecular interactions than the steady-state measurements which are relative. Time-resolved measurements are immune to fluctuations in the excitation source and photoluminescence decay is independent of concentration. Time-resolved fluorescence experiments can show changes in the exciton lifetime of the donor molecule (QDs) engaged in FRET with an acceptor (dye) molecule when brought in proximity and provide independent verification of non-radiative ET. Fig.3 (A-D)depicts the time-resolved fluorescence decay curves of core-shell and alloyed QDs in the absence and presence of RH 640 dye. The decay parameters of QD and QD-dye FRET pairs obtainedfrom the time-resolved experiments are shown in Table 3.

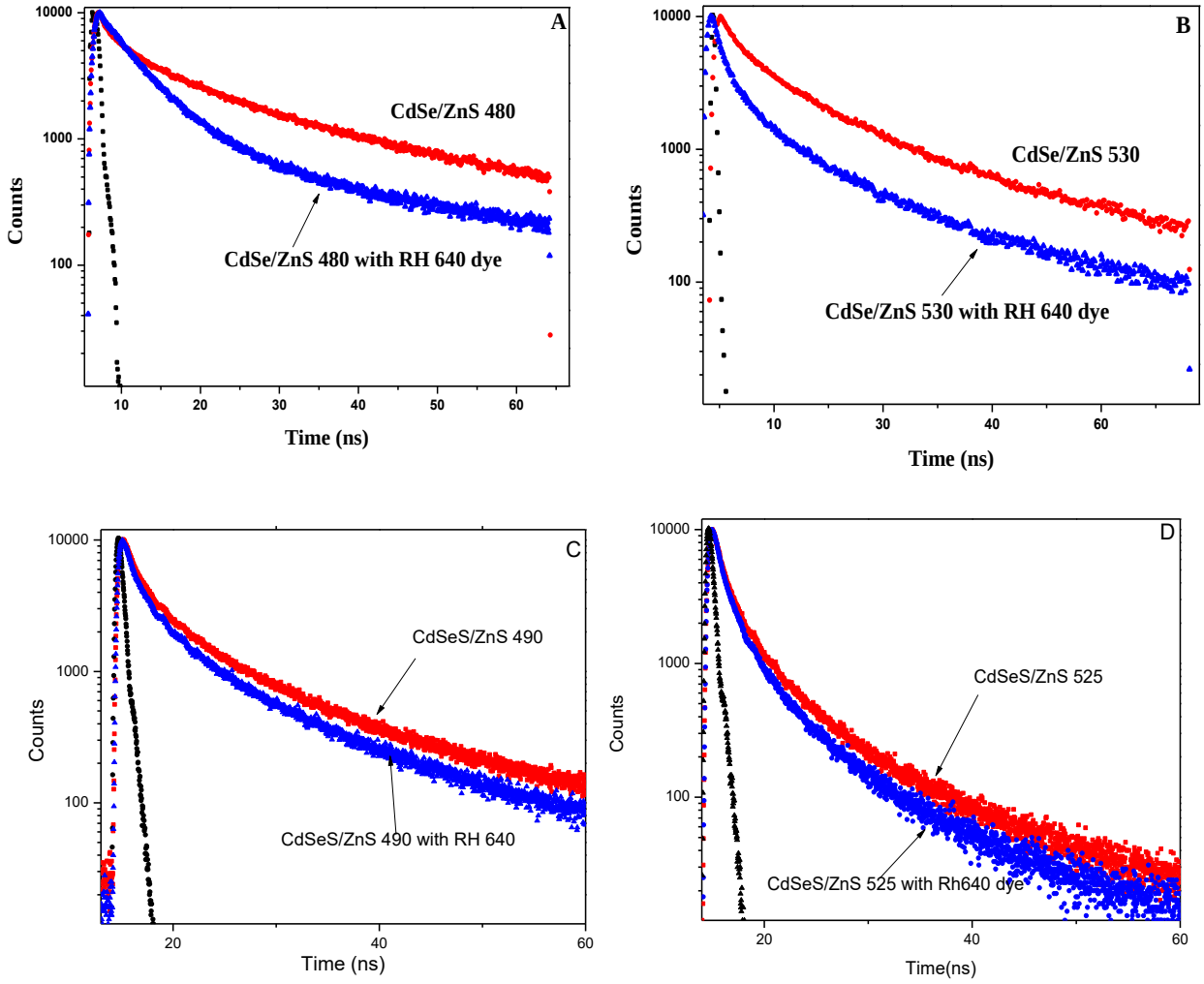

Figure 3(A-D). Semi log scale plot of time-resolved Photoluminescence traces for core-shell QDs CdSe/ZnS 480 (A),CdSe/ZnS 530 alloyed CdSeS/ZnS 490(C) and CdSeS/ZnS 525 (D) in the absence and presence of Rhodamine 640 dye.

The decay profiles are fitted withtri-exponential function with the $\chi 2$ value close to unity:

$$I(t) = \left(A_1\tau_1 + A_2\tau_2 + A_3\tau_3 \right) \quad (5)$$

where τ_1, τ_2 and τ_3 represent the short, long and the longest lifetime components with their normalized pre-exponential factors A_1, A_2 and A_3, respectively. Note that the root of multiexponential emission decay of semiconductor QDs remains a topic of discussion. The short-lived decay component τ_1 reflects the emission the emission from radiative relaxation of the excited electron to ground state and can be attributed to the initially populated core-shell recombination, though, the possible origin of long-lived decay component remains relatively uncertain [28].Recently it has been reported that long-lived decay components in the PL can be attributed to radiative decay from electron-hole recombination on the surface involving surface localized states [28, 29].A distribution of decay times is expected as a result of variation in the non-radiative decay rates for different QDs due to variation in the type and number of the quenching centers.

Table 3 FRET parameters from time-resolved measurements.

FRET System	τ_1(ns)	τ_2(ns)	τ_3(ns)	***A1***	***A2***	***A3***	$<\tau>$(ns)		**E %**
CdSe/ZnS 480	0.73	2.63	16.6	*0.60*	*0.11*	*0.29*	5.54	1.08	15.01
CdSe/ZnS 480+RH 640	0.71	2.77	15.3	0.64	0.15	0.25	4.70	1.11	
CdSe/ZnS 530	0.42	2.82	14.5	0.12	0.25	0.63	9.90	1.13	33.23
CdSe/ZnS 510+RH 640	0.46	2.24	13.1	0.24	0.32	0.44	6.51	1.09	
CdSeS/ZnS 490	0.12	1.28	7.7	0.23	0.32	0.45	3.9	1.23	17.01
CdSeS/ZnS 490+RH 640	0.14	1.25	6.91	0.25	0.35	0.4	3.24	1.21	
CdSeS/ZnS 525	0.26	2.14	8.56	0.11	0.36	0.53	5.34	1.13	34.6
CdSeS/ZnS 525+RH 640	0.19	1.65	7.07	0.2	0.38	0.4	3.49	1.09	

A combination of all these processes, along with the difference between the individual nanocrystals in population, gives rise to multiexponential emission dynamics that result in a spread of luminescence lifetimes for different quantum dots.

The average lifetime w(τ) as calculated using [30, 31]

$$\tau = \frac{\sum A_i\tau_i^2}{\sum A_i\tau_i} \quad (6)$$

where A_i is the normalized preexponential factor and τ_i the fluorescence lifetime.

Decay curves of the core-shell CdSe/ZnS (480, 530 nm) QDs are multi-exponential with three decay components (Table 3). The average photoluminescence decay times are 5.54 ns and 9.90 ns for 480 nm and 530 nm CdSe/ZnS QDs, respectively. However, its average decay time in the presence of the acceptor (RH 640 Dye) drastically reduced to 4.70 ns and 6.51 ns, respectively. Similarly, the decay times for alloyed CdSeS/ZnS (490, 525 nm) QDs are 3.9 and 5.34 ns, respectively. In the presence of RH-640 dye, however, these decrease to 3.24 and 3.49 ns, respectively. Thus, we observed that the lifetimes of both the core-shell and alloyed QDs are significantly shortened on the addition of RH-640 dye and it is one of the characteristics of efficient energy transfer occurring in the donor-acceptor system. Thus, results obtained from the steady-state fluorescence experiments are further strengthened by a pronounced shortening of the QD (CdSe/ZnS and CdSeS/ZnS) exciton lifetime with an increasing number of acceptor dye molecules decrease in the donor lifetime further validates the energy transfer from QDs to RH 640 dye.

The energy transfer efficiency for the FRET pairs is calculated from measured decay time values of the donor (QDs) in the absence and presence of the acceptor, using the equation:

$$E = 1 - \frac{\tau_{DA}}{\tau_D} \qquad (7)$$

where, τ_D and τ_{DA} designate the QD excited-state lifetime without and with the acceptor dye molecule. The calculated ET efficiencies for core-shell CdSe/ZnS (480, 530)-RH 640 dye FRET pairs are 15.01 % and 33.23 %respectively. Similarly for alloyed CdSeS/ZnS (490, 525)-RH 640 dyeFRET pairs are 17.01% and 34.60%, respectively. This result again confirms that the FRET efficiency varies with size and also changes in the composition of quantum dots.Hence, we compare the FRET efficiencies obtained from both the time-resolved and steady-state methods to confirm the steady-state measurement methodology that we adopted.

Here we observed that ET efficiency of alloyed QDs has more efficient than the core-shell CdSe/ZnS QDs. It has been reported that QD emission can be tuned by varying the composition of alloyed QDs while keeping the particle size fixed [25, 32]. Sadhu et al.[32] was found to be QD emission redshifted upon increasing the concentration of cadmium in CdxZn1-xS QD, whereas Swafford et al.[24]noted a blue shift in QD emission upon decreasing the composition ratio of selenium to sulfur present in the CdSeS QD, it is reported that the alloy composition effect on carrier dynamics was systematically examined and found that with increasing sulfur concentration, CdSxSe1-x nanocrystals have a larger concentration of trap states [11], this will affect the radiative recombination fluorescence lifetimes[24]. In addition to fluorescence lifetimes, the increase in trap states affects the optical properties of alloyed nanocrystals. Alloyed core/shell nanocrystals are likely to throw light on discriminating between the intrinsic electron trapping properties of sulfur and surface trapping. Sulfur's intrinsic trapping would not be affected by the shelling layer, leading to a less efficient core/shell. However, shelling should passivate surface trapping, which results in more efficient material with higher quantum yield. Large bandgap material ZnS creates a heteroepitaxial layer on the surface, that suppresses deep trap emission by passivating most of the vacancies and trap sites on the crystalline surface, confining the electrons and holes to the core of alloy, leading to increased PLquantum yield. This indicates an enhanced band-edge emission and elongation of fluorescence lifetime, higher stability (protected from the surrounding matrix), and an order of magnitude increase in the quantum yield.

By knowing the values of R_0 and E determined from time-resolved measurements for each donor-acceptor pair, helps to know the distance of separation between donor and acceptor molecule for each FRET pair using equation:

$$E = \frac{mR_0^6}{mR_0^6 + r_0^6} \tag{8}$$

where*m* is the average number of acceptor molecules interacting with one donor. Using Eq. 7 and 8,the donor-acceptor separation distance for each number "*m*" is calculated using the equation:

$$r_m = R_0 \left(\frac{m(1-E)}{E} \right)^{1/6} \tag{9}$$

In the present study, the estimated intermolecular distance (r) between donor and acceptor for each QD-dye ratio and considered the average of QD-dye ratio. The obtained values for intermolecular distance (r) for core-shell CdSe/ZnS (480, 530)-RH-640 dye FRET pairs are 4.69 and 5.38 nm respectively. Similarly for alloyed CdSeS/ZnS (490, 525)-RH-640 dye FRET pairs are 4.73 and 5.72 nm respectively.

It is observed that, by increasing the both size of the QD and also composition present in the QDs, the intermolecular distance also increases, thus providing a way to monitor the targets at the larger intermolecular distance by employing the larger size of the QDs. Since the distances obtained between donors and acceptors are in the range of 20 to 60 Å, the effective ET obtained for these FRET pairs in this range is helpful in many biomedical applications.

4. Conclusion

In this paper, we have presented the comparative investigation of FRET on core-shell and alloyed to dye systems. Steady-state and time-resolved fluorescence studies on FRET pairs of core-shell studies on FRET pairs of core-shell CdSe/ZnS-RH 640 dye and alloyed CdSeS/ZnS -RH 640 dye systems. At this point, the spectral overlap obtained between the absorption spectra of the acceptor and fluorescence of the donor, as well as the proximity of the donor-acceptor molecules, within the range 1–10 nm, are reasonable conditions for the observation of FRET process. We have demonstrated that the energy transfer from QD to dye varies by changing the size and composition of QDs .Observed higher ET efficiency in composition dependent energy transfer. Thus, the present work opens up new possibilities for designing light harvesting nanostructures for future applications.

5. Acknowledgments

This research was supported by the Department of Atomic Energy,Government of India, under Board of Research in Nuclear Sciences (BRNS), Bombay MajorResearch Project as well as University Grants Commission, NewDelhi under Centre with Potential for Excellence in Particular Area (CPEPA)

6. Reference

[1] Small-particle research: physicochemical properties of extremely A. Henglein Chem. Rev.,(ACS publication) 89 8;1861-73 (1989).

[2] Quantized semiconductor particles: a novel state of matter for materials science. H. Weller Adv Mater (Wiley online library) 5:88–95 (1993).
[3] Synthesis and characterization of nearly mono disperse CdE (E = sulfur, selenium, tellurium) semiconductor C.B .Murray, D.J. Norris and M.G. Bawendi J Am Chem Soc 115:8706 (1993).
[4] Fluorescence intermittency in single cadmium selenidenanocrystals M. Nirmal, B. O. Dabbousi, M. G. Bawendi, J. J. Macklin, J. K. Trautman, T. D. Harris, L.E. Brus, Nature, Vol 383(1996).
[5] Quantum Dot Bioconjugates for Ultrasensitive Nonisotopic Detection C. W. Warren Chan, Shuming Nie Science, Vol. 281(1998)
[6] Synthesis and characterization of strongly luminescing ZnS-capped CdSe nanocrystals, M. A. Hines and P.Guyot-sionnestJ. Phys. Chem.(ACS Publication) 100, 468–471 (1996).
[7] Epitaxial growth of highly luminescent CdSe/CdS core/shell nanocrystals with photostability and electronic accessibility, X.Peng M. C. Schlamp A. V. Kadavanich and A.P. Alivisatos J. Am. Chem. Soc. .(ACS Publication) 119, 7019–7029 (1997).
[8] CdSe/ZnS Core−Shell Quantum Dots: Synthesis and Characterization of a Size Series of Highly Luminescent Nanocrystallites B. O. DabbousiJ. Rodriguez-ViejoF. V. MikulecJ. R. HeineH. MattoussiR. OberK. F. Jensen and M. G. BawendiPhys. Chem. B .(ACS Publication) 101, 46, 9463–9475 (1997).
[9] Semiconductor clusters nanocrystals, and quantum dots science A. P. Alivisatos Science 71, 933–937 (1996).
[10] Room-temperature synthesis and characterization of nanocrystalline CdS, ZnS, and CdxZn1-xS W. Wang, I. Germanenko and M. S.El-Shall Chem. Mater. (ACS Publication)14, 3028–3033 (2002).
[11] Band edge dynamics in CdSenanocrystals observed by ultrafast fluorescence upconversionM. D.GarrettM.J. Bowers, R. James. McBride, L. Rebecca O.Stephen J. Pennycook and S. J. RosenthalJ. Phys. Chem. C (ACS Publication)112, 436–442 (2008).
[12] Size and band-gap dependences of the first hyperpolarizability of CdxZn1-xS nanocrystalsD. V. PetrovB. S. SantosG. A. L. Pereira and C. M. Donegá J. Phys. Chem. B (ACS Publication) 106, 5325–5334 (2002).
[13] Composition-tunable ZnxCd1-xSe nanocrystals with high luminescence and stability X. Zhong, M.HanZ. DongT. J. White and W. KnollJ. Am. Chem. Soc. (ACS Publication)125, 8589–8594 (2003).
[14] J.R. Lakowicz. Principles of fluorescence spectroscopy (Springer) 2006.
[15] Quantum dots and peptides: A bright future together M. Zhou and I. Ghosh Biopolymers (Peptide Science) (Wiley online library), 88 325–39(2006).
[16] A reagentlessbiosensing assembly based on quantum dot–donor Förster resonance energy transfer I. L. Medintz A. R. Clapp J. S. Melinger J. R. Deschamps H. Mattoussi Adv. Mater. (Wiley online library)17(20), 2450–2455 (2005).
[17] Efficiency of Energy Transfer from Organic Dye Molecules to CdSe−ZnS Nanocrystals: Nanorods versus Nanodots M. Artemyev, E. U stinovich, and I. Nabiev J. Am. Chem. Soc. (ACS Publication) 131, 8061–8065 (2009).
[18] Shape Dependence of Resonant Energy Transfer between Semiconductor Nanocrystals J. Schrier and L.W. Wang J. Phys. Chem. CACS Publication)112, 11158–11161(2008).
[19] Spectrally resolved energy transfer using quantum dot donors: Ensemble and single-molecule photoluminescence studies T. Pons, I.L. Medintz, M. Sykora, and H. Mattoussi Phys. Rev. B (APS Physics) 73, 245302 (2006).

[20] FRET from core and core–shell quantum dots to laser dye: A comparative investigation K.S. Adarsh, M.K.Singh, M.A. Shivkumar, M.K. Rabinal, B.N. Jagatap, B.G. Mulimani M.I. Savadatti and S.R.Inamdar J. Lummi.(Elsevier) 160216–222(2015).
[21] Standards for photoluminescence quantum yield measurements in solution A. M. Brouwer Pure. Appl. Chem (IUPAC Technical Report). 83, 2213–2228 (2011).
[22] Novel multi-branched organic compounds with enhanced two-photonabsorption benefiting from the strong electronic coupling Y. Ren, Q. Xin, X. T. Tao,, L. Wang, X. Qiang Y.J. X. Yang and M.H. Jiang Chem. Phys. Lett. (Elsevier) 414, 253–258(2005).
[23] Fluorescence quantum yields of some rhodamine dyes R.F. Kubin And A.N. Fletcher J. Lumin. (Elsevier) 27,455–462 (1982).
[24] Homogeneously Alloyed CdSxSe1-x nanocrystals: synthesis, characterization, and composition/size-dependent band gapL. A Swafford, L. A. Weigand, M. J. Bowers, J. R. McBride, J. L Rapaport, T. L Watt, S. K Dixit, L. C. Feldman, S. J RosenthalJ. Am. Chem. Soc (ACS Publication). 128 (37), 12299–12306 (2006).
[25] Composition-dependent energy transfer from alloyed ternary CdSeS/ ZnS quantum dots to Rhodamine 640 dye K.S.Adarsh, M.G. Kotresh, M.A. Shivakumar and S.R. Inamdar J. Nanophoton. (SPIE) 12(4), 046016 (2018)
[26] High quality CdSeSnanocrystals synthesized by facile single injectionprocess and their electro luminescence,E. Jang, S. Jun and L. Pu Chem. Commun. (Royal Society of Chemistry) 0(24), 2964–2965 (2003).
[27] Self-assembled nanoscale biosensors based on quantum dot FRETdonorsI. L. Medintz, A. R. Clapp, H. Mattoussi, E. R. Goldman, B. Fisher and J Matthew MauroNat. Mater (National Library of materials 2, 630–638 (2003).
[28] Size- and composition-dependent energy transfer from charge transporting materials to ZnCuInS quantum dotsXi Yuan, J. Zhao, P. Jing, W. Zhang, H. Li, L. Zhang, X. Zhong, and Y. Masumoto J. Phys. Chem. C (ACS Publication) 116, 11973–11979 (2012).
[29] Surface modification of CdSe and CdS quantum dots-experimental anddensity function theory investigation,in Nanocrystals—Synthesis, Characterization andApplications, S. Neralla, (Ed.), p. 148 (2012).
[30] Fluorescence enhancement via aggregation effect due to microenvironmental alterations in human hemoglobin protein in presence of carbon quantum dots (CQD): Comparative spectroscopic approach, M. Chakraborty, I. Mitra, K. Sarkar, M. Bardhan, S. Paul , .S Basu, A Goswami, A.Saha, B. Show, T. Ganguly Spectrochimica Acta Part A *215*, 313-326 (2019)
[31] Effects of Carbon Quantum Dots (CQDs) on the energy storage capacity of a novel synthesized short-chain dyad. Mitra, S. Paul, M.Bardhan, S Das, M Saha, A Saha,T. Ganguly Chem Phys Letts *276*, 1-6 (2019)
[32] Composition effects on quantum dot-based resonance energy transfer, S. Sadhu and A. Patra J. Phys. Chem. C (AIP Publication) 116, 15167–15173 (2012)

Karnatak University
Journal of Science

ISSN: 0075-5168

Dispersion of SiO_2 Nanoparticles on Ferroelectric liquid crystal micro domains emanating enhanced luminescence spectral properties

Aradhana Roy
Rajiv Manohar

Aradhana Roy and Rajiv Manohar, “Dispersion of SiO2 Nanoparticles on Ferroelectric liquid crystal micro domains emanating enhanced luminescence spectral properties” Karnatak University Journal of Science 51, 188-195 (2020).

Dispersion of SiO_2 Nanoparticles on Ferroelectric liquid crystal micro domains emanating enhanced luminescence spectral properties

Aradhana Roy and Rajiv Manohar*
Liquid Crystal Research Lab, Physics Department, University of Lucknow, Lucknow-226007, India.
Corresponding author: *rajiv.manohar@gmail.com*

Abstract:

The objective of the present study is to investigate the influence of SiO_2 nanoparticles (NPs) on luminescence properties of Ferroelectric Liquid Crystal (FLC) sample W327. Primary observations recorded include optical micrographs and dielectric a.c conductivity. Addition of 0.2 wt% of SiO_2 NPs generated optimized conductivity with improved alignment of FLC molecules. Further study consists of spectral properties, namely UV-Vis absorbance and Photoluminescence of pure FLC and FLC-NPs composites at room temperature which can be employed in development of thermostable photonic devices. Enhanced luminescence energy of FLC-NP composites is characteristic result of the present investigation which finds its utility in LC based technologies such as low temperature-low charge consumable devices.
Keywords: Ferroelectric liquid crystal; SiO_2 Nanoparticles; Conductivity; Absorbance; Photoluminescence.
Article history: Received: 9 July 2020; Revised: 4 September 2020; Accepted: 9 September 2020

1. Introduction

The optical and spectral properties of liquid crystal have drawn a beautiful picturesque for the global scientific community. Since the experiment of Michael Faraday on bending of electromagnetic wave while traversing through transparent glass, a stir was generated among researchers for innovation of different anisotropic material to manipulate electromagnetic pulse in a more improved manner. Soon many applications were erupted from this experiment of light bending; however the output was accompanied by energy loss and deterioration of material with time. Discovery of liquid crystals infused new technological up gradation in many electromagnetic wave dependent applications with more competent results. Among all the liquid crystals, Ferroelectric liquid crystal (FLC) garnered special attention due to its unique feature of molecular alignment. FLC i.e. chiral smectic C phase (SmC*) has a layer upon layer arrangement of molecules with fixed positional and orientational order imparting stable molecular alignment was discovered by Robert Meyer [1]. The geometrical arrangement of the molecules constructs an angle between layer normal and orientation director. This tilt angle gives rise to helical arrangement of molecules in FLC compounds emanating exotic optical properties. Next phase in LC research came at the dawn of guest-host effect. Amalgamation of nanoparticles (NPs), polymers, dyes, quantum dots, biological entities in LC widened the door for applicability of both with mutual benefit. In this regard, incorporation of NPs in FLC generated a new series of optical observations which can be utilized to marvel competency of any device. Any material to be used for application purpose should demonstrate efficient temporal response over wide range, reduced interference of mobile ions, energy saving as well

environmentally biodegradable. NP-FLC composites satisfy all these primary characteristics thereby creating a vast avenue for device fabrication.

Continuous development is taking place in exploring the dynamics of FLC compounds with dispersion of NPS in presence of an externally applied field. A detail analysis of the dielectric properties and Goldstone Mode exhibited by FLC in presence of SiO_2 NPs has been discussed by Raina and group [2]. Chandran et.al reported fabrication of low power operating optical device from FLC ZLI 3654 dispersed with NiO nanorods [3]. The effect of the electromagnetic field on nano-suspensions dispersed in FLC has been statistically theorized by Majumder and group with potential applications in device fabrications [4]. Haase et.al measured switching characteristics of $LiNbO_3$ and FLC colloids facilitating possible electronic device on nanometric scale [5]. Podgornov et.al observed low relaxation modes near electrical double layers between nanoparticles and the alignment layers, also known as Schwarz's relaxation in FLC-Gold NPs dispersion. The observation indicates possible use of conductive properties of ionic potentials sheathed in between the smectic layers of FLCs [6].

However above study cited are mainly focused on optical properties measured via response time characteristics or dielectric material parameters. In the present investigation, the optical properties chiefly considered are Photoluminescence (PL) and UV-Vis characteristics along with optical micrographs. These parameters throw light on both spectral as well as on optical properties of FLC employed. SiO_2 NPs are dispersed in the investigated FLC due to the strong energy confinement levels of former [7]. Many studies have been conducted by our group on PL and UV-Vis characteristics of FLC compounds [8], [9].

2. Materials and Methods

The FLC material used W327 is a multi-component organic mixture consisting a chiral dopant with following transition scheme [18, 19].

$$SmC^* \xrightarrow{72.5^\circ C} SmA^* \xrightarrow{85.5^\circ C} N \xrightarrow{87.2^\circ C} Iso.$$

SiO_2 NPs are dispersed in N, N- Dimethylformamide (DMF) and then ultrasonicated for 2 hours. The DMF-SiO_2 mixture is then magnetically stirred to obtain homogeneously dispersed solution. 0.2 wt% and 0.4 wt% SiO_2 is added to pure FLC sample to form two composites. Photolithographic techniques treated ITO coated conductive glass plates are employed to fabricate sample holders. The alignment to the investigated sample molecules is provided by unidirectional rubbing of Nylon 6/6 polymer layered glass plates. The planar aligned glass plates are sandwiched together by Mylar spacers to maintain thickness at 8.3μm. The pure FLC and composites are filled in the sample holders through capillary action at isotropic temperature to ensure homogeneity of filled samples. Polarized optical micrographs of the fabricated cells are recorded by electronic microscope (Radical RXLr-5) fitted with an inbuilt camera (Jenoptik ProgresCT3) and a temperature controller hot plate stage (Instec mK1000). Dielectric parameters of the experimental samples are determined by Impedance /Gain Phase Analyser (HP-4194 A) having frequency range between 100 Hz to 40 MHz. The PL spectra of the investigated samples are recorded at room temperature using Agilent Spectrophotometer equipped with a Xenon discharge lamp of power 13W (Cathodeon AXE 3u) as the excitation source. UV-VIS spectrophotometer (SL210) with wavelength region from 190nm to 1100nm is used to observe spectroscopic properties of pure and SiO_2 NPs dispersed FLC matrix. The above mentioned measurements techniques have been employed by our group in various investigations with details provided in following papers respectively. [10-13].

3. Results and Discussions

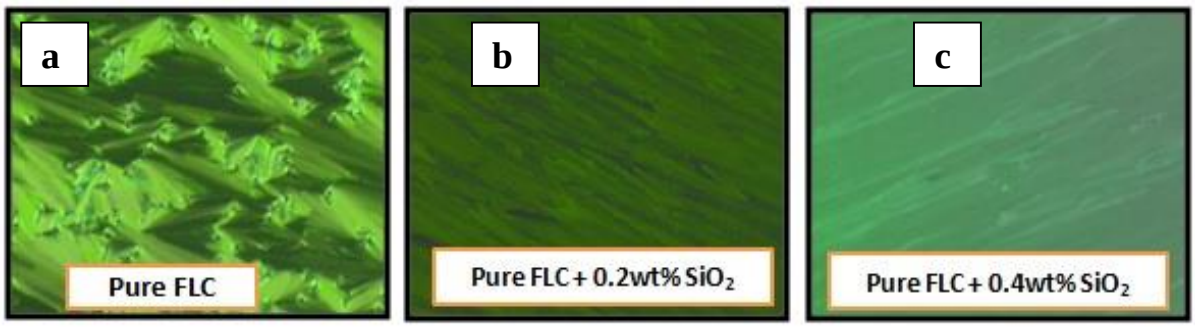

Figure 1. Optical Micrographs of Pure FLC, FLC+0.2wt% SiO_2 and FLC+0.4wt% SiO_2 at temperature 55ºC

Polarizing Optical Micrographs constitutes an essential tool for determining two important characteristics experimental samples: aggregation of NPs in dispersed FLC and alignment of the FLC molecules with respect to polyamide layer and the NPS. Textures of pure and SiO_2 NPs dispersed FLC matrix has been reported at temperature 55ºC concentrating on SmC* mesophase. Figure 1.a shows the broken focal conic texture of chiral smectic mesophase (SmC*) exhibited by the alkyl group of the organic LC compound. Figure 1.b and figure 1.c portrays textures of 0.2wt% and 0.4wt% SiO_2 NPs dispersed FLC matrix depicting homogenous dispersion of NPs in pure FLC. Incorporation of SiO_2 NPs displays enhanced alignment of FLC molecules. The alignment of the FLC molecules increases with increase in NP concentration. Enhanced alignment with minimal aggregation might be due to the capture of mobile ions on the surface of SiO_2 NPs. The presence of the NPs hinders the free rotation of FLC molecules as well as keeps the ionic entities at bay ensuring efficient utilization of input energy.

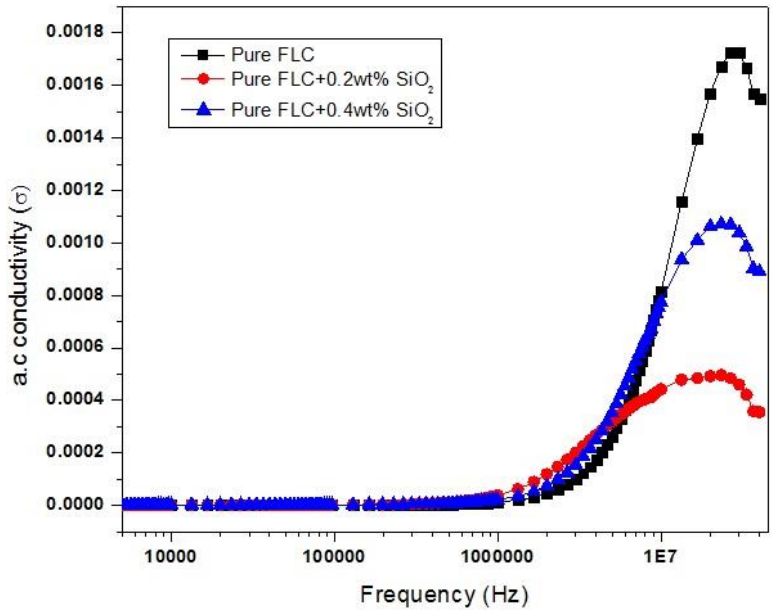

Figure 2. Illustration of conductivity of pure FLC, FLC+0.2wt%SiO_2 and FLC+0.4wt% SiO_2 at 55ºC temperature and 0V

The polarizing response of the pure FLC and FLC-NP composite samples under the influence of external electric field is examined by broadband dielectric spectroscopy. The dielectric spectroscopy measures the permittivity of the system arising due to the elastic mediated interaction between LC molecules and the NPs. However from device fabrication point of view, measurement of a.c conductivity is a significant entity as it determines the interference of ionic charge carriers as well as leakage of incident current. The conductivity for the present investigation has been plotted in Figure 2. It can be clearly seen from the graph that pure FLC shows maximum conductivity but with addition of 0.2 wt% SiO_2 to pure FLC, the conductivity of composite 1 has decreased indicating suppression of the mobile ions. However with further addition of 0.4wt% SiO_2 NPs, the conductivity has again increased. The cause of this effect might be leakage of incident voltage from smectic planes of FLC as the helical conformation suppresses with increase in both temperature and electric field intensity. Thus suppression of FLC helix might not have been able to hold off the field intensity. Another reason that can be cited here is the cluster of NPs in FLC domains. The conductivity of composite 2 might have amplified due to participation of cluster of NPs [14].

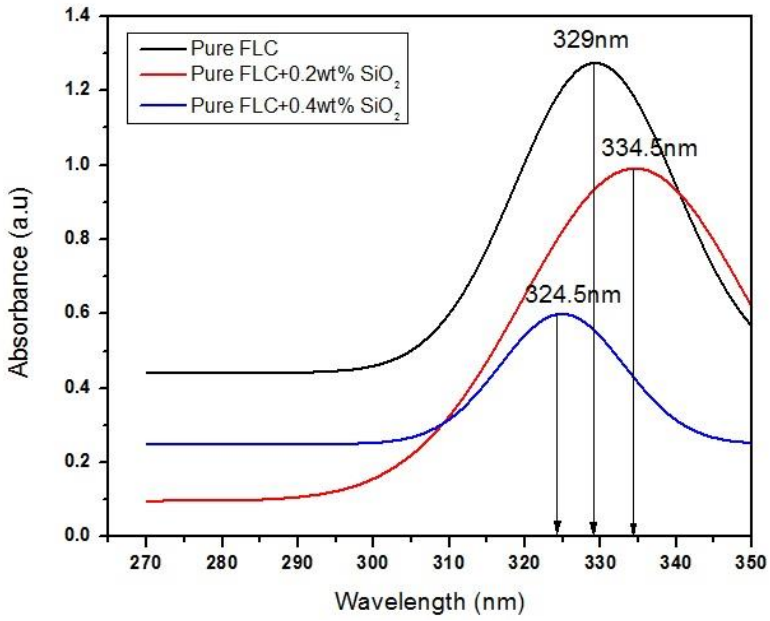

Figure 3. Variation of UV-Visible Absorbance with the function of wavelength (nm) for pure FLC, 0.2wt% and 0.4wt% SiO_2 NPs dispersed FLC.

The UV-Vis absorbance intensity is used to determine the interaction of photons with FLC molecules in presence of dispersed NPs. The UV-Visible absorption spectra of pure FLC and composites are plotted in Figure 3 within the wavelength range from 270nm-350nm. The UV-Vis wavelength of pure FLC is 329nm displaying maximum absorbance at 1.3. Composite 1 and composite 2 shows absorbance at 334.5nm and 324.5nm wavelength respectively. A linear decrement in the absorbance intensity of the FLC composites has been found with increase in concentration of SiO_2 NPs. However, a blue shift is observed in wavelength of composite 2 with respect to pure FLC. This shift in wavelength might have been occurred due to the change in the area cross section of the passage through which the light beam is travelling across the sample holder. This variation in area cross section might be arising due to the change in the concentration of the dispersed NPs which in effect alters the refractive index (RI) of the medium. Thus, as the RI of the medium varies, so does the absorbance wavelength [15].

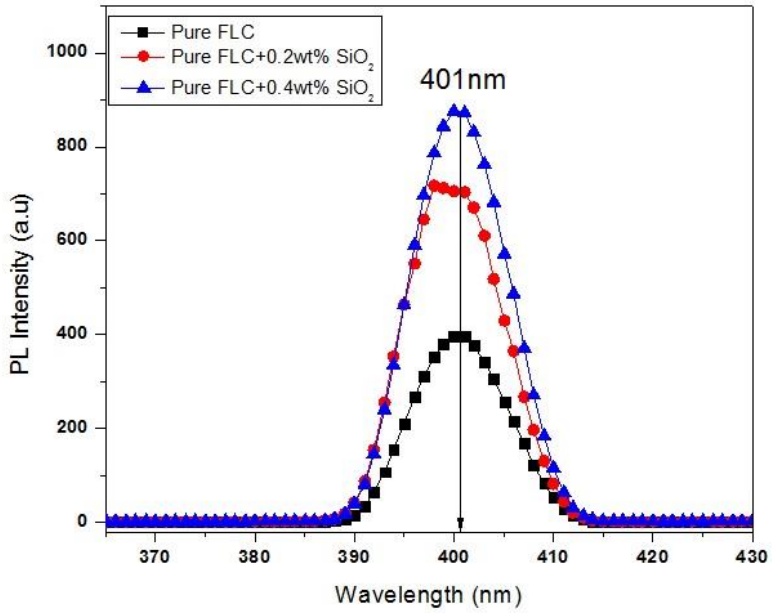

Figure 4. Variation in PL intensity with respect to concentration of SiO_2 NPs in pure FLC.

Photoluminescence phenomenon is observed in any organic or inorganic element or compound which on absorption of photonic energy from monochromatic light source emits photons of a particular wavelength. In LC domains, an inter-transfer of the energy takes place between dispersed NPs to the LC molecules [16], [17]. In our present study we have irradiated pure FLC and its NPs composites with photonic energy of wavelength 329nm (UV-Vis absorbance wavelength of pure FLC) as observed in Figure 3. The photoluminescence plot for the experimental samples has been plotted in Figure 4. As it can be clearly seen from the graph, with increase in the concentration of dispersed SiO_2 in FLC, the PL intensity is increasing. The emission wavelength for all the three samples has been recorded at 401nm and no shift in wavelength has been observed for the FLC-NPs composites. The result clearly implies on efficient energy transfer between the dispersed NPs and FLC molecules owing to improved alignment of the latter. Another reason for amplification in PL intensity can be drawn from the eradication of mobile ionic carriers by the dispersed NPs.

4. Conclusion

In brevity, the effect of SiO_2 NPs on ferroelectric liquid crystal has been investigated in the present study. Incorporation of NPs in FLC has induced alignment as visible from the optical micrographs. The conductivity of the composites has been optimised in contrast to pure FLC with eradication of mobile ion carriers thereby accelerating molecular interactions of NPs with FLC molecules. Further molecular dynamics of the interaction between SiO_2 NP and FLC has been explored by UV-Vis absorbance and Photoluminescence spectra. Enhanced PL emission spectrum of SiO_2 NPs dispersed FLC facilitates fabrication of luminescent screens, spatial modulators and energy efficient and highly conductive photovoltaic/photonic applications.

Acknowledgments

Author A. Roy is sincerely thankful to UGC [F-25-1/2014-2015/7-177/2007 BSR], New Delhi, for providing financial assistance in the form of UGC-BSR Fellowship. R.

Manohar is thankful to UGC for 'MID CAREER AWARD' [F.19-224/2018 (BSR)]. Authors are also thankful to the *APJ Abdul Kalam Centre for Innovation* for the experimental facilities.

References

1. Ferroelectric liquid crystals R. B Meyer, L Liebert, L Strzelecki and P Keller Journal de Physique Lettres, 36**,** 69-71 (1975).
2. Dielectric Studies and Memory Effect in Nanoparticle Doped Ferroelectric Liquid Crystal Films Praveen Malik, Ashok Chaudhary, Rohit Mehra, and K. K. Raina Mol. Cryst. Liq. Cryst., 54, 243-251 (2011).
3. Low-voltage electro-optical memory device based on NiO nanorods dispersed in a ferroelectric liquid crystal Achu Chandran, Jai Prakash, Jitendra Gangwar, Tilak Joshi, Avanish Kumar Srivastava, D. Haranath and Ashok M. Biradar RSC Adv., 6, 53873 (2016).
4. Theory of nanoparticles doped in ferroelectric liquid crystals T. Lahiri, T. Pal Majumder, and N. K. Ghosh Journal of Applied Physics 113, 064308 (2013).
5. Electro-optical behaviour and dielectric dynamics of harvested ferroelectric $LiNbO_3$ nanoparticle doped ferroelectric liquid crystal nanocolloids R. K. Shukla, C. M. Liebig, D. R. Evans and W. Haase RSC Adv., 4, 18529 (2014).
6. Low-frequency relaxation modes in ferroelectric liquid crystal/gold nanoparticle dispersion: impact of nanoparticle shape F. V. Podgornov, R. Wipf, B. Stühn, A. V. Ryzhkova and W. Haase Liquid Crystals, 43, 1536–1547 (2016).
7. Electronic and level statistics properties of Si/SiO2 quantum dots I. Filikhin, S.G.Matinyan, B.K.Schmid, B.Vlahovic Physica E, 42, 1979–1983 (2010).
8. Analysis of optical properties and mechanism of photoluminescence enhancement of a quantum dot – ferroelectric liquid crystal composite Tripti Vimal, Dharmendra P. Singh, Kaushlendra Agrahari, Atul Srivastava, and Rajiv Manohar Photonics Letters Of Poland, 8 (1), 23-25 (2016).
9. Time-Resolved Fluorescence and Absence of Förster Resonance Energy Transfer in Ferroelectric Liquid Crystal-Quantum Dots Composites D. P. Singh, S. Pandey, R. Manohar, S. Kumar, G. H. Pujar and S. R. Inamdar Journal of Luminescence 190, 161-170 (2017).
10. Optimization of the dielectric and optical parameters of 1,2,4-oxadiazole ferroelectric mesophase with the suspension of PVP capped gold nanoparticles AradhanaRoy, Pankaj K. Tripathi, S.Mahabaleshwara, Maddasani Srinivasulu, Rajesh K. Gangwar, Rajiv Manohar Optical Materials (Elsevier) 107, 110021 (2020).
11. $CuInS_2$/ZnS QD-ferroelectric liquid crystal mixtures for faster electro-optical devices and their energy storage aspects Dharmendra P. Singh, Tripti Vimal, Yatin J. Mange, Mahesh C. Varia, Thomas Nann, K. K. Pandey, Rajiv Manohar, and Redouane Douali Journal of Applied Physics 123, 034101 (2018).
12. Effect of gold nanoparticles on intrinsic material parameters and luminescent characteristics of nematic liquid crystals Aradhana Roy, Bhupendra Pratap Singh, Geeta Yadav, Hiba Khan, Sandeep Kumar, Atul Srivastava, Rajiv Manohar Journal of Molecular Liquids 295, 111872 (2019).
13. Dispersion of fluorescent dye in the nematic liquid crystal: Enhanced photoluminescence and high birefringence Govind Pathak, Kaushlendra Agrahari, Aradhana Roy, Atul Srivastava, Olga Strzezysz, Katarzyna Garbat, Rajiv Manohar, Opto-Electronics Review 26, 317–324 (2018).
14. InP/ZnS quantum-dot-dispersed nematic liquid crystal illustrating characteristic birefringence and enhanced electro-optical parameters Aradhana Roy, Govind Pathak,

Jakub Herman, Sanjeev R. Inamdar, Atul Srivastava and Rajiv Manohar Applied Physics A 124, 273 (2018).

15. Enhancing the photoluminescence of ferroelectric liquid crystal by doping with ZnS quantum dots, A. Kumar, J. Prakash, Abhay D. Deshmukh, D. Haranath, P. Silotia, and A. M. Biradar, , Appl. Phy. Lett. 100, 134101 (2012).
16. CdTe quantum dot dispersed ferroelectric liquid crystal: Transient memory with faster optical response and quenching of photoluminescence, S. Pandey, D. P. Singh, K. Agrahari, A. Srivastava, M. Czerwinski, S. Kumar and R. Manohar, J. of Mol. Liq. 237, 71-80 (2017).
17. Mechanism of photoluminescence enhancement and quenching in Nd_2O_3 nanoparticles–ferroelectric liquid crystal nanocomposites P. Goel and M. Arora, RSC Adv. 5, 14974-14981 (2015).

Karnatak University
Journal of Science

ISSN: 0075-5168

Hearing Aid Prototype using MATLAB

Himashree S.I.
Bhavana H.
Jyoti M.G.
Priyanka B.G.
Sharada Sajjan,

Himashree S.I., Bhavana H., Jyoti M.G., Priyanka B.G. and Sharada Sajjan, "Hearing Aid Prototype using MATLAB" Karnatak University Journal of Science 51, 186-193 (2020).

Hearing Aid Prototype using MATLAB

Himashree S.I.*, Bhavana H., Jyoti M.G., Priyanka B.G. and Sharada Sajjan

Department of Electronics and Communication Engineering, SDM College of Engineering & Technology, Dharwad

***Corresponding author**: himu.si@gmail.com*

ABSTRACT

Hearing aid, a tiny electronic appliance, has been a great help for the people with hearing loss. It tunes the amplification according to the user's needs. Analog hearing aids are analogous to a simple radio wherein the sound alone is amplified. But a digital hearing aid does more than just amplifying sound. It avails the user to tune the frequency specific amplification to his or her needs. This is made possible by digital signal processing. In the present study this is carried out in MATLAB software. The speech signal given as input is first de-noised by using noise reduction filters. It is then adjusted to various frequency needs of the user. This is carried out by frequency shaping method. Here, the gain is set for different ranges of frequencies ranging from 0-1000 Hz (low range frequency), 1000-4000Hz (higher range). Low gain is applied for lower range of frequencies and higher gain for higher range of frequencies. The signal is then subjected to amplitude shaping for a better response.

Key words: Hearing aid; Hearing loss; MATLAB; audio processing; simulation

Article history: Received: 20 August 2020; Revised: 4 September 2020**;** Accepted: 6 September 2020

1. INTRODUCTION

A hearing aid generally worn in or behind the ear is a small electronic widget which amplifies some sounds (frequencies, to be specific) louder so as to help an individual person with hearing loss to listen, communicate with others and participate effectively in daily activities [1]. It has been found to help people hear better in quiet as well as noisy situations. The present study demonstrates carefully designed tuning functionality that permits the wearer to adjust the amplification of the sound as per his or her needs. In most cases of hearing impairment amplification of sound has been the treatment of choice for sensorineural problems. Generally the frequency-dependent loss of hearing sensitivity and dynamics caused by outer hair cell damage are addressed by the hearing aids which typically include a variety of signal-processing options. Recognition of voice input and its amplification with simultaneous reduction of background noise are in built parameters of the hearing aid in conversational mode. Trouble-free user interface to keep operation quick and simple is common feature for all hearing aids.

1.1 Methodology

The following table presents different degrees of hearing loss, the understanding of which is essential for the development of suitable hearing aid device [2, 3].

Different degrees of hearing loss:

Classification of Hearing Loss	Hearing level
Normal hearing	-10 dB – 26dB
Mild hearing loss	27dB-40dB
Moderate hearing loss	40dB-70dB
Severe hearing loss	70dB-90dB
Profound hearing loss	Greater than 90dB

1.2 FREQUENCY AND AMPLITUDE SHAPING:

The de noised output from the previous code is taken as the input for frequency shaping.
The transition V -4 elements have the values where the gain changes to next piecewise function.
The time of the transition, from one piecewise function to another is set in elements of the transition vector.
The maximum gain will be 'g' and the minimum gain will be 1.
Gain: used to store the gain co-efficient.
fs: sampling frequency of the input signal.

Further the gain is set for different range of frequencies. The final frequency used will be fs/2, since that is the highest frequency input signal will contain. The overall calculated gain is added with the input signal. Then the result is plotted in frequency domain. Then input signal and gain- added signal are compared.

Below is the Fig. 1 obtained for frequency shaper transfer function.

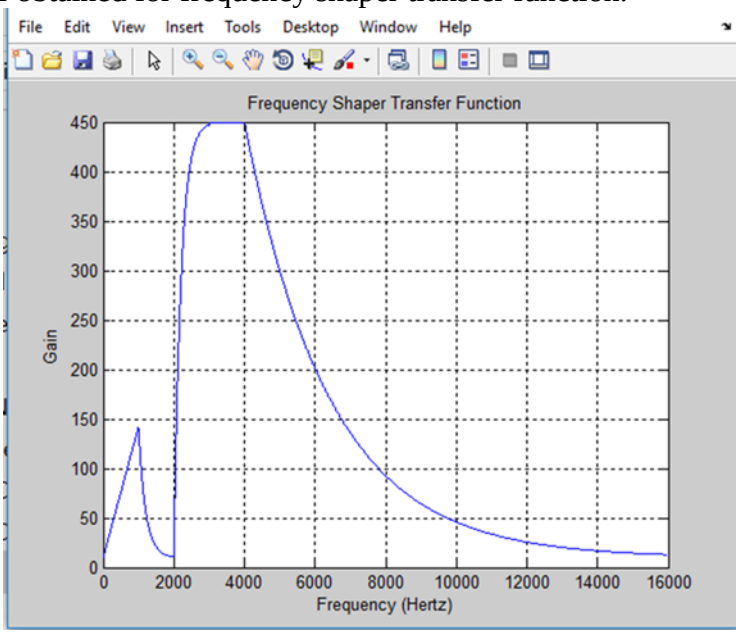

Figure 1. Frequency shaper transfer function

System Block Diagram:

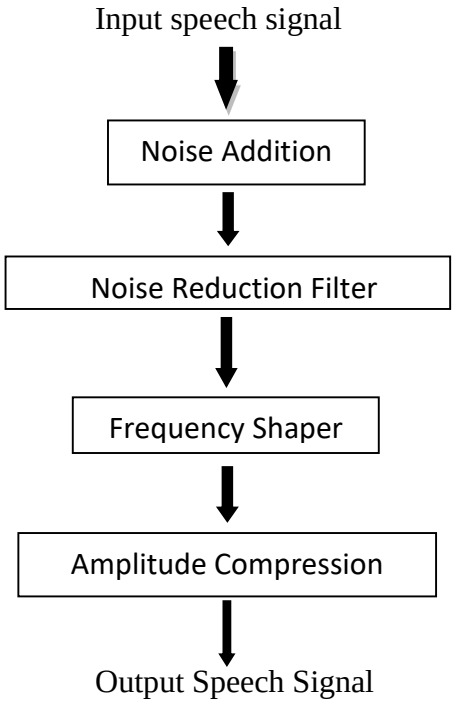

Noise Addition: Some noise has to be added in order to simulate a real situation since the input speech signal for this system is a clean signal. Both Adaptive White Gaussian Noise (AWGN) and random noise are added to the input speech signal in the present system, by using MATLAB functions.

Noise reduction filter: The potential of hearing lies in discriminating the intended speech signal from various frequencies in noisy environment. Hence a noise reduction filter is used to do away with the noise. The design of such filters becomes an important parameter.

Frequency shaper: Majority of the people who use hearing aid often complain that hearing aids amplify all the signals rather than the signal (of particular frequency range) they desire to hear. Most hearing impaired people have difficulty in hearing high frequency signal with clarity. Therefore the use of a frequency shaper becomes imperative to correct for loss of hearing at certain frequencies. The frequency shaper applies predetermined gain for higher frequencies based on requirement of individual patient.

2. SYSTEM DESIGN

2.1 Literature Survey

2.2 SIMULATION

Sl. No	Title of the paper	Publication Details	Abstract	Conclusion
01	Hearing Aid System for	IJCIS	Simulation of the present simple hearing aid was implemented using MATLAB programming	In this hearing aid, sound processing is digitalized. Thus it is possible to refine the

	Impaired People	Volume 2 N1 April 2004	language. Characteristics of noise reduction filter, frequency shaper and amplitude compression are also included herein. People with mild and moderate hearing loss are likely to be benefitted most with this device as its design allows setting of different values of gain in accordance with corresponding levels of hearing loss.	sound signal. The amplification is done when needed thus eliminating the problem of conventional amplifier This digitization helps in precisely filtering and analyzing the signals.

INTRODUCTION TO MATLAB SOFTWARE

MATLAB software is ubiquitously used in multiple areas of applied mathematics, in education and research activities in universities and in industry. MATLAB is acronym for Matrix Laboratory and the software is as such built up around vectors and matrices. While software predominantly useful for linear algebra it also acts as a great tool for solving algebraic, differential equations and numerical integration. Powerful graphic tools which can produce excellent pictures in both 2D and 3D are integral part of MATLAB. It is also a programming language, in fact, one of the easiest for writing mathematical programs. Functional tool boxes useful for signal processing, image processing, optimization, etc. are included in MATLAB.

Implementation and Simulation:

The code written in MATLAB, loads the input wave signal takes the sampling frequency and the number of bits of that signal. Then, Adaptive White Gaussian Noise (AWGN) and random noise are added to the signal before getting processed by various MATLAB functions to obtain an output that is audible to the hearing impaired person.

For simplicity, a Graphic User Interface (GUI) was built to run this Digital Hearing Aid System simulation demo. To run the demo successfully, it is required to input all the parameters viz., maximum gain to be applied, saturation power and the four frequency values where the gain varies.

3. RESULTS:

3.1 TIME DOMAIN REPRESENTATION OF THE AUDIO SIGNALS:

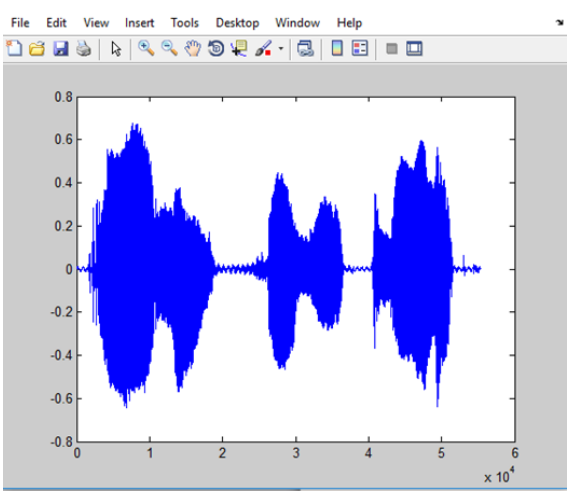

Figure 2. Original Signal

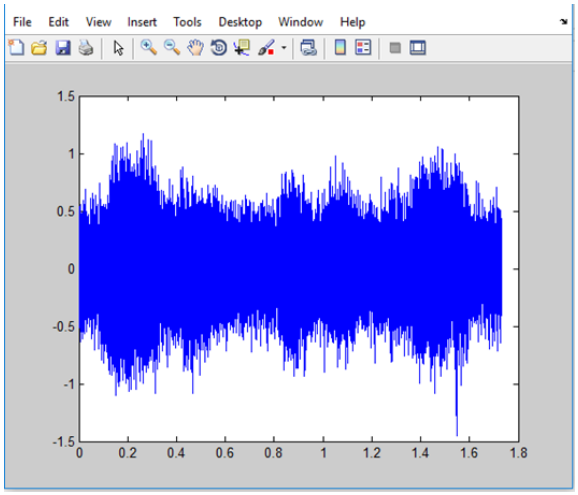

Figure 3. Original Signal after adding noise

The Fig 2 shows the original signal which is a speech signal. The audio signal is originally of 2:00 minutes duration, but it has been trimmed to a length of just 30 seconds. At first, AWGN (Additive White Gaussian Noise) is added to the signal, after which it looks like the one shown in Fig 3. This then it is subjected to further speech processing where the signal is passed into Gaussian filter for noise reduction. The output is then subjected to amplitude compression which then looks like signal in Fig 4.

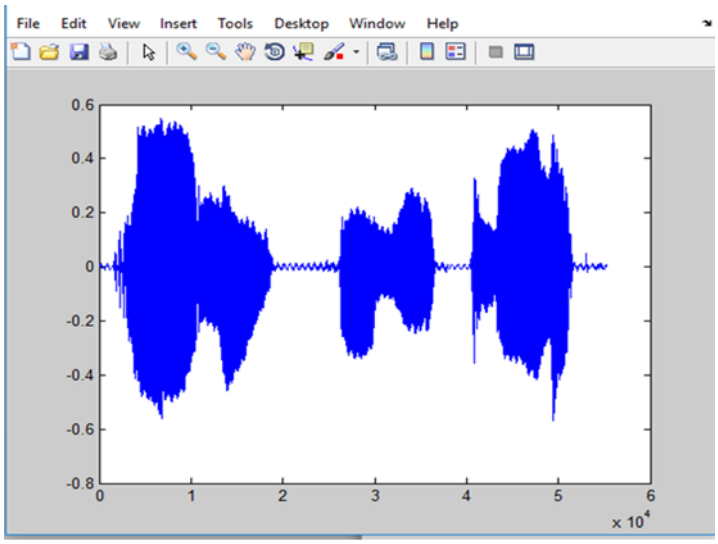

Figure 4. Signal Output after de-noising and filtering

These are the time domain representations of the signals. Similarly, the frequency domain representation of these signals is also shown below.

3.2 FREQUENCY DOMAIN REPRESENTATION OF THE AUDIO SIGNALS:

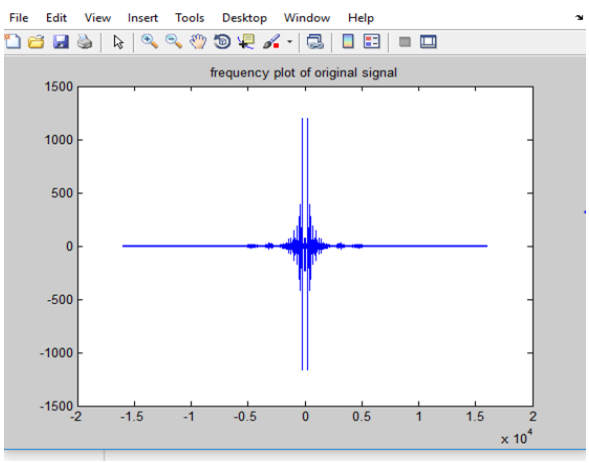

Figure 5. Original Signal

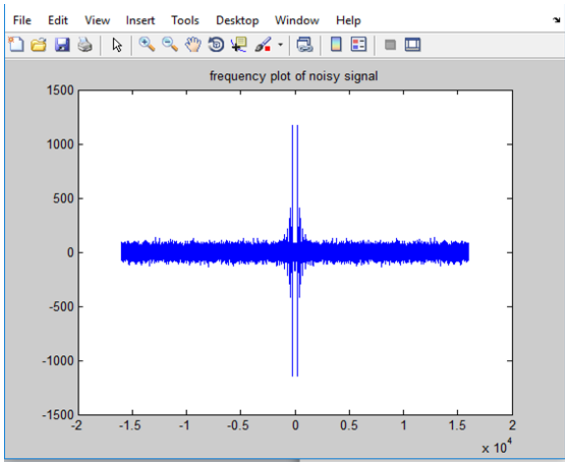

Figure 6. Original Signal after adding noise

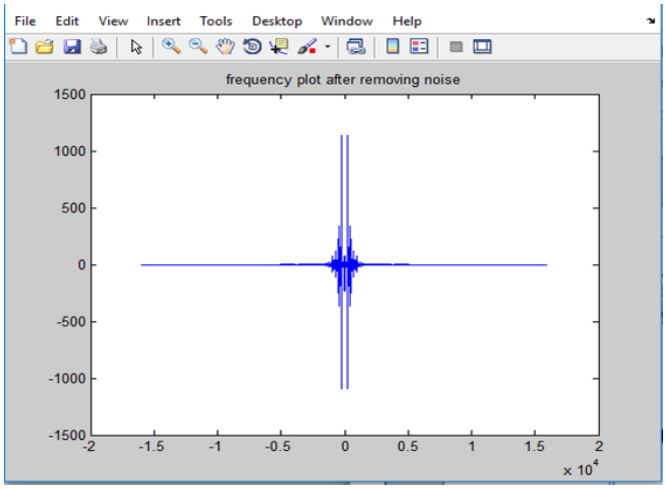

Figure 7. Signal Output after de-noising and filtering

3.3. COMPARISON OF ORIGINAL AND GAIN ADDED SIGNALS:

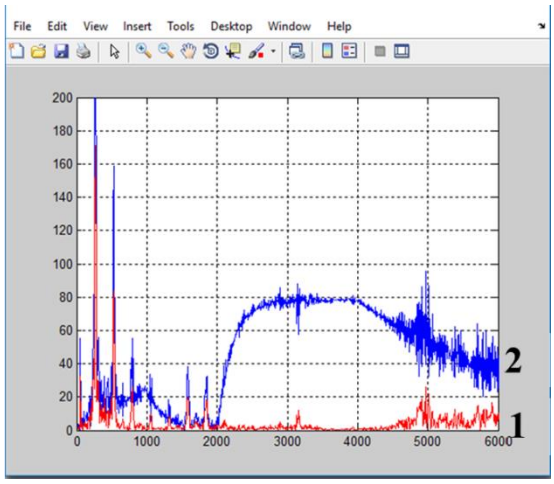

Figure 8. Comparing the original (1) and gain added (2) signals

4. CONCLUSION:

The hearing aid designed here not only just amplifies the audio signal, but also can tune to different frequencies as per the needs of the user. Clarity of the sound to the user is quite high and the use of MATLAB essentially enhances the clarity. The hearing aid designed is just a prototype and can be further developed according to the needs of the patient. Here, we have just used white Gaussian Noise. It can be tested for other types of noises as well like, periodic and coloured noise.

REFERENCES:

[1] Othman O. Khalifa, M.H. Makhtar and M.S. Baharom, Hearing Aid System for Impaired People, International Journal of Computer and Information Sciences, Vol. 2, No.2, (2004).
[2] R. Dhawan, P. Mahalaxmi Ritwik Dhawan, P. Mahalakshmi, Digital filtering in hearing aid system for the hearing impaired", 2016 International Conference on Electrical, Electronics and Optimization Techniques (ICEEOT), 2016.
[3] Brian C. J. Moore. "Diagnosis and quantification of military noise-induced hearing loss", Journal of the Acoustical Society of America, 2020.

Karnatak University
Journal of Science

ISSN: 0075-5168

Influence of hydroxyl group on the absorption and emission behavior of newly synthesized dyes using Reichardt method

Shivaraj A. Patil
Mahantesh B. Budri
Sanjeev R. Inamdar
Kalagouda B. Gudasi

Shivaraj A. Patil, Mahantesh B. Budri, Sanjeev R. Inamdar, Kalagouda B. Gudasi, “Influence of hydroxyl group on the absorption and emission behavior of newly synthesized dyes using Reichardt method” Karnatak University Journal of Science 51, 204-210 (2020).

Influence of hydroxyl group on the absorption and emission behavior of newly synthesized dyes using Reichardt method

Shivaraj A. Patil[a], Mahantesh B. Budri[b], Sanjeev R. Inamdar[a,] *, Kalagouda B. Gudasi[b]
[a]Department of Physics, Karnatak University, Dharwad 580003, India
[b]Department of Chemistry, Karnatak University, Dharwad 580003, India
***Corresponding author.** him_lax3@yahoo.com

Abstract

The absorption and emission spectra of newly synthesized, structurally similar dyes *(E)-N'*-(2-hydroxybenzylidene)-3,5-di-*tert*-butyl-2-hydroxybenzohydrazide (A) and *(E)-N'*-(2-4-dihydroxybenzylidene)-3,5-di-*tert*-butyl-2-hydroxybenzohydrazide (A-OH) in alcohol series were recorded to investigate their solvatochromic behavior. Reichardt's method, which is based on empirical polarity scale E_N^T was used to estimate the difference between ground and excited state dipole moment (Δμ). The computational studies were performed using Gaussian 09 software to study the chemical hardness of the molecules at ground state, which was helpful to study the effect of –OH group. The polarizable continuum model *i.e.* IEF-PCM was used to calculate energy required to excite the molecules in methanol theoretically. On introducing an additional –OH group, Δμ decreases and the molecule gets stabilized.

Keywords: photo-physicalproperties; DFT/TD-DFT; dipole moment; solvatochromism; Reichardt method; hydroxyl group.
Article history: Received: 10 August 2020; Revised: 18 August 2020**;** Accepted: 4 September 2020

1 Introduction

The Schiff base of salicylaldehyde derivatives bear a unique biological and optoelectronic properties. The applications of a molecule is entirely depends on its structure. By logical structural design, one can achieve the desired application. The molecules reported in the present study are specially designed to sense biologically important zinc ion [1, 2]. The difference in the ground and excited-state dipole moment plays an important role in dye-sensitized solar cells, OLED, biological applications, etc. [2]. The presence of electron-donating and electron-accepting groups within a molecule induces the ICT (Intra molecular charge transfer) character. For molecule A, at ground state (HOMO), electron density is located on the right side of the molecule (Fig. 5) but in excited state (LUMO), it is slightly shifted to left side. The same trend is followed in A-OH. This shift in electron density on excitation indicates the ICT process. Therefore, it is important to study the photo-physical properties of these probes.

We can see plenty of papers on the measurement of ground and excited state dipole moment in protic, aprotic and general solvents using Lippert-Mataga, Bilot-Kawski, Kawski-Chamma-Viallet, Bakshiev and other methods [3-10]. Out of these, we have concentrated on Reichardt's method to measure the variation in difference between the ground and excited state dipole moment. In the present work, we have selected two structurally similar probes which are differing by an –OH group. The effect of this hydroxyl group on the absorption and emission behavior of probes in the alcohol series and on the difference in ground and excited state dipole moment by employing

Reichardt's method [3] have been studied. Also, DFT calculations like chemical hardness and excitation energy has been used to support the experimental results.

2 Materials and methods

Spectroscopic grade (99.5%) alcohols were procured from S.D-fine chemicals and SpectroChem Pvt Ltd, Mumbai (India). All the solvents were used as received without further purification. A dual-beam UV-Visible spectrophotometer (PerkinElmer model Lambda 365) and spectrofluorometer (JY Horiba, model Fluoromax4) were used to record steady-state absorption and fluorescence emission spectra respectively. All spectroscopic measurements performed at room temperature (298 K) with an accuracy of ±1 nm. The solute molecules *viz*, *(E)-N'*-(2-hydroxybenzylidene)-3,5-di-*tert*-butyl-2-hydroxybenzohydrazide (A) and *(E)-N'*-(2-4-dihydroxybenzylidene)-3,5-di-*tert*-butyl-2-hydroxybenzohydrazide (A-OH) (Fig.1a and 1b) were synthesized and purified as reported in our earlier work [1]. The concentration of the solute was kept low (~10 μM) in order to reduce possible self-quenching and inner filter effects.

In order to support the experimental results, we have carried out theoretical calculations using the Gaussian 09 software [4]. The hybrid density function Backe-Lee-Young-Parr composite of exchange-correlation functional (B3LYP) method and standard 6-311 g(d) basis set were used to optimize the structure at ground state in gas phase. The ground state optimized structures of the molecules A and A-OH with vector direction of ground state dipole moment is shown in the Fig. 2. The excitation energies were calculated by using time-dependent density functional theory with the same B3LYP/6-311 g (d) basis set.

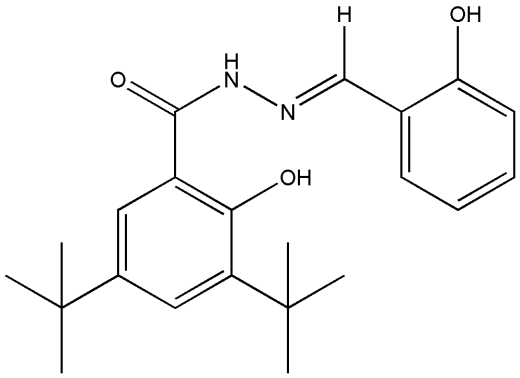

Figure 1a: Structure of A

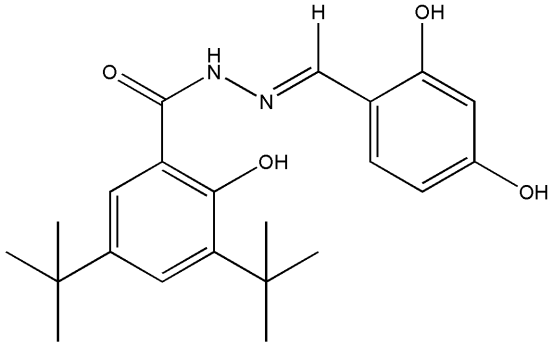

Figure 1b: Structure of A-OH

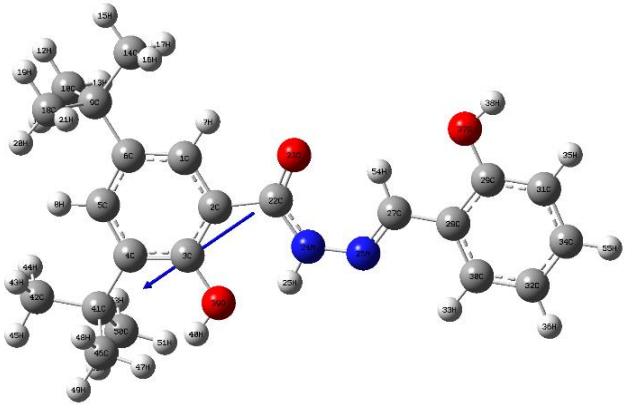

Figure 2a. Ground state optimized structure of A

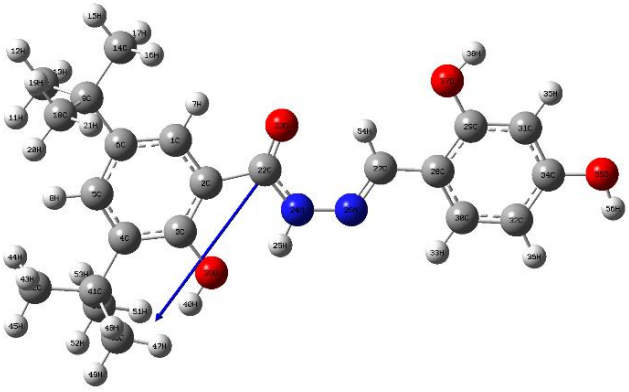

Figure 2b. Ground state optimized structure of A-OH

3 Theory

3.1 Estimation of change in dipole moment on excitation

Reichardt method based on empirical polarity scale E_N^T gives the difference (Δμ) in the ground and excited-state dipole moments. The microscopic solvent polarity E_N^T which is an empirical measure based on the solvatochromic behavior of Betaine dye as a probe molecule correlated with spectral data is given by,

$$\bar{\nu}_a - \bar{\nu}_e = 11307.6\left[\left(\frac{\Delta\mu}{\Delta\mu_B}\right)^2\left(\frac{a_B}{a}\right)^3\right]E_N^T + \text{const.} \quad (1)$$

where a_B= 6.2 Å and $\Delta\mu_B$ = 9 D are the Onsager cavity radius and change in dipole moment upon excitation for Betaine dye. a and Δμ are the corresponding quantities for the solute molecule under study. E_N^T is defined as follows using water ($E_N^T = 1$) and tetramethylsilane (TMS)($E_T^N = 0$) as reference solvents,

$$E_T^N = \frac{E_T(\text{Solvent}) - E_T(\text{TMS})}{E_T(\text{Water}) - E_T(\text{TMS})} = \frac{E_T(\text{Solvent}) - 30.7}{32.4} \quad (2)$$

Where, $E_T(\text{Solvent}) = \frac{hcN}{\lambda_{max}} = \frac{28591}{\lambda_{max}}$ (in Kcal mol^{-1})

λ_{max} is the absorption maxima of dye in the solvent.

Finally, the change in dipole moment ($\Delta\mu$) can be calculated by

$$\Delta\mu = \mu_e - \mu_g = \sqrt{\frac{m \times 81}{\left(\frac{6.2}{a}\right)^3 \times 11307.6}} \quad (3)$$

Where, 'm' is the slope of the linear plot of E_T^N v/s (ν_a- ν_e).

The Onsager cavity radius 'a' of the solute molecule can be calculated from the molecular volume according to Suppan's equation [5] given by,

$$a = \left(\frac{3M}{4\pi\delta N}\right)^{\frac{1}{3}} \quad (4)$$

Where, N is Avogadro's number, M is the molecular weight and δ is the density of the solute. The calculated values of Onsager cavity radius (a) using eq. (4) are 5.2131 Å and 5.2522Å for the molecules A and A-OH respectively.

4 Results and discussion

The electronic structure in both ground and excited state influences the spectral behavior of an organic molecule. The variation of viscosity, refractive index, polarity, dielectric constant or polarizibility of the surrounding medium depends on the solvent. Hence the study of absorption and emission spectra in series of alcohols plays an important role in understanding the electronic structure of the molecule. The choice of solvents was to study the effect of –OH group with relevant change in microenvironment. The empirical polarity scale E_N^T, absorption (ν_a in cm^{-1}) and emission maxima (ν_f in cm^{-1}) of the molecules A and A-OH in alcohol series were presented in Table 1. The difference between first absorption maxima and emission maxima gives Stoke's shift ($\Delta\nu$ in cm^{-1}). The compound A shows more Stoke's shift than A-OH.

The normalized absorption and emission overlap of the molecules A and A-OH were shown in Fig. 3a and Fig. 3b respectively. From Fig. 3 (a and b) it is observed that, the molecule A exhibits a little shift in the emission as compared to A-OH indicating that the effect of –OH group on the optical properties of dyes. The Fig. 4a and 4b shows the graph of normalized solvent polarity parameter versus Stokes shift for the molecules A and A-OH respectively. The slope value given in Table 2 is used to determine the difference between ground and excited state. Table 3 shows the experimentally measured variation in dipole moment (Δμ) on excitation. The Δμ for A is found to be 2.46 D and that of A-OH is 2.27 D. The presence of an extra –OH group decreases the variation in dipole moment on excitation due to increased charge transfer process. The hydroxyl group (-OH), is an electron donating group. The presence of more hydroxyl groups, enhance the ICT character. From Table 4, we can observe that, the ICT character of molecule A with ΔE=4.2080 eV has increased by adding a hydroxyl group with ΔE=4.0899 eV. Lower ΔE indicate higher resonance. Hence ICT enhancement is due to the addition of hydroxyl group.

The chemical stability of a molecule can be explained by chemical hardness (η) which can be calculated as half of the difference between LUMO and HOMO energies. i,e.,

$$\eta = \frac{E_{LUMO} - E_{HOMO}}{2} \quad (5)$$

Table 4 gives the Energy of HOMO, LUMO and chemical hardness. The η values of A and A-OH are 2.1040 and 2.0449 respectively. From these values it is clear that, the molecule A-OH is softer than of A and it requires small energy to excite. Fig. 5 shows the HOMO, LUMO of the molecules A and A-OH with the energy values in eV.

Another notable change due to addition of hydroxyl group is excitation energy. Table 5 presents the experimental and theoretical energy required to excite the molecule A and A-OH in methanol. From Table 5 it can be concluded that, on introducing an extra –OH group, the energy required to excite the molecule decreases.

Table 1. Empirical polarity scale E_N^T for alcohols and spectroscopic data of A and A-OH molecules in alcohols

S. No.	Solvent	$^{\#}E_N^T$	A			A-OH		
			Absorption ν_a (cm^{-1})	**Emission ν_a (cm^{-1})**	**Stokes Shift $\Delta\nu$ (cm^{-1})**	**Absorption ν_a (cm^{-1})**	**Emission ν_f (cm^{-1})**	**Stokes Shift $\Delta\nu$ (cm^{-1})**
1	Methanol	0.762	29940.12	21097.05	8843.07	29154.52	20283.98	8870.54
2	Ethanol	0.654	29940.12	20576.13	9363.99	28985.51	20408.16	8577.34
3	Propanol	0.617	29850.75	20449.90	9400.85	29069.77	20283.98	8785.79
4	Butanol	0.586	29761.90	20491.80	9270.10	29069.77	20408.16	8661.60
5	Pentanol	0.568	29673.59	20366.60	9306.99	28985.51	20366.60	8618.91
6	Hexenol	0.559	29761.90	20408.16	9353.74	28985.51	20366.60	8618.91
7	Heptanol	0.549	29761.90	20283.98	9477.93	28985.51	20408.16	8577.34
8	Octanol	0.537	29673.59	20366.60	9306.99	28985.51	20366.60	8618.91
9	Nonanol	0.528	29673.59	20408.16	9265.43	28985.51	20408.16	8577.34
10	Decanol	0.525	29585.80	20325.20	9260.60	28985.51	20366.60	8618.91

→ Ref. [3]

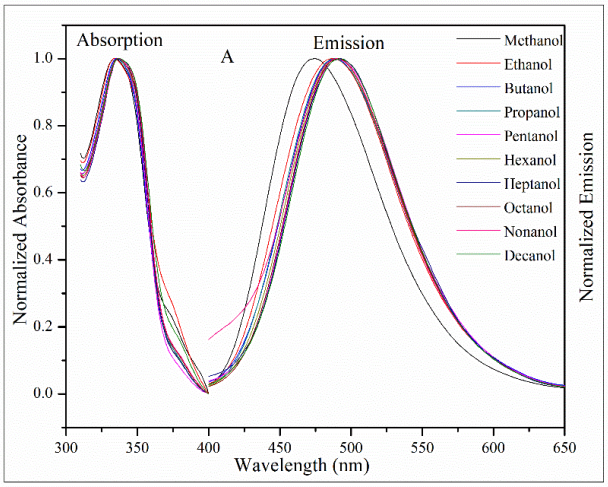

Figure 3a. Absorption and emission overlap of A

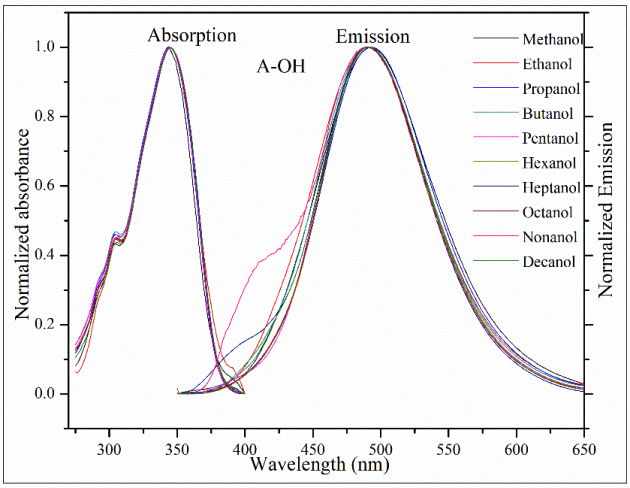

Figure 3b. Absorption and emission overlap of A-OH

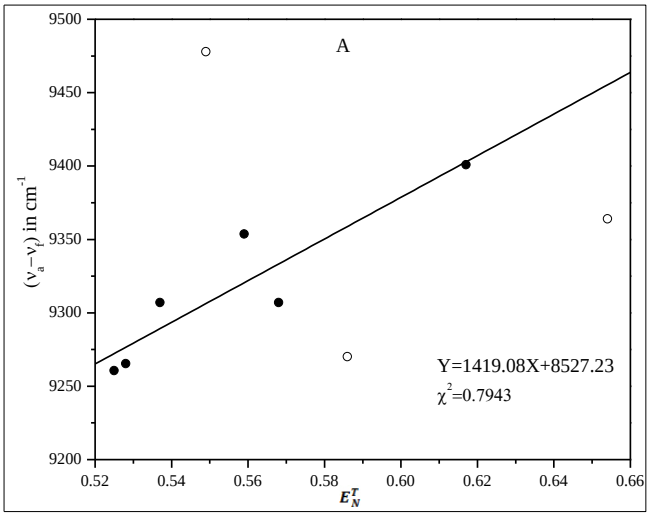

Figure 4a. The plot show E_N^T vs ν_a- ν_e for A

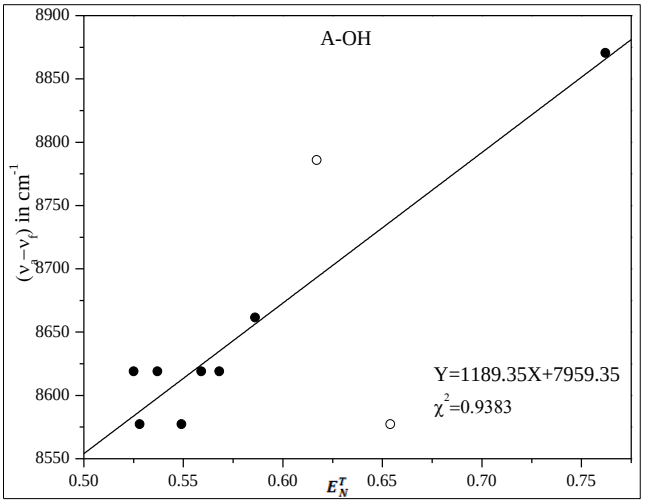

Figure 4b. The plot show E_N^T vs ν_a- ν_e for A-OH

Table 2: Graphical data of E_N^T vs (ν_a- ν_e)

	A	A-OH
Slope	1419.08	1189.35
Intercept	8527.23	7959.35
R^2	0.79	0.94

Table 3: Experimental variation in dipole moment on excitation

	Δμ in D
A	2.46
A-OH	2.28

Table 4: Energy of HOMO, LUMO and chemical hardness

	Energy in eV	
	A	A-OH
LUMO	-1.4261	-1.5009
HOMO	-5.6341	-5.5908
ΔE	4.2080	4.0899
η	2.1040	2.0449

Table 5: Experimental and theoretical Excitation energies in eV

	Excitation energy in eV	
	Experimental	Theoretical
A	3.7121	3.6263
A-OH	3.6147	3.4963

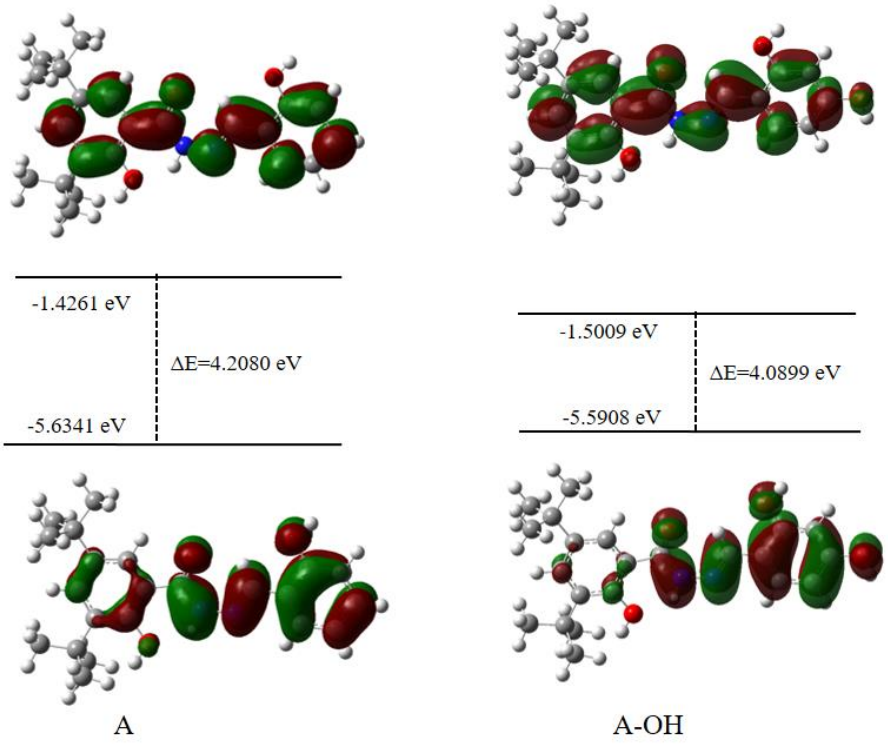

Figure 5. HOMO and LUMO of the molecules A and A-OH

Conclusion

In present work, we have explained solvatochromic behavior of the molecules A and A-OH in alcohol series. The theoretically calculated HOMO-LUMO energies and chemical hardness value suggests that the molecule A-OH is softer than the molecule A. The same has been reflected in the experimental and theoretical excitation energy calculations. The soft molecule A-OH require less

energy to excite than the molecule A. The difference between electronic ground and excited state dipole moment has been determined experimentally. From the results, we can conclude that the presence of an additional –OH group in second molecule induces large ICT character resulting in decreased dipole moment difference. The work will be extended to measure ground and excited state dipole moment in protic and aprotic solvents.

Acknowledgement

The authors thank USIC, Karnatak University, Dharwad for UV-Visible Spectrophotometer. One of the authors (SAP) is grateful to Karnataka state (BCWD) govt. for providing PhD fellowship.

References

[1] A Novel Switch on Optical Probe for Selective Sensing of Zn (II) Ion in Acetonitrile Medium: Spectroscopic and Computational Studies Mahantesh Budri, Geeta Chimmalagi, Ganesh Naik, Shivaraj Patil, Kalagouda Gudasi and Sanjeev Inamdar Journal of Fluorescence 29:1065–1077 (2019).

[2] A novel switch on and reversible optical sensor as an efficient, selective receptor for Zn(II) ion and its biological application Mahantesh Budri, Ganesh Naik, Shivaraj Patil, Prajakta Kadolkar, Kalagouda Gudasi, Sanjeev Inamdar Spectrochemica Acta Part A: 224, 117462 (2020).

[3] Solvatochromic Dyes as Solvent Polarity Indicators, Christian Reichardt, Chemical Reviews, 1594, *94*, 231S2358.

[4] Gaussian 09, Revision D.01, M. J. Frisch, G. W. Trucks, H. B. Schlegel, G. E. Scuseria, M. A. Robb, J. R. Cheeseman, G. Scalmani, V. Barone, B. Mennucci, G. A. Petersson, H. Nakatsuji, M. Caricato, X. Li, H. P. Hratchian, A. F. Izmaylov, J. Bloino, G. Zheng, J. L. Sonnenberg, M. Hada, M. Ehara, K. Toyota, R. Fukuda, J. Hasegawa, M. Ishida, T. Nakajima, Y. Honda, O. Kitao, H. Nakai, T. Vreven, J. A. Montgomery, Jr., J. E. Peralta, F. Ogliaro, M. Bearpark, J. J. Heyd, E. Brothers, K. N. Kudin, V. N. Staroverov, T. Keith, R. Kobayashi, J. Normand, K. Raghavachari, A. Rendell, J. C. Burant, S. S. Iyengar, J. Tomasi, M. Cossi, N. Rega, J. M. Millam, M. Klene, J. E. Knox, J. B. Cross, V. Bakken, C. Adamo, J. Jaramillo, R. Gomperts, R. E. Stratmann, O. Yazyev, A. J. Austin, R. Cammi, C. Pomelli, J. W. Ochterski, R. L. Martin, K. Morokuma, V. G. Zakrzewski, G. A. Voth, P. Salvador, J. J. Dannenberg, S. Dapprich, A. D. Daniels, O. Farkas, J. B. Foresman, J. V. Ortiz, J. Cioslowski, and D. J. Fox, Gaussian, Inc., Wallingford CT, 2013.

[5] Excited-state dipole moments from absorption/fluorescence solvatochromic ratiosP. Suppan, Chemical Physics Letters 94, 272 (1983).

[6] Effect of hydroxyl group on the photophysical properties of benzo[a]xanthenes – Solvatochromic studies and estimation of dipole moment Komal Aggarwal, Jitender M. Khurana Journal of Photochemistry and Photobiology A: Chemistry 276, 71– 82 (2013).

[7] Investigation of Solvent Effects on Photophysical Properties of New Aminophthalimide Derivatives-Based on Methanesulfonate Ayse Tan, Ebru Bozkurt & Yunus Kara Journal of Fluorescence 27:981–992 (2017).

[8] Estimation of ground- and excited-s3tate dipole moments of Nile Red dye from solvatochromic effect on absorption and fluorescence spectra A. Kawski, P. Bojarski, B. Kuklin´ ski Chemical Physics Letters 463, 410–412 (2008).

[9] Molecular volumes and the Stokes-Einstein equation John T. Edward Journal of Chemical Education Volume 47, Number 4, 261-270 (1970).
[10] Effect of solvent polarity on the photo-physical properties of chalcone derivatives Rekha Kumari, Anitha Varghese, Louis George and Sudhakar Y. N. *RSC Adv*ances 7, 24204 (2017).

KARNATAK UNIVERSITY JOURNAL OF SCIENCE

INSRTUCTIONS TO THE AUTHORS

General Information

Manuscript must be submitted as Microsoft Word document with text in Times New Roman font with size 12. The manuscript be structured as: Abstract, Introduction, Materials and Methods, Results and Discussions, Conclusions, Acknowledgment followed by References. The length of MS should not exceed 12 typed pages.

1. Title of research article should be centered and followed by authors, their affiliation, along with contact e-mail ID of the corresponding author.
2. Name of the corresponding author should be identified by an asterisk (*).
3. Abstract not exceeding 250 words be included on Title page followed by 4-5 key words. Each key word must be separated by a semicolon (;).
4. The references should be cited in text with a square bracket [21] and be limited to 30.
5. Subtitles used in the manuscript must be in bold, and follow the numbering order as: 1, 1.1, 1.2; 2, 2.1, 2,2; etc.
6. Text after the subtitle should follow directly without paragraph, whereas subsequent paragraphs must start with paragraphs.
7. Coloured figures will be included in print copy, if necessary.
8. Representation of figure, scheme and table should be in the body of the text as **Fig. 1, Scheme 1** and **Table1,** respectively. If the sentence starts with the indication of any Figure then it should be written as **Figure 1** (For example). The examples of figure, scheme and table captions are to be represented as:

Figure1. Fluorescence spectra of ternary quantum dots.

Scheme1. Synthesis of chromophores.

Table 1. Physical and thermal properties of NLO materials.

9. Style of references

   a. Books

i. W. J. Koros, B. T.Chen, R. T. Chem, Handbook of Separation Process Technology, Wiley-Interscience: New York, USA, p67 (1987)

b. Book Chapter

i. M. Zhu, T. Y. Jhab, K. K. Sirkar, Optical plastics – a wonderful material, In: Basics of Non-linear Optics, T. Brouse, R. A. Huggins, eds. Elsevier: New York, USA, p54 (2001)

c. Journals

i. Photophysics and rotational diffusion dynamics of large prolate non-polar laser dyes Sanjeev R. Inamdar, J.R. Mannekutla, M.S. Sannaikar, M.N. Wari, B.G. Mulimani and M.I. Savadatti J. Mol. Liquids (Elsevier), 268C, 66-76 (2018)

ii. P. M. Patil, Monisha Roy, A. Shashikant, S. Roy and E. Momoniat (2018): Triple diffusive mixed convection from an exponentially decreasing mainstream velocity, International Journal of Heat and Mass Transfer (Elsevier) 124, 298-306 (2018)

iii. S. Sebastian, N. Sundaraganesan, Spectrochim. Acta (Elsevier), A75, 941-952 (2010).

d. Conference Proceedings

i. K.P. Medium, A.S.R. Usha, C.K. Menon, Proc. 5th Annual Conference on Polymers, Istanbul, Turkey, Sept. 5-21, p. 47 (1997).

10. You may submit the manuscript as a single MS word file containing all the figures, tables, schemes, figure captions. Include a cover letter addressed to Chief Editor, KU J Science, Department of Physics, Karnatak University, Dharwad 580003 (e-mail: srinamdar@kud.ac.in; him_lax3@yahoo.com) that must contain the names and contact details of at least two potential reviewers.